Imperial College London

The Seismic Monitoring of Heavy Oil Reservoirs

A dissertation submitted to the Department of Earth Science and Engineering

Imperial College London

In fulfillment of the requirements for the degree of

Master of Philosophy

Author:

Hussam A. Busfar

Supervisor:
Prof. Ann Muggeridge

May 2019

Abstract

Most of the oil produced nowadays comes from aging fields where the rate at which it is replaced by new field discoveries has been declining in recent decades. Conventional light oil is becoming harder to find so companies are looking to exploit huge resources of more viscous oil. Advances in drilling technology, increased computational power and improved reservoir management made it easier and cheaper to produce more oil from the vast reserves of heavy oil worldwide. Steam injection is the most widely used enhanced oil recovery method for these oils. Better monitoring of the steam chamber in a steam injection operation helps to increase the sweep efficiency and improve the management of the reservoir.

This thesis investigates the feasibility for using AVO to better monitor steam injection in heavy oil reservoirs. Many factors such as temperature, pressure, fluid saturations and oil viscosity interact during thermal production of heavy oil, which complicates the interpretation of seismic data.

The investigation is based upon a geological model inspired by a real field case of Emlichheim oil field in Germany. The research uses a combination of reservoir simulation, rock physics and amplitude versus offset seismic analysis to investigate the characterization of the vertical extent of the steam chamber using AVO. This is done by first using a reservoir simulation software (STARS) to model the dynamics of steam injection into a heavy oil reservoir with properties similar to those of Emlichheim. The reservoir properties obtained from the simulation are then used as input into a rock physics code that was developed in MATLAB. This code calculates the P- and S-wave velocities along with the densities of the saturated rock. This is then used as input into HampsonRussell software, which calculates the intercept and gradient of the two-term Aki-Richards approximation of the amplitude versus offset

(AVO) equation. A sensitivity study was conducted to test the effect of temperature, porosity, pressure, steam saturation and oil API on the intercept and gradient of the AVO approximation. Pre steam injection, the AVO gradient and intercept are most sensitive to porosity and pressure changes at the top of the reservoir. Post steam injection, the AVO intercept and gradient are most sensitive to porosity, pressure and steam saturation at the top of the reservoir, while at the bottom of the steam chamber they are most sensitive to steam saturation, porosity and pressure.

In this thesis we study factors that influence steam flood performance and sensitivity of the AVO response to various possible rock and fluid properties. The study of the gradient and intercept of the AVO at the base of the steam chamber concluded that they are both positive at the base of the steam chamber within the reservoir. This led to a novel technique in estimating the bottom of the steam chamber, thus estimating the thickness of the steam chamber. This is a very important and powerful tool as it allows us to be more confident in our pick of the bottom of the steam chamber when it is not possible to visually identify the bottom of the steam chamber using time-lapse seismic surveys. This helps to delineate the vertical extent of the steam front, which can be used for history matching and improving the reservoir simulation which ultimately helps increase the sweep efficiency and the oil recovery factor by better managing the oil reservoir.

Declaration of Originality

I declare that the work in this thesis is my own and that any work produced by others is appropriately referenced. The research was supervised by Prof. Ann Muggeridge and was partially supervised by Prof. Helmut Jakubowicz, Dr. Ian Bradford and Dr. Adam Booth.

Hussam Busfar
Department of Earth Science and Engineering
Imperial College London

Copyright Declaration

The copyright of this thesis rests with the author and is made available under a Creative Commons Attribution Non-Commercial No Derivatives license. Researchers are free to copy, distribute or transmit the thesis on the condition that they attribute it, that they do not use it for commercial purposes and that they do not alter, transform or build upon it. For any reuse or redistribution, researchers must make clear to others the license terms of this work.

Hussam Busfar

Department of Earth Science and Engineering

Imperial College London

Acknowledgements

I would like to thank my supervisor Prof. Ann Muggeridge for her patience, support and guidance throughout my time here at Imperial College. This work wouldn't have been completed without her support.

I would like to thank Saudi Aramco for sponsoring me. I would also like to thank Prof. Helmut Jakubowicz for his supervision at the beginning of the research until he left Imperial College. The same goes to Dr. Adam Booth who helped me with the AVO related part of this research. Many thanks to Prof. Robert Zimmerman for answering many of my late night rock physics questions along with being my 9-months report examiner. I would like to extend my gratitude to both Prof. Joanna Morgan and Prof. Karl Stephen for agreeing to be my internal and external examiner, respectively. Dr. Ian Bradford from Schlumberger in Cambridge was a great mentor at the beginning of this research and until he left us unexpectedly. May he rest in peace.

My colleagues at Imperial College: Prof. Ahmad Abushaikha, Dr. Zaki Al Nahari, Dr. Shamsudeen Abubakar, and Dr. Morteza Nejati were helpful on both the academic and personal level while in London. My life in London wouldn't be the same without Mayed Al Qasimi, Quentin Leclerc, Lucas Conzen and Hisham Al-Hassan. I am grateful to Manuela Montenegro for all her love, companionship and support during the past few years.

Last but by no means least, I would like to thank my family, especially my amazing and beloved parents, Abdullah Busfar and Ferial Eghbalian, for always being there for me and for their unconditional love. This work is dedicated to them.

Publications

Busfar, H., & Toksöz, M. N. (2013). Determining the focal mechanisms and depths of relatively small earthquakes using a few stations by full waveform modelling. Geophysical Prospecting,1-13. doi:10.1111/1365-2478.12018

Busfar, H., & Muggeridge, A. (2019). The Seismic Monitoring of Heavy Oil Reservoirs. Geophysical Prospecting, (in progress)

Table of Contents

ABSTRACT **2**

ACKNOWLEDGEMENTS **6**

LIST OF FIGURES **11**

LIST OF TABLES **20**

1. INTRODUCTION **22**

1.1 MOTIVATION 22

1.2 AIMS AND OBJECTIVES 25

1.3 SUMMARY OF REMAINDER OF THESIS 26

2. BACKGROUND AND LITERATURE REVIEW **28**

2.1 INTRODUCTION 28

2.2 HEAVY OIL PRODUCTION USING STEAM INJECTION 31

2.2.1 Steam assisted gravity drainage (SAGD) *32*

2.2.2 Cyclic steam simulation *32*

2.2.3 Steam flooding *33*

2.3 SWEEP EFFICIENCY 34

2.4 CASE STUDY 35

2.5 TIME-LAPSE SEISMIC MONITORING OF STEAM INJECTION 38

2.6 SUMMARY 45

3. RESERVOIR SIMULATION **47**

3.1 INTRODUCTION 47

3.2 METHOD 47

3.3 Results 57

3.4 Sensitivity of the growth of the steam chamber to different inputs 63

3.5 Summary 73

4. ROCK PHYSICS MODELLING 75

4.1 Grain Moduli 76

4.2 Dry Rock Moduli 77

4.3 Fluid Bulk Moduli 79

4.4 Brine Bulk Moduli 80

4.5 Oil Bulk Moduli 82

4.6 Mixing Laws 89

4.7 Validation against Experimental and Published Data 93

4.8 Sensitivity of Vp and Vs to Different Inputs 102

5. AVO ANALYSIS 106

5.1 Introduction 106

5.2 Theory and Methodology 107

5.3 Results and Discussion 109

5.3.1 Sensitivity analysis with 5 degrees of freedom 109

5.3.1.1 Pre steam injection 110

5.3.1.2 Post steam injection 118

5.3.2 Using AVO to determine the thickness of steam chamber 132

5.3.2.1 Validation using model A 134

5.3.2.1 Validation using model B 143

5.4 Summary 152

6. SENSITIVITY OF THE AVO ANALYSIS TO NOISE 155

6.1 Testing AVO procedure robustness using model A 156

6.2 Testing AVO procedure robustness using model B..... 164

6.3 Summary..... 172

7. CONCLUSIONS AND FUTURE WORK..... 175

7.1 Conclusions..... 175

7.2 Future Work..... 180

APPENDIX 181

Appendix A: Reservoir Simulation (STARS input file) 181

Appendix B: Steam saturations for the 7 other models in the sensitivity study 193

Appendix C: MATLAB Rock Physics Code..... 204

REFERENCES..... 207

List of Figures

FIGURE 1.1: DIFFERENT FORECASTS OF WORLD OIL PRODUCTION (SORRELL ET AL., 2010). 23
FIGURE 1.2: DIFFERENT FORECASTS OF WORLD OIL DEMAND IN MB/D (DALE & FATTOUH, 2018). 23
FIGURE 1.3: FORECAST OF THE WORLD'S OIL PRODUCTION SOURCES (ALEKLETT ET AL., 2010)..... 24
FIGURE 1.4: GENERAL WORKFLOW APPLIED TO THE SYNTHETIC EMLICHHEIM FIELD MODEL..... 26
FIGURE 2.1: STEAM ASSISTED GRAVITY DRAINAGE (THOMAS, 2008). 32
FIGURE 2.2: CYCLIC STEAM INJECTION (AFTER ALVAREZ & HAN, 2013). 33
FIGURE 2.3: STEAM FLOODING (SHAH ET AL, 2010). 34
FIGURE 2.4: GLOBAL THERMAL ENHANCED OIL RECOVERY INCREMENTAL PRODUCTION IN 2008 ALONG WITH THE NUMBER OF STEAM INJECTION PROJECTS (BRANDT & UNNASCH, 2010). IN SITU COMBUSTION DATA IS NOT INCLUDED BECAUSE IT IS OF SECONDARY IMPORTANCE. 36
FIGURE 2.5: ENHANCED OIL RECOVERY METHODS BY LITHOLOGY BASED ON A TOTAL OF 1507 PROJECTS (ALVARADO & MANRIQUE, 2010)..... 37
FIGURE 2.6: LOCATION MAP OF THE EMLICHHEIM OILFIELD AND THE ADJACENT OILFIELDS IN THE AREA WEST OF THE RIVER EMS (LEONHARDT, 2001). 38
FIGURE 2.7: VERTICAL CROSS SECTIONS SHOWING SEISMIC VELOCITY VARIATIONS OVER A PERIOD OF 12 WEEKS OF STEAM INJECTION IN A SAGD OPERATION. STEAM WAS INJECTED IN THE UPPERMOST HORIZONTAL WELL. THE RED COLOUR CORRESPONDS TO SLOWER SEISMIC VELOCITY (FORGUES ET AL., 2011). 41
FIGURE 2.8: VERTICAL CROSS-SECTIONS SHOWING SEISMIC AMPLITUDE VARIATIONS OVER A PERIOD OF 12 WEEKS OF STEAM INJECTION IN A SAGD OPERATION. OIL IS PRODUCED FROM THE SOUTHERN MOST HORIZONTAL WELL WHERE A DECREASE IN SEISMIC AMPLITUDE IS OBSERVED AND REPRESENTED BY THE GREEN COLOUR (FORGUES ET AL., 2011)..... 42
FIGURE 2.9: CROSS SECTION SHOWING THE ESTIMATED TIME-LAPSE VELOCITY STRUCTURE IN A 43
FIGURE 2.10: AMPLITUDE REFLECTIONS SHOWING GAS IN THE GULF OF MEXICO (COOPER, 2010). 44
FIGURE 3.1: WATER-OIL RELATIVE PERMEABILITIES. 50
FIGURE 3.2: LIQUID-GAS RELATIVE PERMEABILITIES. 51
FIGURE 3.3: TERNARY SATURATION AFTER 10 YEARS OF CONTINUOUS STEAM INJECTION USING 50×1×10 GRID BLOCKS. 52
FIGURE 3.4: TERNARY SATURATION AFTER 10 YEARS OF CONTINUOUS STEAM INJECTION USING 100×1×20 GRID BLOCKS. 53
FIGURE 3.5: TERNARY SATURATION AFTER 10 YEARS OF CONTINUOUS STEAM INJECTION USING 100×1×40 GRID

blocks. 53
Figure 3.6: Ternary saturation after 10 years of continuous steam injection using 200×1×40 grid blocks. 54
Figure 3.7: Ternary saturation after 10 years of continuous steam injection using 200×1×80 grid blocks. 54
Figure 3.8: Cumulative oil production over 10 years of steam flooding for simulations with five different grids. The number of grid blocks in the x, y, and z direction are 50×1×10, 100×1×20, 100×1×40, 200×1×40, and 200×1×80 using a 1 ft wellbore radius. 56
Figure 3.9: Steam to oil ratio over 10 years of steam flooding for simulations with five different grids. The number of grid blocks in the x, y, and z direction are 50×1×10, 100×1×20, 100×1×40, 200×1×40, and 200×1×80 using a 1 ft wellbore radius. 56
Figure 3.10: Temperature distribution at 1, 4 and 10 years of steam flooding. The steam injection well is at the left section of each of the 3 cross-sections while the production well at the right end. 58
Figure 3.11: Ternary saturation at 1,4 and 10 years of steam flooding. The steam injection well is at the left section of each of the 3 cross-sections while the production well is at the right end. 60
Figure 3.12: Pressure distribution at 1, 4 and 10 years of steam flooding. The steam injection well is at the left section of each of the 3 cross-sections while the production well is at the right end. 62
Figure 3.13: Cumulative oil production vs. time. The baseline model is shown along with 8 other models corresponding to the different parameter ranges. 65
Figure 3.14: Steam to oil ratio vs. time. The baseline model is shown along with 8 other models corresponding to the different parameter ranges. 66
Figure 3.15: Water cut at the production well vs. time. The baseline model is shown along with 8 other models corresponding to the different parameter ranges. 66
Figure 3.16: Cross section showing steam saturation for the baseline model after 1, 4 and 10 years of steam injection with all parameters set to the reference values listed in Table 3.5. The injection well is on the left while production well is on the right. 69
Figure 3.17: Cross section showing steam saturation for the case where the horizontal permeability is 600 mD after 1, 4 and 10 years of steam injection with all other parameters set to the reference values listed in Table 3.5. The injection well is on the left while

PRODUCTION WELL IS ON THE RIGHT. 70
FIGURE 3.18: CROSS SECTION SHOWING STEAM SATURATION FOR THE CASE WHERE THE HORIZONTAL AND VERTICAL PERMEABILITY IS 600 MD AND 300 MD, RESPECTIVELY, AFTER 1, 4 AND 10 YEARS OF STEAM INJECTION WITH ALL OTHER PARAMETERS SET TO THE REFERENCE VALUES LISTED IN TABLE 3.5. THE INJECTION WELL IS ON THE LEFT WHILE PRODUCTION WELL IS ON THE RIGHT. 72
FIGURE 4.1: BULK MODULUS, DENSITY AND P-WAVE VELOCITY OF BRINE CALCULATED USING THE ABOVE-MENTIONED EQUATIONS FOR EACH OF THE PARAMETERS. 82
FIGURE 4.2: BULK MODULUS, DENSITY AND P-WAVE VELOCITY OF 10° API OIL. 84
FIGURE 4.3: MEASURED SHEAR MODULUS VS. TEMPERATURE FOR AN 8° API OIL (ADOPTED FROM HAN ET AL., 2008). BULK MODULUS VALUES ARE PRESENTED AS DIAMONDS AND SHEAR MODULUS VALUES ARE PRESENTED AS SQUARES FOR AN API 8° GRAVITY HEAVY OIL. A SHEAR MODULUS APPEARS AND THE BULK MODULUS-TEMPERATURE TREND CHANGES SLOPE AT A LIQUID POINT TEMPERATURE (T_L) OF 40 °C. 86
FIGURE 4.4: FIVE POINTS ARE SHOWN FOR THE MEASURED SHEAR MODULUS AS A FUNCTION OF TEMPERATURE. A LINEAR MODEL WAS CHOSEN, GIVEN ITS FIT TO THE MEASURED SHEAR MODULI VS. TEMPERATURE DATA. THE LOWER GRAPH DISPLAYS THE ERROR BETWEEN THE MEASURED DATA POINTS AND THE PREDICTED VALUES FROM THE LINEAR FIT MODEL. 86
FIGURE 4.5: MEASURED V_S VS. TEMPERATURE FOR DIFFERENT HEAVY OILS (AFTER HAN ET AL., 2008). 87
FIGURE 4.6: FOUR POINTS ARE SHOWN DISPLAYING THE TEMPERATURE AT WHICH THE BULK MODULUS IS EQUAL TO ZERO AS A FUNCTION OF OIL API. A QUADRATIC MODEL WAS OBTAINED FROM REGRESSION ANALYSIS TO DESCRIBE THE RELATIONSHIP BETWEEN THESE PARAMETERS, GIVEN ITS FIT TO THE DATA. THE LOWER GRAPH DISPLAYS THE ERROR BETWEEN THE MEASURED DATA POINTS AND THE PREDICTED VALUES FROM THE QUADRATIC FIT MODEL. 88
FIGURE 4.7: SHEAR MODULI OF SOME HEAVY OILS WITH DIFFERENT API VALUES VERSUS TEMPERATURE. 88
FIGURE 4.8: VP AND VS IN KM/S FOR A SAND VERSUS OIL CONTINUOUS PHASE AT DIFFERENT TEMPERATURES (^{O}C) AND PRESSURES (MPA). 92
FIGURE 4.9: PREDICTED S-WAVE VELOCITY VS. TEMPERATURE IN A SATURATED ROCK. THE TOP PLOT IS AFTER EASTWOOD (1993), WHILE THE BOTTOM PLOT IS OUR RESULTS. THE SUDDEN INCREASE IN S-WAVE AT AROUND 280 °C IS DUE TO THE BRINE CHANGING PHASE FROM LIQUID TO STEAM. 94
FIGURE 4.10: PLOTS OF VP AND VS VERSUS TEMPERATURE (AFTER BAUER ET AL., 2011) ON THE TOP COMPARED TO OUR RESULTS ON THE BOTTOM. THE SUDDEN INCREASE IN S-WAVE AND DECREASE IN P-WAVE VELOCITIES AT AROUND 280 °C IS DUE TO BRINE CHANGING PHASE FROM LIQUID TO STEAM. 95
FIGURE 4.11: THE TOP PLOT IS FOR A 5° API OIL SAMPLE (AFTER BATZLE ET AL., 2006) COMPARED TO OUR

RESULT AT THE BOTTOM. 96
FIGURE 4.12: V_P VERSUS TEMPERATURE FOR A 7° API OIL AT PRESSURES 4 AND 1.2 MPA ON THE TOP (AFTER BATZLE ET AL., 2006) COMPARED TO OUR RESULT AT THE BOTTOM..... 97
FIGURE 4.13: DENSITY OF OIL VERSUS TEMPERATURE ON THE TOP (AFTER MOCHINAGA ET AL., 2006) COMPARED TO OUR RESULT ON THE BOTTOM. 99
FIGURE 4.14: V_P VS. PRESSURE IN THE TOP PLOT (AFTER YUAN AND HAN, 2013) COMPARED TO OUR RESULT ON THE BOTTOM..... 100
FIGURE 4.15: V_P VS. OIL SATURATION ON THE TOP (AFTER DAN ET AL., 2007) COMPARED TO OUR RESULT ON THE BOTTOM..... 102
FIGURE 4.16: POROSITY VS. VERTICAL EFFECTIVE STRESS FOR LOOSE SANDS WITH DIFFERENT COMPOSITION AND GRAIN SIZE (AFTER CHUHAN ET AL., 2003)..... 103
FIGURE 4.17: POROSITY LOSS VERSUS GRAIN SIZE FOR DIFFERENT TYPE OF SANDS (AFTER CHUHAN ET AL., 2003). 104
FIGURE 4.18: $\%\Delta V_P$ VS. RESERVOIR PROPERTIES. 105
FIGURE 4.19: $\%\Delta V_S$ VS. RESERVOIR PROPERTIES. 105
FIGURE 5.1: PRE STEAM INJECTION PARETO CHART FOR AVO INTERCEPT. 112
FIGURE 5.2: PRE STEAM INJECTION PARETO CHARTS FOR AVO GRADIENT..... 113
FIGURE 5.3: TERM EFFECT OF TEMPERATURE, POROSITY, PRESSURE, BRINE SATURATION AND OIL API ON THE AVO INTERCEPT IN THE PRE STEAM INJECTION CASE. 114
FIGURE 5.4: TERM EFFECT OF TEMPERATURE, POROSITY, PRESSURE, BRINE SATURATION AND OIL API ON THE AVO GRADIENT IN THE PRE STEAM INJECTION CASE. 115
FIGURE 5.5: AVO INTERCEPT VERSUS GRADIENT FOR LOW AND HIGH VALUES OF TEMPERATURE, POROSITY, EFFECTIVE PRESSURE, BRINE SATURATION AND OIL API IN THE PRE STEAM INJECTION CASE. 116
FIGURE 5.6: TOP OF STEAM CHAMBER PARETO CHART FOR AVO INTERCEPT. 120
FIGURE 5.7: TOP OF STEAM CHAMBER PARETO CHART FOR AVO GRADIENT. 121
FIGURE 5.8: TERM EFFECT OF TEMPERATURE, POROSITY, PRESSURE, BRINE SATURATION AND OIL API ON THE AVO INTERCEPT AT THE TOP OF THE STEAM CHAMBER IN THE POST STEAM INJECTION CASE. 122
FIGURE 5.9: TERM EFFECT OF TEMPERATURE, POROSITY, PRESSURE, BRINE SATURATION AND OIL API ON THE AVO GRADIENT AT THE TOP OF THE STEAM CHAMBER IN THE POST STEAM INJECTION CASE. 123
FIGURE 5.10: AVO INTERCEPT VERSUS GRADIENT FOR LOW AND HIGH VALUES OF TEMPERATURE, POROSITY, EFFECTIVE PRESSURE, BRINE SATURATION AND OIL API FOR THE TOP OF THE STEAM CHAMBER IN THE POST STEAM INJECTION CASE..... 124

FIGURE 5.11: BOTTOM OF STEAM CHAMBER PARETO CHART FOR AVO INTERCEPT. 127
FIGURE 5.12: BOTTOM OF STEAM CHAMBER PARETO CHART FOR AVO GRADIENT. 128
FIGURE 5.13: TERM EFFECT OF TEMPERATURE, POROSITY, PRESSURE, BRINE SATURATION AND OIL API ON THE AVO INTERCEPT AT THE BOTTOM OF THE STEAM CHAMBER IN THE POST STEAM INJECTION CASE. 129
FIGURE 5.14: TERM EFFECT OF TEMPERATURE, POROSITY, PRESSURE, BRINE SATURATION AND OIL API ON THE AVO GRADIENT AT THE BOTTOM OF THE STEAM CHAMBER IN THE POST STEAM INJECTION CASE..... 130
FIGURE 5.15: AVO INTERCEPT VERSUS GRADIENT FOR LOW AND HIGH VALUES OF TEMPERATURE, POROSITY, EFFECTIVE PRESSURE, BRINE SATURATION AND OIL API FOR THE BOTTOM OF THE STEAM CHAMBER IN THE POST STEAM INJECTION CASE. 131
FIGURE 5.16: MODEL A: CROSS-SECTION SHOWING STEAM SATURATION AFTER 10 YEARS OF STEAM FLOOD WHERE THE HORIZONTAL PERMEABILITY IS 600 MD WHILE THE OTHER PARAMETERS ARE SET TO THE REFERENCE VALUE AS PER TABLE 3.5. BLUE ARROWS MARK THE LOCATIONS WHERE STEAM THICKNESSES WERE STUDIED. THE INJECTION WELL IS TO THE LEFT WHILE THE PRODUCTION WELL IS TO THE RIGHT..... 135
FIGURE 5.17: P- AND S-WAVE VELOCITIES AND DENSITIES AT LOCATION 1 IN MODEL A CALCULATED FROM THE RESERVOIR SIMULATION RESULTS USING THE MATLAB ROCK PHYSICS CODE. 135
FIGURE 5.18: THE INTERCEPT AND GRADIENT OF THE TWO-TERM AKI-RICHARDS APPROXIMATION OF THE AVO EQUATION AT LOCATION 1 IN MODEL A USING A 100 HZ RICKER WAVELET. 136
FIGURE 5.19: THE INTERCEPT AND GRADIENT OF THE TWO-TERM AKI-RICHARDS APPROXIMATION OF THE AVO EQUATION AT LOCATION 1 IN MODEL A USING A 50 HZ RICKER WAVELET. 137
FIGURE 5.20: P- AND S-WAVE VELOCITIES AND DENSITIES AT LOCATION 2 IN MODEL A CALCULATED FROM THE RESERVOIR SIMULATION RESULTS USING THE MATLAB ROCK PHYSICS CODE. 138
FIGURE 5.21: THE INTERCEPT AND GRADIENT OF THE TWO-TERM AKI-RICHARDS APPROXIMATION OF THE AVO EQUATION AT LOCATION 2 IN MODEL A USING A 100 HZ RICKER WAVELET. 139
FIGURE 5.22: THE INTERCEPT AND GRADIENT OF THE TWO-TERM AKI-RICHARDS APPROXIMATION OF THE AVO EQUATION AT LOCATION 2 IN MODEL A USING A 50 HZ RICKER WAVELET. 139
FIGURE 5.23: P- AND S-WAVE VELOCITIES AND DENSITIES AT LOCATION 3 IN MODEL A CALCULATED FROM THE RESERVOIR SIMULATION RESULTS USING THE MATLAB ROCK PHYSICS CODE. 141
FIGURE 5.24: THE INTERCEPT AND GRADIENT OF THE TWO-TERM AKI-RICHARDS APPROXIMATION OF THE AVO EQUATION AT LOCATION 3 IN MODEL A USING A 100 HZ RICKER WAVELET. 142
FIGURE 5.25: THE INTERCEPT AND GRADIENT OF THE TWO-TERM AKI-RICHARDS APPROXIMATION OF THE AVO EQUATION AT LOCATION 3 IN MODEL A USING A 50 HZ RICKER WAVELET. 143
FIGURE 5.26: MODEL B: CROSS-SECTION SHOWING STEAM SATURATION AFTER 10 YEARS OF STEAM FLOOD

where the horizontal and vertical permeabilities are 600 mD and 300 mD, respectively. Other parameters are set to the reference value as per Table 3.5. Blue arrows mark the locations where steam thicknesses were studied. The injection well is to the left while the production well is to the right. 144
Figure 5.27: P- and S-wave velocities and densities at location 1 in model B calculated from the reservoir simulation results using the MATLAB rock physics code. 145
Figure 5.28: Model B: Cross-section showing ternary saturation after 10 years of steam flood where the horizontal and vertical permeabilities are 600 mD and 300 mD, respectively. Other parameters are set to the reference value as per Table 3.5. Blue arrows mark the locations where steam thicknesses were studied. The injection well is to the left while the production well is to the right. 145
Figure 5.29: The intercept and gradient of the two-term Aki-Richards approximation of the AVO equation at location 1 in model B using a 100 Hz Ricker wavelet 146
Figure 5.30: The intercept and gradient of the two-term Aki-Richards approximation of the AVO equation at location 1 in model B using a 50 Hz Ricker wavelet 147
Figure 5.31: P- and S-wave velocities and densities at location 2 in model B calculated from the reservoir simulation results using the MATLAB rock physics code. 148
Figure 5.32: The intercept and gradient of the two-term Aki-Richards approximation of the AVO equation at location 2 in model B using a 100 Hz Ricker wavelet 149
Figure 5.33: The intercept and gradient of the two-term Aki-Richards approximation of the AVO equation at location 2 in model B using a 50 Hz Ricker wavelet 149
Figure 5.34: P- and S-wave velocities and densities at location 3 in model B calculated from the reservoir simulation results using the MATLAB rock physics code. 150
Figure 5.35: The intercept and gradient of the two-term Aki-Richards approximation of the AVO equation at location 3 in model B using a 100 Hz Ricker wavelet 151
Figure 5.36: The intercept and gradient of the two-term Aki-Richards approximation of the AVO equation at location 3 in model B using a 50 Hz Ricker wavelet 151
Figure 6.1: P-wave and S-wave velocities and densities at location 1 in model A after adding 4% uniformly distributed random noise. 157
Figure 6.2: Intercept and gradient of the AVO at location 1 in model A for the case of 4% uniformly distributed added noise. 158
Figure 6.3: P-wave and S-wave velocities and densities at location 1 in model A after adding 6%

uniformly distributed random noise. 159
Figure 6.4: Intercept and gradient of the AVO at location 1 in model A for the case of 6% uniformly distributed added noise. 160
Figure 6.5: P-wave and S-wave velocities and densities at location 1 in model A after adding 8% uniformly distributed random noise. 160
Figure 6.6: Intercept and gradient of the AVO at location 1 in model A for the case of 8% uniformly distributed added noise. 161
Figure 6.7: P-wave and S-wave velocities and densities at location 1 in model A after adding 10% uniformly distributed random noise. 161
Figure 6.8: Intercept and gradient of the AVO at location 1 in model A for the case of 10% uniformly distributed added noise. 162
Figure 6.9: P-wave and S-wave velocities and densities at location 1 in model A after adding 12% uniformly distributed random noise. 163
Figure 6.10: Intercept and gradient of the AVO at location 1 in model A for the case of 12% uniformly distributed added noise. 164
Figure 6.11: P-wave and S-wave velocities and densities at location 2 in model B after adding 4% uniformly distributed random noise. 165
Figure 6.12: Intercept and gradient of the AVO at location 2 in model B for the case of 4% uniformly distributed added noise. 166
Figure 6.13: P-wave and S-wave velocities and densities at location 2 in model B after adding 6% uniformly distributed random noise. 166
Figure 6.14: Intercept and gradient of the AVO at location 2 in model B for the case of 6% uniformly distributed added noise. 167
Figure 6.15: P-wave and S-wave velocities and densities at location 2 in model B after adding 8% uniformly distributed random noise. 167
Figure 6.16: Intercept and gradient of the AVO at location 2 in model B for the case of 8% uniformly distributed added noise. 168
Figure 6.17: P-wave and S-wave velocities and densities at location 2 in model B after adding 10% uniformly distributed random noise. 169
Figure 6.18: Intercept and gradient of the AVO at location 2 in model B for the case of 10% uniformly distributed added noise. 170
Figure 6.19: P-wave and S-wave velocities and densities at location 2 in model B after adding 12%

uniformly distributed random noise. 170
Figure 6.20: Intercept and gradient of the AVO at location 2 in model B for the case of 12% uniformly distributed added noise. 171
Figure 6.21: P-wave and S-wave velocities and densities at location 2 in model B after adding 14% uniformly distributed random noise. 171
Figure 6.22: Intercept and gradient of the AVO at location 2 in model B for the case of 14% uniformly distributed added noise. 172
Figure B-1: Cross-section showing steam saturation for the case where the initial reservoir pressure is 4 MPa after 1, 4 and 10 years of steam injection with all other parameters set to the reference values listed in Table 3.5. The injection well is on the left while production well is on the right. 194
Figure B-2: Cross-section showing steam saturation for the case where the horizontal permeability is 10 Darcy after 1, 4 and 10 years of steam injection with all other parameters set to the reference values listed in Table 3.5. The injection well is on the left while production well is on the right. 195
Figure B-3: Cross-section showing steam saturation for the case where the steam injection temperature is 270 °C after 1, 4 and 10 years of steam injection with all other parameters set to the reference values listed in Table 3.5. The injection well is on the left while production well is on the right. 197
Figure B-4: Cross-section showing steam saturation for the case where the oil API is 14° after 1, 4 and 10 years of steam injection with all other parameters set to the reference values listed in Table 3.5. The injection well is on the left while production well is on the right. 198
Figure B-5: Cross-section showing steam saturation for the case where porosity is 20% after 1, 4 and 10 years of steam injection with all other parameters set to the reference values listed in Table 3.5. The injection well is on the left while production well is on the right. 200
Figure B-6: Cross-section showing steam saturation for the case where the vertical permeability is 0.2 of the horizontal permeability after 1, 4 and 10 years of steam injection with all other parameters set to the reference values listed in Table 3.5. The injection well is on the left while production well is on the right. 201
Figure B-7: Cross-section showing steam saturation for the case where the vertical permeability is 0.5 of the horizontal permeability after 1, 4 and 10 years of steam injection with all other parameters set to the reference values listed in Table 3.5. The injection well is on the left

WHILE PRODUCTION WELL IS ON THE RIGHT..... 203

List of Tables

TABLE 2.1: OIL CLASSIFICATION BASED ON API GRAVITY (MAGOON, 1988). 29

TABLE 3.1: INITIAL RESERVOIR & WELL PROPERTIES. 48

TABLE 3.2: TEMPERATURE VS. VISCOSITY FOR THE 24° API OIL IN THE RESERVOIR (LEONHARD, 2001). 49

TABLE 3.3: WATER-OIL RELATIVE PERMEABILITIES. 49

TABLE 3.4: LIQUID-GAS RELATIVE PERMEABILITIES. 50

TABLE 3.5: TYPICAL RANGES OR VALUES AND REFERENCE VALUES FOR DIFFERENT PARAMETERS IN EMLICHHEIM OIL FIELD. 64

TABLE 4.1: BULK MODULUS (K), SHEAR MODULUS (μ) AND DENSITY (ρ) OF COMMON MINERALS THAT MAKE UP SEDIMENTARY ROCKS (MAVKO ET AL., 2009). 76

TABLE 5.1: TYPICAL RANGES AND REFERENCE VALUES FOR EACH PARAMETER FOR EMLICHHEIM OIL FIELD. 108

TABLE 5.2: ALL COMBINATIONS OF FIVE FACTORS AND THE CORRESPONDING AVO INTERCEPT AND GRADIENT FOR THE PRE STEAM INJECTION CASE. 111

TABLE 5.3: REGRESSION STATISTICS FOR THE AVO INTERCEPT IN THE PRE STEAM INJECTION CASE. 117

TABLE 5.4: REGRESSION STATISTICS FOR THE AVO GRADIENT IN THE PRE STEAM INJECTION CASE. 118

TABLE 5.5: ALL COMBINATIONS OF FIVE FACTORS AND THE CORRESPONDING AVO INTERCEPT AND GRADIENT AT THE TOP AND BOTTOM OF THE STEAM CHAMBER FOR THE POST STEAM INJECTION CASE. 119

TABLE 5.6: REGRESSION STATISTICS FOR THE AVO INTERCEPT AT THE TOP OF THE STEAM CHAMBER IN THE POST STEAM INJECTION CASE. 124

TABLE 5.7: REGRESSION STATISTICS FOR THE AVO GRADIENT AT THE TOP OF THE STEAM CHAMBER IN THE POST STEAM INJECTION CASE. 125

TABLE 5.8: REGRESSION STATISTICS FOR THE AVO INTERCEPT AT THE BOTTOM OF THE STEAM CHAMBER IN THE POST STEAM INJECTION CASE. 131

TABLE 5.9: REGRESSION STATISTICS FOR THE AVO GRADIENT AT THE BOTTOM OF THE STEAM CHAMBER IN THE

POST STEAM INJECTION CASE 132

TABLE 6.1: SUMMARY OF RESULTS AFTER ADDING UNIFORMLY DISTRIBUTED NOISE TO LOCATION 1 IN MODEL A. 173

TABLE 6.2: SUMMARY OF RESULTS AFTER ADDING UNIFORMLY DISTRIBUTED NOISE TO LOCATION 2 IN MODEL B. 173

1. Introduction

1.1 Motivation

Most oil produced nowadays comes from aging fields; moreover the rate at which reserves are replaced by new field discoveries has been declining in recent decades (Alvarado & Manrique, 2010). Most forecasts of world oil production predict a decrease from the current rate of 91 mb/d by the year 2030 as shown in Figure 1.1 (Oil Market Report, 2013; Sorrell et al., 2010). At the same time demand for oil is expected to continue to increase with some projections suggesting that global oil demand could peak soon after 2025 while others expect demand to continue to grow out to 2040 and beyond as shown in Figure 1.2 (Dale & Fattouh, 2018). The most and least optimistic forecasts for world oil production by the year 2030 are approximately 95 and 40 mb/d, respectively, with all other predictions shown in Figure 1.1 (Sorrell et al., 2010). In another study, Aleklett et al (2010) predict that world oil production will increase to about 105 mb/d by 2030 as shown in Figure 1.3.

However, Aleklett et al (2010) predict that production from currently producing fields will continue to decrease while production from additional enhanced oil recovery and non-conventional fields will increase (Aleklett et al., 2010). In order to bridge the gap between future supply and demand, we need to find ways to increase oil production. One way to achieve this is by increasing the recovery factor, especially of heavy and extra heavy oils, which are harder to extract (Shah et al., 2010). The global average recovery factor from oil fields is about 20% to 50% and this has been increased to about 50% to 70% in some fields using enhanced oil recovery techniques (Muggeridge et al., 2014).

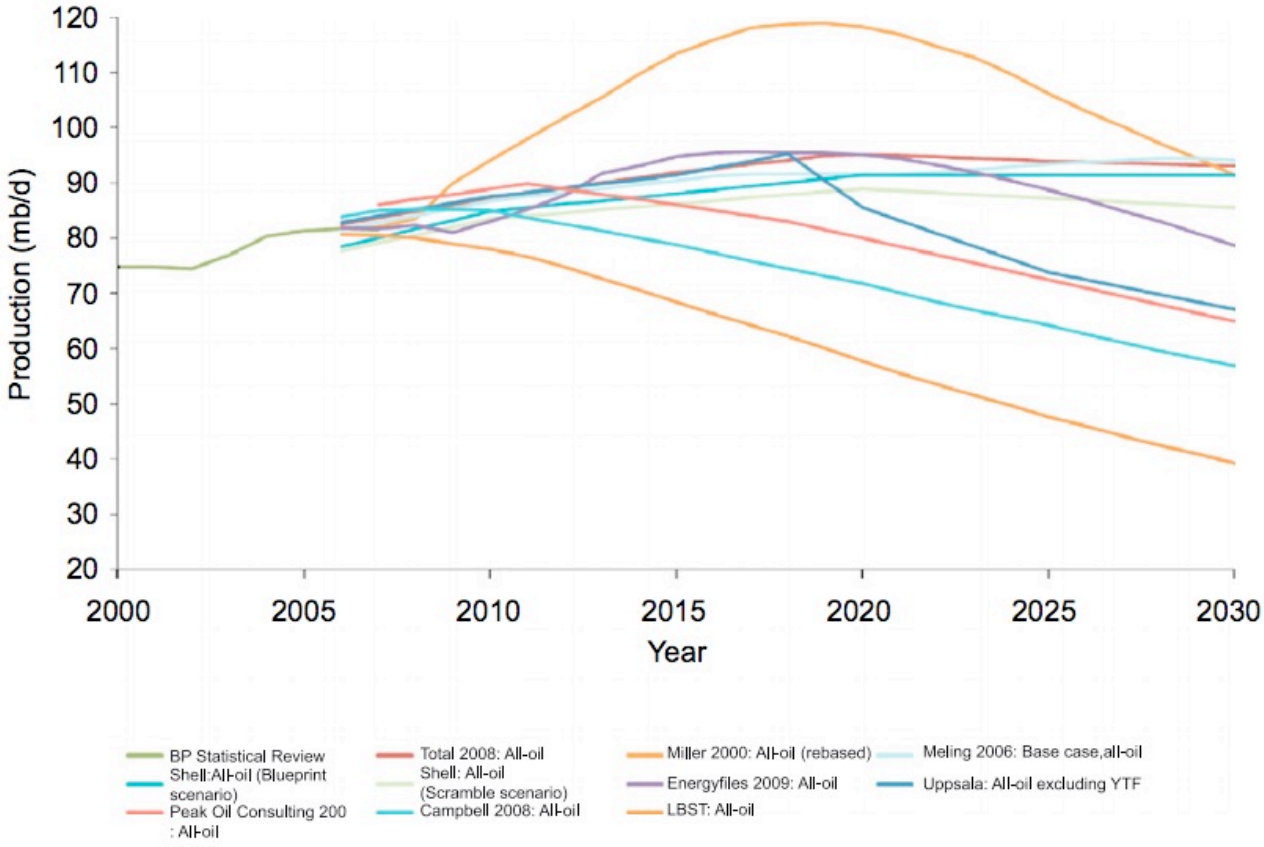


Figure 1.1: Different forecasts of world oil production (Sorrell et al., 2010).

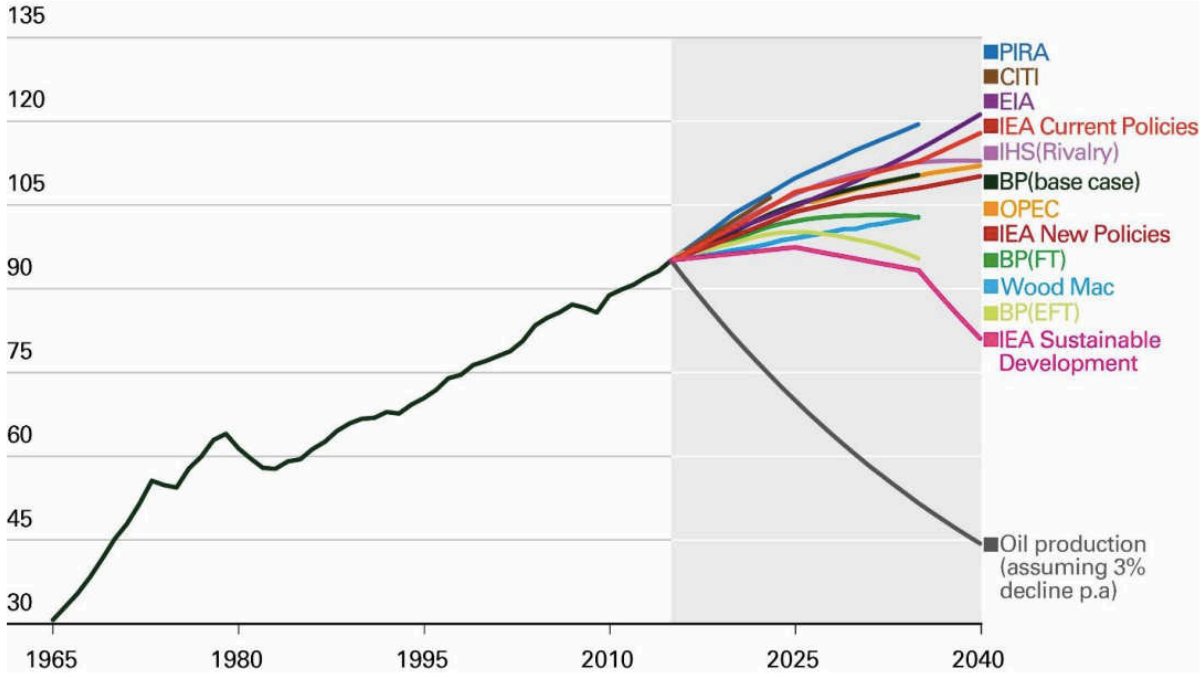


Figure 1.2: Different forecasts of world oil demand in Mb/d (Dale & Fattouh, 2018).

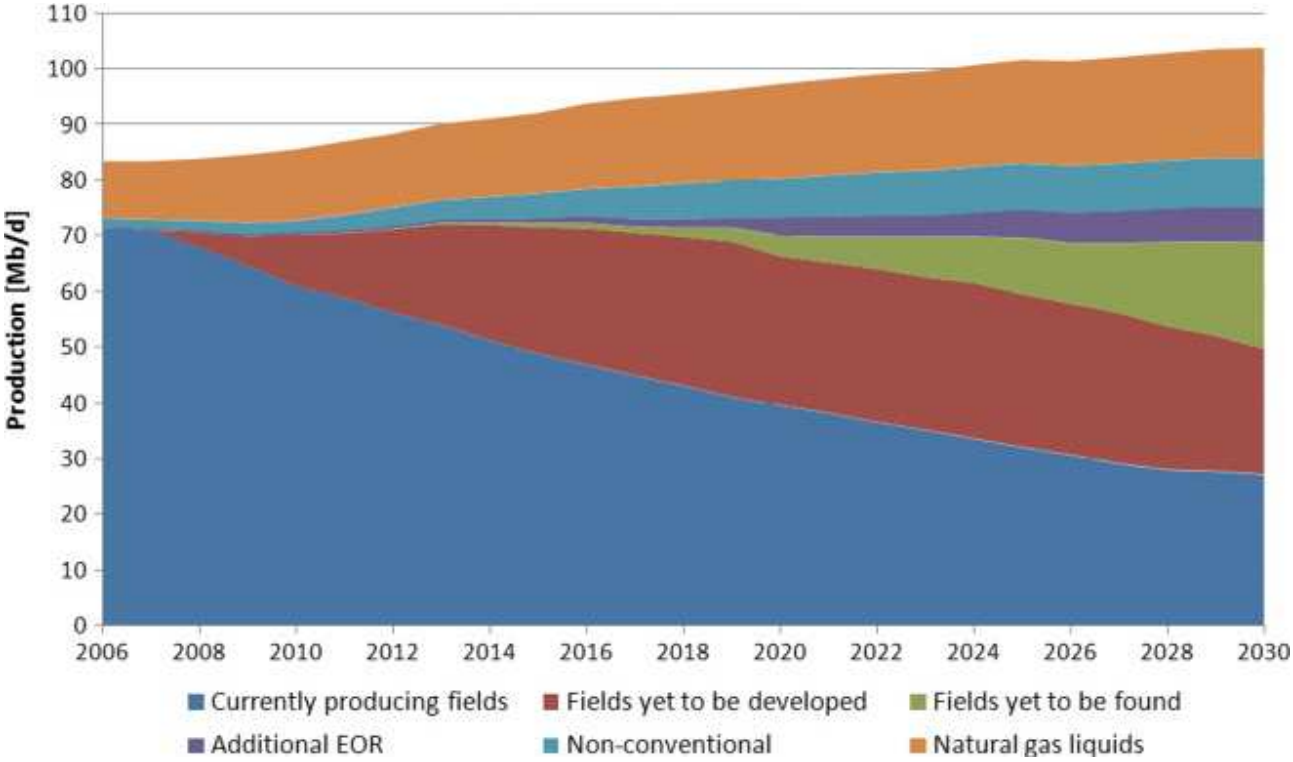


Figure 1.2: Forecast of the world's oil production sources (Aleklett et al., 2010).

Steam flooding is the most widely used EOR method to increase the recovery factor of oil from heavy oil reservoirs (Passalacqua and Strack, 2016). Knowledge of the geometry of the steam chamber can help to increase the sweep efficiency by reducing the amount of oil left behind, hence increasing the recovery factor. We can predict the exact geometry of the steam chamber in an ideally homogeneous reservoir by using a reservoir simulation software. However, in reality, all reservoirs are heterogeneous and this complicates the actual geometry of the steam chamber within the heterogeneous reservoir.

Time-lapse seismic monitoring of reservoirs is widely used to delineate the steam chamber in a steam flood operation (Jenkins et al., 1997; Lumley, 1995; Lumley, 2001; Paydayesh et al., 2018). However, this comes with its limitations and challenges. It is difficult to determine the lateral extent of the steam tongue because the lateral change in the elastic moduli and density due to the presence or absence

of steam is small compared to the change in elastic moduli and density at the top of the reservoir. In terms of vertical resolution, reflection seismology can only resolve steam thicknesses that are larger than the tuning thickness. Even if this criterion is satisfied, it is sometimes difficult or impossible to visually pick the bottom of the steam because the amplitude of the reflection from the bottom of the steam within the reservoir is small compared to the reflections from the top and bottom of the reservoir. This can sometimes cause the stronger reflections from the top or bottom of the reservoir to mask the weaker reflection from the bottom of the steam making it impossible to determine the thickness of the steam chamber. Rather than only studying zero offset seismic reflectivity data, we look at how the amplitude of reflected seismic waves vary with distance away from the seismic source. An AVO procedure is developed where we can determine the range of depth at which the bottom of the steam is located, thus improving the vertical delineation of the steam chamber.

1.2 Aims and Objectives

The aim of this study is to improve the delineation of the vertical extent of the steam chamber in an enhanced oil recovery by steam flooding operation. This will be achieved by analyzing the intercept and gradient of the two-term Aki-Richards approximation of the amplitude versus offset (AVO) equation. This will effectively help to increase the sweep efficiency, thus improving reservoir management and characterization. The properties of the reservoir model are chosen to mimic Emlichheim, which is an existing heavy oil field in Northern Germany operated by Wintershall (Leonhardt, 2001). Figure 1.4 demonstrates our developed general workflow, which is applied to the synthetic Emlichheim field model.

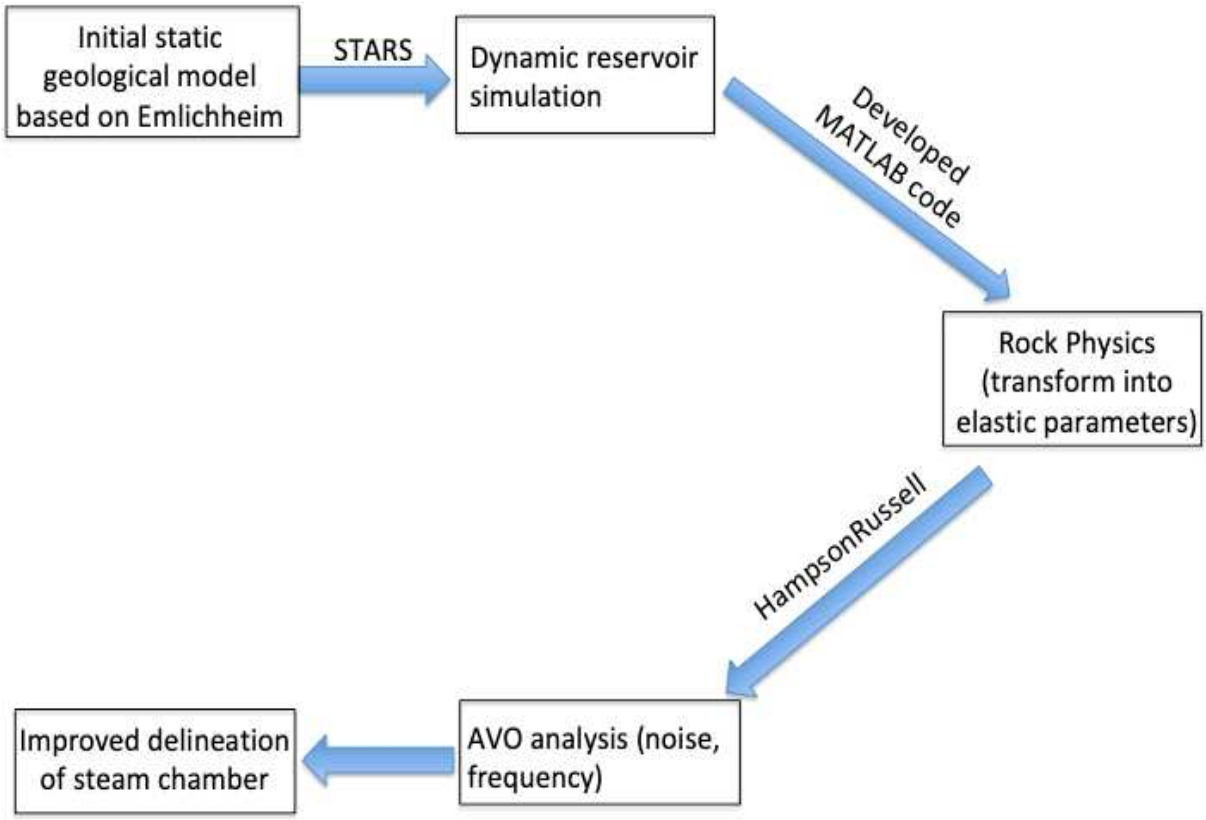


Figure 1.3: General workflow applied to the synthetic Emlichheim field model.

1.3 Summary of Remainder of Thesis

In chapter 2, a literature review is conducted where we look at what was done using reflection seismology to delineate a steam chamber in a steam flood operation. In chapter 3, STARS is used for the reservoir simulation to obtain the properties of the reservoir such as pressure, porosity, temperature, oil saturation, gas saturation, water saturation and water salinity as well as studying the sensitivity of the reservoir simulation to different ranges of parameters. In chapter 4, a MATLAB rock physics code was developed that takes these properties as input and calculates the P-wave and S-wave velocities and densities. A detailed sensitivity analysis is conducted on the P- and S-wave velocities to study how they are affected by the different reservoir properties and various oil API values. In chapter 5, HampsonRussell software is used

to calculate the gradient and intercept of the amplitude versus offset of the seismic waves reflected at different incidence angles. A sensitivity study is conducted to gauge the sensitivity of the intercept and gradient of the AVO to temperature, porosity, pressure, brine saturation and oil API pro and post steam injection. A multi variable linear regression analysis is performed to find the best least squares fit to the AVO data. We then develop an AVO procedure to estimate the thickness of the steam chamber and apply it at three different locations in two different models. In chapter 6, we test the robustness of our AVO procedure by adding different levels of noise until the AVO procedure breaks downs and we reach its limitation. In Chapter 7, we discuss the conclusions and future work.

2. Background and literature review

2.1 Introduction

It is estimated that if we rely solely on conventional oil recovery methods, about 2 billion and 5 billion barrels of conventional oil and heavy oil, respectively; will be left behind in reservoirs around the world (Thomas, 2008). For some time, heavy hydrocarbons have been overlooked as a valuable energy resource because of the high costs and technical difficulties associated with its extraction. As the reserves of conventional oil continue to dwindle while the heavy oil reserves remain almost untouched, it is essential to increase the recovery factor of oil by improving current enhanced oil recovery methods and by better monitoring and managing these reservoirs in order to meet future energy demand (Berron et al, 2015; Alvarado and Manrique, 2010).

While there are a myriad of factors that dictate how easy or difficult oil reserves can be put into production such as permeability, porosity, depth, pressure, and geological heterogeneity, the density and viscosity of the oil in the reservoir is a very important factor (Wang et al, 2006; Larter et al, 2008). The density and viscosity of oil in place helps to determine the method of extraction a company will employ (Thomas, 2008). Most oil production methods have focused on the production of conventional oils, which are easier and cheaper to extract. Heavy oils have not been popular because of the high cost associated with its extraction. As a result, heavy oil production presents unique challenges that are not entirely insurmountable (Ambastha, 2008).

Crude oil has a spectrum of densities and viscosities, which are significant factors for an oil producer. In particular, the viscosity of oil in a reservoir varies with

temperature, which determines the ease of oil mobility (Alusta et al., 2012). While viscosity is a vital factor for an oil producer for its mobility, composition comprises the most vital factor for a refiner because it represents the yield after distillation. It is critical to note that scholars present no documented relationship between the two (Ambastha, 2008).

Oil reservoirs exist at various depths and have different ambient temperatures. Although viscosity varies significantly with temperature, density is used as the standard in the classification of oilfields. The density of crude oil is commonly expressed in degrees of American Petroleum Institute (API) gravity, which is associated with specific gravity and it is calculated using equation 2.1.

$$\text{API gravity} = \frac{141.5}{\text{SG oil}} - 131.5 \qquad (2.1)$$

Where SG oil stands for specific gravity of the crude oil, which is calculated at 60º F using equation 2.2.

$$SG\ oil = \frac{\rho_{\text{oil}}}{\rho_{\text{water}}} \qquad (2.2)$$

Where ρ_{oil} and ρ_{water} are density of oil and water, respectively.

The lower the API gravity, the denser the oil is. Crude oil is classified according to its API gravity as shown in Table 2.1.

Oil classification	API range
Extra heavy or bitumen	<10º
Heavy	10º ≤ API ≤ 20º
Medium	20º < API ≤ 30º
Light	30º < API < 45º
Condensate	≥ 45º

Table 2.1: Oil classification based on API gravity (Magoon, 1988).

Crude oil becomes heavy after considerable degradation after entrapment and during devolatilization. Degradation occurs through several chemical and biological processes as oil reservoirs become contaminated by bacteria through subsurface water (Gray et al, 2010). The bacteria then break down some of the components of crude oil into heavy components making it more viscous. The water also carries away the low molecular weight hydrocarbons in solution form since they are more soluble. When a poor-quality seal encloses crude oil, lighter molecules escape leaving behind the heavier components through devolatilization (Curtis et al, 2002).

Heavy oils are commonly found in geologically young formations since they are shallow and have less efficient seals, therefore providing the conditions for the formation of heavy oil (Chopra et al., 2010). Oil recovery involves three stages of extraction; primary, secondary and tertiary production. Primary recovery is the first stage of oil production and it involves using the natural reservoir energy, such as water drive, gas drive or gravity drainage, to displace the oil in the reservoir into the wellbore and eventually up to the surface (Solaimany-Nazar & Zonnouri, 2011). For conventional oil, cold production has a recovery factor of 10-20%, while for heavy oil the recovery factor is 5-10% (Ambastha, 2008).

A new variation of the cold production method that is used only with heavy oil production is known as Cold Heavy Oil Production with Sand (CHOPS) which creates a wormhole or void where oil and sand gets pulled from the surrounding unconsolidated sandstone towards the wellbore (Shah et al., 2010). These methods are termed as cold production since they are used at reservoir temperature. When the natural pressure gradient is not sufficient to displace and produce any oil, primary production would have reached its extraction limit, and the next step would be the implementation of secondary recovery.

Secondary recovery methods involve the maintenance of reservoir pressure through the injection of other fluids into the reservoir. The method injects water, natural gas, carbon dioxide or any other fluid under high pressure into the reservoir, which displaces the oil and pushes it towards the wellbore and eventually up to the surface (Moulds, 2005). The two cold production recovery methods have a combined recovery factor of 10-20%, depending on the properties of the oil in place and the lithology of the reservoir (Istchenko & Gates, 2013).

Tertiary recovery is the third stage of hydrocarbon production, which involves gas injection, chemical flooding or thermal methods (Iglauer et al, 2010). Tertiary recovery is sometimes used interchangeably with enhanced oil recovery, but due to the fact that enhanced oil recovery methods can be applied nowadays at any stage of the hydrocarbon production process, the term tertiary recovery is used less than before (Schlumberger, 2017).

2.2 Heavy oil production using steam injection

Heavy oil reservoirs pose a challenge during extraction even after applying the cold oil production techniques discussed above due to the high viscosity of the oil in place. Several techniques have been investigated and are employed in heavy oil recovery. Thermal Enhanced Oil Recovery (TEOR), mainly steam injection, is the most efficient and most widely used method to reduce the viscosity of heavy oil (Alvarado & Manrique, 2010). The steam is injected into the reservoir at high pressure and temperature where it heats the heavy oil, reducing its viscosity and allowing it to mobilize. There are three types of steam injection methods; namely steam flooding, cyclic steam injection and steam assisted gravity drainage. All of these methods work by reducing viscosity, easing flow, and ultimately increasing production (Abdel-Halim et al., 2002).

2.2.1 Steam assisted gravity drainage (SAGD)

Steam-Assisted Gravity Drainage (SAGD), shown in Figure 2.1, involves the use of horizontal wells, one on top of the other and just a few metres apart. The top horizontal well is used to inject steam that heats up the surrounding heavy oil, which then flows into the bottom horizontal production well (Butler, 1994). The steam assisted gravity drainage method recovers about 60-70% of the entire oil volume (Alvarez & Han, 2013).

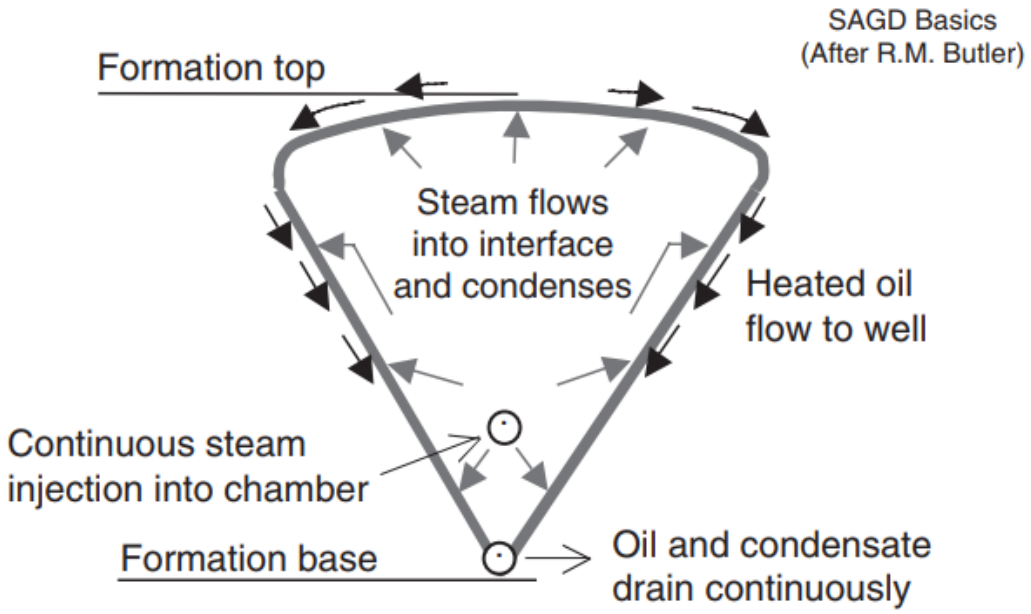


Figure 2.1: Steam assisted gravity drainage (Thomas, 2008).

2.2.2 Cyclic steam simulation

Cyclic Steam Stimulation (CSS), also known as cyclic steam injection or huff-and-puff, is a method in which steam is injected into the heavy oil reservoir where, because of the high pressure, it enters the pore space and sometimes even ruptures the reservoir rocks (Sarma et al., 2017). This high-temperature, high-pressure steam is left for some time in the reservoir, from several days to a few weeks so that the oil can absorb the heat and substantially reduce the viscosity of

the heavy oil in place (Shabelansky et al., 2015). There is no consensus regarding the soaking time, which may vary from days to weeks. However, shorter soaking times are favored for operational considerations.

The heated oil is then produced from the same well. Initially, production is high because of high reservoir pressure, lower oil viscosity and high initial oil saturation (Sheng, 2013). However, after some time, oil production declines because of lower pressure, lower oil saturation and higher oil viscosity due to the loss of heat to the rock formation and the fluids within the pores (Sheng, 2013). Cyclic injection becomes less efficient in oil production as the number of cycles increases (Trigos et al, 2016). The process of alternating cycles of injection and extraction is repeated until it becomes uneconomical to do so (Bao et al., 2016). These three stages namely, steam injection; soak and production are shown in Figure 2.2. Cyclic steam injection recovers about 10-40% of the entire oil volume (Alvarez & Han, 2013).

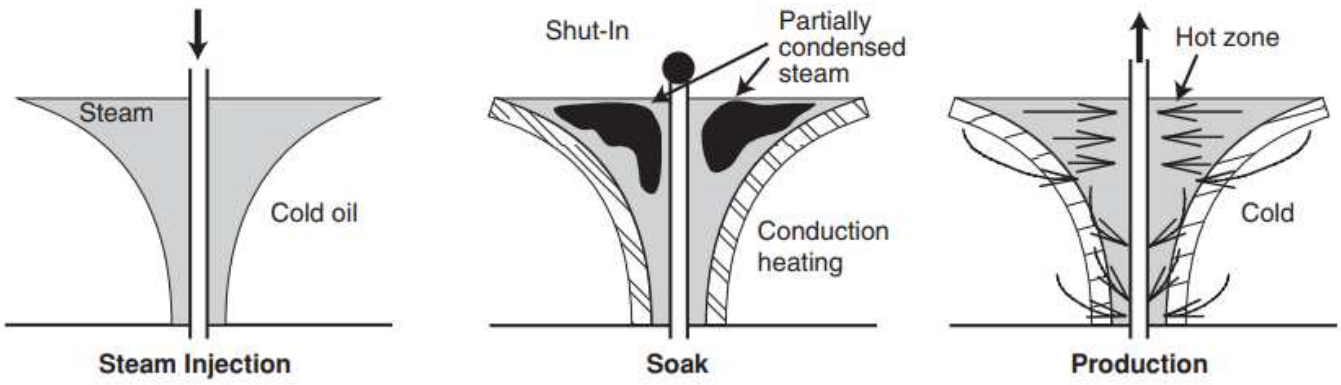


Figure 2.2: Cyclic steam injection (after Alvarez & Han, 2013).

2.2.3 Steam flooding

The third thermal enhanced oil recovery method is continuous steam injection, sometimes referred to as steam flooding, shown in Figure 2.3. It involve injects pressurized steam through the injection well into the reservoir where it heats up and displaces the more mobile oil up the production well (Yitang et al, 2008). Advances in

the acquisition and processing of 4D seismic data and the increase in the processing power of computers have enabled this method to be more efficient (Yitang et al, 2008). Steam flooding recovers about 50-60% of the entire oil volume (Alvarez & Han, 2013). Due to the high costs involved in a steam flooding operation, careful evaluations, in-depth study of the nature and type of the oil are necessary for both economic and application purposes (Berron et al., 2015).

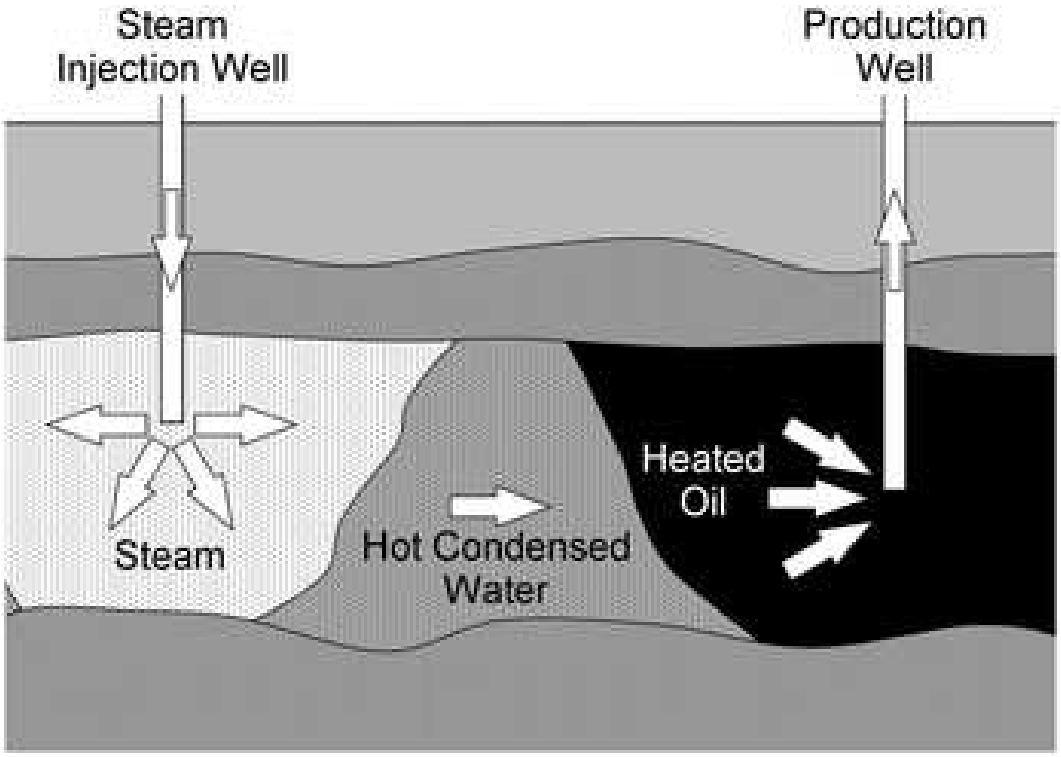


Figure 2.3: Steam flooding (Shah et al, 2010).

2.3 Sweep efficiency

The implementation of enhanced oil recovery techniques for residual heavy oil can be expensive due to the energy and materials required (Alusta, 2012). Sweep efficiency is a measure of the effectiveness of an enhanced oil recovery method, which depends on the total volume of the reservoir that the injected fluid comes into contact with. Sweep efficiency is affected by mobility ratio, directional permeability, reservoir heterogeneity, cumulative injected water and injection pattern between

injectors and producers (Muggeridge et al., 2014).

Injection patterns can change during the lifetime of a reservoir. This happens when new injection wells are drilled in areas where maximum volume of contact can be achieved, thus improving the sweep efficiency (Sydansk & Seright, 2007).

Geological heterogeneity and the large density difference between the steam and the oil can affect our ability to predict the sweep. Geological heterogeneity is the spatial distribution of porosity and permeability in a reservoir rock. Permeability is the number of pores and their interconnectedness in a rock; the existence of different layers in a rock with different permeability is a manifestation of geological heterogeneity. Permeability depends on the range and uniformity of grain size, the shape of the grains, consolidation, cementation, stratification and discontinuities (Bell et al., 1986).

When steam injection takes place, steam and water flow through the higher permeable layers of the rock, bypassing the less permeable oil-rich layers and causing low sweep efficiency and early water production. If the geological heterogeneity of a reservoir is known, the injection patterns could be designed to be directed to the less permeable layers of the oil reservoir. The challenge in this is that the permeability distribution of the reservoir is uncertain and hard to determine because of the limitations of our current reservoir characterization tools (Wilson, 2014). An effective way to monitor sweep efficiency is by implementing time-lapse seismic surveys (Muggeridge et al., 2014).

2.4 Case Study

Steam injection is the most commonly used thermal enhanced oil recovery method by volume of oil produced (Brandt & Unnasch, 2010). It has been used

mainly in sandstone formations in Canada, U.S.A., Venezuela, Indonesia and China, as shown in Figures 2.4 and 2.5 (Alvarado & Manrique, 2010; Brandt & Unnasch, 2010; Issa & Fleming, 2011). The expansion of steam injection is currently focused on Saudi Arabia and Alberta in Canada (Brandt & Unnasch, 2010).

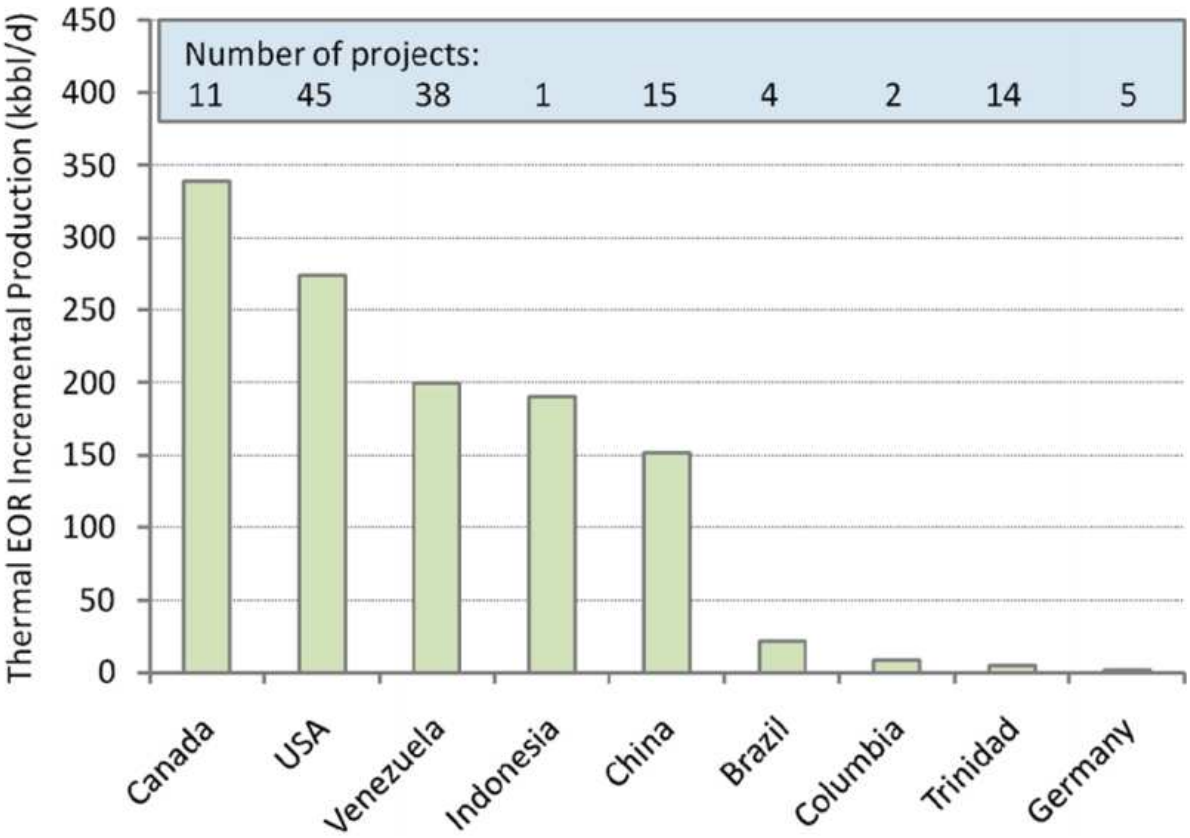


Figure 2.4: Global thermal enhanced oil recovery incremental production in 2008 along with the number of steam injection projects (Brandt & Unnasch, 2010). In situ combustion data is not included because it is of secondary importance.

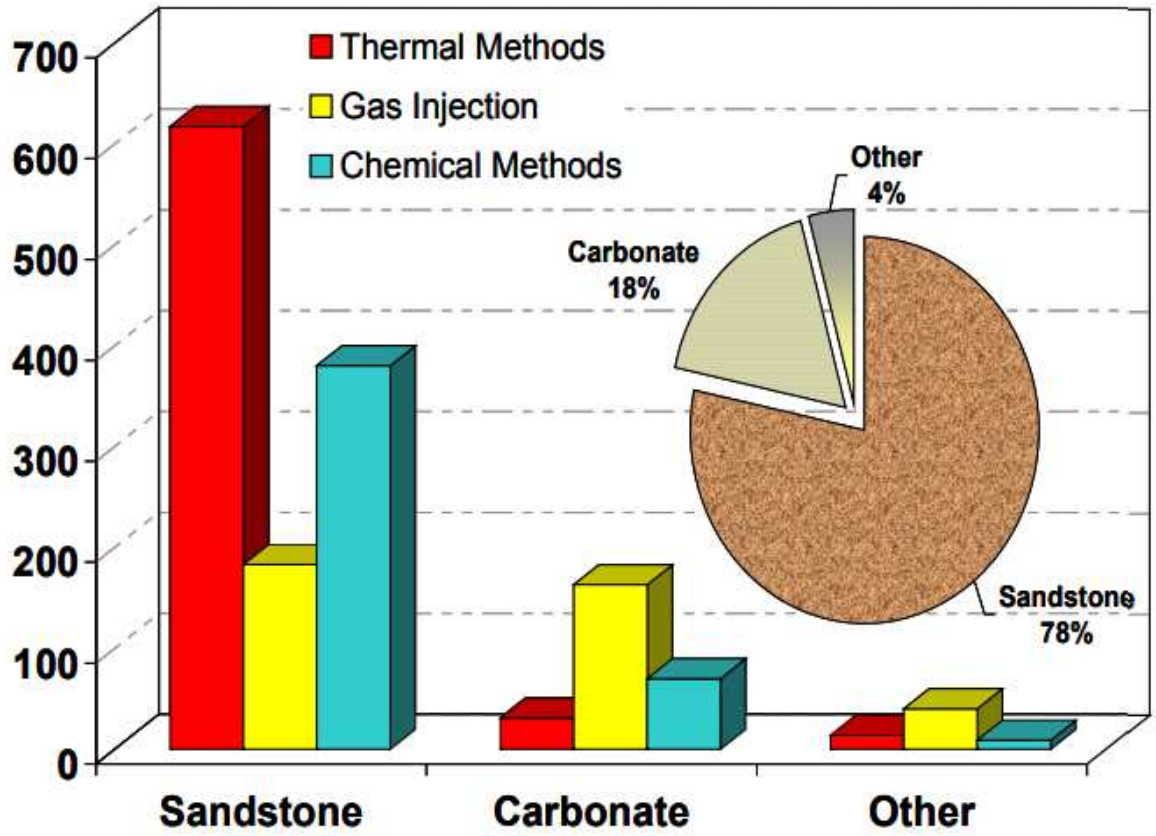


Figure 2.5: Enhanced oil recovery methods by lithology based on a total of 1507 projects (Alvarado & Manrique, 2010).

For the purpose of this thesis, we choose to mimic Emlichheim, which is an oilfield found in an anticline in North-West-Germany on the border with the Netherlands as shown in Figure 2.6 (Leonhardt, 2001). It was discovered in 1943 and soon after production started in 1944 on the German side (Leonhardt, 2001). Emlichheim oil field is currently operated by Wintershall (Wintershall, 2012). Production slowly declined until 1981, when the first steam flood operation was implemented to recover the 24^{o} API oil (Leonhardt, 2001). The reservoir is in Bentheimer sandstone, which is a marine Sandstone that was deposited during the lower Cretaceous about 135 million years ago (Dreier, 2009; Geo ExPro, 2006).

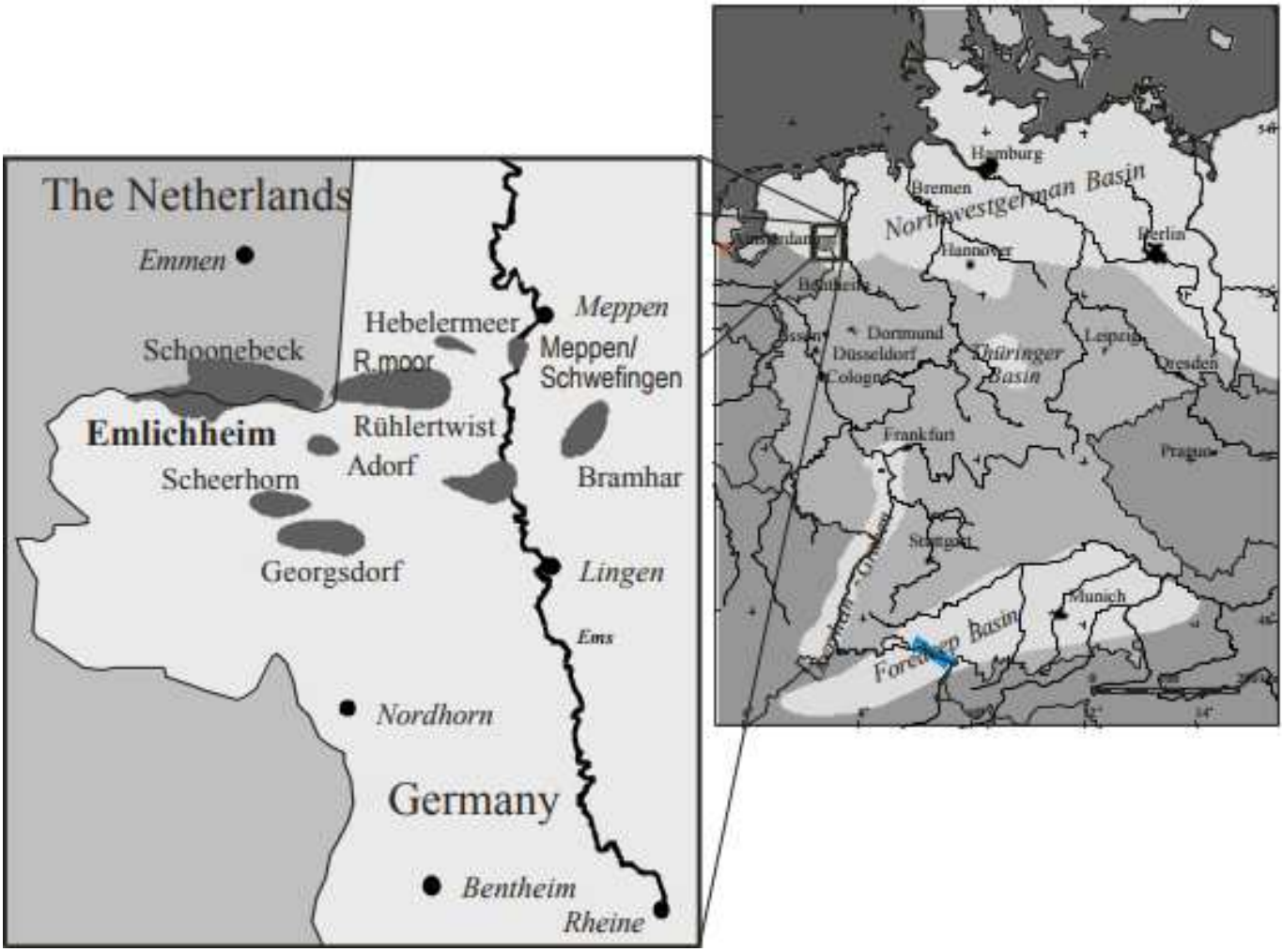


Figure 2.6: Location map of the Emlichheim oilfield and the adjacent oilfields in the area west of the river Ems (Leonhardt, 2001).

2.5 Time-lapse Seismic Monitoring of Steam Injection

Time-lapse seismic is a repeated seismic survey of the same area but at different times. These seismic surveys are calibrated, processed and compared, and the differences between them are closely analyzed to interpret changes in fluid properties and migration (Ross & Altan, 1997). This is essential because it enables reservoir management to act prudently by properly allocate their finite resources in a way that optimizes oil production (Fanchi, 2001).

We stressed the importance of time lapse seismic in monitoring sweep efficiency in heavy oil reservoirs undergoing steam injection. Heavy oil is mostly found in shallow reservoirs less than 1 km deep (Han et al., 2008). Using seismic

waves to image the near surface is challenging because of various factors. Noise is one of the main problems in near-surface reflection seismology (Robertsson et al., 1996). It can be divided into two categories; noise caused by external sources, such as wind or moving objects, and noise caused by the seismic source itself. External noise can be removed using different processing techniques, such as muting and filtering. However, noise caused by reflections and refractions from near-surface heterogeneities interferes with the original signal due to its proximity to the seismic source and receiver (Butler, 2005).

The high velocity at which seismic waves travel makes it more difficult to distinguish and pick shallow reflectors that are within such close proximity to the seismic source and receiver because the time difference is so short that it is difficult to resolve. Another challenge is the fact that sediments near the surface, also known as the weathering layer, usually have a lower quality factor resulting in more attenuation of the seismic signal, especially of higher frequency content (Busfar & Toköz, 2013). Higher frequency content is can be useful in detecting changes in rock physics properties, such as fluid saturation (Francese et al., 2002). However, the fact that most heavy oil reservoirs are shallow results in less attenuation of the seismic signal compared to if they were deeper in the Earth. This results in the presence of higher frequency content, which can reflect more detail about the subsurface including changes in fluid and rock properties within the reservoir. All these factors mean that seismic survey designs intended to monitor shallow targets are usually different to those intended to monitor conventional deep hydrocarbon reservoirs (Fourie & van Dam, 2008). Broadband geophones are sometimes buried up to a few metres deep to increase ground coupling and minimize the effects of the near surface sediments. The number of geophones is increased by decreasing their separation in order to increase the fold number, which helps in eliminating some of

the noise by stacking common shot records in the processing stage (Upadhyay, 2004).

Seismic waves have been used, usually in conjunction with other geophysical methods, to monitor steam injection in heavy oil reservoirs. In a study by Statoil Canada, geomechanical and 4D seismic data were incorporated into numerical models that simulated SAGD and used to improve history-matching studies (Gu et al., 2011). EnCana Corporation conducted a thermal pilot project in Christina Lake, Canada, where they combined 4D and cross-well seismic data to understand the effects of geology on the SAGD process (Zhang et al., 2007).

Other studies used 4D seismic data alone to map the steam chamber extent during an enhanced oil recovery operation using steam injection (Lumley, 2001;Tanaka et al., 2010; Cotton et al, 2012). In a pilot project in Alberta, Total and ConocoPhillips used high frequency time-lapse seismic data with frequencies of up to 300 Hz to monitor heavy oil SAGD operation at a depth of 400 metres (Forgues et al., 2006). They were able to detect travel time variations less than 0.1 millisecond due to data repeatability and the geophone array being buried 9 metres below the surface, which improved the signal to noise ratio significantly. This enabled them to better delineate the steam chamber, which in effect improved their management of the SAGD operation. However, a seismic frequency of 300 Hz is much higher than the range of frequencies used in typical seismic exploration or delineation operations.

Forgues and others also observed variations in velocity and amplitude of seismic waves in a steam flooded heavy oil field over a period of 5 years using both active time-lapse and passive seismic monitoring (Forgues et al., 2011). Results of travel time and amplitude variations through the reservoir are shown in Figures 2.7 and 2.8, respectively. Steam is injected in the upper horizontal well while oil is

produced from the lower well. Injecting steam increases the pore pressure, which decreases seismic velocity. This is observed in Figure 2.7 by the occurrence of the red colour, which corresponds to slower seismic velocity due to the presence of steam. On the other hand, Figure 2.8 shows a notable decrease in seismic amplitude due to oil production from the southern horizontal well. However, this study detects the lateral extent of the steam chamber but does not help delineate the steam chamber vertically. It also involved using seismic sources and geophones that are buried to a depth of 80m and 12m, respectively, which is not always feasible.

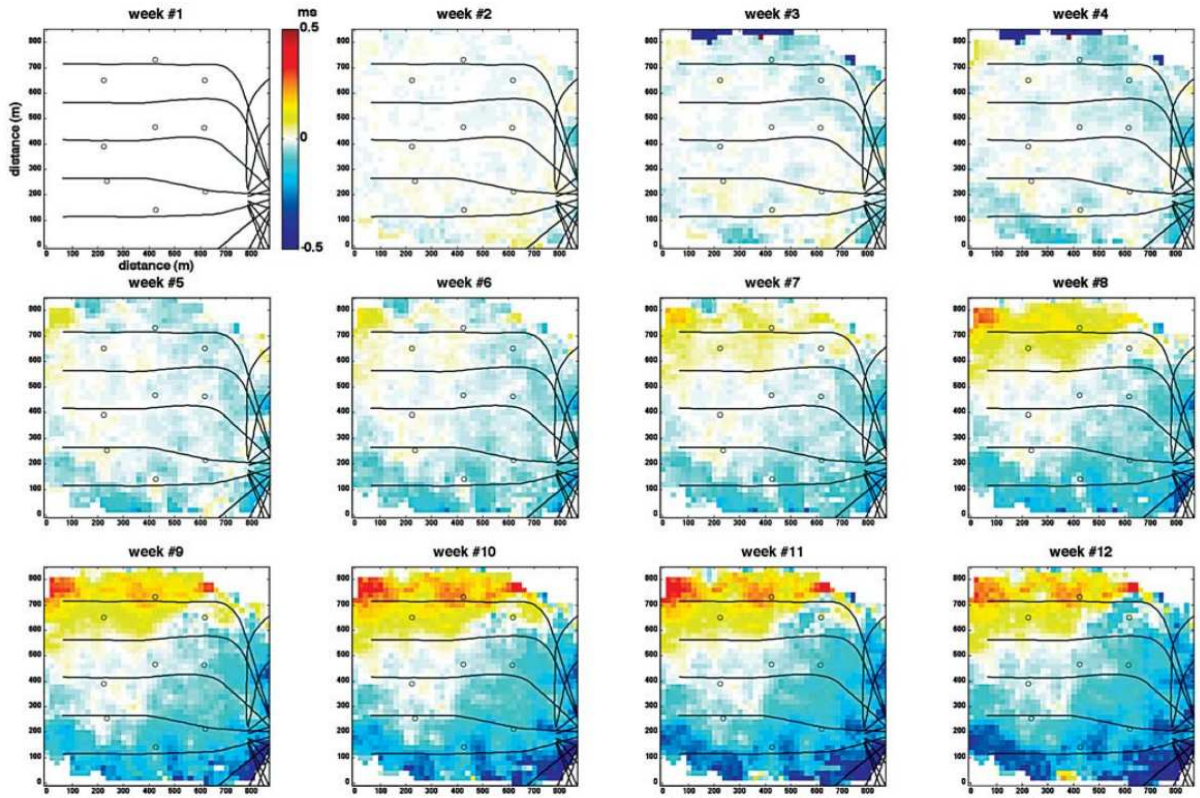


Figure 2.7: Vertical cross sections showing seismic velocity variations over a period of 12 weeks of steam injection in a SAGD operation. Steam was injected in the uppermost horizontal well. The red colour corresponds to slower seismic velocity (Forgues et al., 2011).

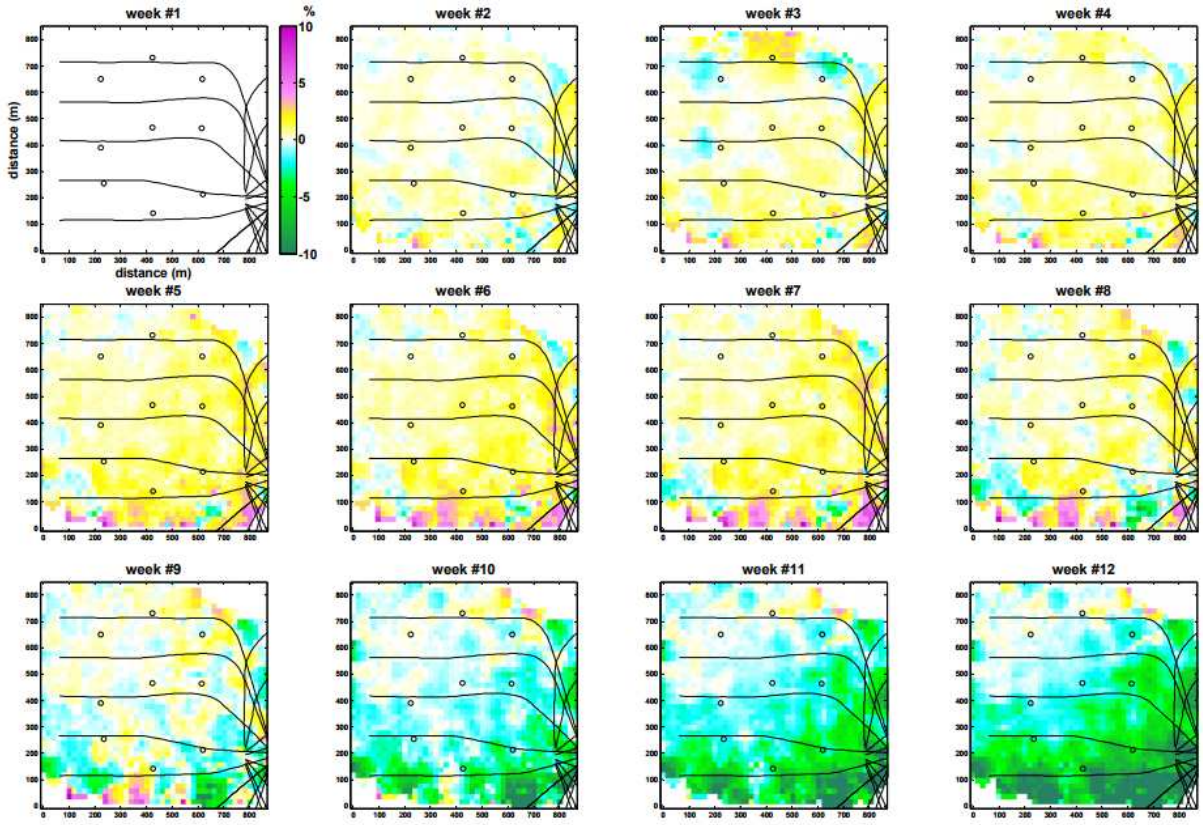


Figure 2.8: vertical cross-sections showing seismic amplitude variations over a period of 12 weeks of steam injection in a SAGD operation. Oil is produced from the southern most horizontal well where a decrease in seismic amplitude is observed and represented by the green colour (Forgues et al., 2011).

Time-lapse cross-well seismic data has also been used for inter-well velocity profiling which can be used to map steam fronts in heavy oil reservoirs (Spetzler, 2006; Nalonnil & Marion, 2012). Spetzler's results showing a cross section of the estimated time-lapse velocity structure using inverted seismic phase and amplitude data are shown in Figure 2.9 (Spetzler, 2006). It clearly shows a seismic velocity decrease around the area at which steam is injected due to increase in pore pressure.

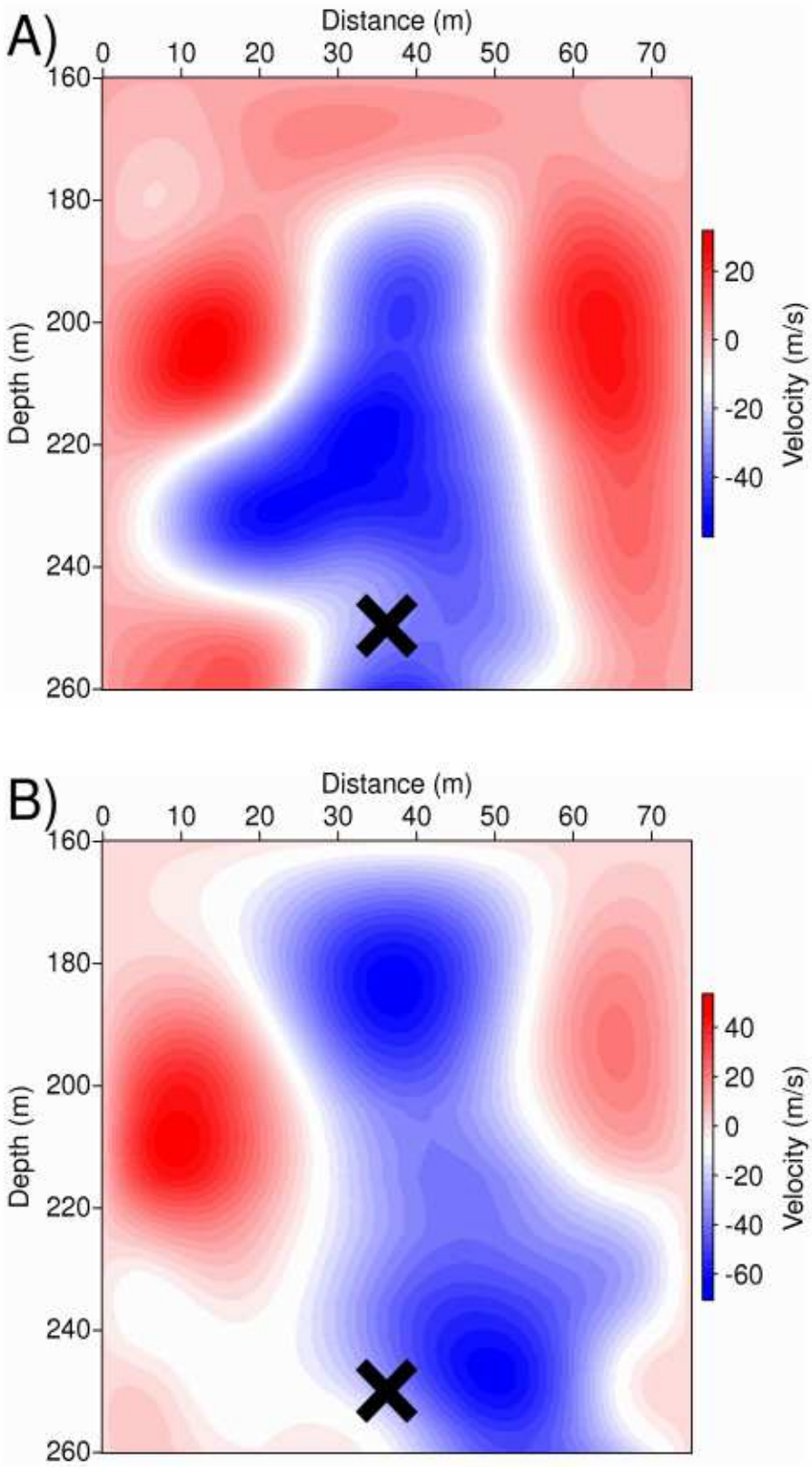


Figure 2.9: Cross section showing the estimated time-lapse velocity structure in a heavy oil reservoir. The top figure shows the estimated velocity structure using phase inversion while the bottom one uses amplitude inversion. The black cross mark indicates the location of the horizontal steam-injecting well (Spetzler, 2006).

The presence of gas can introduce a sharp acoustic impedance contrast resulting in a sharp increase in amplitude creating what is referred to as a “bright spot” as shown in Figure 2.10 (Cooper, 2010). The blue colour corresponds to high amplitude contrast due to the presence of gas-sand in this case, while the red colour below it corresponds to a contrast in the opposite polarity due to the presence of shale.

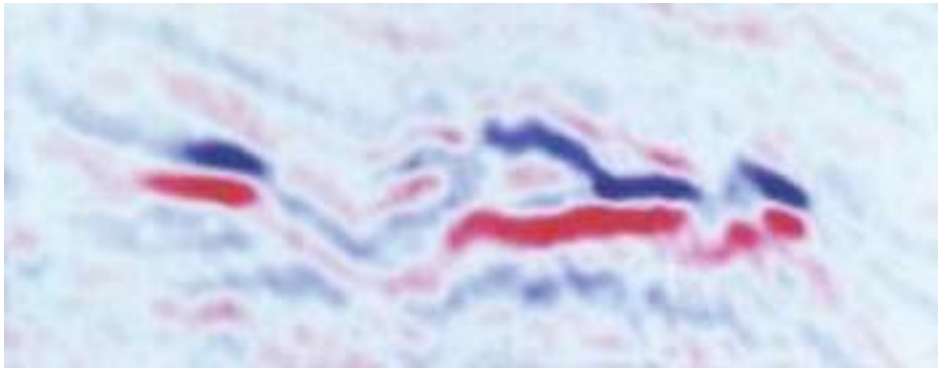


Figure 2.10: Amplitude reflections showing gas in the Gulf of Mexico (Cooper, 2010).

Most of the aforementioned studies attempt to extract as much information as possible about the reservoir properties directly from seismic data. Another approach to monitoring the changes in a reservoir is by solving the forward problem. A paper published by IFP Energies is an example of attempting to solve the forward problem by linking an initial static model, coupled fluid-flow and geo-mechanical models that simulate thermal production, and time-lapse synthetic seismic maps (Lerat et al., 2010). Forward modeling is important because it improves our ability to perform seismic inversion in which we predict rock and fluid properties, as well as, in this context, the steam chamber lateral and vertical extent. In forward modelling, we are interested in detecting changes to the seismic signals through time, e.g. V_p and V_s, as a result of changes in rock or fluid properties. This would be useful in mapping steam fronts and determining areas of the reservoir that has not been swept, which in effect improves our ability to optimize the productivity of the reservoir.

In addition, production from shallow heavy oil reservoirs with unconsolidated sands can result in compaction (Robertson et al., 2012), which changes the density and hence the velocity of seismic waves (Fawad et al., 2011). Studying the changes in the amplitude of the reflected seismic wave with changing distance between the source and the geophones, commonly known as amplitude verses offset, is a powerful tool to detect changes in the reservoir and fluid properties (Dadashpour et al., 2009). In one study, Wandler et al. (2007) looked at the AVO response of a mixture of brine, oil and carbon dioxide. The AVO was plotted in the intercept-gradient domain at both the top and bottom of the fluid and they were able to distinguish between fluids that contained oil from those that did not (Wandler et al, 2007). However, this was done in the lab using ultrasonic frequencies on the order of 1-10MHz, which is much higher than the frequencies used in near surface exploration geophysics.

2.6 Summary

Conventional oil reserves around the world are declining and this has to be compensated for by producing more of the vast reserves of heavy oil around the world. Advancements in drilling and monitoring technologies are allowing us to achieve this goal. One particular area that can be improved is sweep efficiency as it increases the recovery factor in steam flood operations. Using time-lapse seismic surveys to monitor and delineate the steam chamber is vital to better manage the reservoir and its production.

Knowing the distribution of the steam in a steam flood operation is important because it helps us to better manage the reservoir and increase the sweep efficiency, thus increasing the oil recovery factor. For example, reservoir engineers need to decide where to drill additional injection and production wells. We use

reservoir simulators to try to get a general idea of the distribution of the steam within the reservoir. However, reservoir simulation results do not accurately represent the geometry of the steam in the reservoir because the model that we feed it does not capture the actual unknown heterogeneity in the oil reservoir.

This is why 4D seismic reflection surveys are used to better define the distribution of the steam within a reservoir undergoing steam flood operation, which can then be used for seismic history matching and improving the reservoir simulation results (Lopez et al., 2015). The issue with seismic reflection is that it cannot always determine the bottom of the steam, thus the thickness of the steam chamber, as we will show in chapter 5. This is why we develop an AVO procedure, which helps to determine the range at which the bottom of the steam is located, thus giving us a range for the thickness of the steam chamber.

We will study the AVO intercept and gradient at the top and bottom of a steam chamber using a synthetic reservoir scale data that mimic a real oil old field located in Germany that is called Emlichheim. Being able to monitor the steam using 4D seismic data more precisely can be very beneficial because it would enable us to better map steam fronts and have a better understanding of the areas of the reservoir that have not been swept. This information helps to increase the sweep efficiency and better manage the reservoir's production.

3. Reservoir Simulation

3.1 Introduction

In this chapter, STARS is used, which is a commercial reservoir simulation software developed by the Computer Modelling Group (CMG), to simulate a heavy oil field undergoing a steam flood to enhance oil recovery. The conservation, fluid flow and heat flux equations are solved numerically in the STARS software. The purpose of the simulation is to describe the evolution of the steam chamber so we can compare the steam chamber geometry estimated from our AVO analysis procedure with the actual geometry. We did not analyse data acquired from a real field because we wanted to have full control on the input and know exactly what is controlling the response. The reservoir properties are chosen to mimic Emlichheim, which is a heavy oilfield in Germany, in order to have a realistic reservoir model (Leonhardt, 2001). The dynamics and geometry of the steam front are predicted using STARS, and are used in the next chapter as inputs into our MATLAB rock physics code.

The parameters investigated in the rock physics chapter were effective pressure, temperature, porosity, fluid saturations, brine salinity and oil API. We will show the distribution of each of the parameters mentioned above throughout a cross section of the reservoir at different time intervals along with oil recovery with time and discuss these results.

3.2 Method

The initial reservoir parameters are chosen to mimic Emlichheim whenever possible and are recorded in Table 3.1. Table 3.2 provides the temperature and viscosity relationship for the heavy oil in the reservoir. The last four viscosity values

were estimated by extrapolating the temperature versus viscosity curve for the oil in Emlichheim (Leonhard, 2001). Table 3.3 and 3.4 provide the water-oil relative permeabilities and liquid-gas relative permeabilities, respectively. These used the curves from Abubakar (Abubakar, 2016) with the saturations rescaled to the end point saturations observed in Emlichheim.

Porosity	30%	
Permeability	Horizontal (k_h)	300mD to 10D
	Vertical (k_v)	k_h/10
Initial pressure	1250 psi	
Initial reservoir temperature	99 °F	
Thermal conductivity of	Reservoir rock	24 *Btu/*ft.day.F
	Water	8.5 *Btu/*ft.day.F
	Oil	4 *Btu/*ft.day.F
	Overlying formation	24 *Btu/*ft.day.F
	Underlying formation	24 *Btu/*ft.day.*F*
Volumetric heat capacity of the rock	35 *Btu/ft*^{3}*F*	
Initial saturations	Oil	0.92
	Brine	0.08
Oil API	24°	
Reservoir depth	2500 ft	
Reservoir thickness	100 ft	
Injection fluid temperature	600 °F	
Maximum bottom hole pressure at injection well	3000 psi	
Minimum bottom hole pressure at producer well	20 psi	
Injection rate	100 bbl/day	
Steam quality	0.8	

Table 3.1: Initial reservoir & well properties.

Porosity is assumed to be constant while permeability is broken down into vertical and horizontal permeability. Horizontal permeability varies linearly from 300mD at the bottom of the reservoir to 10 Darcy at the top. Vertical permeability is assumed to always be one tenth of the horizontal permeability. Steam quality is the mass fraction in a saturated mixture that is vapour. It can be calculated by dividing

the mass of the vapour by the mass of the total mixture (Cengel & Boles, 2002). The overlying rock is assumed to be Claystone, which acts as a seal that prevents any fluid from migrating upwards pre and post steam injection (Kockel et al, 1994). The boundary conditions at the top and the bottom of the reservoir are set so that heat conduction is permitted while mass transfer, heat convection and heat radiation are not permitted as the reservoir is sealed.

Temperature (°F)	Viscosity cP
99	175
150	50
200	22
250	12
300	7
350	5
400	3.5
450	2.5
500	1.8
550	1.3
600	1.0
650	0.8
700	0.7

Table 3.2: Temperature vs. viscosity for the 24° API oil in the reservoir (Leonhard, 2001).

S_w	K_w	K_{row}
0.08	0.0	0.4
0.1185	0.000056	0.361
0.17625	0.000552	0.30625
0.2725	0.00312	0.225
0.36875	0.00861	0.15625
0.465	0.01768	0.1
0.56125	0.03088	0.05625
0.6575	0.04871	0.025
0.696	0.05724	0.016
0.75375	0.07162	0.00625
0.79225	0.08229	0.00225
0.85	0.1	0.0

Table 3.3: Water-oil relative permeabilities.

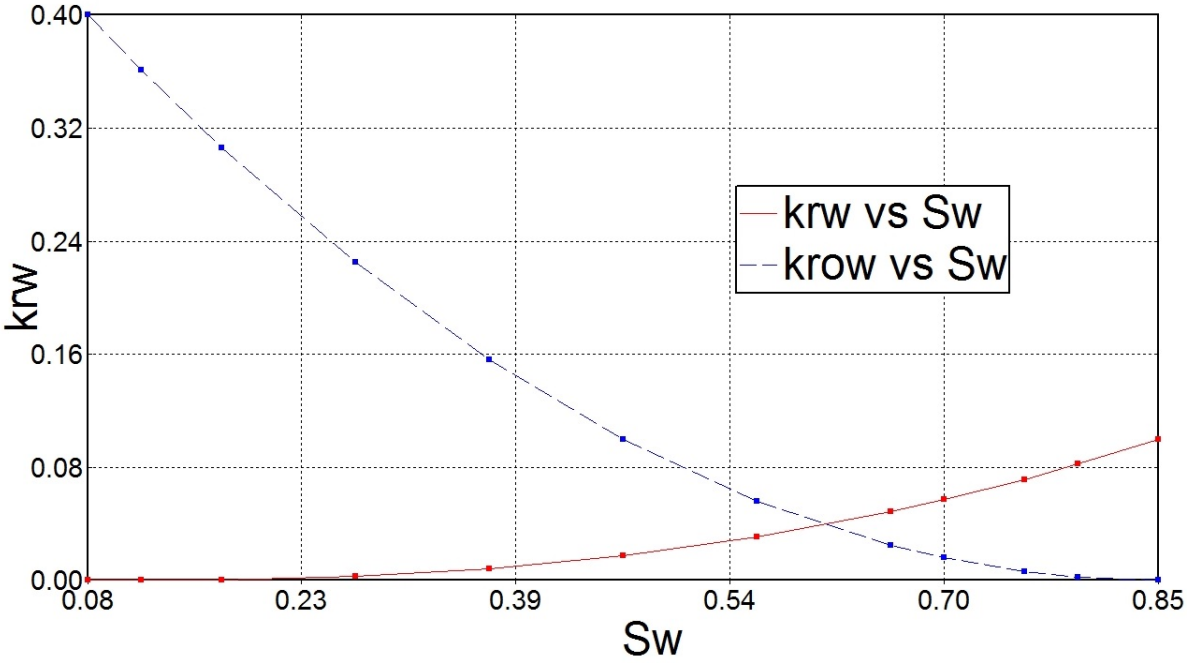


Figure 3.1: Water-oil relative permeabilities.

S_l	K_{rg}	K_{rog}
0.08	0.2	0.0
0.55	0.14202	0.0
0.57	0.13123	0.00079
0.60	0.11560	0.00494
0.62	0.10555	0.00968
0.65	0.09106	0.01975
0.67	0.08181	0.02844
0.70	0.06856	0.04444
0.72	0.06017	0.05709
0.75	0.04828	0.07901
0.77	0.04087	0.09560
0.80	0.03054	0.12346
0.83	0.02127	0.15486
0.85	0.01574	0.17778
0.87	0.01080	0.20227
0.90	0.00467	0.24198
0.92	0.00165	0.27042
0.94	0.0	0.30044
1.0	0.0	0.4

Table 3.4: Liquid-gas relative permeabilities.

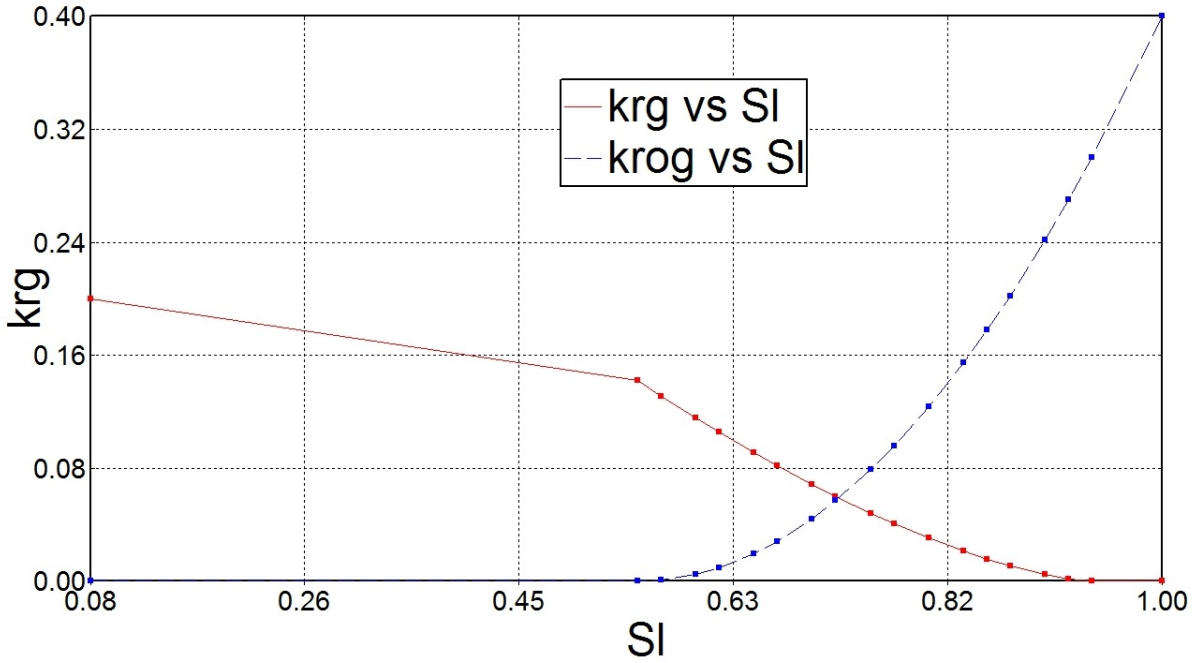


Figure 3.2: Liquid-gas relative permeabilities.

The distance between a steam injection well and a producing well in a steam flood operation is 100 to 200m (Leonhardt, 2001; Abdullah 1976). The bottom hole pressure at the injection well is set to a maximum of 3000 psi to maintain a constant rate between the two wells in the case where the horizontal permeability is assumed to be constant at 600 mD as we will see later in this chapter when we conduct the sensitivity analysis. The model is a 2D grid in the x and z direction with dimensions of 500×10×100ft. The well perforations of the injection well are in the centre of each grid cell on the very left column while the perforations of the producing well are in the centre of each grid cell on the far right column in the 2D cross section shown in Figure 3.3. We performed a grid refinement study in STARS to determine the best grid size to use for future simulations based on changes in cumulative oil production, steam oil ratio with time, and CPU run time. The dimensions of the grid were kept constant at 500×10×100ft in the x, y and z directions, respectively. The number of grid blocks were varied in the x and z directions. Five grid dimensions were used, namely, 50×10, 100×20, 100×40, 200×40 and 200×80. The last two grids, namely

200×40 and 200×80, were to examine the influence of vertical resolution assuming the flow is gravity dominated. Plots showing ternary saturation values (steam, brine, oil) after 10 years of steam flooding are presented along with plots showing the cumulative oil production and steam to oil ratio to monitor changes resulting from using different grid block numbers. It is important to note here that changing the number of grid blocks also changes the size of each of these grid blocks because we are fitting equal number of grid blocks in the same space in each dimension. For example, the k dimension, i.e. vertical direction, is always 100ft. When we choose to have 20 grid blocks in the vertical direction, each grid block would have to be 5ft long in the k axis. Figures 3.3, 3.4, 3.5, 3.6 and 3.7 show the fluid distribution after 10 years of steam flooding for the grids 50×1×10, 100×1×20, 100×1×40, 200×1×40 and 200×1×80, respectively.

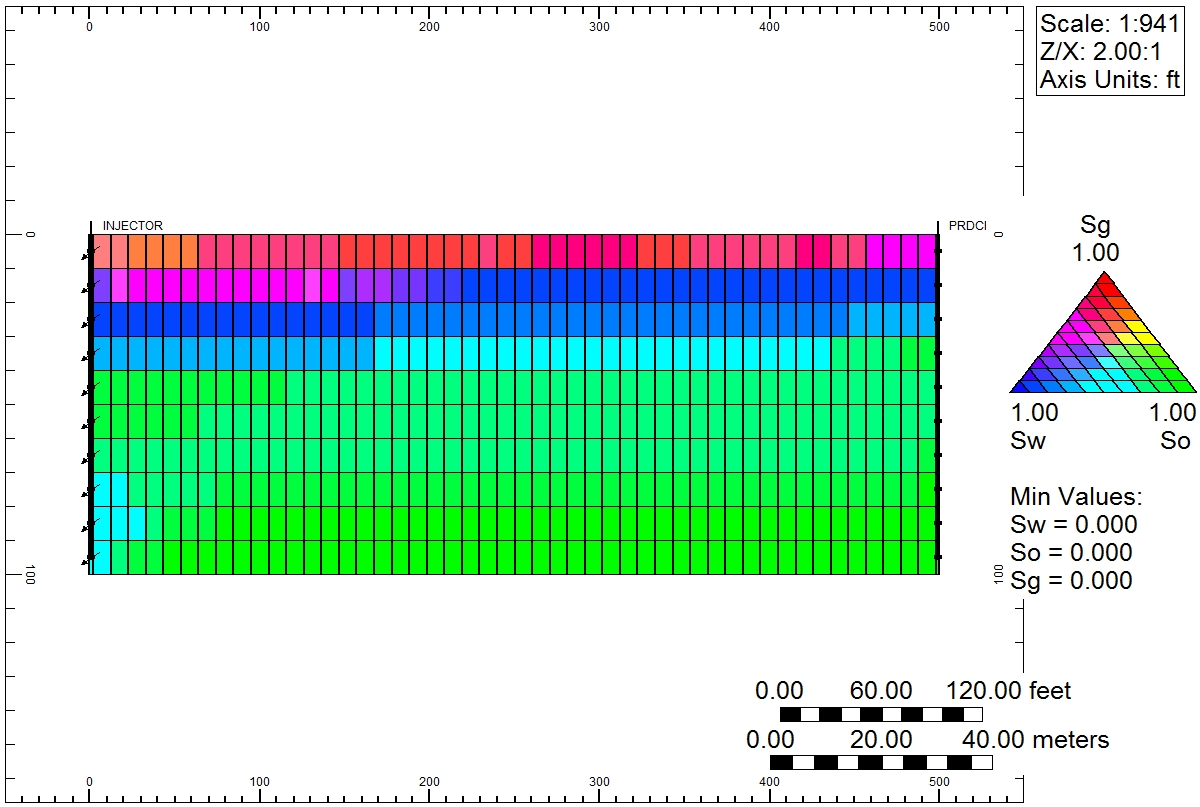


Figure 3.3: Ternary saturation after 10 years of continuous steam injection using 50×1×10 grid blocks.

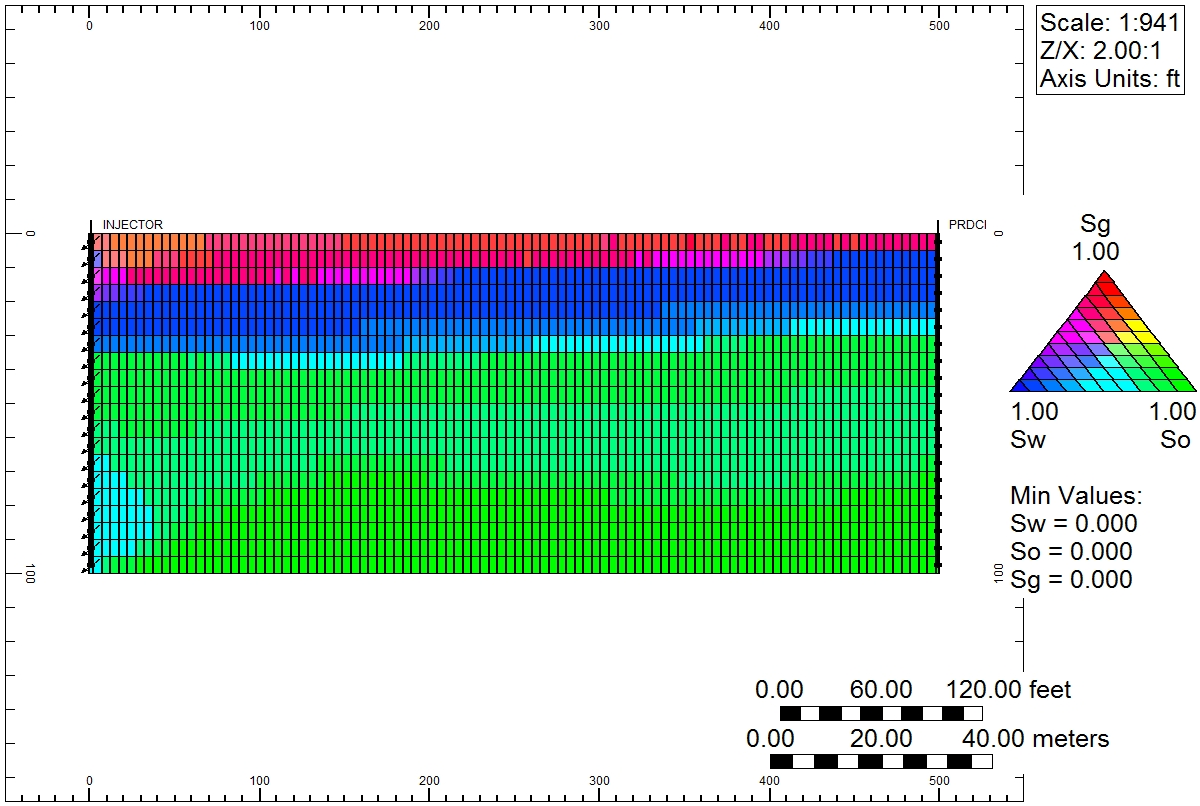


Figure 3.4: Ternary saturation after 10 years of continuous steam injection using 100×1×20 grid blocks.

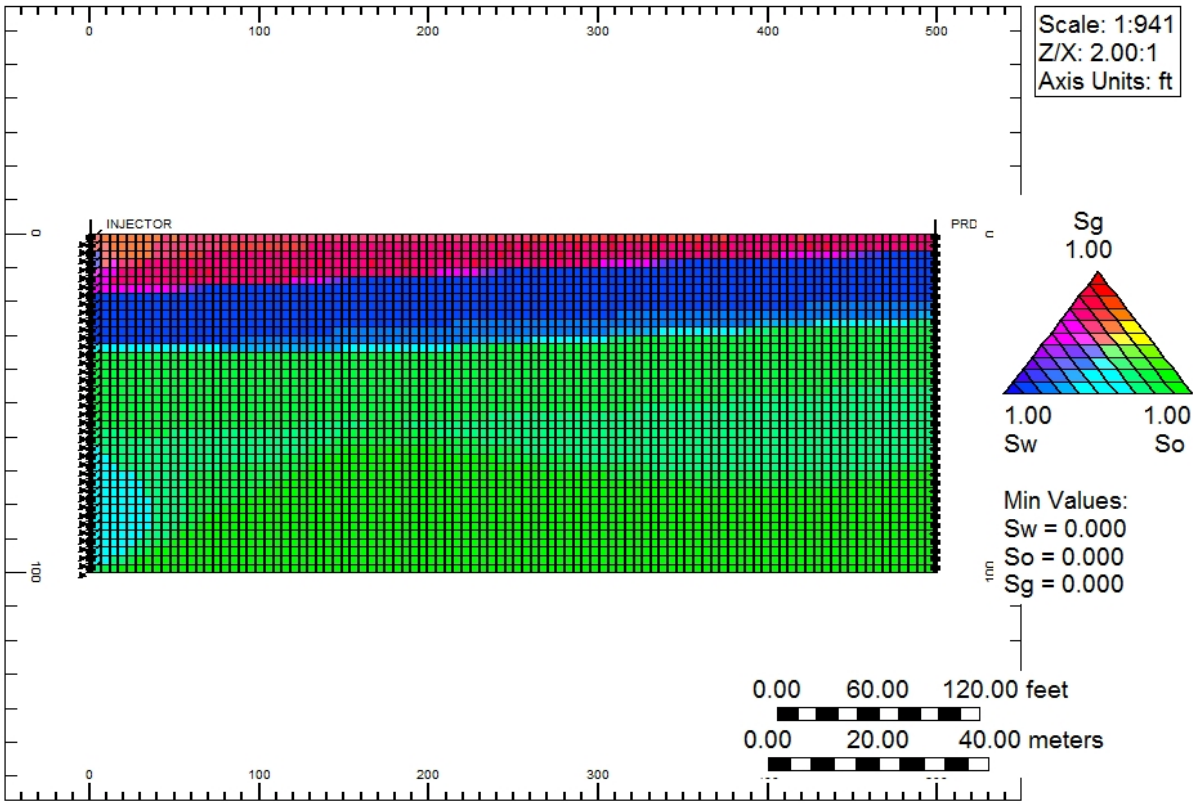


Figure 3.5: Ternary saturation after 10 years of continuous steam injection using 100×1×40 grid blocks.

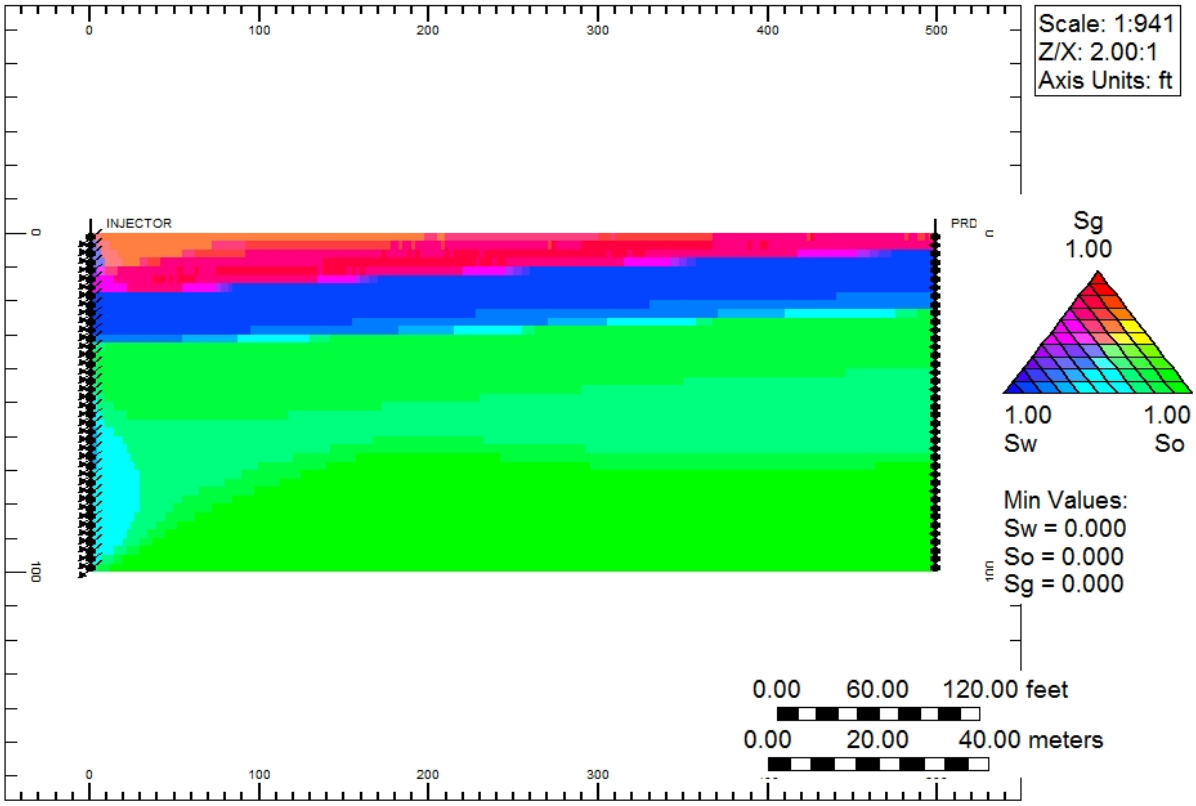


Figure 3.6: Ternary saturation after 10 years of continuous steam injection using 200×1×40 grid blocks.

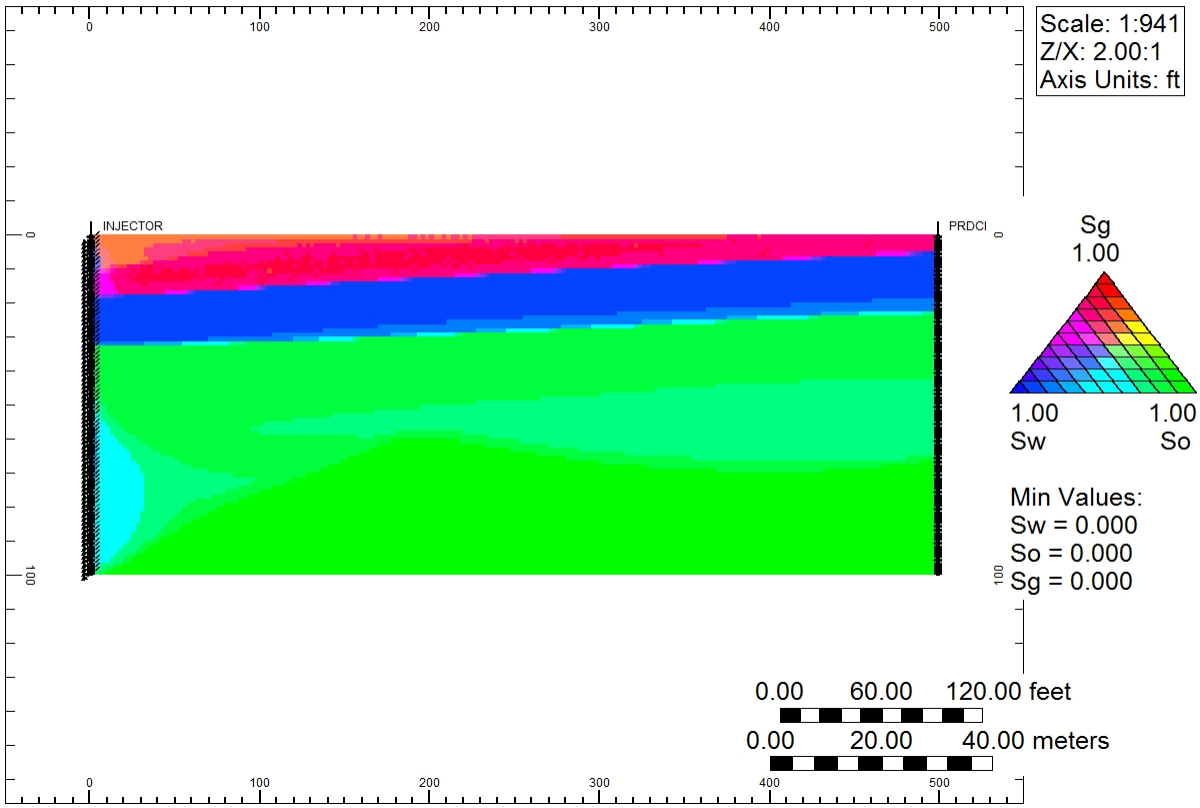


Figure 3.7: Ternary saturation after 10 years of continuous steam injection using 200×1×80 grid blocks.

A curved zone with higher water saturation appears to form within the middle of the water/oil saturated zone in Figures 3.3 to 3.7. This is due to water trying to fall to the bottom of the reservoir after condensing from steam. A sphere of condensed water gradually detaches from the water layer above it to form a sphere of condensed water at the bottom of the injection well where the permeability decreases linearly with depth.

The cumulative oil production and steam to oil ratio for the various grid sizes is shown in Figure 3.8 and 3.9, respectively, to help better quantify and visualize the effect of changing the size of the grid blocks. The thickness of the tongue decreases with increasing vertical grid refinement, thus decreasing the cumulative oil production as demonstrated by the difference between the yellow and purple lines in Figure 3.8. The CPU run time for the grid sizes 100×1×20, 100×1×40, 200×1×40 and 200×1×80 increased compared to the initial grid size 50×1×10 by a factor of 4, 10, 48 and 117, respectively. The difference in production behaviour in all 5 cases is relatively small. We choose the grid size 100×1×40 as the optimal option because it results in a finer vertical resolution of 2.5ft while not being too expensive in term of processing time.

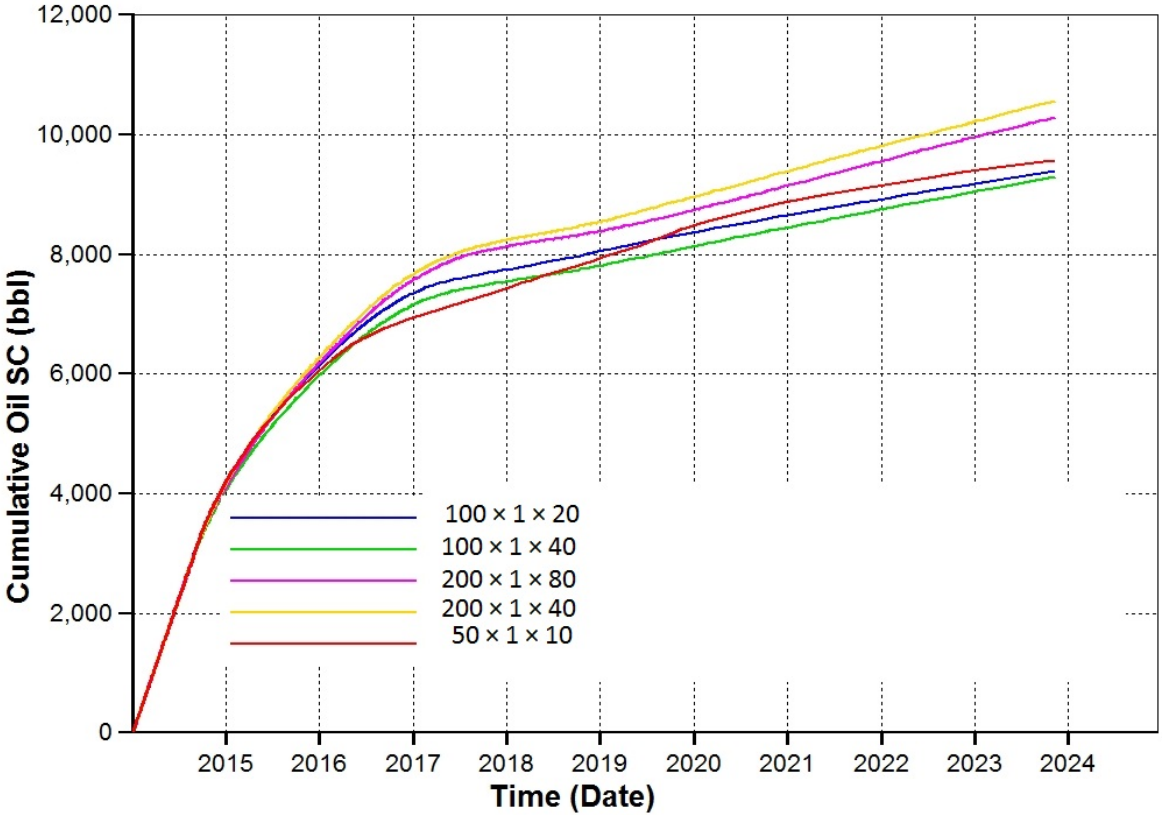


Figure 3.8: Cumulative oil production over 10 years of steam flooding for simulations with five different grids. The number of grid blocks in the x, y, and z direction are 50×1×10, 100×1×20, 100×1×40, 200×1×40, and 200×1×80 using a 1 ft wellbore radius.

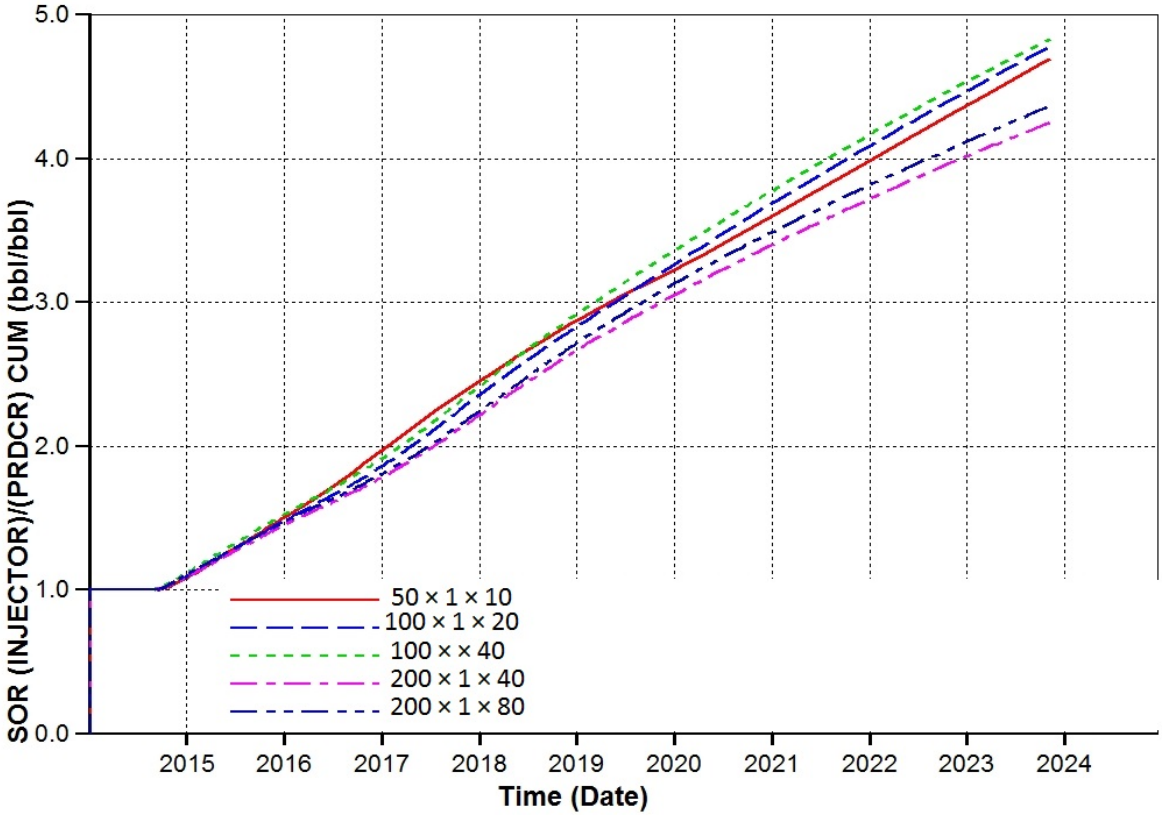
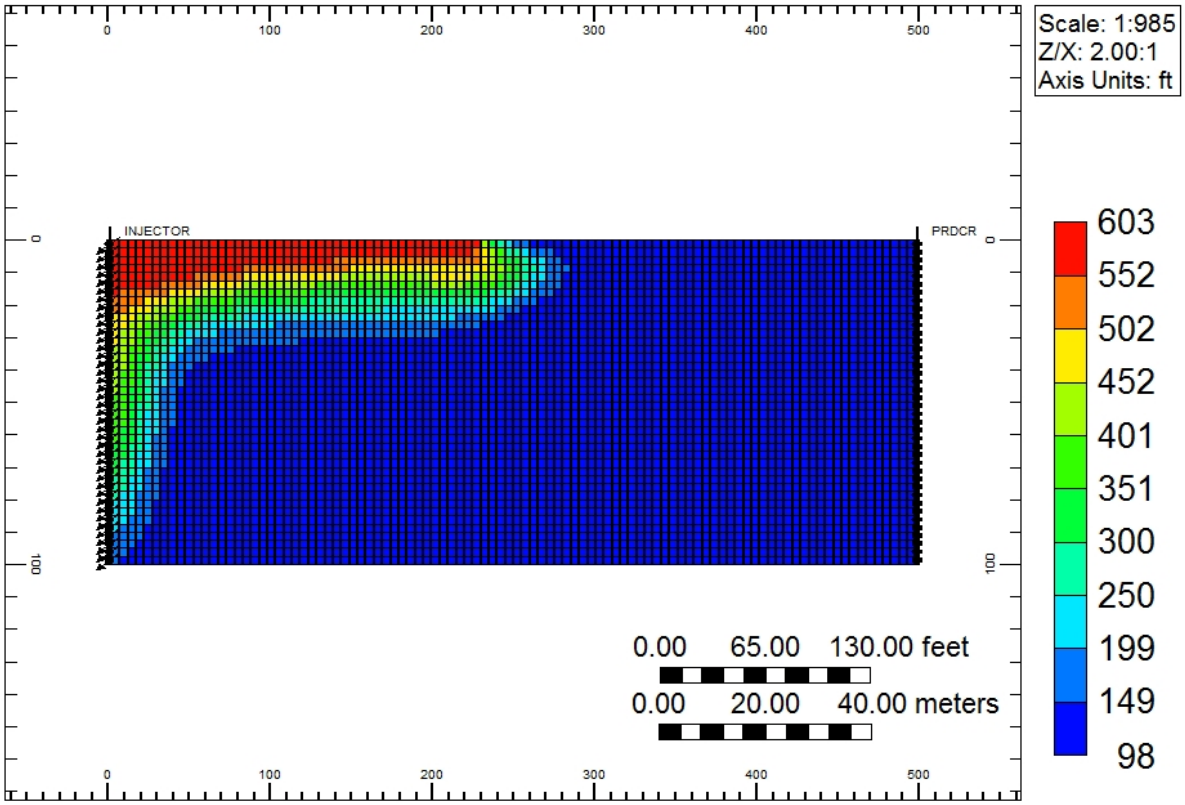


Figure 3.9: Steam to oil ratio over 10 years of steam flooding for simulations with five different grids. The number of grid blocks in the x, y, and z direction are 50×1×10, 100×1×20, 100×1×40, 200×1×40, and 200×1×80 using a 1 ft wellbore radius.

3.3 Results

The reservoir simulation is set to output results in increments of 3 months. Results showing the distribution of temperature, fluid saturations and pressure are shown for 3 time intervals in Figures 3.10, 3.11 and 3.12, respectively. The first time interval that we present is after 1 year of steam flooding to get an idea of how the reservoir looks at an early stage as the steam front starts to propagate and sweep the reservoir starting from the injection well on the left towards the producing well on the right. The second time interval is after 4 years of steam flooding. That is the time step preceding the steam's breakthrough at the production well. The third and last time interval we present is after 10 years of steam flooding.



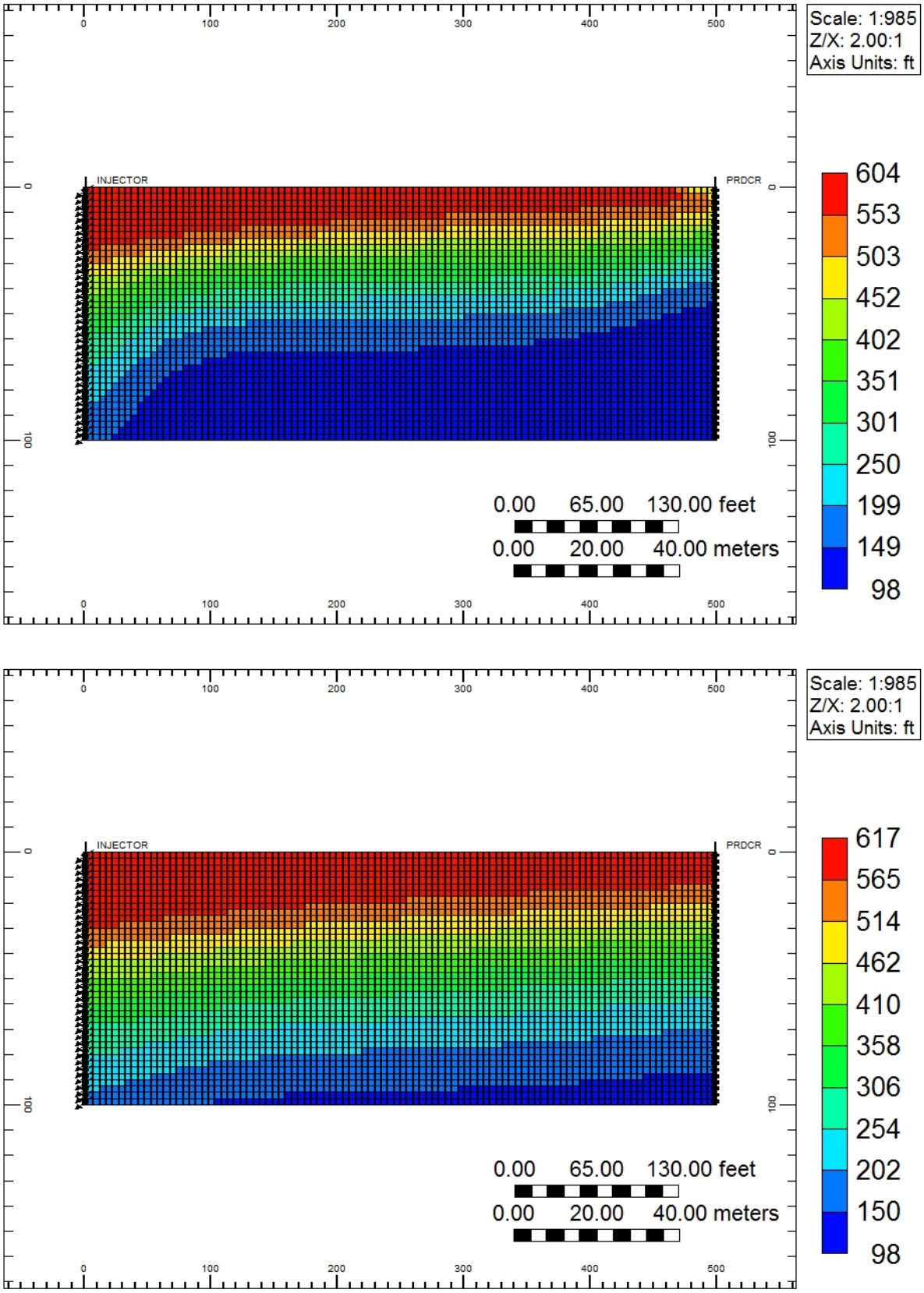
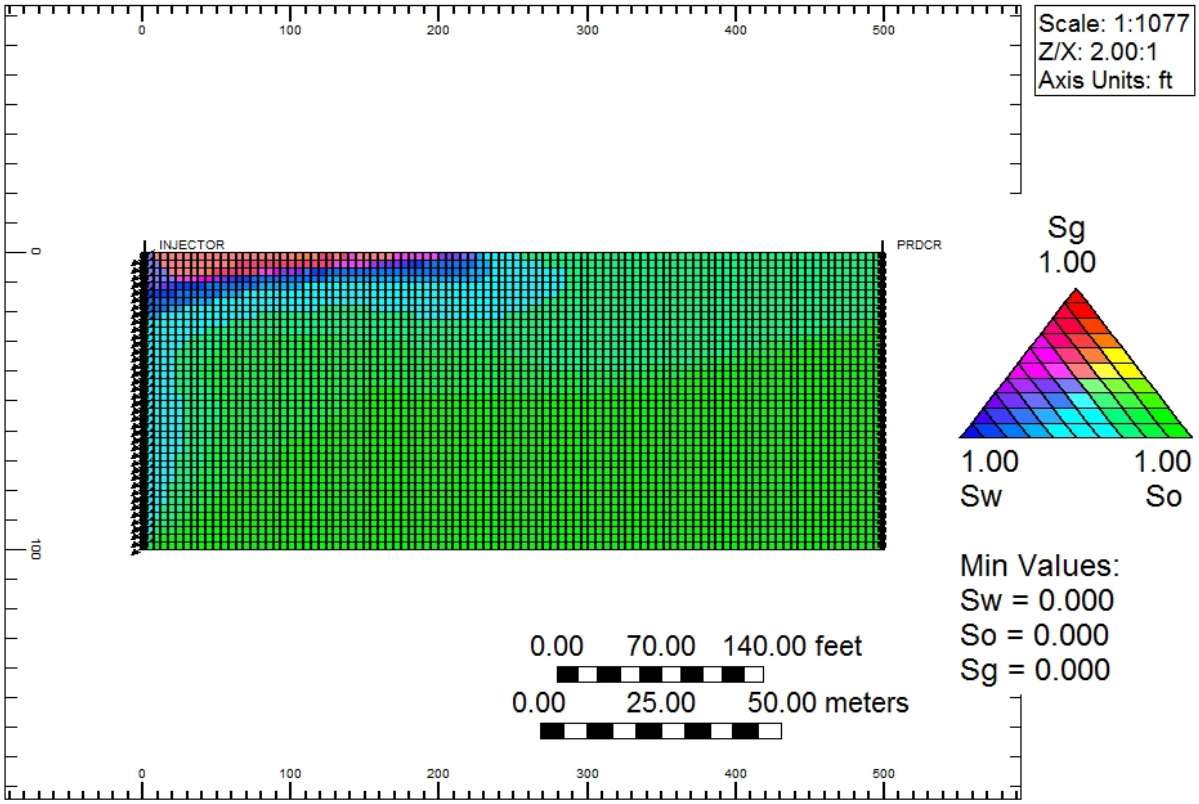
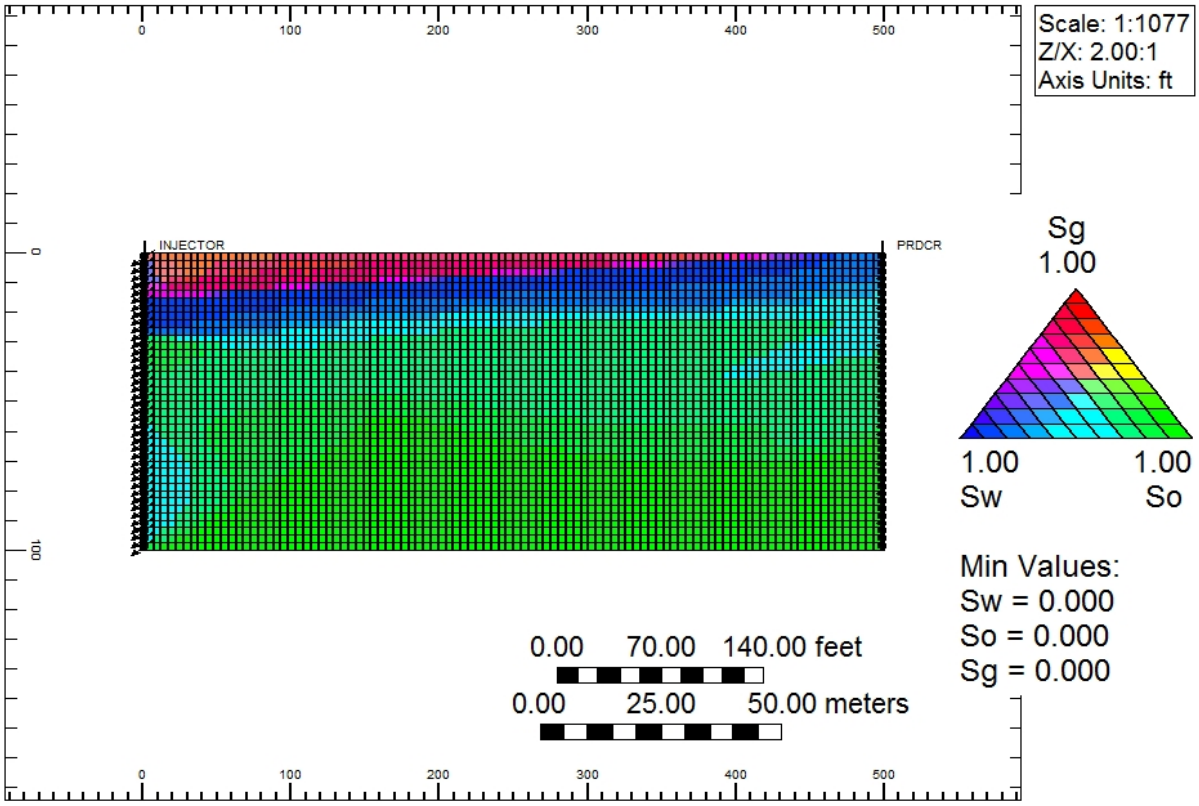


Figure 3.10: Temperature distribution at 1, 4 and 10 years of steam flooding. The steam injection well is at the left section of each of the 3 cross-sections while the production well at the right end.

The temperature distribution along a cross section of the reservoir in the i and k directions is shown in Figure 3.10. It ranges from the initial reservoir temperature of 100 °F to 617 °F. We clearly see the development of the steam override, as it tends to migrate to the top of the reservoir and towards the producing well because of its lower density and the pressure gradient, respectively.





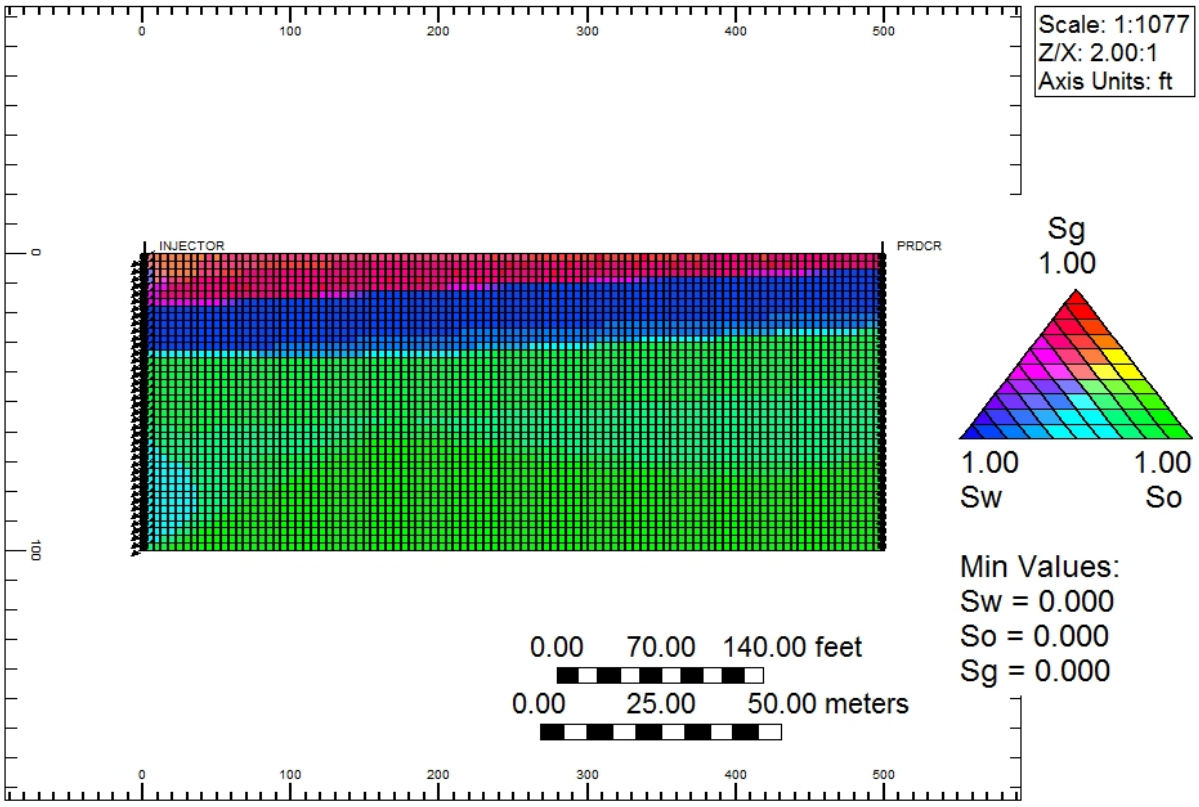
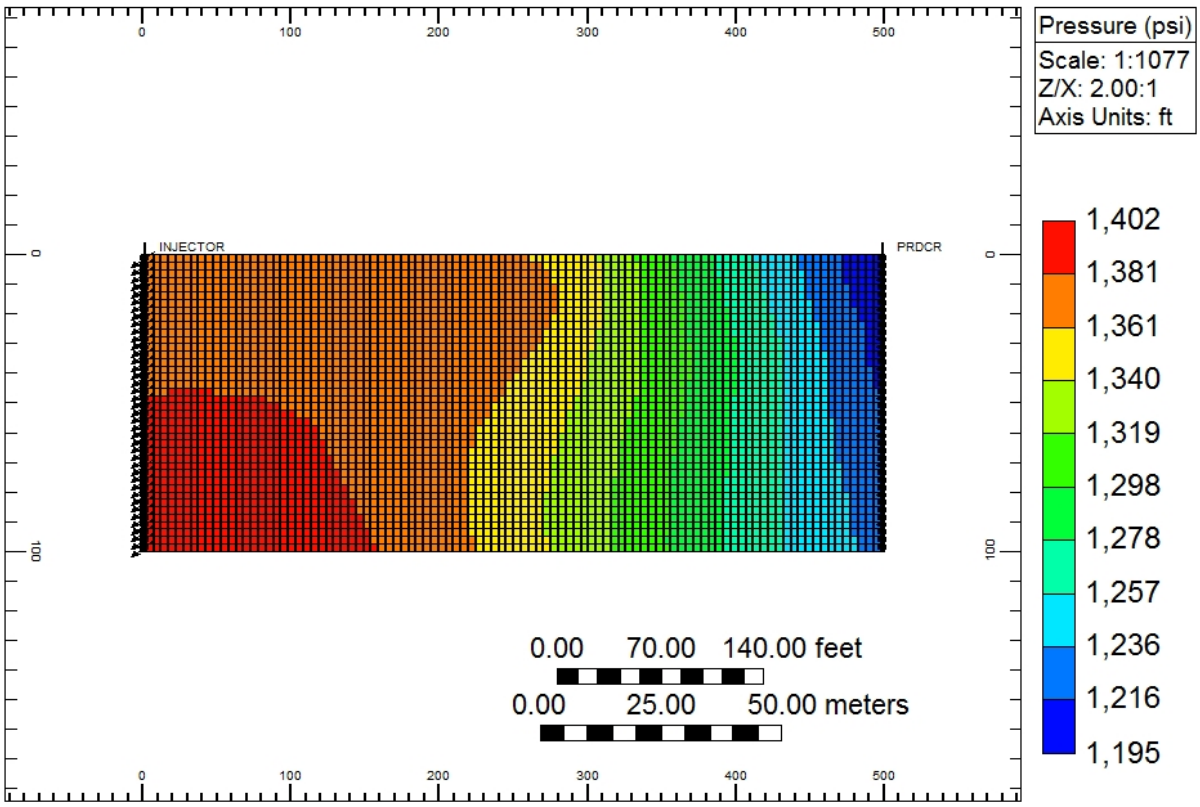


Figure 3.11: Ternary saturation at 1,4 and 10 years of steam flooding. The steam injection well is at the left section of each of the 3 cross-sections while the production well is at the right end.

The oil saturation plots in Figure 3.11 correspond to the temperature plots in Figure 3.10 and show that more oil is produced from the upper part, as the oil saturation is lower there because of the behaviour of the steam chamber. The steam heats the oil and reduces its viscosity making it easier to displace the oil and brine and push them towards the production well. A curved zone with higher water saturation appears to form within the middle of the water/oil saturated zone in Figure 3.11. This is due to the water trying to fall to the bottom of the reservoir after condensing from steam. Less than a year into the steam flood, a sphere of condensed water gradually detaches from the water layer above it to form a sphere of condensed water at the bottom of the injection well.



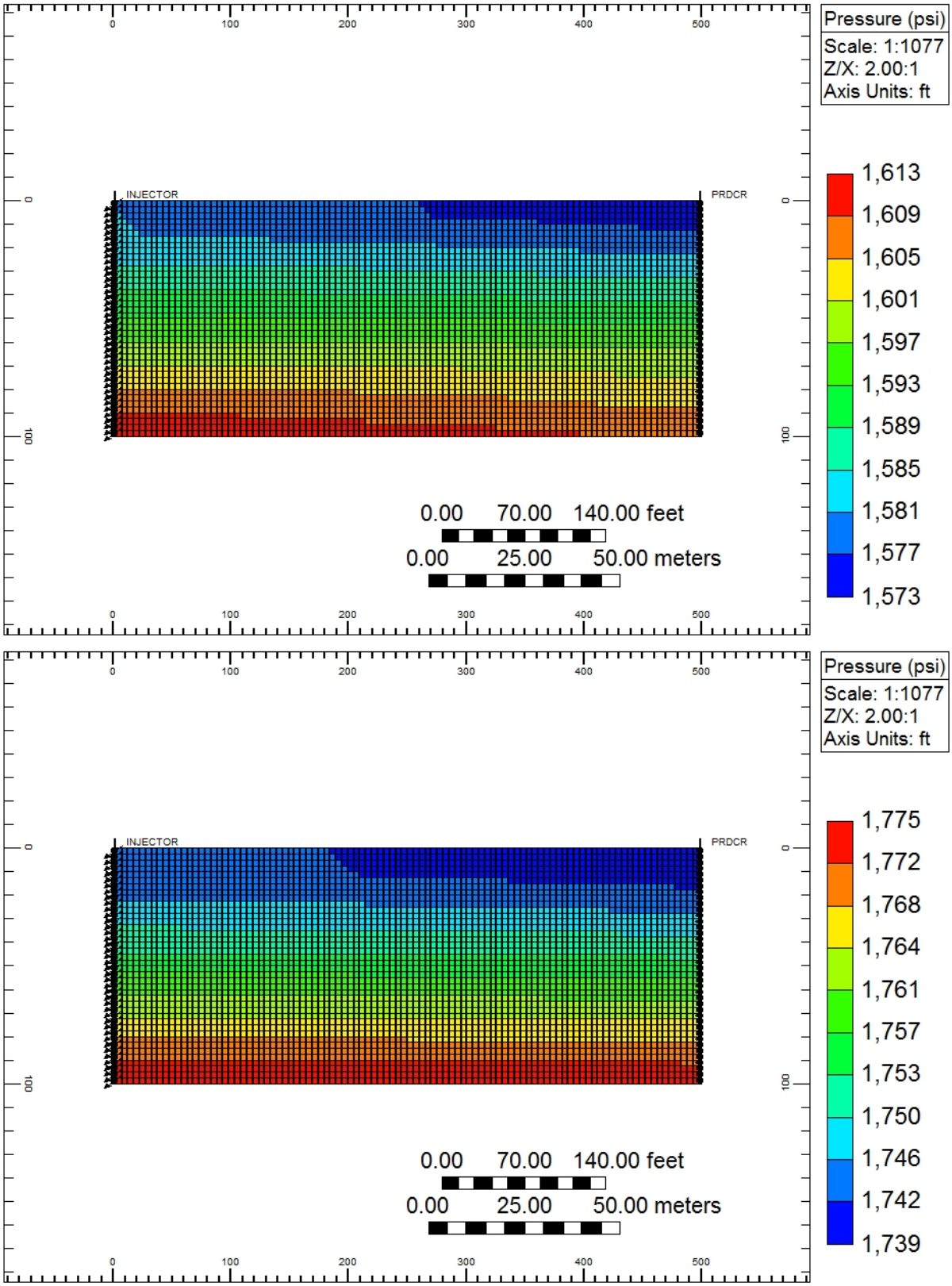


Figure 3.12: Pressure distribution at 1, 4 and 10 years of steam flooding. The steam injection well is at the left section of each of the 3 cross-sections while the production well is at the right end.

The pressure distributions after 1, 2 and 4 years of steam flooding are shown in Figure 3.12. After 1 year of steam flooding, the pressure ranges from 1400 psi at and around the base of the injection well due to the steam injection and drops to 1195 psi at the top of the production well where brine and oil is being produced. This pattern continues while the steam chamber propagates towards the producing well with the difference that the pressure becomes slightly higher at lower depths due to hydrostatic pressure. After 4 years of steam flooding and before the steam breaks through, we notice that the pressure range becomes narrower going from a range of 1195-1400 psi to a range of 1573-1613 psi. This pressure gradient becomes even narrower after the steam breaks through as can be seen in the bottom most figure of Figure 3.12. Hydrostatic pressure causes the pressure to be slightly higher deeper in the reservoir and slightly lower in the shallower parts of the reservoir.

3.4 Sensitivity of the growth of the steam chamber to different inputs

We conduct a sensitivity study to explore the effects of varying different parameters on the production behaviour and the growth of the steam tongue in heavy oil reservoirs. Table 3.5 lists the typical range or values for each parameter along with a reference value corresponding to Emlichheim oil field. We run the reservoir simulation at both ends of the range or values for each parameter while keeping all other parameters at the reference value. In the case of permeability, we run three cases where the horizontal permeability is 600mD, 10D and linearly varying from 300mD at the bottom of the reservoir to 10D at the top of the reservoir, which mimics Emlichheim. The vertical permeability is set to 0.1, 0.2 and 0.5 of the horizontal permeability. A baseline simulation, where each parameter in Table 3.5 is set to the reference value, is used as a reference model in the sensitivity analysis.

Parameter		Range	Reference value	References
Oil API		14°-24°	24°	Leonhard, 2001
Initial reservoir pressure		4-8 MPa	8 MPa	Leonhard, 2001
Temperature of injected steam		270-320°C	320°C	Leonhard, 2001
Porosity		20-30%	30%	Leonhard, 2001 Bjorkum & Nadeau, 1998
Permeability	Horizontal (k_h)	600mD, 10D	10D at top to 300mD at bottom	Leonhard, 2001 Dandekar, 2013
	Vertical (k_v)	$\frac{k_h}{2}, \frac{k_h}{5}$	$\frac{k_h}{10}$	

Table 3.5: Typical ranges or values and reference values for different parameters in Emlichheim oil field.

The sensitivity analysis results for the cumulative oil production, the steam to oil ratio and the water cut at the production well, versus time are shown in Figures 3.13, 3.14 and 3.15, respectively. In each of these figures, the baseline model, where all parameters are set to the reference value, is plotted in solid red line and is used as a reference model. Two models in Figures 3.13 to 3.15 stand out in terms of their production behaviour in comparison to the remaining models. These two models are representative of when the horizontal permeability is 10 Darcy and 600 mD. It is worth noting here that changes in production behaviour due to variations in the vertical permeability were insignificant because the ratio of the vertical to horizontal permeabilities were too high to impact gravitational segregation and would only make a difference if the ratio were less than 0.1. This leads us to conclude that the reservoir's production behaviour is most sensitive to variations in the horizontal permeabilities for the ranges of vertical and horizontal permeabilities used here to mimic Emlichheim.

As can be seen in Figure 3.13, the cumulative oil production during the first 4.5

years of steam flooding is larger for the case where the horizontal permeability is 10 Darcy compared to the case where it is 600 mD. This is because the steam breakthrough occurs after about 4 years of steam flooding in the case where the horizontal permeability is constant at 10 Darcy, and as a result the gradient of the cumulative oil production decreases. A similar behaviour is observed with the steam to oil ratio shown in Figure 3.14. Figure 3.15 shows that the water cut percentage at the production well for all 9 models converge to about 93%. However, the water cut rate of convergence for the case where the horizontal permeability is 600 mD is slower. That is because in this case the thickness of the steam tongue that pushes the oil towards the production well, as shown in Figure 3.17, is larger compared to the thickness of the steam chamber for the other models as shown in Figure 3.17 and Figure B-1 to Figure B-7 in the appendix.

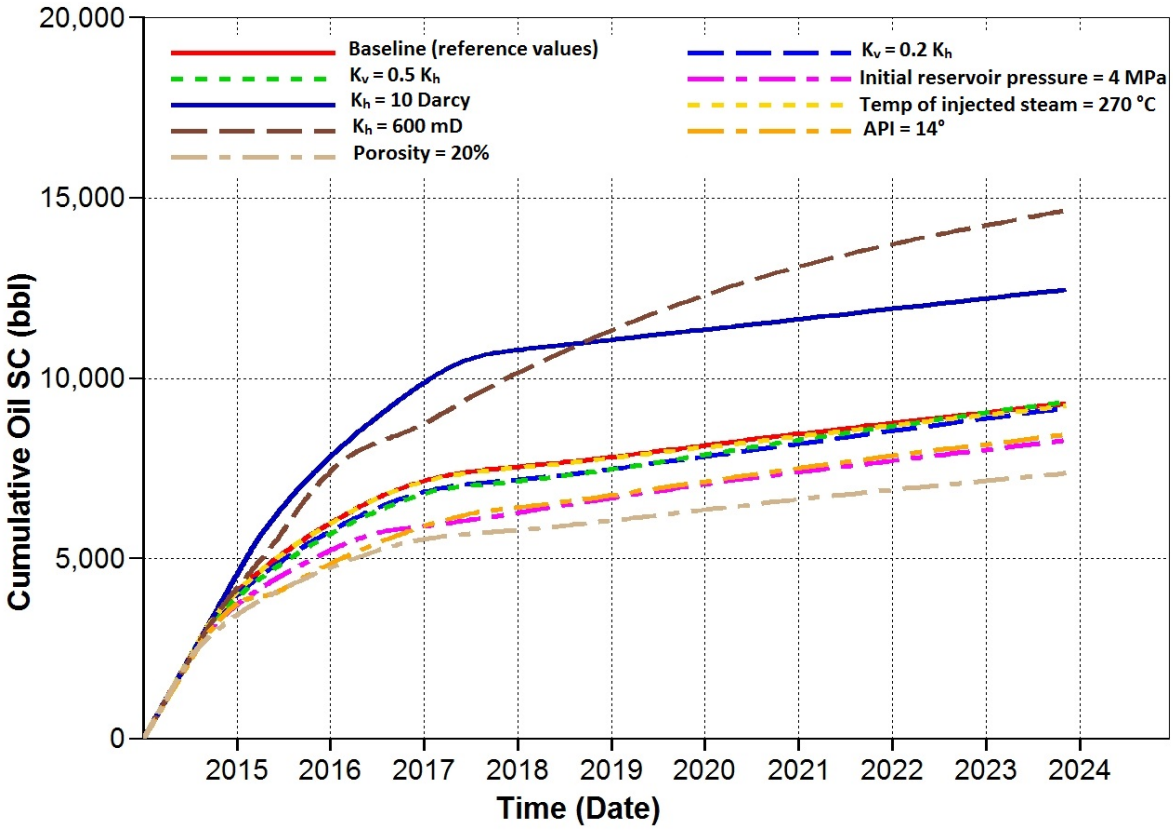


Figure 3.13: Cumulative oil production vs. time. The baseline model is shown along with 8 other models corresponding to the different parameter ranges.

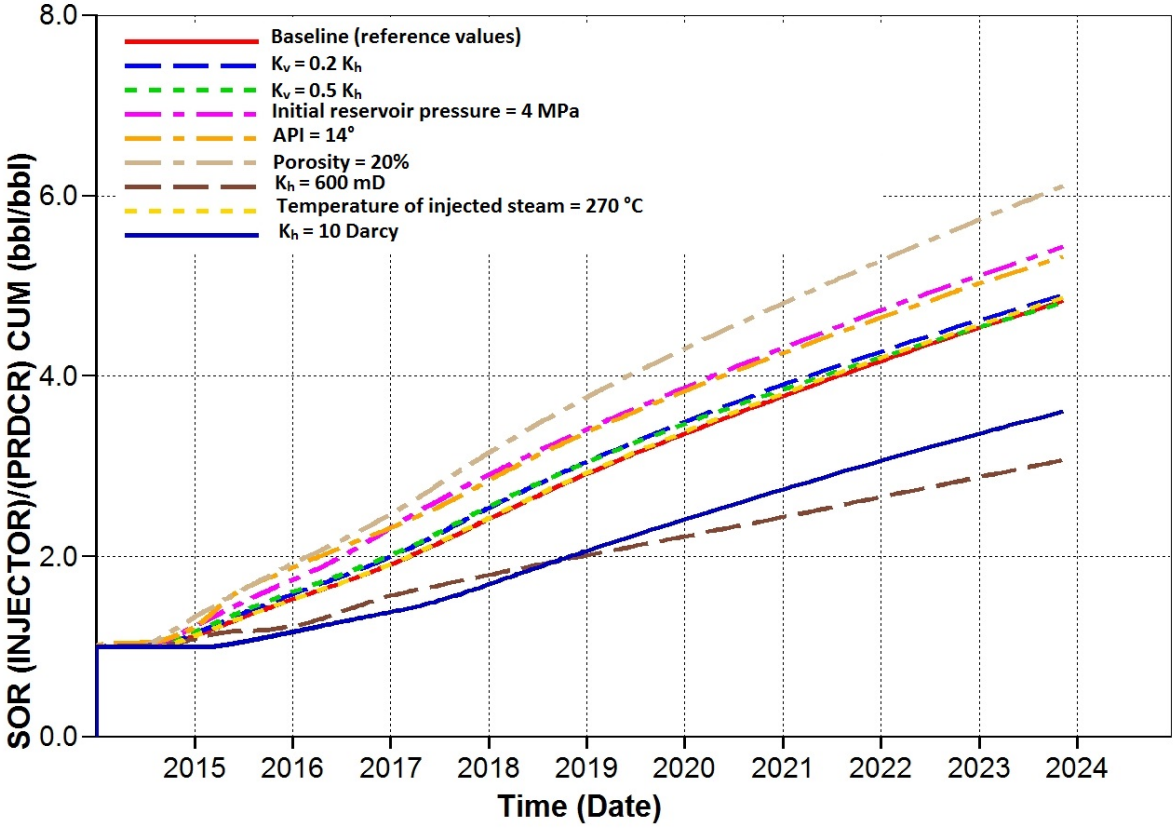


Figure 3.14: Steam to oil ratio vs. time. The baseline model is shown along with 8 other models corresponding to the different parameter ranges.

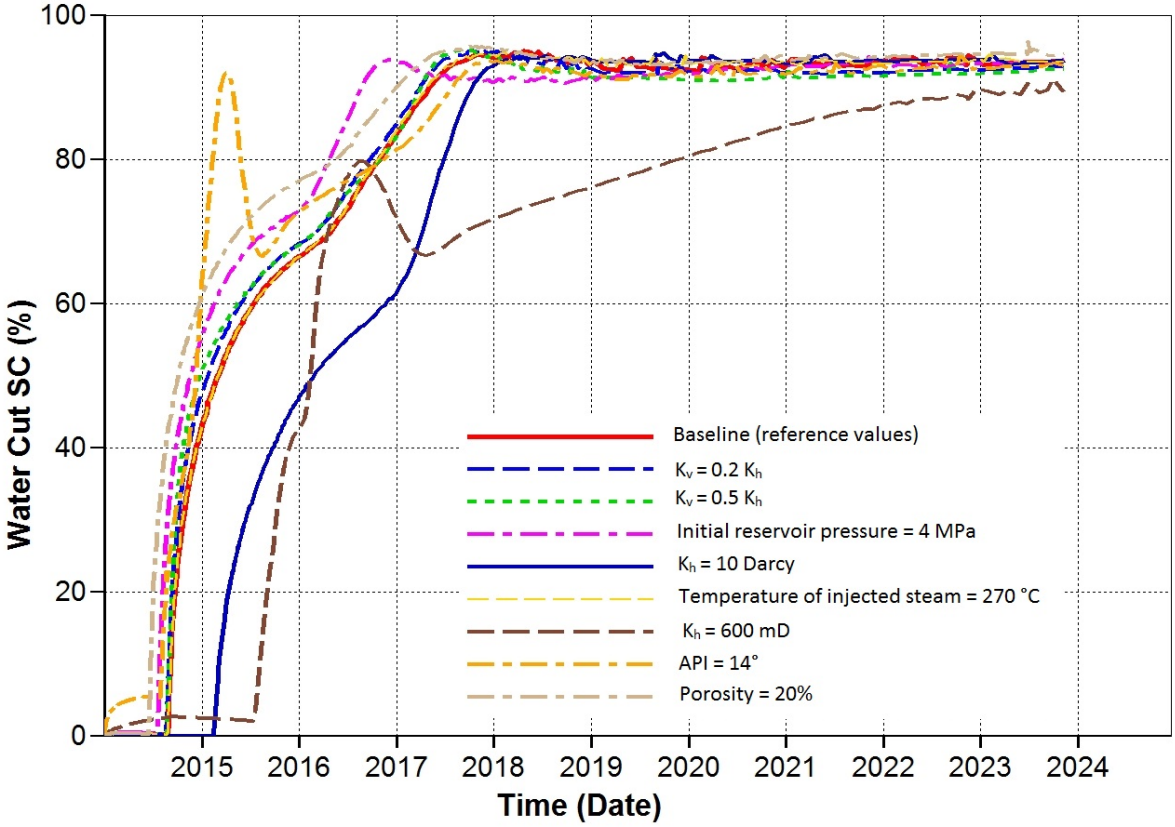
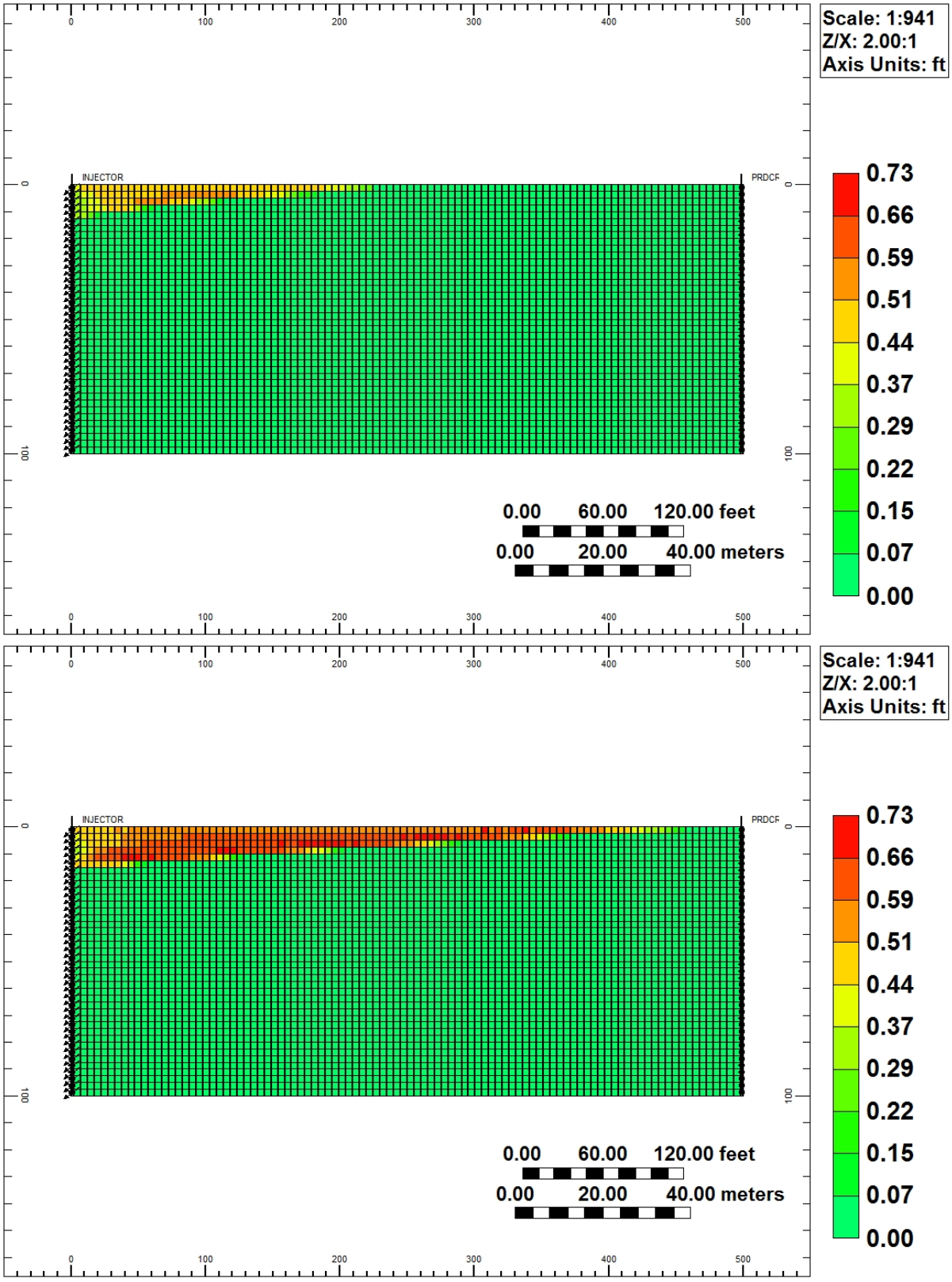


Figure 3.15: Water cut at the production well vs. time. The baseline model is shown along with 8 other models corresponding to the different parameter ranges.

Decreasing the temperature of the injected steam from 320°C to 270°C has an insignificant effect on the production behaviour, which implies that it is more economical to inject steam with a temperature of 270°C rather than 320°C as the latter will add to the cost without any significant increase in the cumulative oil produced. The heavier the oil, the less the total oil produced and the later the steam breakthrough occurs because more heat is needed to mobilize the oil by reducing its viscosity. The model with 20% porosity produces the same amount of oil as the baseline case during the first 3 months after which the gap between the two widens significantly up to when the steam breaks through just before 1 year of steam injection.

We are most interested in the thickness of the steam tongue because the AVO analysis procedure that will be developed in later chapters ideally requires a steam tongue that gradually varies in thickness from more than 35 ft, which is the vertical resolution of our seismic waves, to less than that. The steam saturation along a cross section of the reservoir for the baseline case is shown in Figure 3.16. The steam migrates towards the top of the reservoir displacing water and oil due to the fact that the steam is less dense. It also migrates horizontally towards the producer well due to the pressure gradient between the injector and producer well.

There are no significant differences in the thickness of the steam tongue in all the models except for the case when the horizontal permeability is kept constant at 600mD, in which case the steam is the thickest as shown in Figure 3.17. This implies that when we perform our AVO analysis in later chapters that we can only use the model where the horizontal permeability is 600 mD because it is the only model that results in a steam tongue that is thick enough to perform our AVO procedure.


Scale: 1:941
Z/X: 2.00:1
Axis Units: ft
INJECTOR
PRDCR
0.00 60.00 120.00 feet
0.00 20.00 40.00 meters
0.73
0.66
0.59
0.51
0.44
0.37
0.29
0.22
0.15
0.07
0.00
Scale: 1:941
Z/X: 2.00:1
Axis Units: ft
INJECTOR
PRDCR
0.00 60.00 120.00 feet
0.00 20.00 40.00 meters
0.73
0.66
0.59
0.51
0.44
0.37
0.29
0.22
0.15
0.07
0.00

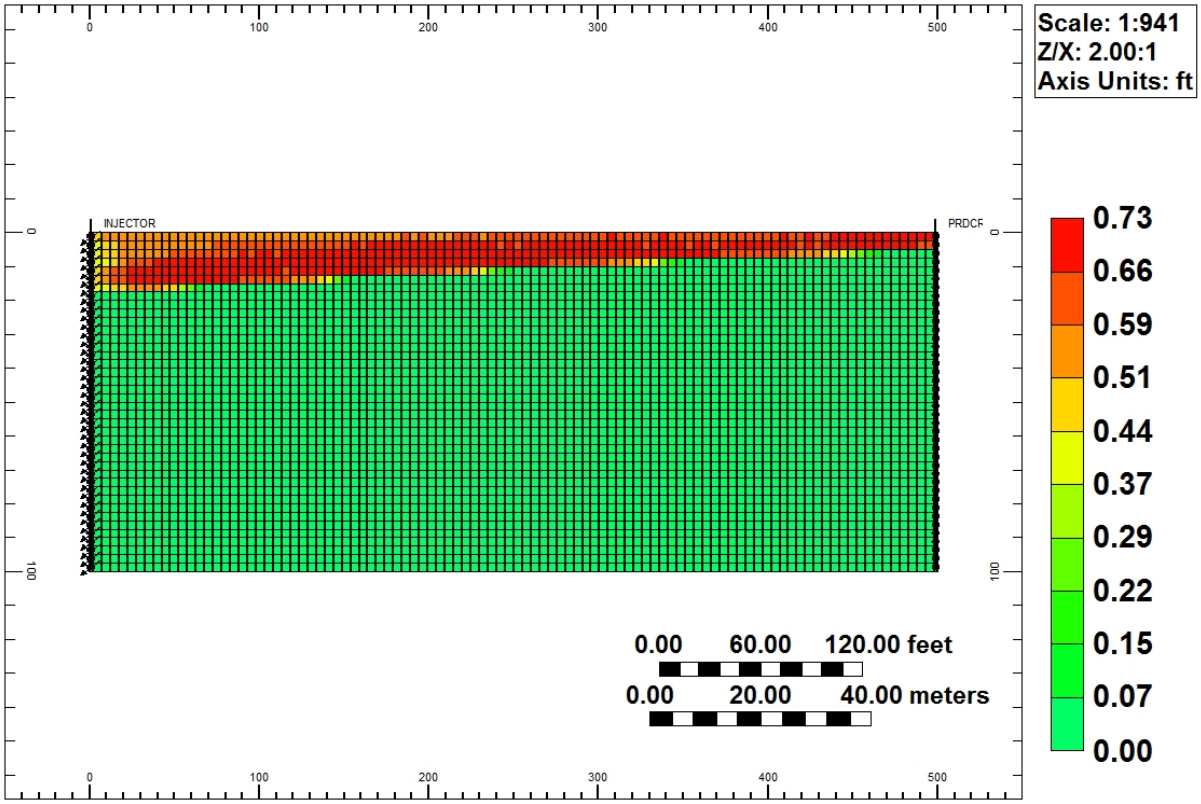
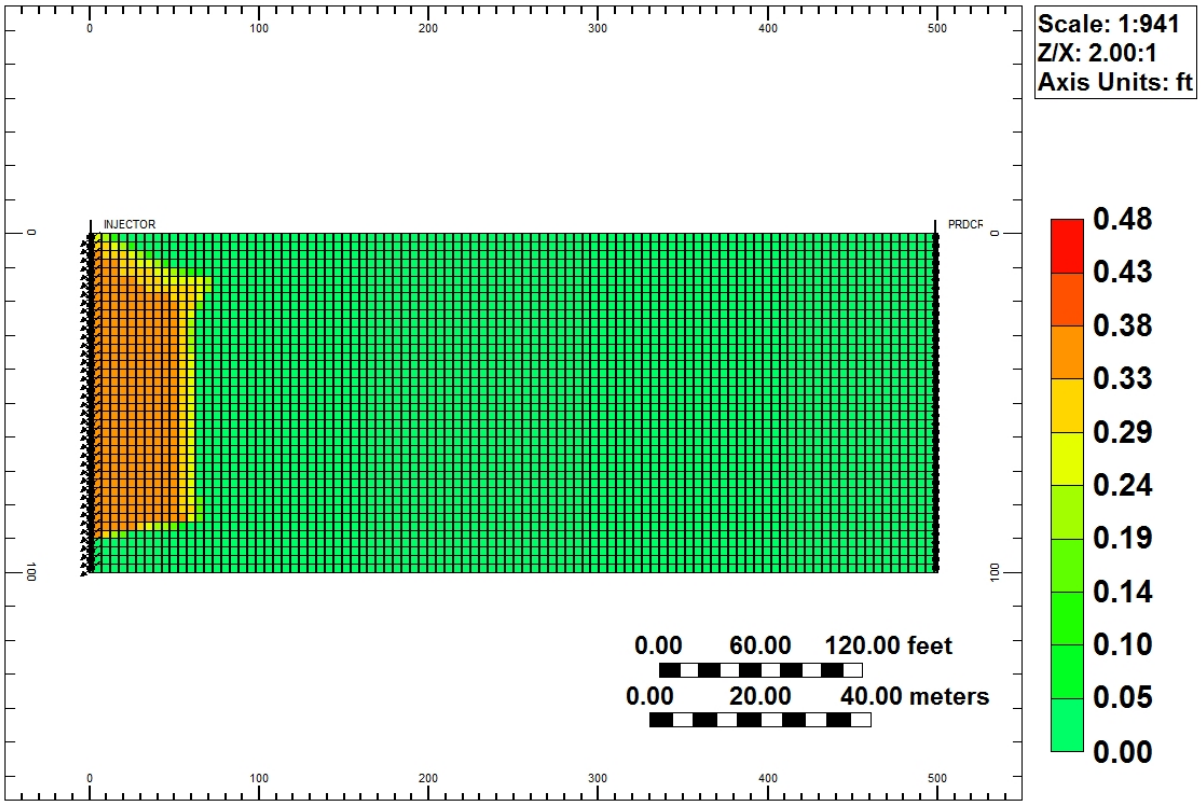


Figure 3.16: Cross section showing steam saturation for the baseline model after 1, 4 and 10 years of steam injection with all parameters set to the reference values listed in Table 3.5. The injection well is on the left while production well is on the right.



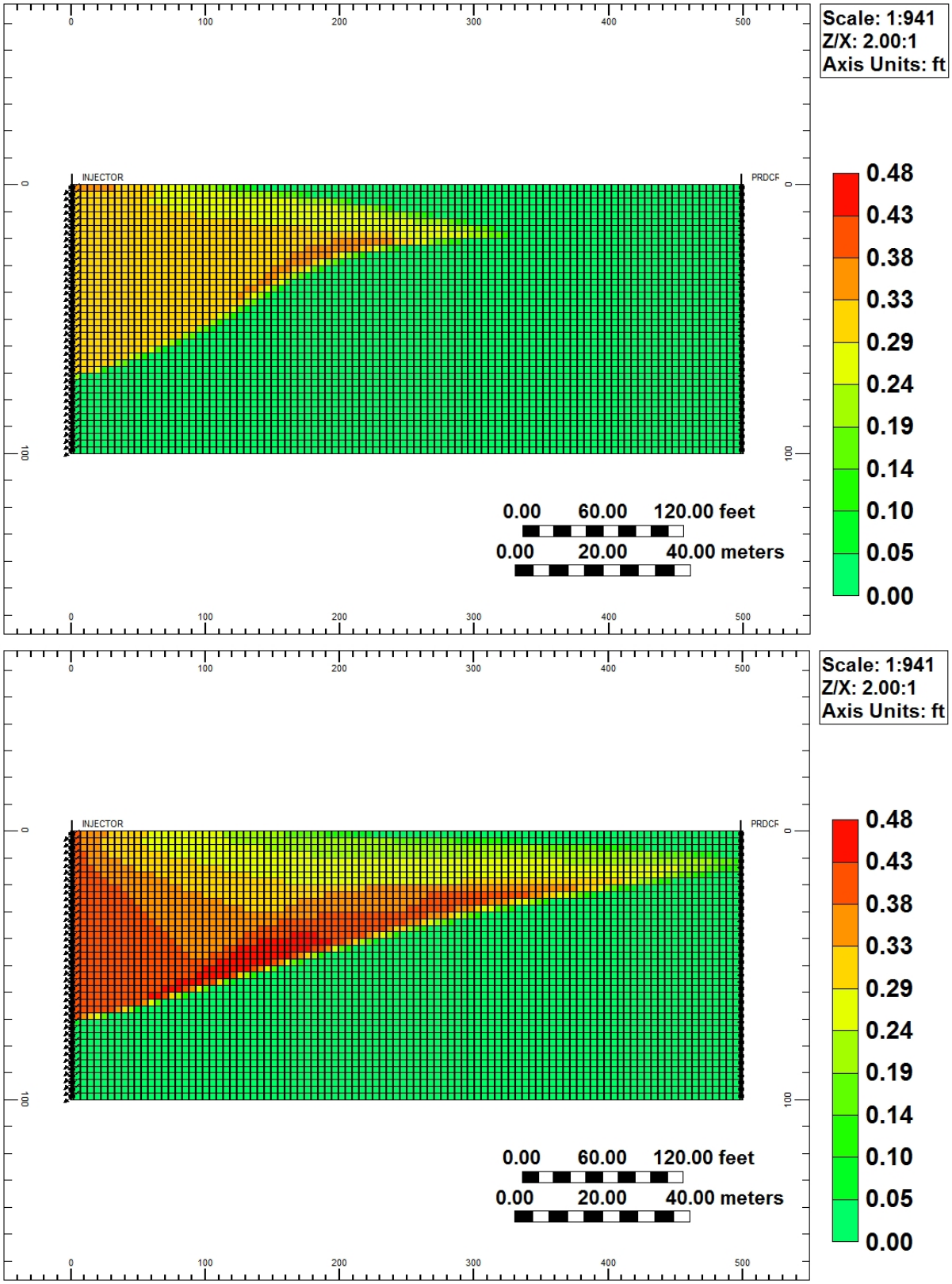
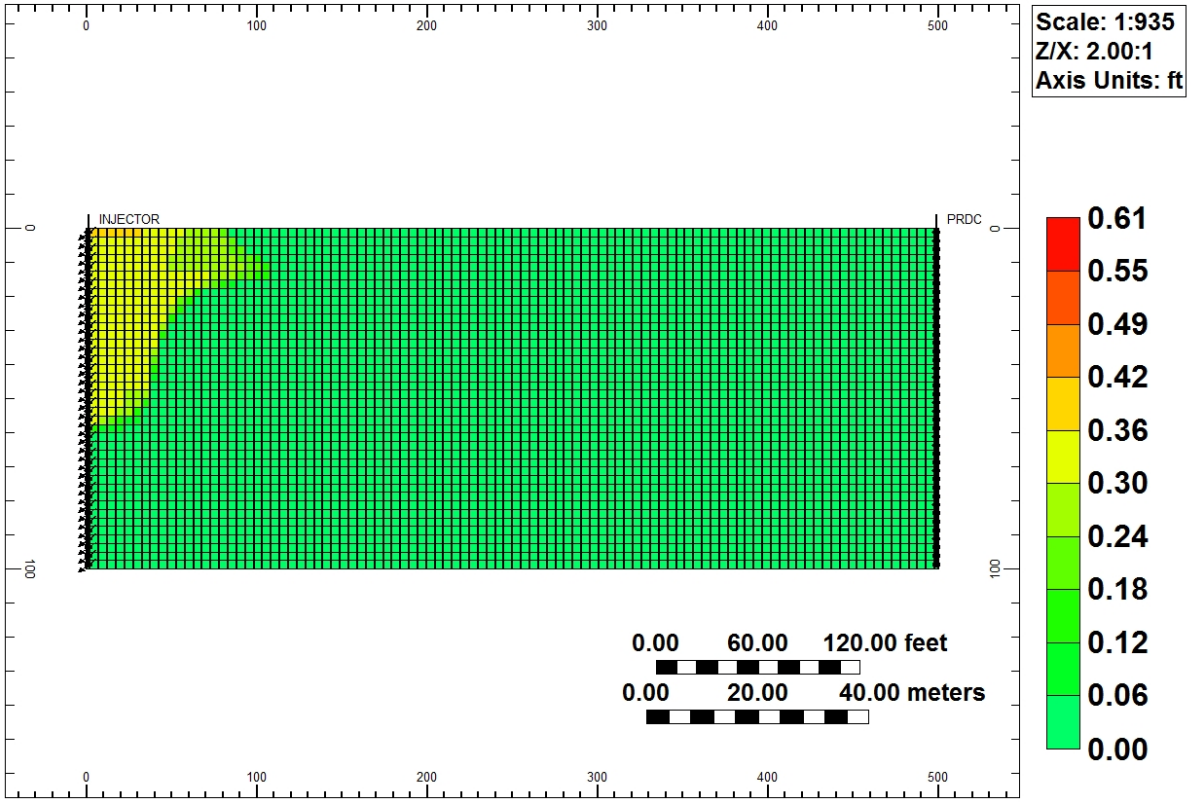


Figure 3.17: Cross section showing steam saturation for the case where the horizontal permeability is 600 mD after 1, 4 and 10 years of steam injection with all other parameters set to the reference values listed in Table 3.5. The injection well is on the left while production well is on the right.

For the purpose of having a second model which we can use to apply the AVO analysis on in later chapters, we create a second model with a horizontal and vertical permeability of 600 mD and 300 mD, respectively, with all other parameters set to the reference values listed in Table 3.5. Cross sections showing the steam saturation for this second model after 1, 4 and 10 years of steam injection are shown in Figure 3.18. Figures showing cross sections of the steam saturations after 1, 4 and 10 years of steam flood for the rest of the models can be found in the appendix.



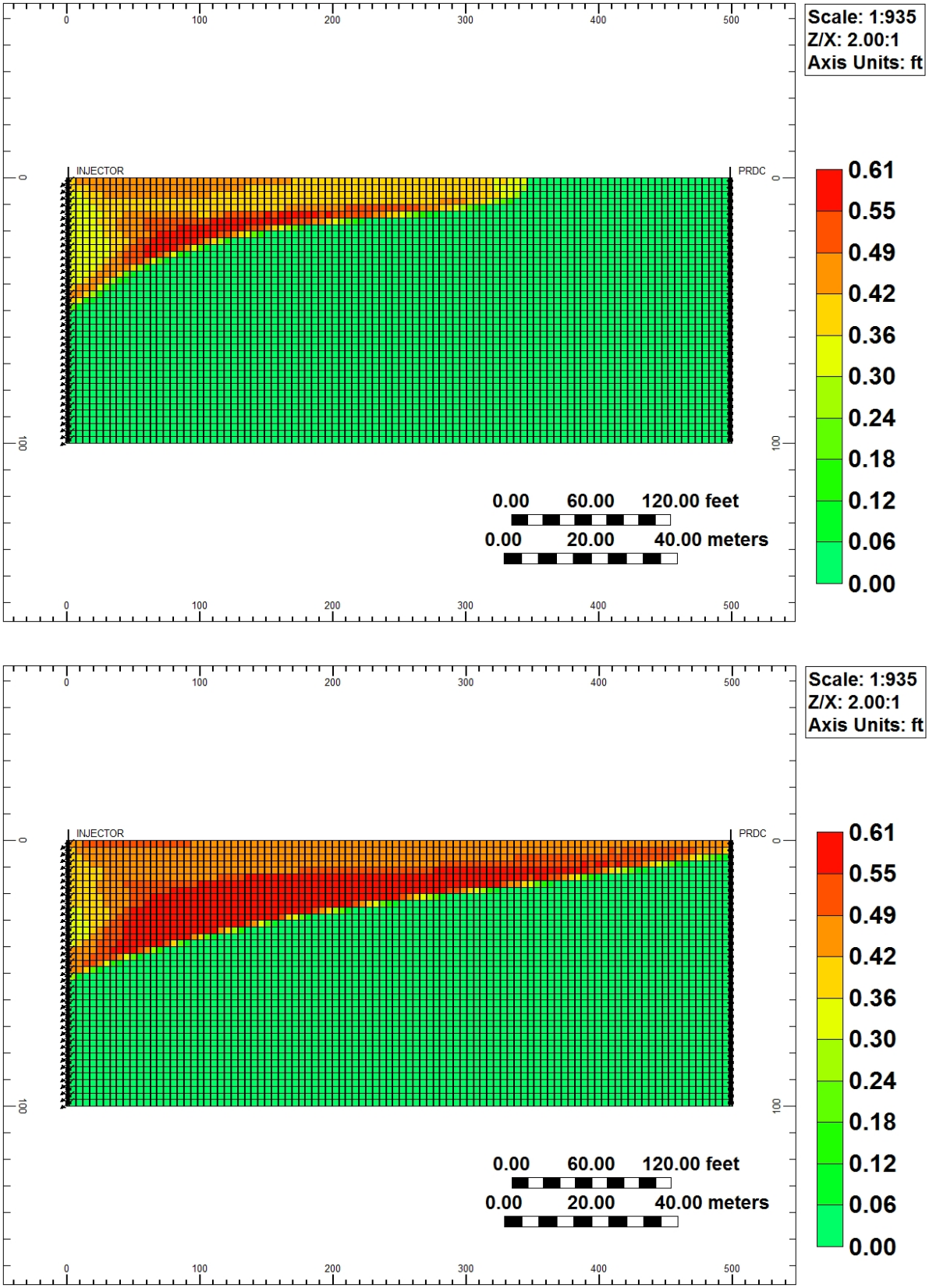


Figure 3.18: Cross section showing steam saturation for the case where the horizontal and vertical permeability is 600 mD and 300 mD, respectively, after 1, 4 and 10 years of steam injection with all other parameters set to the reference values listed in Table 3.5. The injection well is on the left while production well is on the right.

The steam saturations vary both vertically and horizontally as can be seen from the steam saturation Figures 3.16 to 3.18 and Figures B-1 to B-7 in the appendix. These variations in steam saturation will not affect our AVO analysis. However, the thickness of the steam will, as it has to be larger than the tuning thickness of the seismic waves that will be used which is about 35 ft. We are unable to apply the AVO analysis in locations where the steam thickness is less than the seismic resolution. It is also important to point out that the top of the steam is not always the same as the top of the reservoir, which is the case in Figure 3.17. This will not affect the AVO analysis because it is applied only at the bottom of the steam tongue.

3.5 Summary

We showed the distribution of pressure, ternary saturation and temperature after 1, 4 and 10 years of steam flooding for a reservoir with properties similar to the Gildehaus formation in Emlichheim oil field. We then conducted a sensitivity study where we studied the sensitivity of production behaviour and steam chamber growth to various ranges in oil API, horizontal permeability, vertical permeability, temperature of injected steam, initial reservoir pressure and porosity.

Production behaviour and thickness of the steam chamber in a steam flood operation is most sensitive to variations in horizontal permeability for the ranges of parameters used in this study. Over the whole period of our simulations, which was 10 years, smaller horizontal permeabilities result in more recovered oil, lower steam to oil ratio, lower water cut at production well and thicker steam tongue. The thickness of the steam is critical, as we will see in chapter 5, because the AVO analysis can be used to detect the bottom of the steam only when the thickness of the steam tongue is larger than the seismic resolution.

In reality all reservoirs are heterogeneous which results in a more complicated production behaviour and steam chamber growth. For example, permeability heterogeneity could result in the development of multiple steam tongues at different locations within the reservoir. However, our simulations represent a more idealized case, as we are interested in a well-developed steam tongue that varies in thickness from larger to smaller than the seismic resolution of about 35 ft on which we can apply our AVO analysis to better identify the bottom of the steam, thus improve the delineation of the steam chamber.

The information obtained from these simulations is very important, as we will need the values of these properties, which includes fluid saturations and densities, pressure and temperature in each grid cell. These will be used to calculate the elastic moduli and densities at each grid cell using our MATLAB rock physics code, which will be developed and discussed in Chapter 4. This will then be used in the amplitude versus offset study to help delineate the steam chamber.

4. Rock Physics Modelling

Rock and fluid properties were obtained for each grid cell from the reservoir simulation model. The work was presented in Chapter 3, entitled “Reservoir Simulation”. The rock physics model relates changes in rock and fluid properties to changes in seismic signal and is constructed using available theory. A typical reservoir rock is comprised of pore spaces that are filled with fluids, which can be liquid, gas, or both. To effectively calculate the seismic response from a saturated rock, the grain moduli, the dry moduli and the fluid moduli need to be calculated. These are then used to calculate the effective P and S wave velocities using Gassmann’s equation (Gassmann, 1951). Gassmann’s equations, shown later in Equation 4.27, assume that the rock is homogeneous and isotropic, the pore space is connected and the seismic frequency is low enough for the pore pressure to equilibrate over a length scale smaller than the seismic wavelength (Smith et al., 2003). The critical length (L_c) needed for the pressure to equilibrate in the fluid is calculated using Equations 4.1 and 4.2 (Sengupta and Mavko, 2003):

$$L_c \approx \sqrt{\frac{4D}{f}} \qquad (4.1)$$

$$D = \frac{k\,K_{fl}}{\eta} \qquad (4.2)$$

Where D is the diffusivity in $m^2.s^{-1}$, f is the frequency in Hz, k is the permeability in m^2, K_{fl} is the fluid bulk modulus in Pa, and η is the fluid dynamic viscosity in Pa.s.

The critical length changes according to the parameters in Equations 4.1 and 4.2. We estimate the largest and smallest value for L_c to be 6.9 m and 4×10^{-6} m, respectively. The estimate of the largest value for L_c is based on the assumptions

that k = 2×10^{-12}, K_{fl} = 3 GPa, η = 10^{-5} Pa.s, and *f* = 50 Hz. Meanwhile, the estimate of the smallest value for L_c is based on the assumptions that $k = 2\times10^{-12}$, K_{fl} = 1000 Pa, η = 10 Pa.s, and *f* = 50 Hz. The wavelength of a 50 Hz seismic wave travelling with the speed of 1500 m/s is 30 m, which is larger than the largest critical distance needed for the pressure to equilibrate. Therefore, the fluid phases are mixed below the critical length scale making it a homogeneous distribution.

4.1 Grain Moduli

Rocks are made of different minerals each with its own bulk and shear moduli, and density. Table 4.1 lists the main minerals that make up most sedimentary rocks.

Mineral	K (GPa)	μ (GPa)	ρ (kg/m^3)
Quartz	37.0	44.0	2650
Feldspar	37.5	25.6	2620
Clay	25.0	9.0	2550
Calcite	76.8	32.0	2650
Pyrite	147.4	132.5	3550

Table 4.1: Bulk modulus (K), shear modulus (μ) and density (ρ) of common minerals that make up sedimentary rocks (Mavko et al., 2009).

In order to calculate the elastic moduli of a rock composed of a mixture of grains and pores, we need to know the elastic moduli of the different phases, the volume fraction of each phase and finally the geometrical details of how these phases are arranged. If we only know the constituent moduli and the volume fraction, then we can use the Walpole bounds (Walpole, 1966), sometimes referred to as Hashin-Shtrikman-Walpole bounds (Hashin and Shtrikman, 1963), which can be used for a mixture of more than two phases (Berryman, 1995) and is calculated using the

following equations:

$$K^{HS+} = \Lambda\,(\mu_{max}), K^{HS-} = \Lambda\,(\mu_{min}) \qquad (4.3)$$

$$\mu^{HS+} = \Gamma(\xi(K_{max}, \mu_{max})), \mu^{HS-} = \Gamma(\xi(K_{min}, \mu_{min})) \qquad (4.4)$$

Where

$$\Lambda\,(z) = \langle \frac{1}{K(r) + \frac{4}{3}z} \rangle^{-1} - \frac{4}{3}z \qquad (4.5)$$

$$\Gamma\,(z) = \langle \frac{1}{\mu(r) + z} \rangle^{-1} - z \qquad (4.6)$$

$$\xi\,(K, \mu) = \frac{\mu}{6}\left(\frac{9K + 8\mu}{K + 2\mu}\right) \qquad (4.7)$$

The brackets in Equations 4.5 and 4.6 indicate an average over the medium, which is equivalent to the average over the different constituents weighted by their volume fractions. It is necessary to use either bounds or their average because many effective- medium models assume a homogeneous mineral modulus (Mavko et al., 2009). The upper bound is used when the stiffer material forms the shell while the lower bound is used when it forms the core (Mavko et al., 2009). For simplicity and since we are dealing with uncemented sand reservoirs, we assume that quartz make up the entire grain framework.

4.2 Dry Rock Moduli

Many models are used to calculate the dry rock elastic moduli such as the Walton, Digby, Hertz-Mindlin (Mavko et al., 2009). We use the uncemented sand model because we are interested in heavy oil reservoirs, which are mostly shallow unconsolidated sandstone formations (Curtis et al., 2002). This model assumes that

the cement is initially deposited away from grain contacts. It also assumes that the initial framework is a dense pack of identical spherical grains with a porosity of 0.36 and average number of contacts per grain C=5 to 9. The value of C increases with decreasing porosity. We use an empirical equation derived by Garcia and Medina (2006), shown in Equation 4.8, which fits their numerical simulations relating porosity and the number of contact between grains. Given these conditions, the Hertz-Mindlin theory (Mindlin, 1949) is modified by adding grains to the pore space causing the sorting to deteriorate and the stiffness to slightly increase (Avseth et al., 2005), resulting in the following expression for the dry bulk and shear moduli shown in Equations 4.9-4.11 (Mavko et al., 2009):

$$C = 4.46 + 9.7\,(0.384 - \emptyset)^{0.48} \qquad (4.8)$$

$$K_{HM} = \left[\frac{C^2(1-\emptyset_c)^2\mu_{grain}^2}{18\pi^2\left(1-v_{grain}\right)^2}\,P_{eff}\right]^{\frac{1}{3}} \qquad (4.9)$$

$$\mu_{HM} = \frac{5-4v}{5(2-v)}\left[\frac{3C^2(1-\emptyset_c)^2\mu_{grain}^2}{2\pi^2\left(1-v_{grain}\right)^2}\,P_{eff}\right]^{\frac{1}{3}} \qquad (4.10)$$

$$v_{grain} = \frac{3K_{grain} - 2\mu_{grain}}{6K_{grain} + 2\mu_{grain}} \qquad (4.11)$$

Where $\emptyset_c$ is critical porosity and is equal to 0.36. P_{eff} is the hydrostatic pressure, which is the difference between the lithostatic pressure and the pore pressure; K_{HM} and μ_{HM} are the dry bulk and dry shear moduli, respectively, corresponding to the critical porosity; and v_{grain} is the grain Poisson ratio. A modified Hashin-Shtrikman equation is used to calculate the dry rock bulk and shear moduli at a different porosity (Mavko et al., 2009):

$$K_{dry} = \left[\frac{\frac{\phi}{\phi_c}}{K_{HM} + \frac{4}{3}\mu_{HM}} + \frac{1 - \frac{\phi}{\phi_c}}{K + \frac{4}{3}\mu_{HM}}\right]^{-1} - \frac{4}{3}\mu_{HM} \qquad (4.12)$$

$$\mu_{dry} = \left[\frac{\frac{\phi}{\phi_c}}{\mu_{HM} + z} + \frac{1 - \frac{\phi}{\phi_c}}{\mu_{grain} + z}\right]^{-1} - z \qquad (4.13)$$

$$z = \frac{\mu_{HM}}{6}\left[\frac{9K_{HM} + 8\mu_{HM}}{K_{HM} + 2\mu_{HM}}\right] \qquad (4.14)$$

Where the squared brackets are indicative of an average over the medium, which is the same as an average of the constituents that are weighted by the volume fraction of each constituent (Mavko et al., 2009).

4.3 Fluid Bulk Moduli

Calculating the fluid bulk modulus is more difficult compared to calculating the grain and dry rock bulk moduli, as it involves predicting the effective bulk moduli of the group of fluids occupying the pore space (Avseth et al., 2005). The bulk modulus of a fluid quantifies its resistance to compression while the shear modulus refers to its resistance to shear. In the case of unconventional and heavy oils, it is generally adequate to assume that there are no associated gases in the pore space under in situ conditions (Dusseault, 1980). Fluids have a zero shear modulus, except for heavy oils, which we will discuss later. The three fluids that can coexist in the pore space are brine, oil and steam. Bulk modulus is calculated using Equation 4.15, where K is the fluid bulk modulus in Pa, ρ is density in kg/m3 and v is P-wave velocity in m/s.

$$K = \rho v^2 \qquad (4.15)$$

4.4 Brine Bulk Moduli

Acoustic velocities in reservoir fluids are summarized by Batzle and Wang (Batzle and Wang, 1992). They suggest calculating the P-wave velocity in pure water in m/s using Equation 16.

$$V_w = \sum_{i=0}^{4}\sum_{j=0}^{3} \omega_{ij} T^i P^j \qquad (4.16)$$

The coefficients ω_{ij} are:

$\omega00 = 1402.85$	$\omega01 = 1.524$	$\omega02 = 3.437\times10^{-3}$	$\omega03 = -1.197\times10^{-5}$
$\omega10 = 4.871$	$\omega11 = -0.0111$	$\omega12 = 1.739\times10^{-4}$	$\omega13 = -1.628\times10^{-6}$
$\omega20 = -0.04783$	$\omega21 = 2.747\times10^{-4}$	$\omega22 = -2.135\times10^{-6}$	$\omega23 = 1.237\times10^{-8}$
$\omega30 = 1.487\times10^{-4}$	$\omega31 = -6.503\times10^{-7}$	$\omega32 = -1.455\times10^{-8}$	$\omega33 = 1.327\times10^{-10}$
$\omega40 = -2.197\times10^{-7}$	$\omega41 = 7.987\times10^{-10}$	$\omega42 = 5.23\times10^{-11}$	$\omega43 = -4.614\times10^{-13}$

Parameters T and P are temperature in degrees Celsius and pore pressure in MPa, respectively. The P-wave velocity in brine is calculated using Equation 4.17. The variable S is salinity in fraction of one (parts per million divided by 10^6).

$$V_B = V_w + S(1170 - 9.6T + 0.055T^2 - 8.5\times10^{-5}T^3 + 2.6P - 0.0029TP - 0.0476P^2) + S^{\frac{3}{2}}(780 - 10P + 0.16P^2) - 1820S^2 \qquad (4.17)$$

The density, in g/cm^3, of pure water (ϱ_w) and brine (ϱ_B) are calculated using Equations 4.18 and 4.19, respectively (Mavko et al., 2009).

$$\sigma_w = 1 + 10^{-6}(-80T - 3.3T^2 + 0.00175T^3 + 489P - 2TP + 0.016T^2P - 1.3\times10^{-5}T^3P - 0.333P^2 - 0.002TP^2) \qquad (4.18)$$

$$\sigma_B = \sigma_w + S(0.668 + 0.44S + 10^{-6}[300P - 2400PS + T(80 + 3T - 3300S - 13P + 47PS)]) \qquad (4.19)$$

We calculated the bulk moduli of brine using Equation 4.15 knowing the acoustic velocity and density of brine. Figure 4.1 shows the bulk modulus, density and P-wave velocity of brine with a salinity of 0.2 (as a fraction of 1) for the temperature and pressure ranges of 10-300 °C and 0-15 MPa, respectively. These ranges of pressure and temperature are typical of a reservoir that is buried up to a depth of around 700m and subjected to steam injection. Lithostatic or overburden pressure (P) can be calculated using Equation 4.20.

$$P = \rho . g . h \qquad (4.20)$$

The density of the overlying rock (ρ) is typically on the order of 2000 kg/m^3, g is gravitational acceleration and is equal to 9.8 m/s^2, and the height of the rock column (h) is in metres.

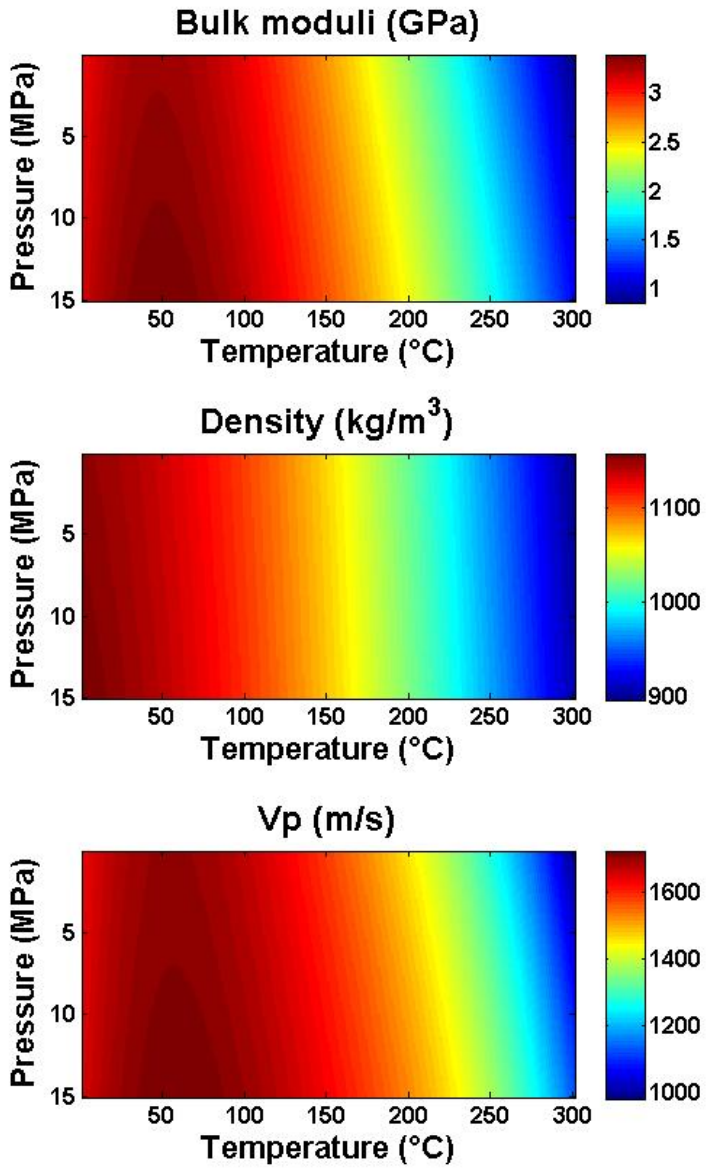


Figure 4.1: Bulk modulus, density and P-wave velocity of brine calculated using the above-mentioned equations for each of the parameters.

4.5 Oil Bulk Moduli

Petroleum engineers typically describe oil density in terms of API, which is calculated using Equation 4.21.

$$\text{API} = \frac{141.5}{SG_{oil}} - 131.5 \;\; ; \;\; SG_{oil} \text{ at } 60\,^{\circ}\text{F} = \frac{\rho_{\text{oil}}}{\rho_{\text{w}}} \qquad (4.21)$$

Where SG is specific gravity measured at 60 °F, ρ_{oil} and ρ_w are density of oil and water, respectively.

Conventional oil is less dense than water and has an API gravity that is larger than 10°. This is further sub-categorized into heavy oil (10-20°API), medium oil (20-30° API) and light oil (>30° API). Unconventional oil is denser than water and has an API that is less than 10°. Unconventional oil does not flow at reservoir conditions and needs to be heated or mined (Owen et al., 2010).

Most heavy oils have little or no dissolved gas (Dusseault, 1980). We assume this is the case in this thesis. The effects of pressure (P) and temperature (T) on the oil's density are independent. The pressure dependence (ρ_p) of the density of oil is described by Equation 4.22. The temperature dependence of the density of oil at a given pressure is given by Equation 4.23. The P-wave velocity in oil with a predefined API is given in Equation 4.24. Note that ρ_p is density in g/cm^3; P is pressure in MPa and T is temperature in degrees Celsius. The bulk modulus of each fluid can be calculated using Equation 4.15 given we already have the P-wave velocity and density of each fluid. The bulk modulus, density, and P-wave velocity versus temperature and pressure for a 10° API oil are shown in Figure 4.2.

$$\rho_p = \rho_0 + (0.00277\ P - 1.71 \times 10^{-7}\ P^3) \times (\rho_0 - 1.15)^2 + 3.49 \times 10^{-4}\ P \qquad (4.22)$$

$$\rho_{oil} = \frac{\rho_p}{0.972 + 3.81 \times 10^{-4}(T + 17.78)^{1.175}} \qquad (4.23)$$

$$V_{p-oil} = 2096 \left(\frac{\rho_0}{2.6 - \rho_0}\right)^{\frac{1}{2}} - 3.7\ T + 4.64\ P \qquad (4.24)$$

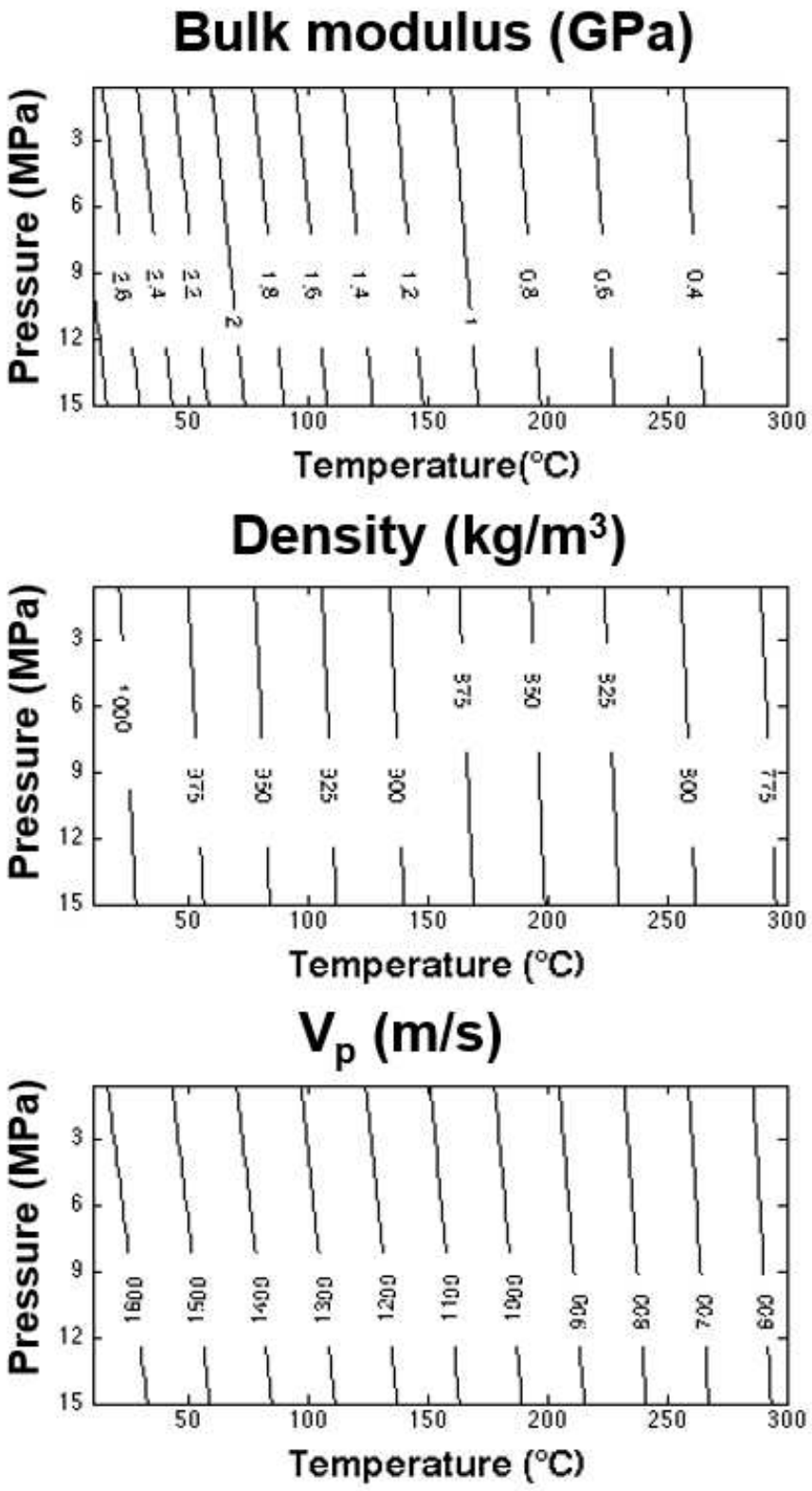


Figure 4.2: Bulk modulus, density and P-wave velocity of 10° API oil.

Several papers report a non-linear decrease of V_p with increasing temperatures for heavy oils below a certain temperature followed by a more linear behaviour at

higher temperatures (Han et al., 2008; Eastwood, 1993; Wang & Nur, 1990; Wang & Nur, 1986; Kato et al., 2008; Wang, 2001). This is due to the fact that unconventional oils have a nonzero shear modulus at low temperatures, which affects V_p since both the bulk and shear moduli are used to calculate V_p. Our rock physics model assumed a zero shear modulus for oils, which is a reasonable assumption so long as the oil is not exceptionally heavy and not at low temperatures at the same time. However, these conditions are not satisfied all the time. Therefore, we modified our rock physics model so that it would account for cases where the oil is extra heavy and temperatures are relatively low by estimating the nonzero shear modulus and including it in the calculation of V_p and V_s.

The shear modulus of an oil sample versus temperature is shown in Figure 4.3 (after Han et al., 2008). For this specific oil sample the shear modulus is nonzero for temperatures less than or equal to 40 °C, i.e. it acts as a solid. After that the shear modulus is assumed to be zero, i.e. it acts as a liquid. Therefore, V_p drops significantly beyond 40 °C since the shear modulus is used in the calculation of V_p. The data points from Figure 4.3 are plotted and fitted with a linear fit. Figure 4.4 shows this fit along with the residuals. The linear equation that relates the shear moduli and temperature of this 8° API oil sample is given in Equation 4.25. However, this equation is only valid for an 8° API oil.

$$\mu_{\text{oil}} = -0.0081\,\text{T} + 0.41 \qquad (4.25)$$

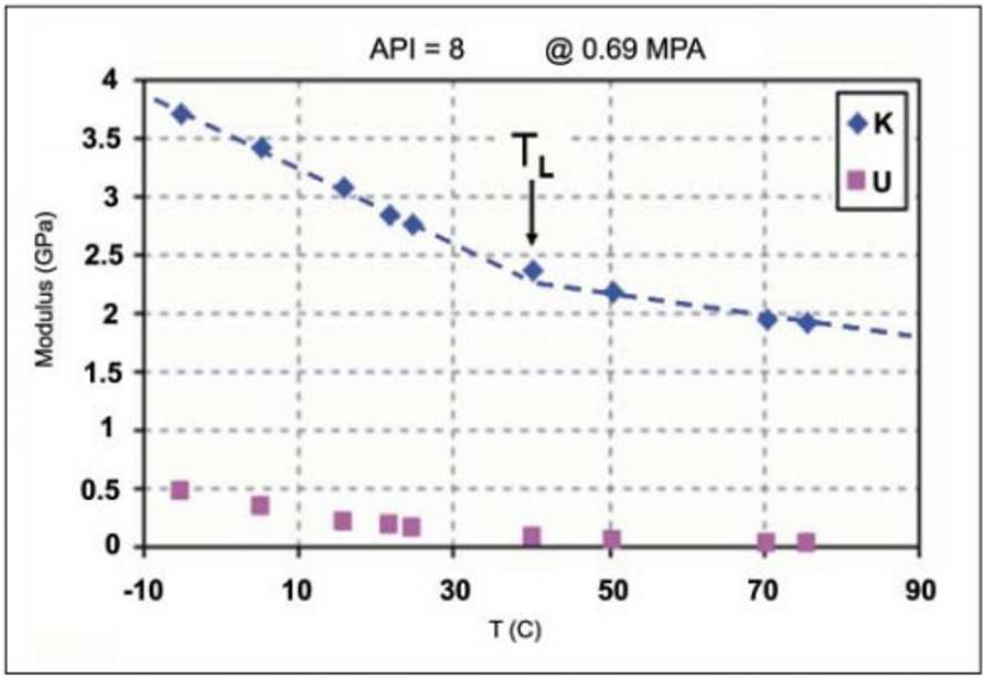


Figure 4.3: Measured shear modulus vs. temperature for an 8° API oil (adopted from Han et al., 2008). Bulk modulus values are presented as diamonds and shear modulus values are presented as squares for an API 8° gravity heavy oil. A shear modulus appears and the bulk modulus-temperature trend changes slope at a liquid point temperature (T_L) of 40 °C.

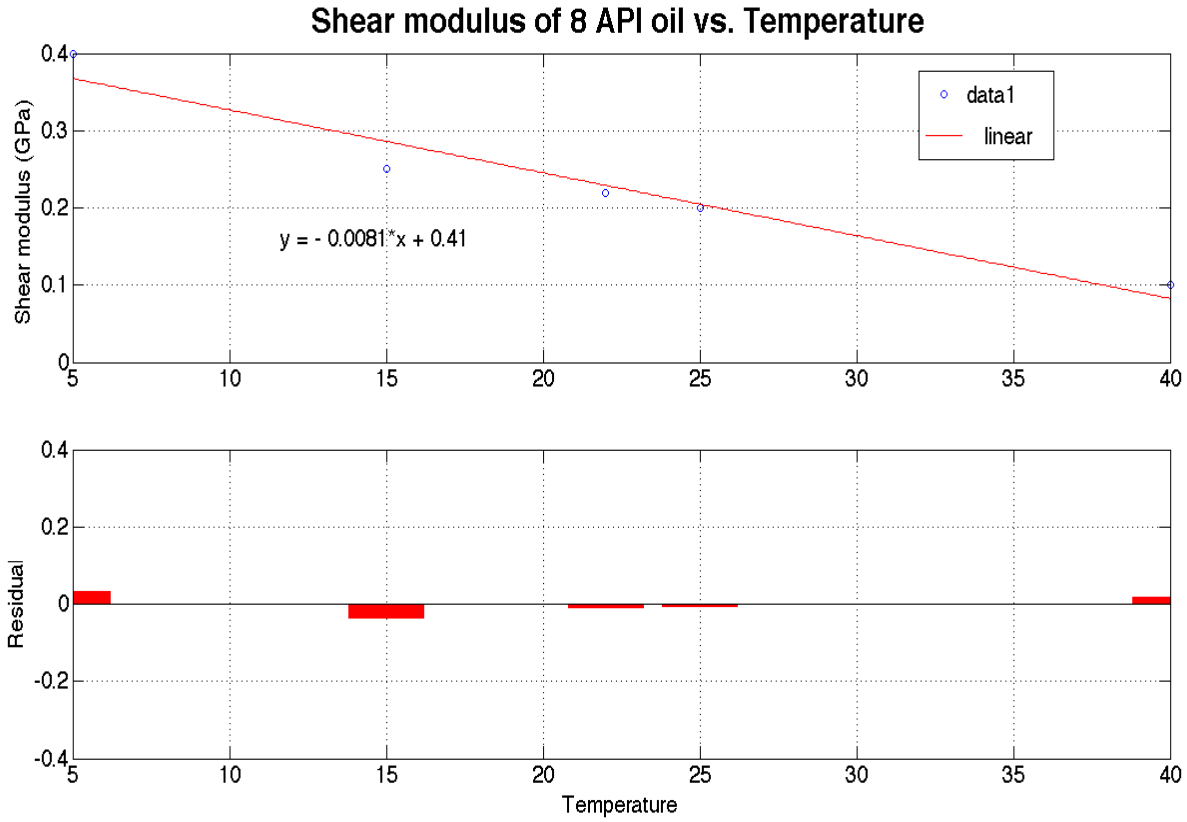


Figure 4.4: Five points are shown for the measured shear modulus as a function of temperature. A linear model was chosen, given its fit to the measured shear moduli vs. temperature data. The lower graph displays the error between the measured data points and the predicted values from the linear fit model.

Figure 4.5 shows V_s versus temperature for a few heavy oils. We assume that the slope of the shear modulus vs temperature is constant for all heavy oils. We also assumed that the temperature at which the shear modulus is zero (T_0) is at Vs = 0.2 km/s because the uncertainty increases significantly below this velocity and the value of the shear modulus is insignificant and can be assumed to be zero (Han et al., 2008). A quadratic fit is used for the values of T0 for different heavy oils as shown in Figure 4.6 along with the residuals. We derive Equation 4.26, which calculates the shear modulus of heavy oils in GPa given the oil's API gravity and temperature in Celsius (T). Figure 4.7 shows the shear modulus of heavy oils with API values of 2°, 4°, 6°, 8° and 10° versus temperature. Negative shear moduli values are set to zero.

$$\mu_{oil} = -0.0081\,T + 0.0402\,(API)^2 - 0.8422\,(API) + 4.5751 \qquad (4.26)$$

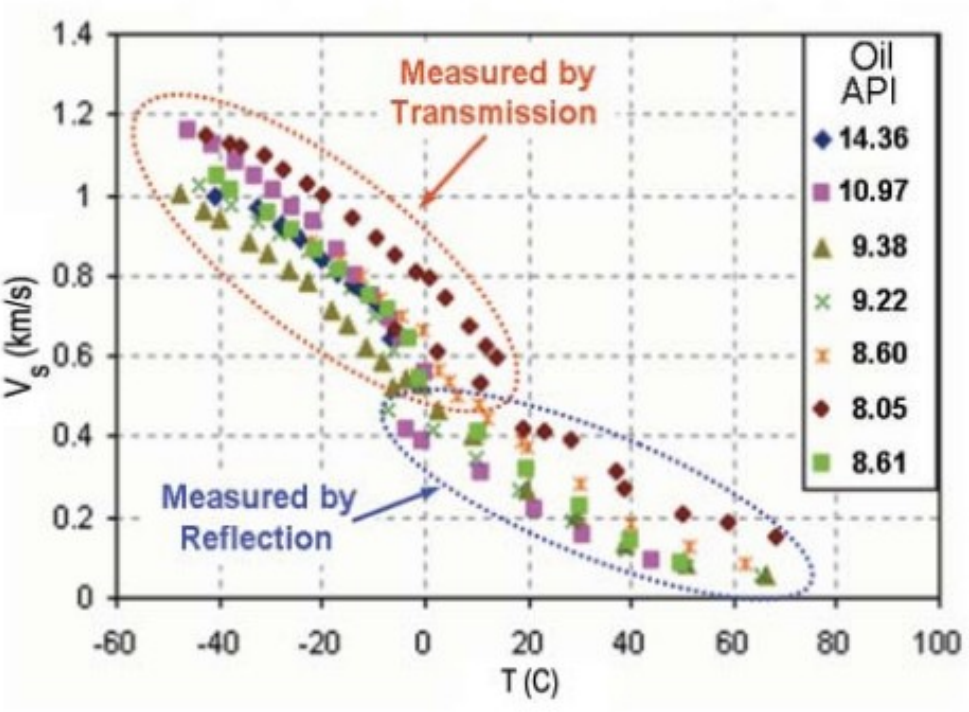


Figure 4.5: Measured V_s versus temperature for different heavy oils (after Han et al., 2008).

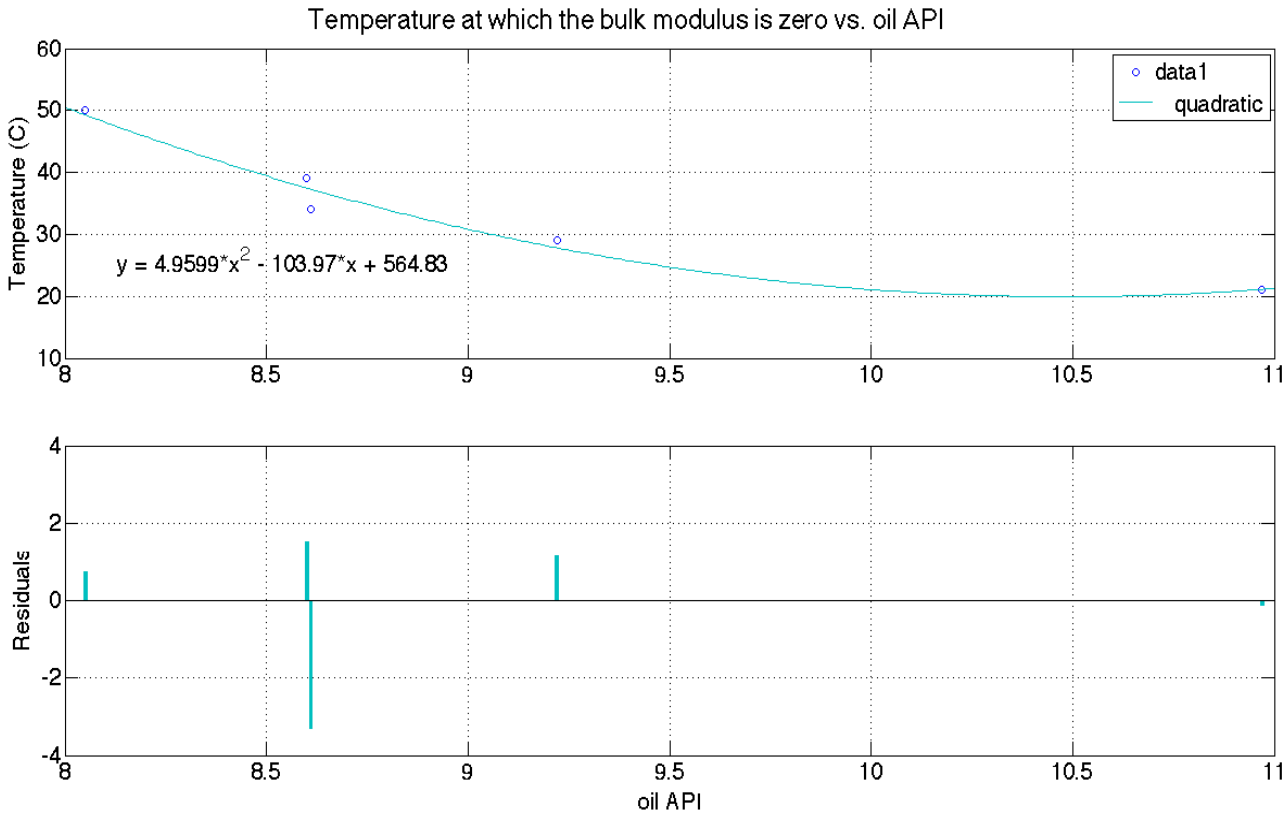


Figure 4.6: Four points are shown displaying the temperature at which the bulk modulus is equal to zero as a function of oil API. A quadratic model was obtained from regression analysis to describe the relationship between these parameters, given its fit to the data. The lower graph displays the error between the measured data points and the predicted values from the quadratic fit model.

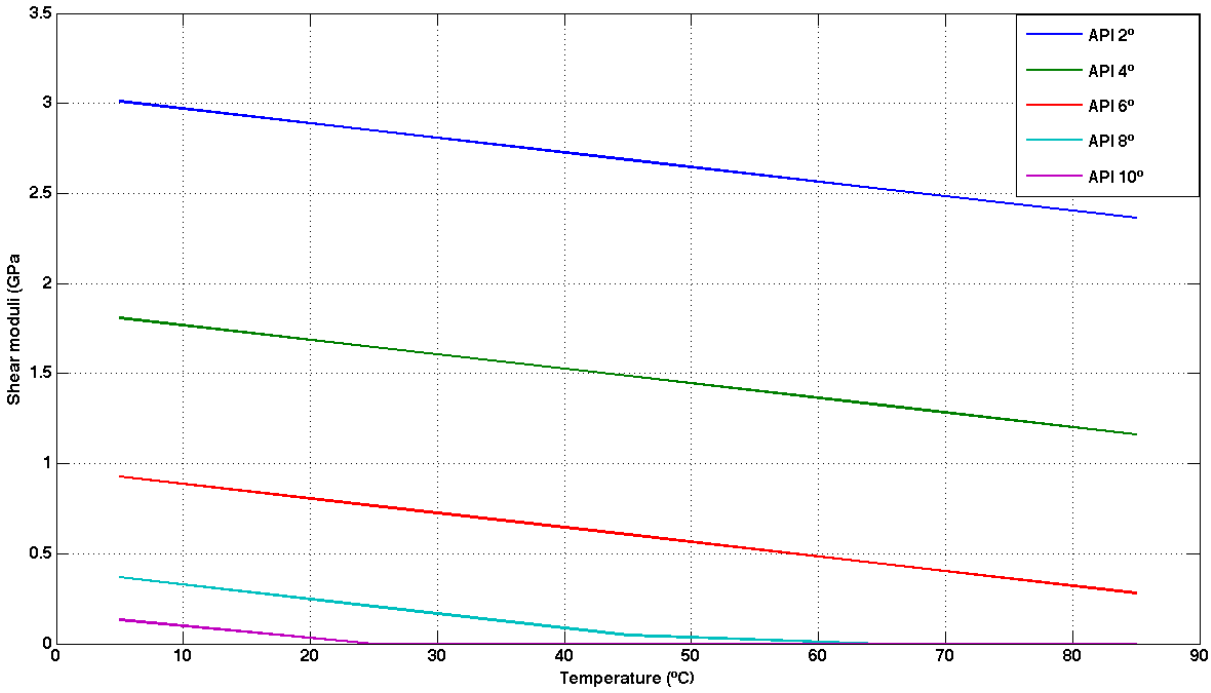


Figure 4.7: Shear moduli of some heavy oils with different API values versus temperature.

4.6 Mixing Laws

As previously discussed, a typical reservoir rock is comprised of pore spaces that are filled with fluids, which can be liquid, gas, or both. To effectively calculate the seismic response from a saturated rock, the grain moduli, the dry moduli and the fluid moduli need to be calculated. These are then used to calculate the effective P and S wave velocities using Gassmann's equation (Gassmann, 1951). Mixing laws are needed to determine the fluid modulus in the presence of more than one phase, which is then used to determine the effective elastic moduli of the saturated rock.

We consider two cases when calculating the effective elastic moduli for V_p and V_s of the saturated rock. In the first case, we assume that the heavy oil, brine and steam fill the pore spaces. In the second case we assume that the oil is the continuous phase and the rock grains are suspended in the oil, given that the sand is unconsolidated. The effective bulk modulus for the first case is calculated using Gassmann's equation shown in Equation 4.27. The effective shear modulus is simply equal to the shear modulus of the dry rock, as shown in Equation 4.28, because the shear moduli of fluids are zero. However, in the case of heavy oil being the continuous phase, we use Reuss's bound, shown in equation 4.29, to calculate the effective shear modulus of the saturated rock because it gives the exact value of the elastic modulus when any of the constituents is fluid with zero shear modulus (Mavko et al., 2009). It is important to note that the K in Equation 4.29 can represent any modulus. The index "i" in Equations 4.29 represents the different phases - i.e., brine, steam and oil.

Reuss's bound is also used to calculate the effective bulk modulus of a mixture of fluids that are finely mixed below the seismic resolution (Reuss, 1929). It is sometimes referred to as the isostress average because it gives the ratio of the

average stress to average strain when all constituents have the same stress. When one of the constituents is liquid or gas with zero shear modulus, the Reuss average bulk and shear moduli for the composite are exactly the same as the Hashin-Shtrikman lower bound (Mavko et al., 2009). Nauroy et al. (Nauroy et al., 2012) also use the Reuss average to calculate the effective bulk modulus of fluids in heavy oil sand reservoirs. It is also important to note that in the reservoir simulations of chapter 3, we assumed that the reservoir is homogeneous as what we are interested in is seeing a well-developed steam tongue on which we can apply our AVO procedure to improve the delineation of the steam chamber.

If the fluid phases are mixed on length scales larger than the seismic resolution, then the Voigt upper bound is used to calculate the effective elastic modulus of the mixture of fluids (Cairns, 2012). However, the seismic frequency that we will be using in this thesis corresponds to a wavelength of about 40m, which is much larger than the fluid mixture heterogeneities. Therefore, we use the Reuss equation rather than the Voigt to calculate the elastic properties of the mixture of oil and brine in the pore spaces. The density of the saturated rock is calculated using Equation 4.30 (Mavko et al., 2009). The saturated bulk and shear moduli are used in Equations 4.31 and 4.32 to calculate the P and S wave velocities, respectively. It is important to note that the Reuss and Voigt bounds assume that each constituent is isotropic, linear and elastic.

$$K_{sat} = K_{dry} + \frac{(1 - \frac{K_{dry}}{K_{grain}})^2}{\frac{\emptyset}{K_f} + \frac{(1-\emptyset)}{K_{grain}} - \frac{K_{dry}}{K_{grain}^2}} \qquad (4.27)$$

$$\mu_{sat} = \mu_{dry} \text{ ; if } \mu_{oil} = 0 \qquad (4.28)$$

$$K_f = \left(\sum_{i=0}^{n} \frac{S_i}{K_i} \right)^{-1} \qquad (4.29)$$

$$\rho_{sat} = \emptyset \, S_{oil} \, \rho_{oil} + \rho \, S_B \, \rho_B + (1 - \emptyset) \, \rho_{rock} \qquad (4.30)$$

$$V_p = \sqrt{\frac{K + \frac{4}{3}\mu}{\rho}} \qquad (4.31)$$

$$V_s = \sqrt{\frac{\mu}{\rho}} \qquad (4.32)$$

We mentioned that in the second case the rock grains are discontinuous. In other words, the rock grains are surrounded by oil. In this case, the elastic moduli are calculated using the Reuss bound shown in Equation 4.29. Figure 4.8 compares V_p and V_s for the continuous versus discontinuous sand phase at different temperatures and pressures. It assumes a porosity of 25% and 60% for the continuous and discontinuous sand phases, respectively. In both cases we assumed the salinity, grain bulk modulus, grain shear modulus, rock density and oil API values to be 0.5, 37 GPa, 44 GPa, 2.65 gm/cm3 and 10° API, respectively. As we would expect, the primary velocity when sand is the continuous phase is higher compared to when it is not.

Another observation is that V_p when the sand is continuous is equally sensitive to both temperature and pressure, while in the sand discontinuous case it is much more sensitive to temperature variations. This is expected since the bulk modulus of the rock is more sensitive to pressure variations, while the bulk modulus of the heavy oil does not increase as much with increasing pressure while it decreases considerably with increasing temperature. This is characteristic of heavy oils. On the other hand, V_s does not change much with increasing temperature in

the continuous sand phase because the shear modulus of the rock does not change with temperature.

The slight increase in Vs with increasing temperature in the model is due to the slight decrease in the fluid's density with increasing temperature. Shear velocity is zero in the oil continuous phase, which is expected since it acts as a fluid with a zero shear modulus. However, in reality, V_s actually slightly increases, as we will discuss later in this chapter. Shear velocity is zero in the oil continuous phase, which is expected since the reservoir acts as a fluid with a zero shear modulus.

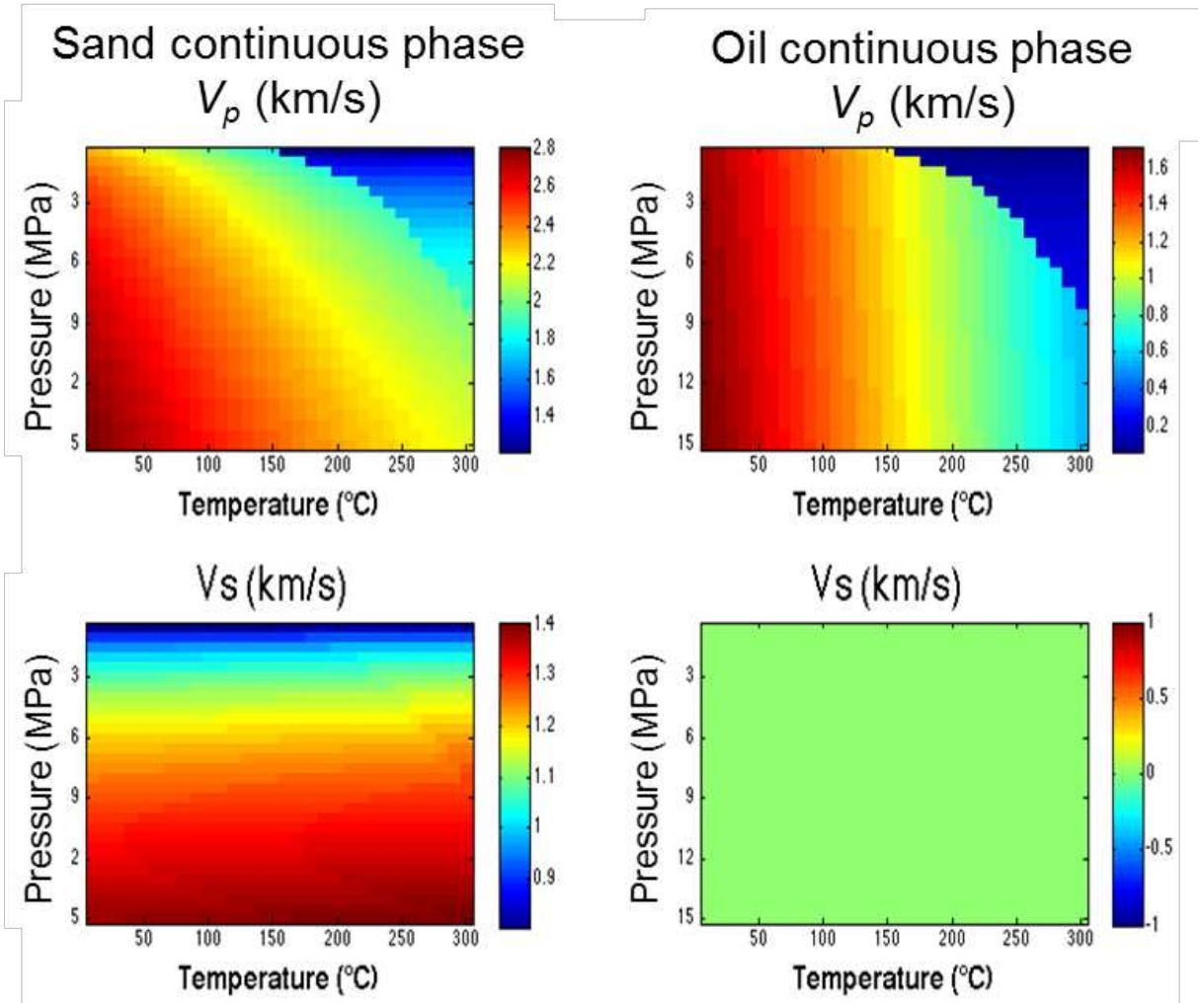
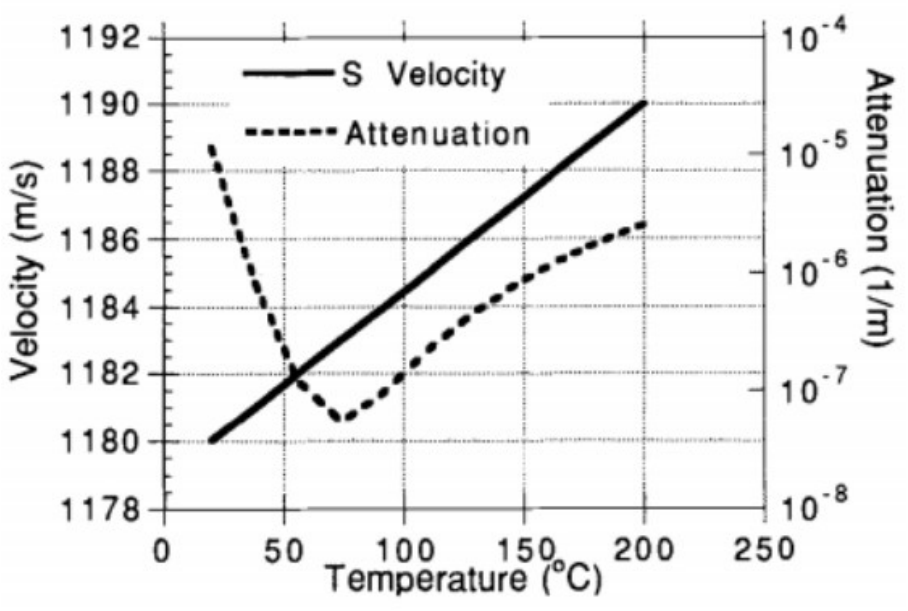


Figure 4: Vp and Vs in km/s for a sand versus oil continuous phase at different temperatures (^oC) and pressures (MPa).

4.7 Validation against Experimental and Published Data

In this section we compare our results to those published. We start by comparing our predictions of V_s in a saturated rock, which showed a very slight increase in V_s (less than 1%), which is counter-intuitive, with increasing temperature as shown in the bottom left plot of Figure 4.8. S-wave velocity is calculated by taking the square root of the shear modulus divided by the density as shown in Equation 4.32. While we assume that the shear modulus of the saturated rock is not sensitive to changes in temperature, the overall density is and it decreases with increasing temperatures. This causes V_s in our model to slightly increase with increasing temperatures. Figure 4.9 shows a similar trend from a published paper along with our results (Eastwood, 1993). The author makes the same argument to justify his results. Figure 4.10 shows another example of this same prediction from a conference paper compared to our results (Bauer et al., 2011). The range of temperature in Figures 4.9 and 4.10 is extended to 300 °C while keeping the pressure constant at 7 MPa. The brine changes phase from liquid to steam at around 280 °C which explains the sudden increase and decreases in V_s *and* V_p, respectively in Figures 4.9 and 4.10.



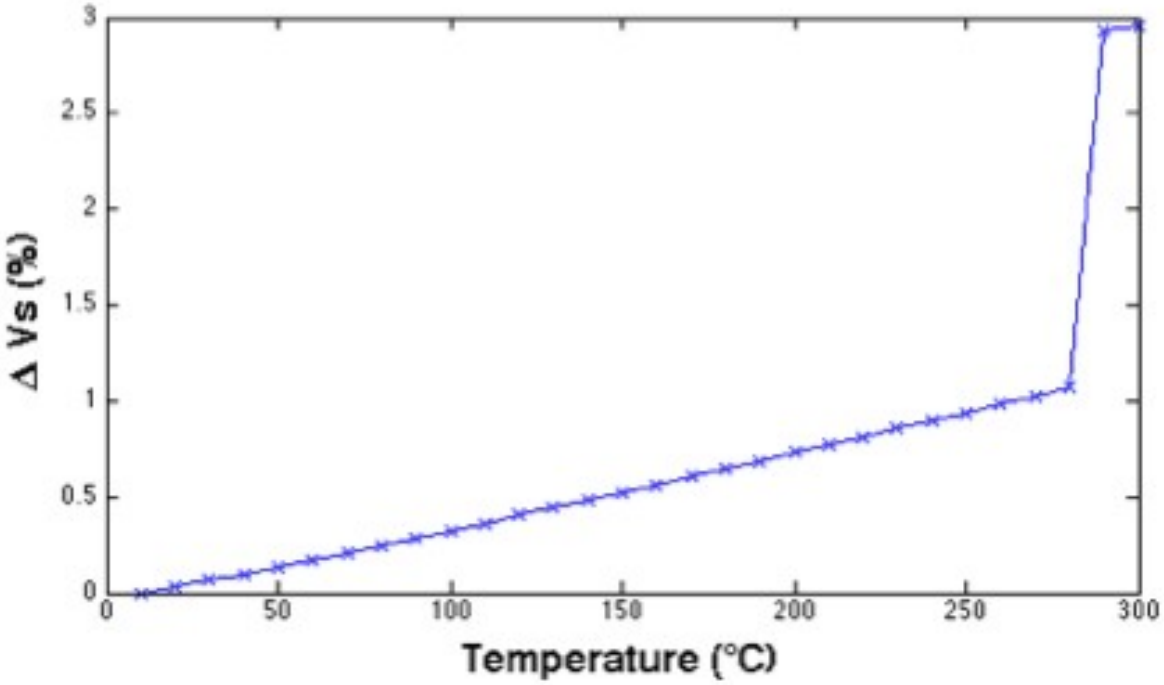


Figure 5: Predicted S-wave velocity vs. temperature in a saturated rock. The top plot is after Eastwood (1993), while the bottom plot is our results. The sudden increase in S-wave at around 280 °C is due to the brine changing phase from liquid to steam.

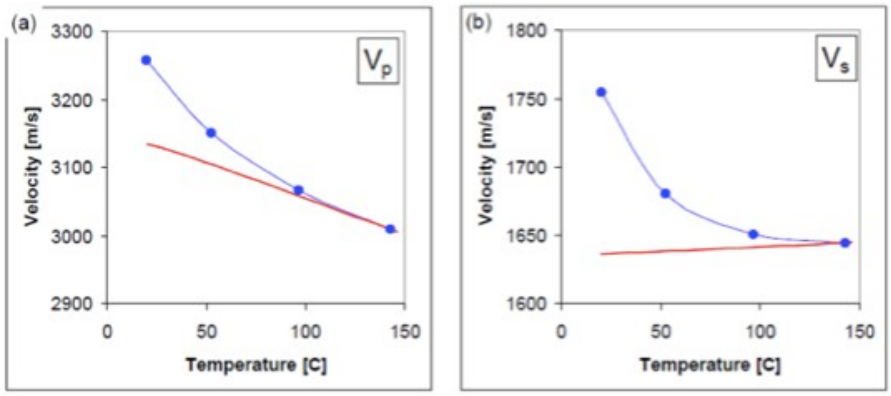


Fig. 3: V_p (a) and V_s (b) as a function of temperature measured under virgin in-situ stress and pore-pressure conditions (symbols). The red lines represent calculated velocities using the Gassmann model with the fluid properties being calculated by FLAG and the dry-rock bulk and shear moduli assumed temperature independent and adjusted to fit the high-temperature data (K_{dry} = 9 GPa, μ_{dry} = 5.8 GPa, K_0 = 37 GPa, ϕ = 28%, S_{oil} = 80%, S_{brine} = 20%, GOR = 0, brine salinity = 13000 ppm).

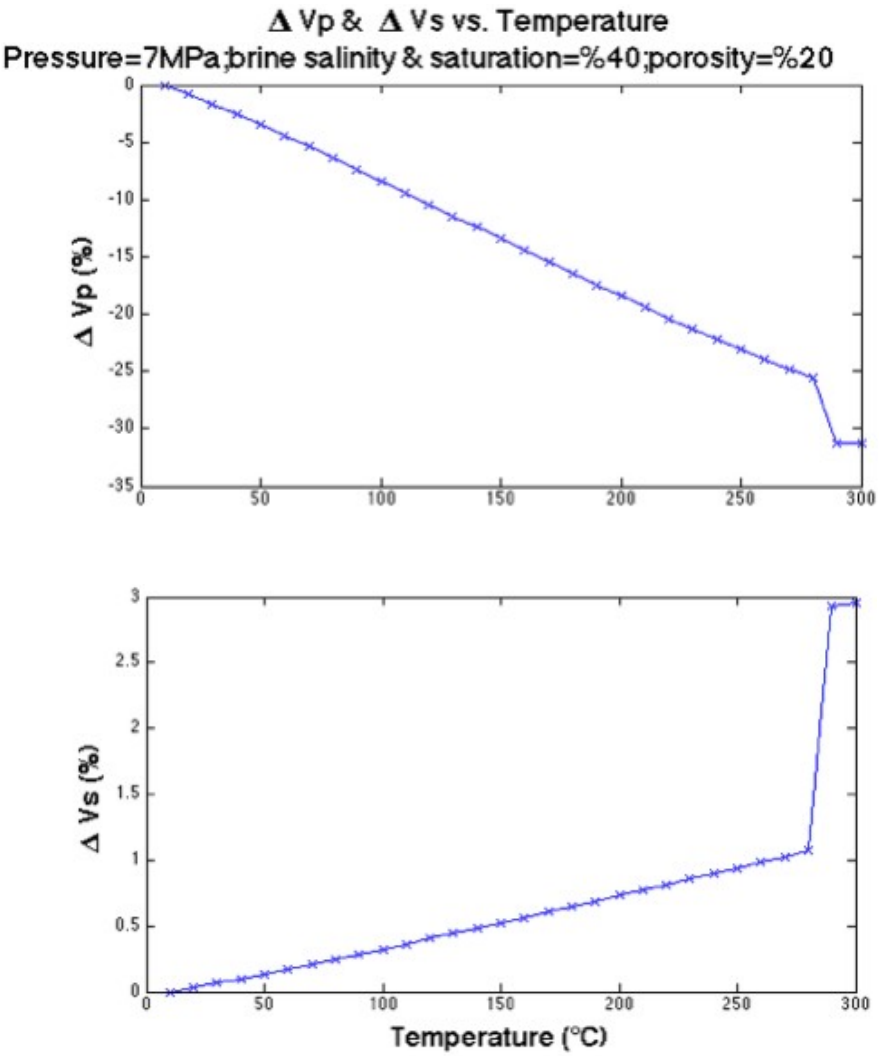


Figure 6: Plots of V_P and V_S versus temperature (after Bauer et al., 2011) on the top compared to our results on the bottom. The sudden increase in S-wave and decrease in P-wave velocities at around 280 °C is due to brine changing phase from liquid to steam.

The elastic modulus of a heavy oil sample versus temperature is shown in Figure 4.11 (Batzle et al., 2006) along with our results assuming a pressure of 15 MPa. The pressure is not specified in the published paper. Figure 4.12 shows another comparison from the same paper (Batzle et al., 2006) of V_p versus temperature at two different pressures along with our results. The results are in good agreement except for the fact that our results show a linear behaviour at lower temperatures compared to a nonlinear trend in the published paper. The difference is minimal and causes discrepancies in V_p that are less than 1%. Our results show a change in the slope of V_p at 80 °C as the oil transforms from solid to liquid and the

shear modulus of the oil diminishes to zero.

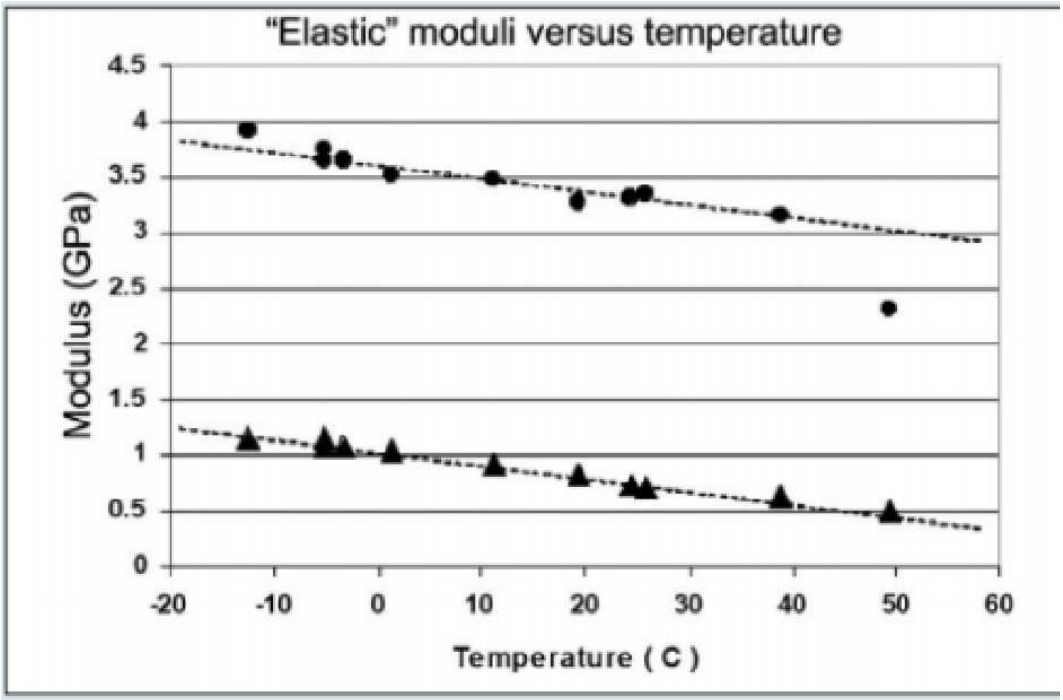


Figure 13. Elastic moduli of the heavy oil from ultrasonic data. The effective shear modulus (triangles) drops toward zero as temperatures approach 80° C.

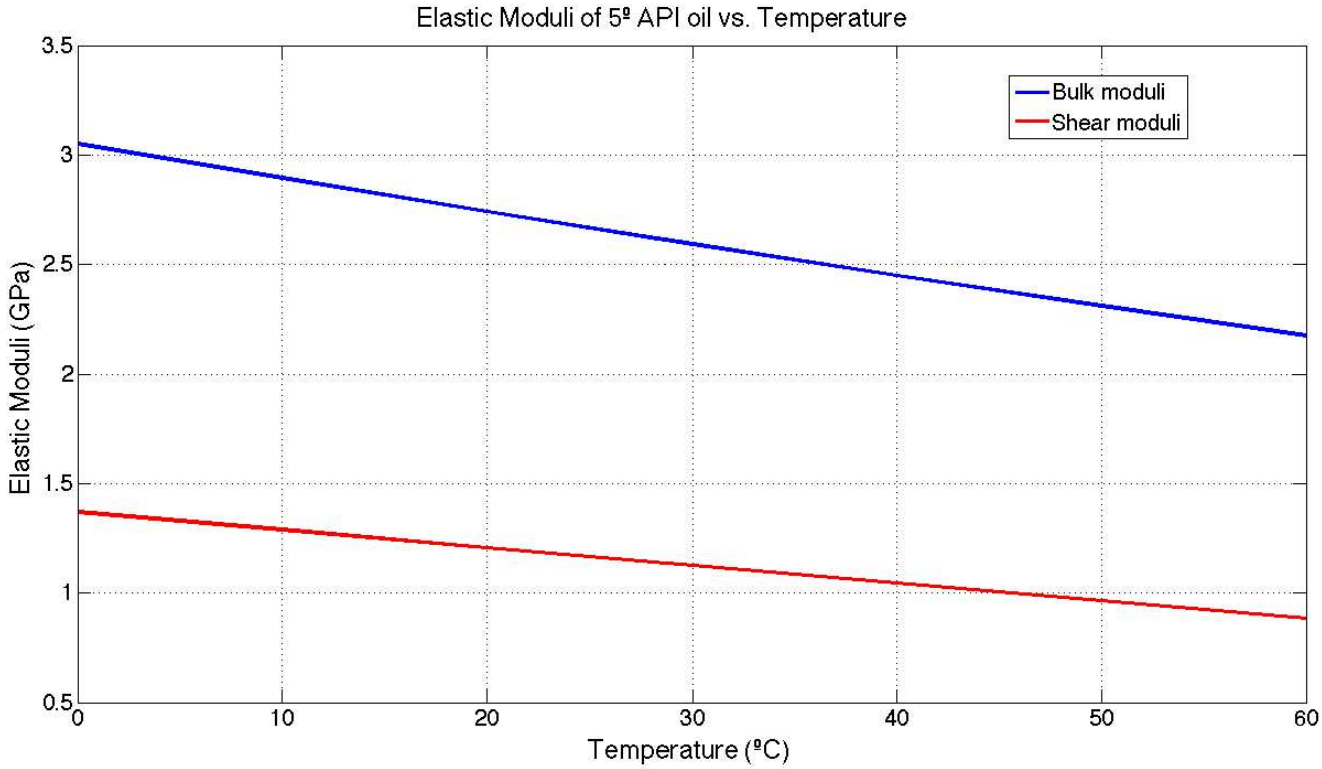


Figure 7: The top plot is for a 5° API oil sample (after Batzle et al., 2006) compared to our result at the bottom.

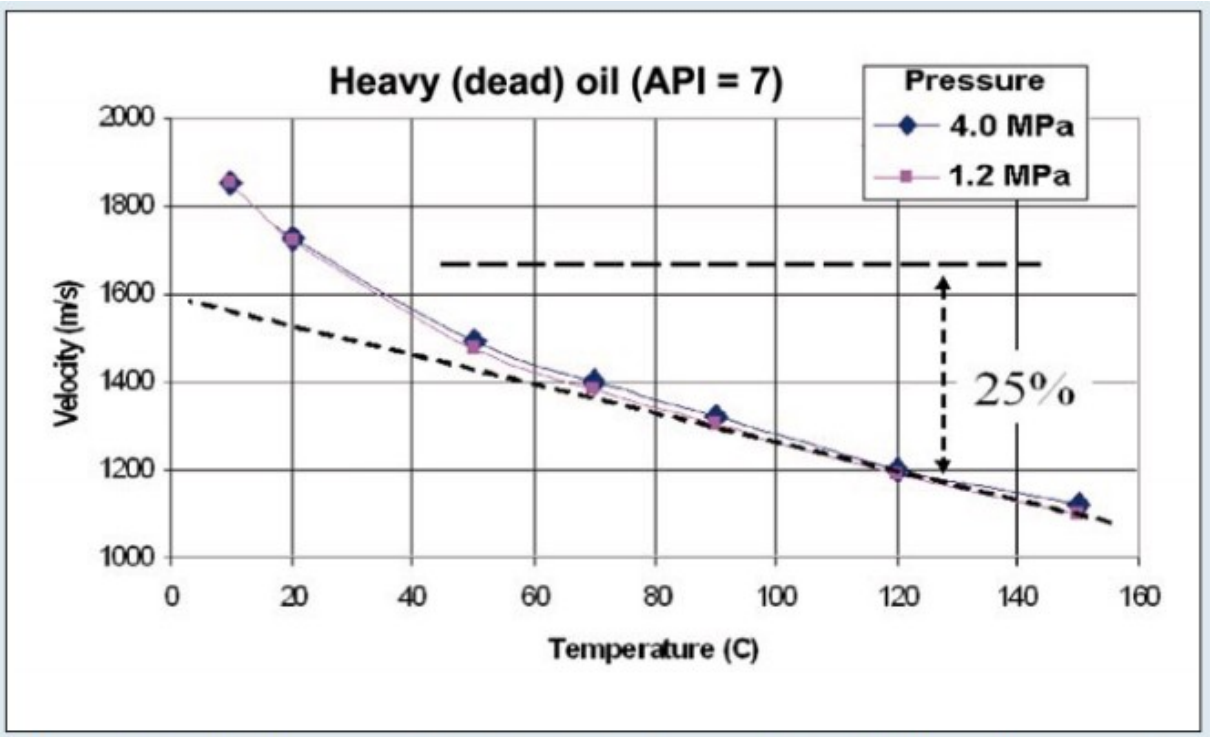


Figure 11. *This heavy-oil velocity also drops substantially with increasing temperature. At temperatures below about 70° C, the temperature-velocity relation becomes strongly nonlinear.*

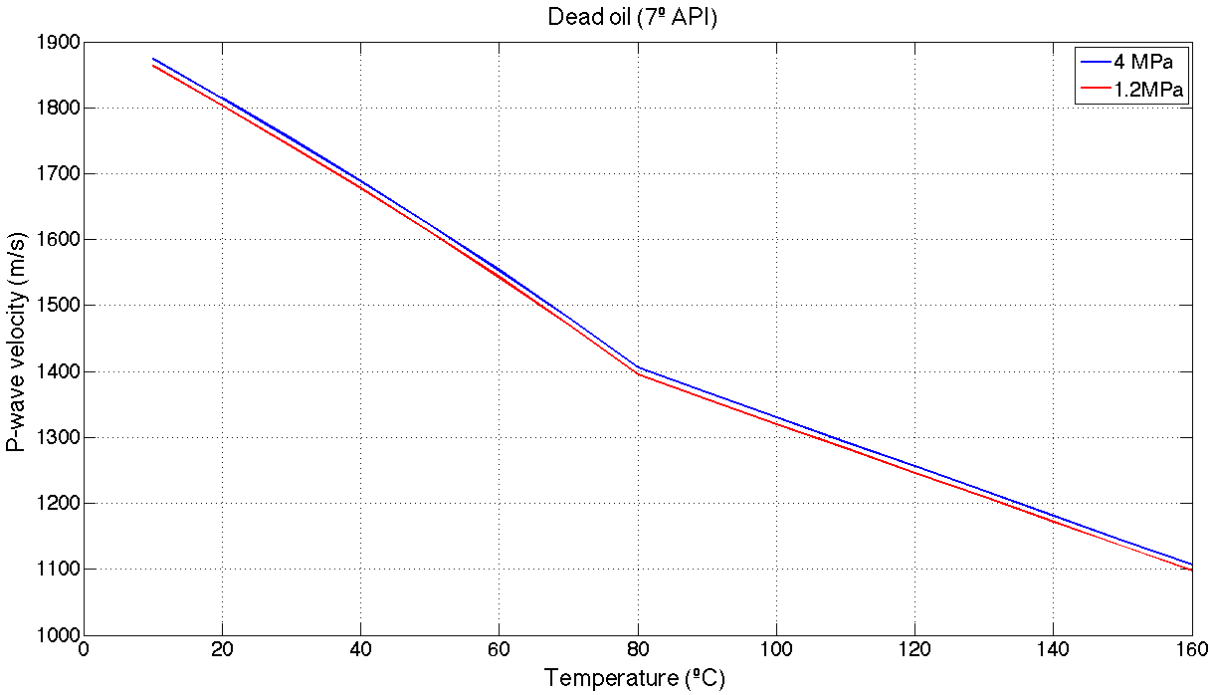
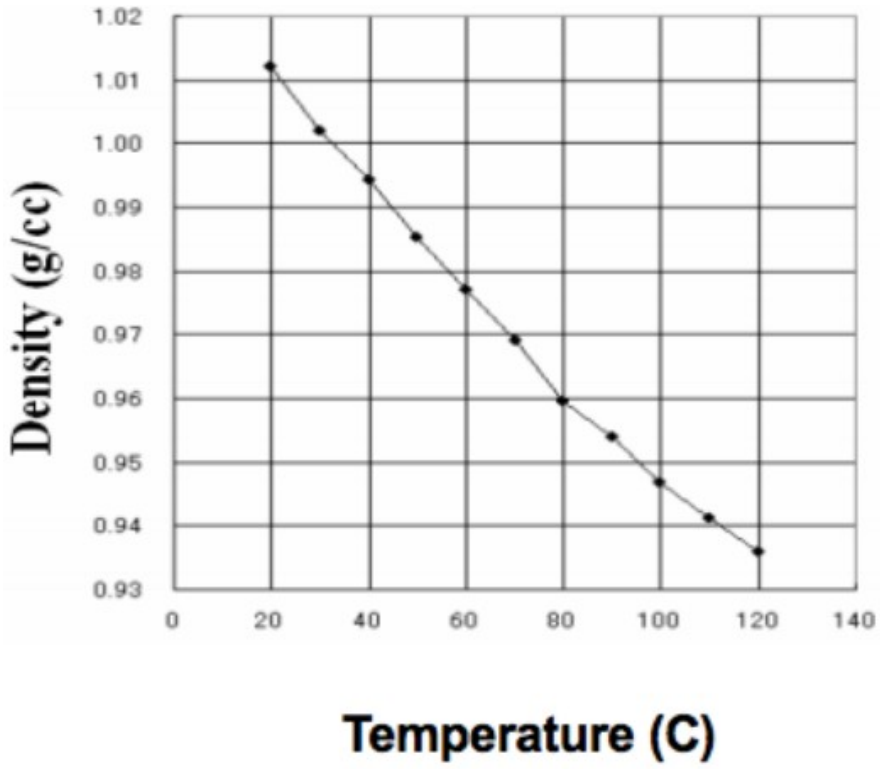


Figure 8: Vp versus temperature for a 7° API oil at pressures 4 and 1.2 MPa on the top (after Batzle et al., 2006) compared to our result at the bottom.

Moving on to the density variation of oil with temperature, we produced the plot on the right in Figure 4.13, which is very similar to the results shown in the left plot (Mochinaga et al., 2006). The pressure was not specified in the paper but its effect is minimal compared to the effect of temperature as we tried changing the pressure by as much as 10 MPa with very small change in density compared to temperature. We choose a pressure of 0.5 MPa as an examples since the density of oil is not sensitive to pressure variations.



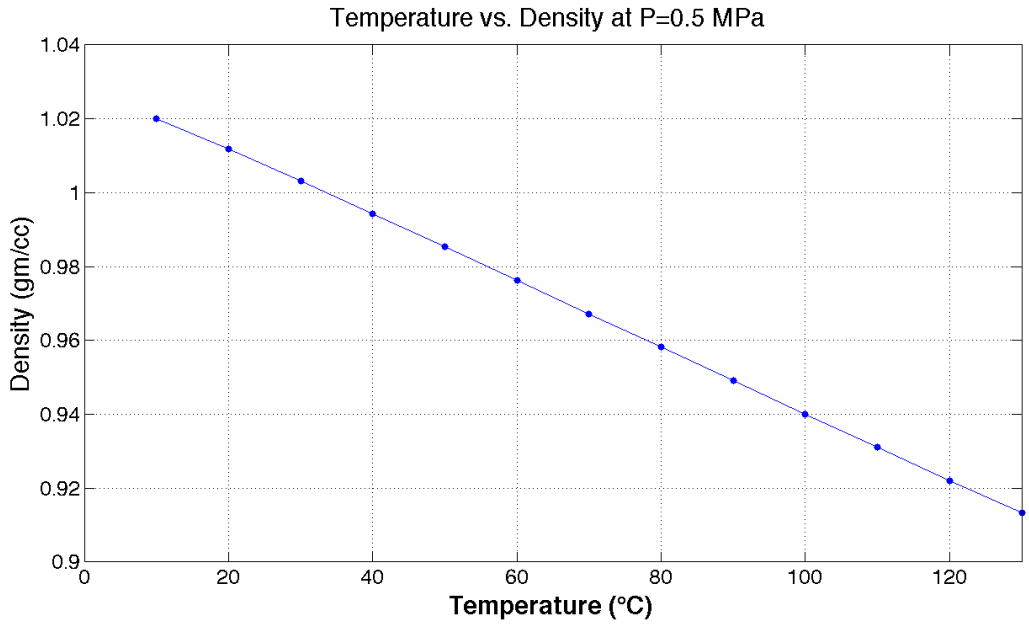


Figure 9: Density of oil versus temperature on the top (after Mochinaga et al., 2006) compared to our result on the bottom.

Looking at the pressure effects, Figure 4.14 compares our results with those from Yuan and Han (2013). The authors did not specify the temperature and porosity of the oil sand sample. We produced a plot assuming the porosity and temperature values to be 35% and 100 °C, respectively. The blue triangles in the left plot agree very well with the blue 'x' marks in the right plot.

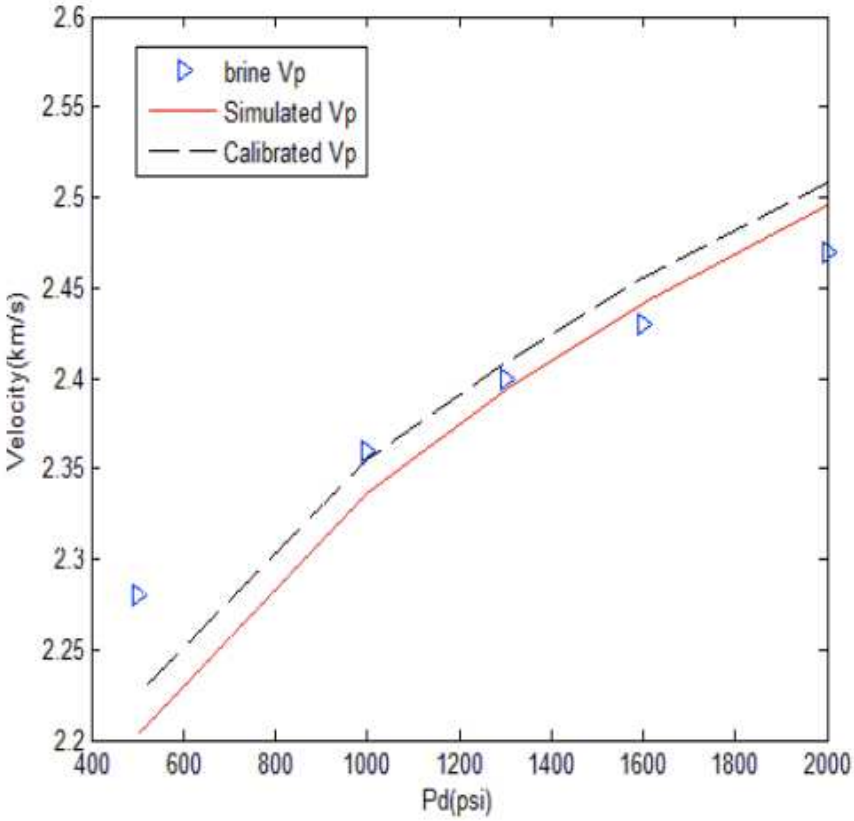


Figure 4. Oil sand P-wave velocity versus differential pressure. The blue triangular is the measured brine-saturated sands P-wave velocity, the red curve is the simulated result with unconsolidated sand model, and the red dashed line is the calibrated Vp.

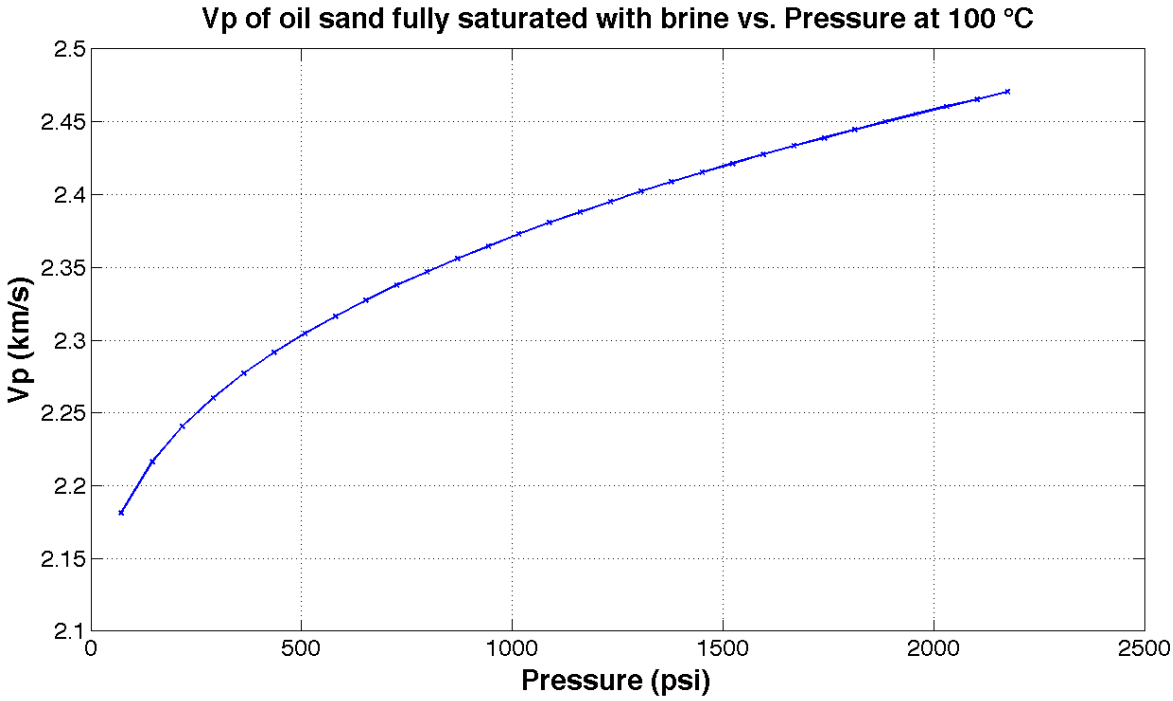
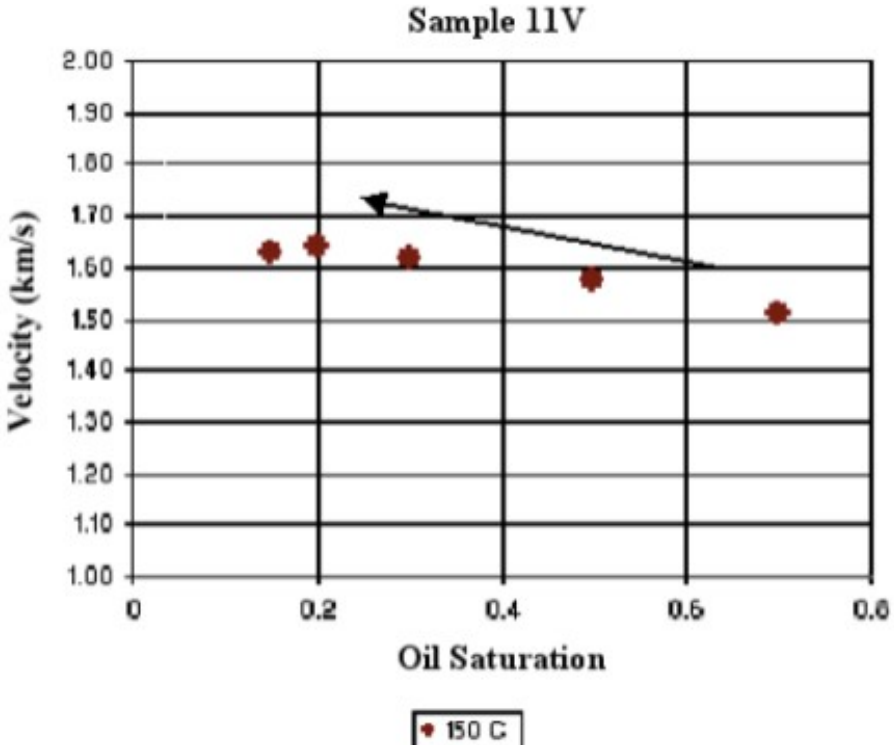


Figure 10: Vp vs. pressure in the top plot (after Yuan and Han, 2013) compared to our result on the bottom.

Moving on to oil saturation effects, we used a temperature of 150 °C as specified by Dan et al. (2007) to produce Figure 4.15. However, they did not specify the pressure nor the porosity of the oil sand sample. We assumed values of 0.5 MPa and 35% for pressure and porosity, respectively. The compressional velocity values do not agree exactly with the values presented by Dan et al. (2007) due to the uncertainty in pressure and porosity. However, our results show a similar trend of decreasing V_p with increase in oil saturation as can be seen by comparing the two plots.



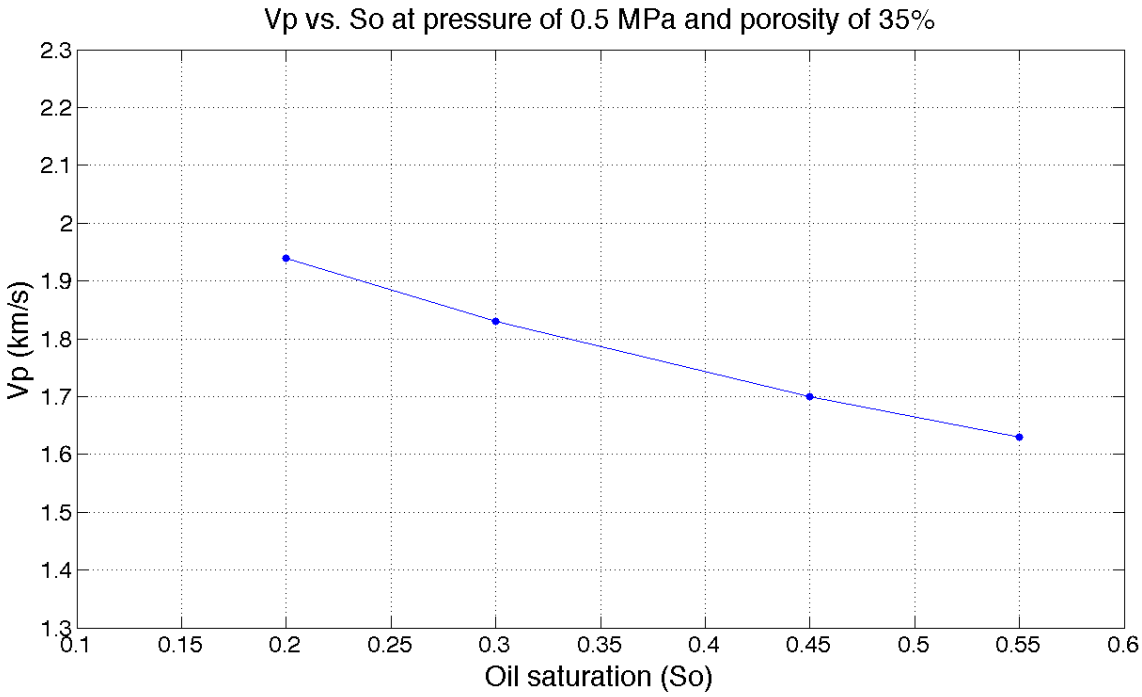


Figure 11: V_p vs. oil saturation on the top (after Dan et al., 2007) compared to our result on the bottom.

4.8 Sensitivity of Vp and Vs to Different Inputs

We studied the effects of temperature, porosity, brine saturation, pressure and salinity on the final V_p and V_s of a saturated rock. We started by conducting a literature review on the expected variations in porosity of a loose sand reservoir. Chuhan et al. (2003) describe how porosity changes with pressure and other factors such as grain size, grain roundness and clay content. Figure 4.16 shows that the porosity drop due to vertical stresses less than 10 MPa is usually less than 5% although in some cases it can drop by almost 10%. Figure 4.17 shows porosity loss for different grain sizes and sands. Based on this information, we allowed the porosity to change by as much as 20%. Figures 4.18 and 4.19 are tornado charts showing the expected percentage change in the final V_p and V_s due to predefined changes in different parameters. Any change smaller than %5 is considered undetectable. We conclude that changes in temperature, porosity and brine saturation can be detectable using V_p. On the other hand only porosity and pressure changes can be detectable using V_s.

Fig. 7. One-dimensional compression behaviour of sands with various compositions in different grain-size categories: (*a*) n = 47% in fine-grained sands, (*b*) n = 47% in medium-grained sands, (*c*) n = 44% in coarse-grained sands, (*d*) n = 43% in very coarse grained sands, and (*e*) n = 43% in granule-size sands. In coarse- to granule-size sands the initial porosity of the carbonate sand is the minimum porosity, as it was not possible to bring the porosities to the very low values of the other sands.

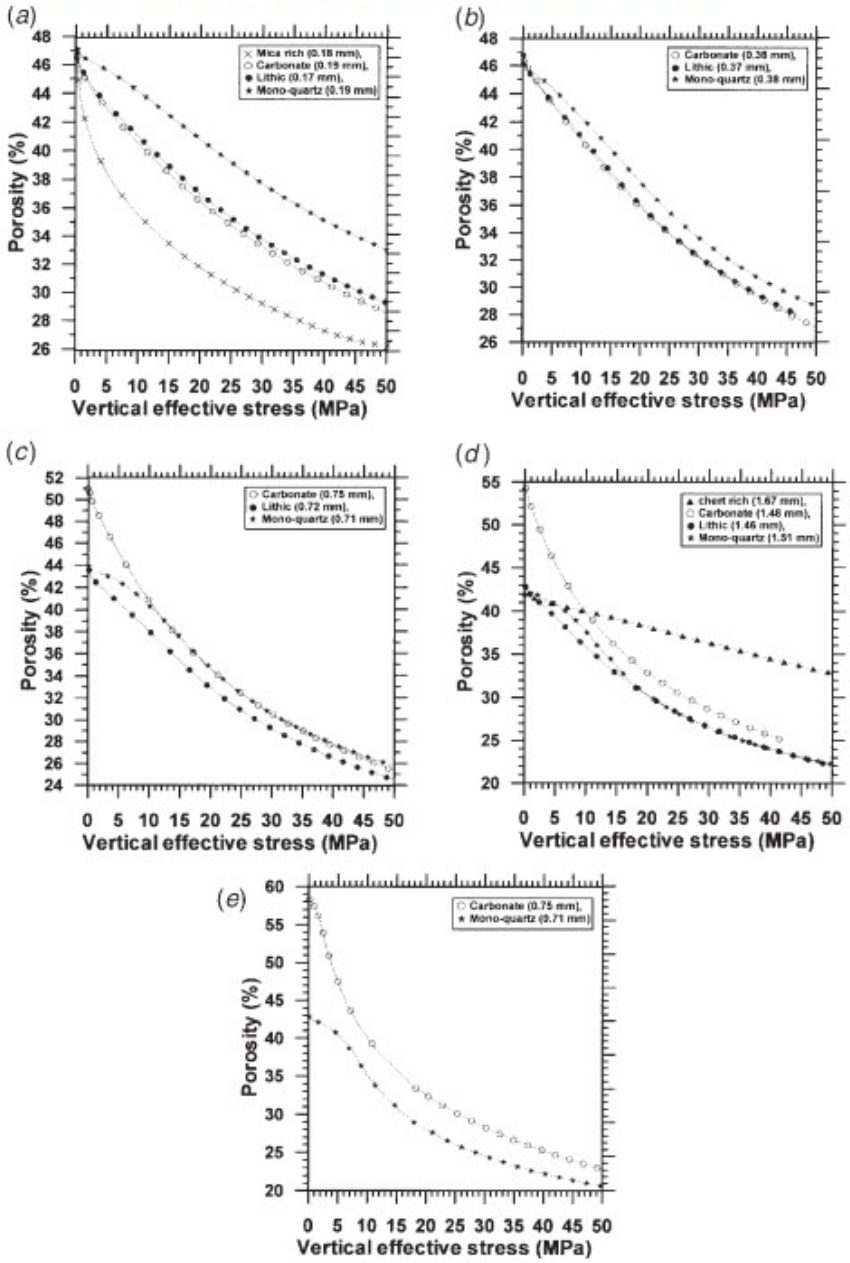


Figure 12: Porosity vs. vertical effective stress for loose sands with different composition and grain size (after Chuhan et al., 2003).

Fig. 6. Effects of grain-size variation in mono-quartz, lithic, and carbonate sands on porosity loss in (*a*) the low (0–5 MPa), (*b*) intermediate (5–25 MPa), and (*c*) high (25–50 MPa) stress intervals and on porosities at (*d*) 5, (*e*) 25, and (*f*) 50 MPa vertical effective stresses.

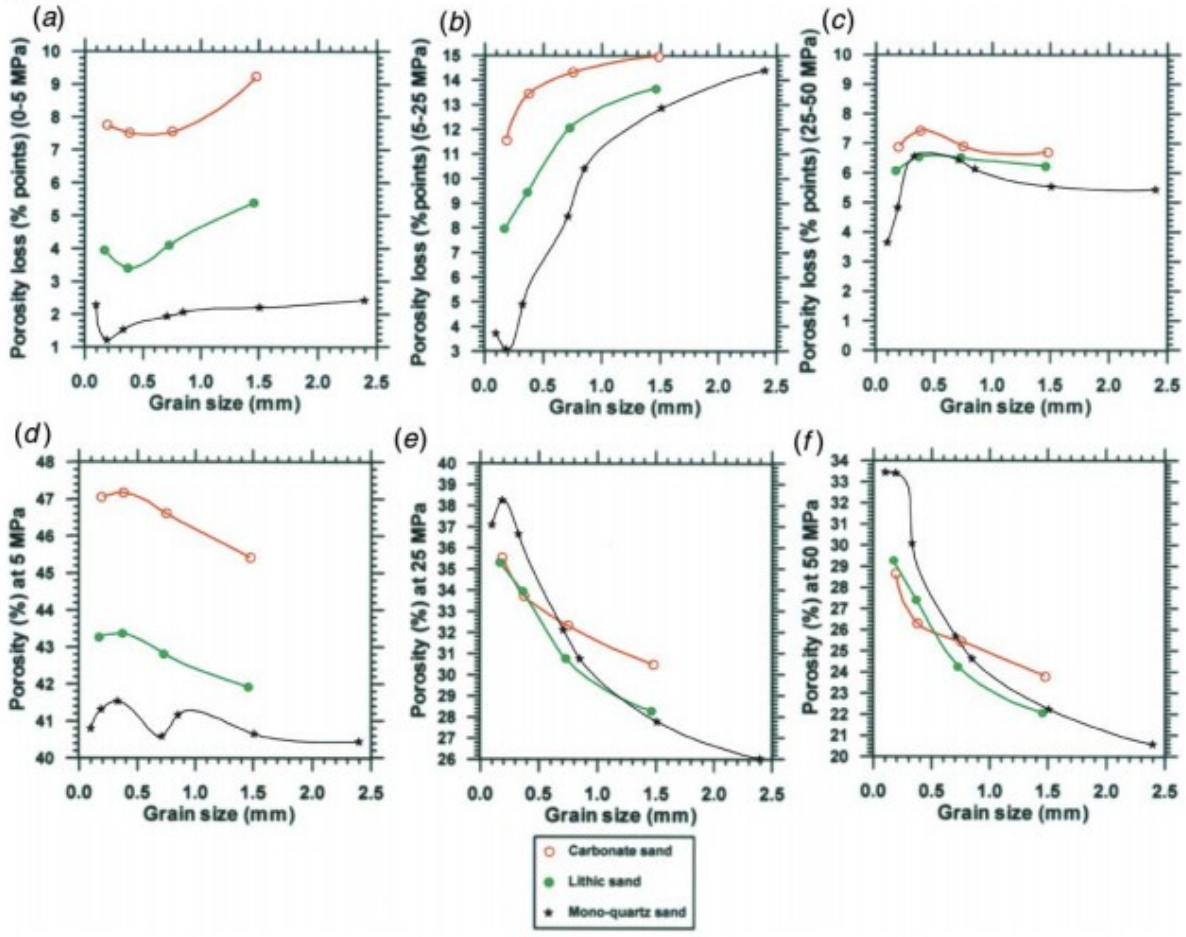


Figure 13: Porosity loss versus grain size for different type of sands (after Chuhan et al., 2003).

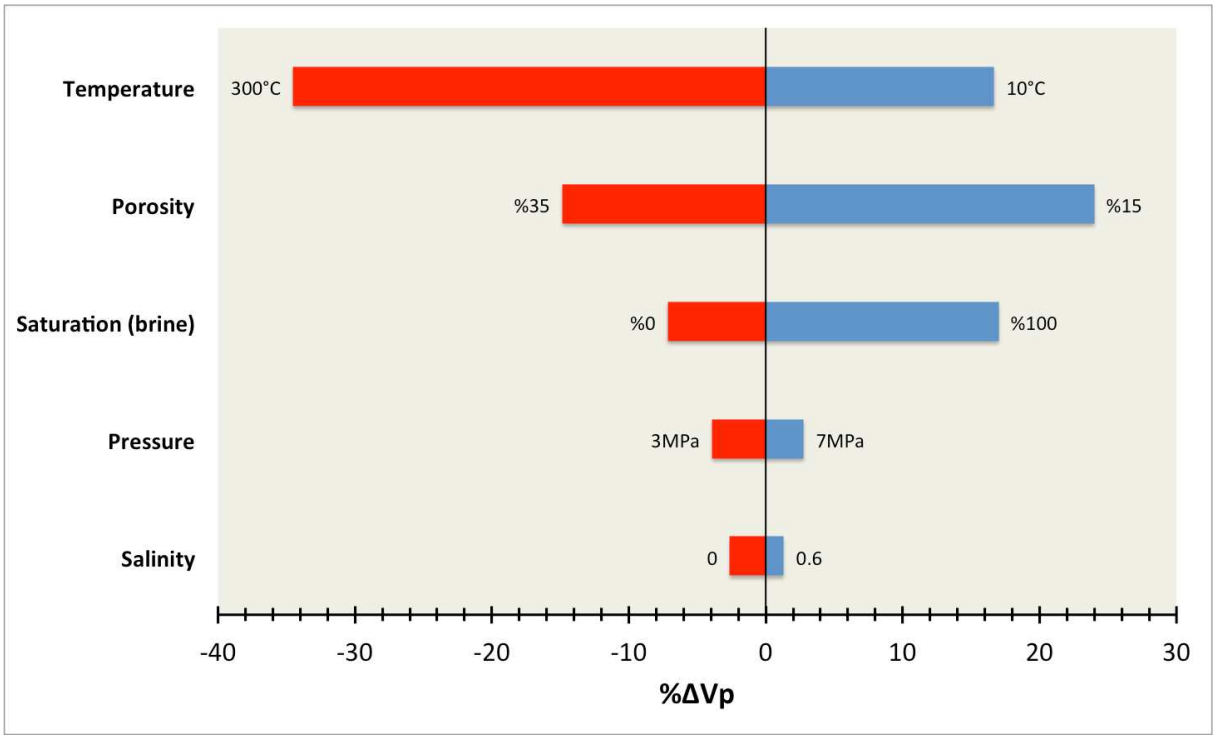


Figure 4.18: %ΔVp vs. reservoir properties.

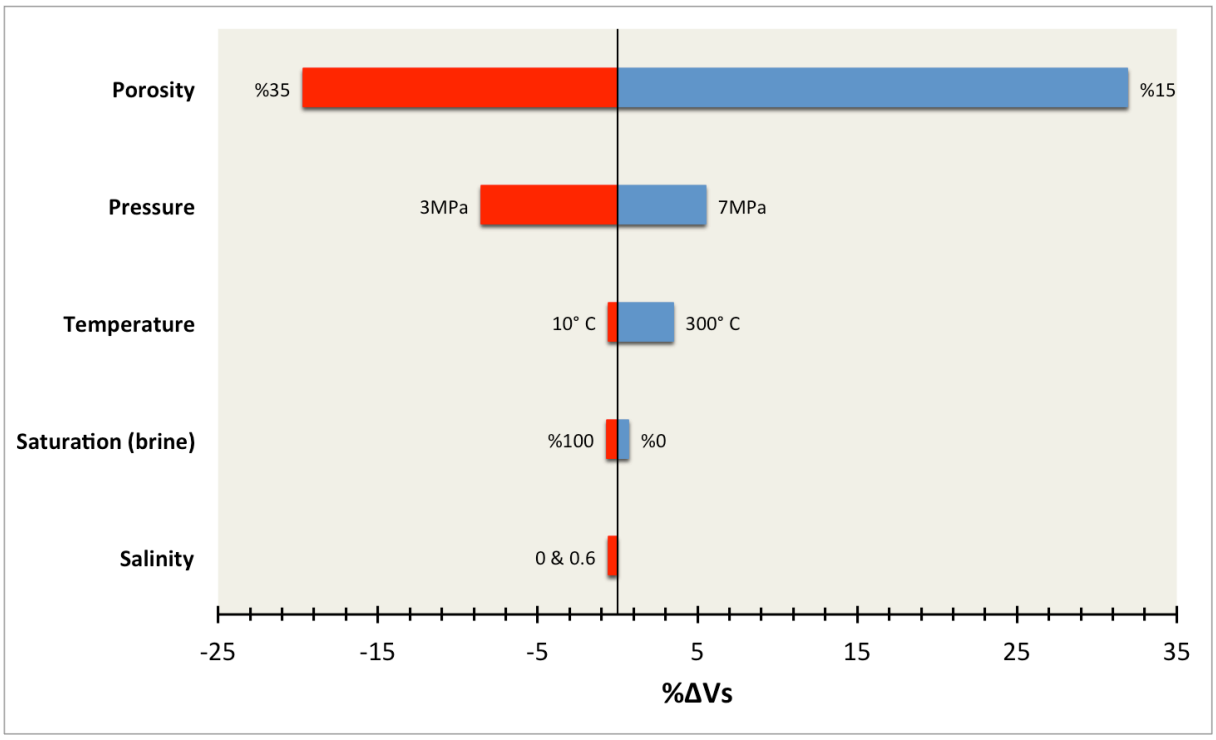


Figure 4.19: %ΔVs vs. reservoir properties.

5. AVO Analysis

5.1 Introduction

Using exploration seismology, we cannot differentiate between water and oil because the seismic properties of both water and oil are very similar (Han and Batzle, 2002). However, improving our knowledge of the lateral and vertical extent of the steam chamber tells us which parts of the reservoir were swept, hence improving our management of the reservoir. We use amplitude versus offset to better delineate the vertical resolution of the steam chamber.

The amplitudes of reflected seismic waves vary with varying angles of incidence and the medium through which they propagate. The term used to refer to this variation is amplitude versus offset (AVO) or amplitude versus angle (AVA). However, AVO is more commonly used because we have control over the distance between the seismic source and receiver, which in turn changes the incident angle. This chapter consists of two parts. In the first part, we analyse the AVO's sensitivity to reservoir properties. In the second part of this chapter, we use AVO to better resolve the lower boundary of the steam chamber, thus better approximating the thickness of the steam chamber.

In the first part, we conduct a sensitivity study in which we explore how the zero offset reflectivity of the AVO approximation, also known as the intercept, and the gradient of the AVO approximation vary with varying oil API, brine saturation, steam saturation, porosity, temperature and pressure. Some of these parameters are dependent on each other, e.g. temperature and pressure, and can vary in space and time in a reservoir undergoing a steam flooding operation. The AVO analysis is conducted using HampsonRussell software, which is a geophysical interpretation tool

for reservoir characterization developed by the French geophysical services company (CGG). In the pre steam injection case, we will calculate the AVO at the boundary between the overburden and the top of the reservoir. In the post injection case we will calculate the AVO at two boundaries, namely, the overburden and top of the reservoir boundary, which represents the top of the steam chamber, and the bottom of the steam chamber. The overburden was assumed to have a constant P-wave velocity, S-wave velocity and density of 3200 m/s, 1700 m/s and 2600 kg/m^3, respectively.

5.2 Theory and Methodology

The typical range for each parameter and the reference values for Emlichheim are listed in Table 5.1.

Parameter	Range	Reference values	References	Comments
Temperature	0-300 °C	37-300°C	Lumley et al., 1995 Li et al., 2001 Leonhardt, 2001 Laine, 1987	We do not consider the case of sub-zero temperatures as the majority of reservoirs do not fall in that category. Initial reservoir temperature in Emlichheim is 37°C.
Pressure	0.5-22 MPa	1-8 MPa	Lumley et al., 1995 Leonhardt, 2001 Laine, 1987 Altunina & Kuvshinov, 2008	Initial reservoir pressure in Emlichheim is 8 MPa. This will decrease with steam injection as the pore pressure increases.
Porosity	15-45%	30%	Hoversten et al., 2004 Leonhardt, 2001 Lumley et al., 1995 Li et al., 2001	Some of the rock physics models that we use assume a critical porosity value of 38%. Porosity in Emlichheim is 30% and does not change much over time unless a lot of sand is produced.
Brine saturation	0-100%	8-100%	Setiawan et al., 2014 Davis et al., 2013 Lumley et al., 1995 Leonhardt, 2001	Connate water/oil will always be present in the pores. Emlichheim has an initial brine saturation of 8%.

Brine salinity	0.05-20%	0.05-2%	Meents et al., 1966 Waxman & Smits, 2003 Hanor, 1994	Salinity increases with depth. We are dealing with shallow reservoirs typically less than 1000m. 2% is sensible as the reference salinity.
API	8-25°	25°	Lumley et al., 1995 Leonhardt, 2001 Ferguson et al., 2001 Rivero & Mamora, 2005	The oil in Emlichheim is medium heavy oil with an API of 25° which remains constant.
Reservoir depth	100-1300m	700m	Lumley et al., 1995 Liu, 1987 Leonhardt, 2001	The lower and higher limits are bounded by fracture pressure and critical pressure of steam, respectively. The reservoir in Emlichheim is about 700m deep.
Reservoir thickness	>3m	30m	Leonhardt, 2001	Lower limit is bound by heat loss to overburden. The reservoir in Emlichheim is about 30m thick.

Table 5.1: Typical ranges and reference values for each parameter for Emlichheim oil field.

Seismic waves travel through a medium and are reflected at the interface at which the seismic impedance changes. Seismic impedance is the product of velocity and density. When the density of a medium changes, as a result of change in lithology or in fluid content and saturation, the impedance changes, thus changing the reflectivity of seismic waves. Amplitude versus offset (AVO) is a powerful technique used in reflection seismology to determine the rock and fluid properties such as, density, porosity and seismic velocity. It originates from the Zoeppritz Equations and involves studying the relationship between reflection and transmission coefficients, and the angle of incidence, which can be changed by varying the distance between the seismic source and receiver (Zoeppritz, 1919). Shuey's approximation, shown in Equation 5.1, is used when the spacing between geophones is small enough so that the angle of incidence of seismic waves is less than 30°, which is the case in most seismic surveys (Chen et al., 2010):

$$R\ (\theta) = R(0) + \ G\ sin^2\theta \qquad (5.1)$$

Where

$$R\,(0) = \frac{1}{2}\,\left(\frac{\Delta v_p}{v_p} + \frac{\Delta \rho}{\rho}\right) \qquad (5.2)$$

And

$$G = \frac{1}{2}\,\frac{\Delta v_p}{v_p} - 2\,\frac{\Delta {v_s}^2}{{v_p}^2}\left(\frac{\Delta \rho}{\rho} + 2\,\frac{\Delta v_s}{v_s}\right) \qquad (5.3)$$

Where θ is the angle of incidence of the reflected wave; $R(\theta)$ is the reflection coefficient at incidence angle θ; $R(0)$, also known as the AVO intercept, is the reflection coefficient at normal incidence; G, also known as the AVO gradient, describes the variation of seismic reflection amplitudes with offset; V_p and V_s are P and S-wave velocity in the medium, respectively; ΔV_p and ΔV_s are P and S-wave velocity contrast across the interface, respectively; ρ is the density of the medium; Δρ is the density contrast across the interface.

5.3 Results and Discussion

5.3.1 Sensitivity analysis with 5 degrees of freedom

In this section we will study the AVO response before and after steam injection. In the case of the pre steam injection, we only study the boundary between the top of the reservoir and the reservoir. For the post injection case, we study the AVO response at the top of the steam, which is assumed to be the top of the reservoir, and at the bottom of the steam chamber. We define the bottom of the steam when steam saturation is zero to be where the bottom of the steam would have been if steam were present. This is because we want to test the sensitivity of the dependent variables, which are the intercept and gradient of the AVO, to the presence of steam or the lack of it.

5.3.1.1 Pre steam injection

The intercept and gradient of the Aki-Richards approximation of the AVO equation, shown in Table 5.2, were calculated using pre steam injection conditions. The range of each factor is summrized in Table 1. For the case of temperature, we assumed the highest surface temperature to be 50°C. The temperature gradient is 25°C/km and steam injection is used for reservoirs that are less than 1 km deep making the highest ambient temperature in a reservoir at this depth to be about 75°C. The effective pressure is equal to the lithostatic pressure minus the pore pressure (Fossen, 2016). The lithostatic pressure (P_l) is calculated using Equation 5.4.

$$P_l = \rho . g . h \qquad (5.4)$$

Assuming an average overburden density of 2300 kg/m^3, g = 9.81 m/s^2 and depths of 40 and 1000 m, the lithostatic pressure range would be 0.9-22.5 MPa.

The pore pressure can be calculated using Equation 5.4 assuming the pore pressure is equal to the hydrostatic pressure. Using the density of water instead of a typical rock and the same depth range as we did for the lithostatic pressure, we find that the range of pore pressure is 0.4-10 MPa. Therefore, the range of effective pressure is about 0.5-13 MPa. We assume that the upper limit of porosity is 38% rather than 45% because the critical porosity in the rock physics model is %38, which makes it not applicable for cases where the porosity is higher than 38%.

Treatment name	Factors					Intercept	Gradient
	A (temp=0/ 75°C)	B (porosity= 15/38%)	C (pressure= 0.5/13MPa)	D (brine sat=0/100%)	E API (8°-25°)		
1	-	-	-	-	-	0.0135	0.4026
a	+	-	-	-	-	-0.0297	0.3488
ab	+	+	-	-	-	-0.2871	0.5137
abc	+	+	+	-	-	-0.2164	0.443
abcd	+	+	+	+	-	-0.2064	0.4467
abcde	+	+	+	+	+	-0.2064	0.4467
ac	+	-	+	-	-	0.0782	-0.0199
ad	+	-	-	+	-	-0.015	0.3667
ae	+	-	-	-	+	-0.0625	0.3174
abd	+	+	-	+	-	-0.2639	0.5281
abe	+	+	-	-	+	-0.3409	0.4981
acd	+	-	+	+	-	0.0823	-0.012
ace	+	-	+	-	+	0.0612	-0.0403
ade	+	-	-	+	+	-0.015	0.3667
b	-	+	-	-	-	-0.2172	0.5513
bc	-	+	+	-	-	-0.1602	0.4784
bcd	-	+	+	+	-	-0.2064	0.4467
bce	-	+	+	-	+	-0.201	0.4554
bcde	-	+	+	+	+	-0.2064	0.4467
bd	-	+	-	+	-	-0.1804	0.4364
bde	-	+	-	+	+	-0.1804	0.4364
be	-	+	-	-	+	-0.2697	0.5313
c	-	-	+	-	-	0.1019	0.0311
cd	-	-	+	+	-	0.0823	-0.012
cde	-	-	+	+	+	0.0823	-0.012
ce	-	-	+	-	+	0.0847	-0.0031
d	-	-	-	+	-	-0.015	0.3667
de	-	-	-	+	+	-0.015	0.3667
e	-	-	-	-	+	-0.0177	0.3664
acde	+	-	+	+	+	0.0823	-0.012
abde	+	+	-	+	+	-0.2639	0.5281
abce	+	+	+	-	+	-0.2549	0.4247

Table 5.2: All combinations of five factors and the corresponding AVO intercept and gradient for the pre steam injection case.

Factors in order of most influencial on the AVO intercept and gradient are shown using Pareto charts in Figures 5.1 and 5.2, respectively. The AVO intercept is most sensetive to porosity followed by effective pressure then temperature. On the other hand, AVO gradient is most sensitive to porosity then effective pressure

followed by a combination of both while temperature has negligeble effect on the gradient. Brine saturation and oil API have negligible effect on both the AVO intercept and gradient because the physical properties of brine and oil are similar and the brine is in liquid phase.

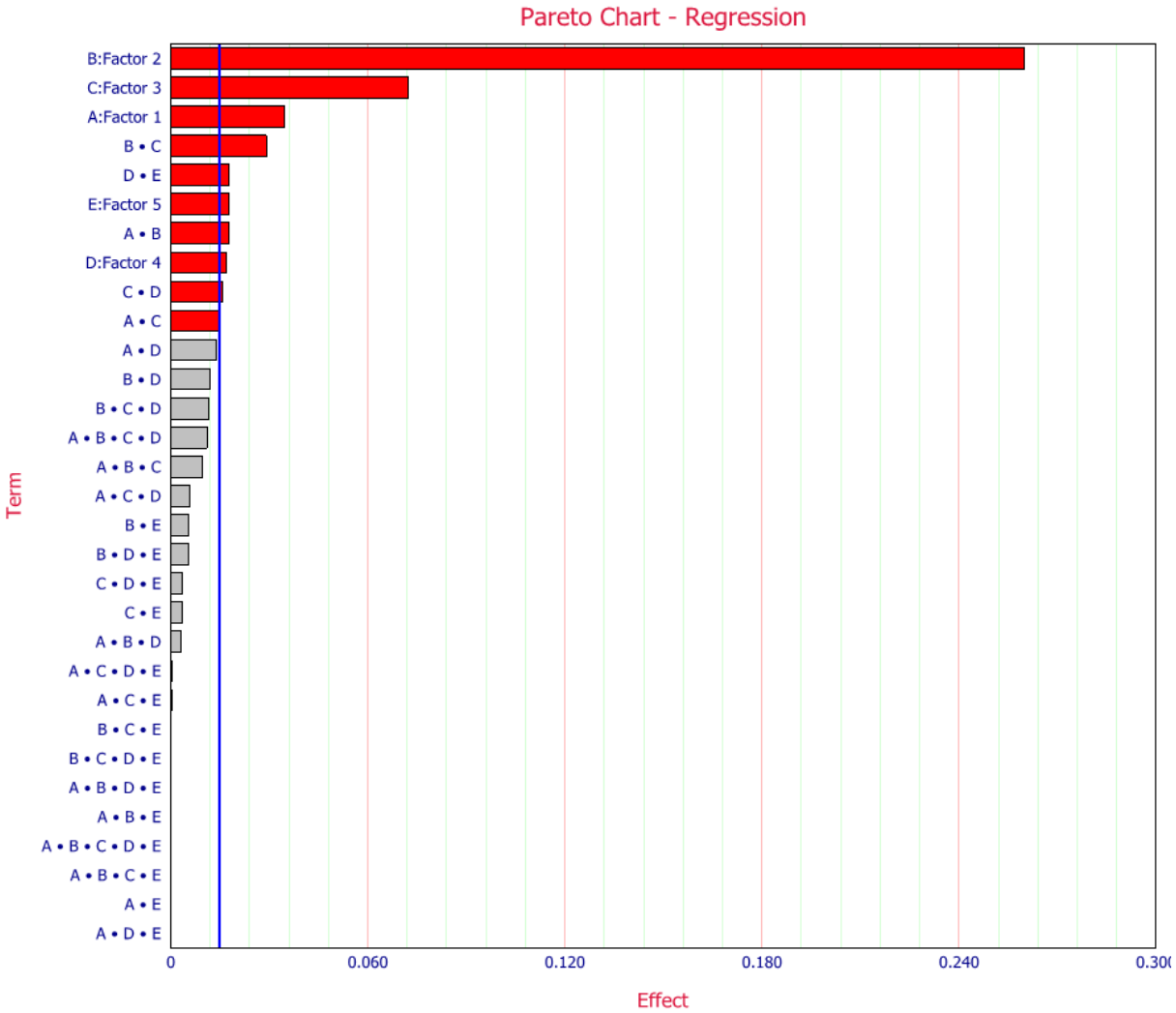


Figure 5.1: Pre steam injection Pareto chart for AVO intercept.

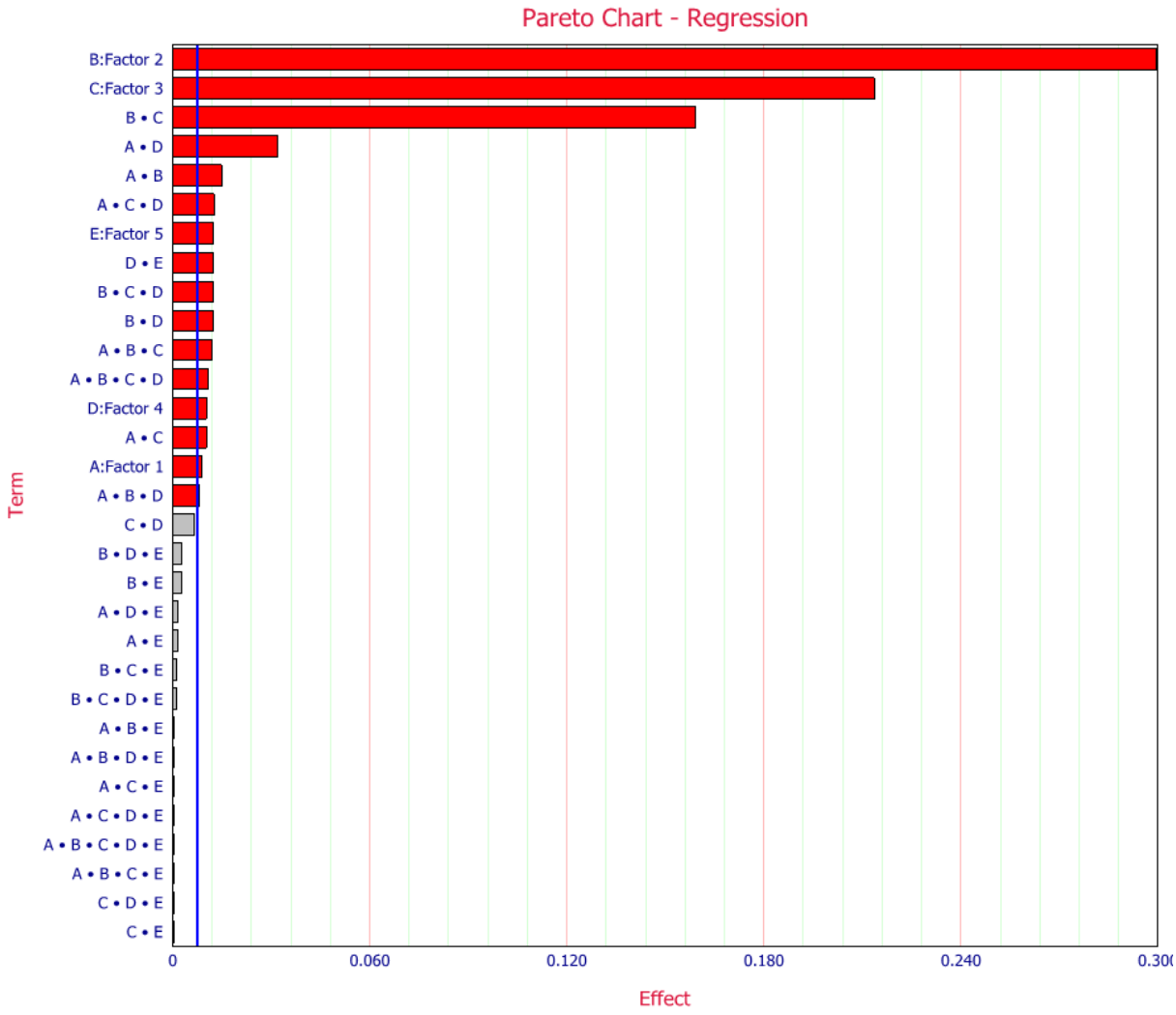


Figure 5.2: Pre steam injection Pareto charts for AVO gradient.

The effects of temperature, porosity, pressure, brine saturation and oil API on the AVO intercept and gradient are shown in Figures 5.3 and 5.4, respectively. The AVO intercept is not very sensitive to temperature changes because steam is not present at the range of 0-75°C. However, temperature affects the intercept more than it does the gradient. The magnitude of the AVO intercept increases with increasing temperature in the pre steam injection case mainly due to the decrease in viscosity of the oil in the pore space. Brine saturation and oil API has the least effect on both the AVO intercept and gradient for the ranges specified in Table 1. The magnitude of the AVO intercept decreases with increasing brine saturation because brine is usually denser than oil causing the contrast in P-wave velocities between the reservoir and

the overburden to become smaller. This is assuming that only brine and oil occupy the pore space. A decrease in contrast also occurs when the effective pressure of the reservoir increases. The AVO intercept shifts polarity from positive to negative with increasing porosity. This is due to the fact that at low porosities the P wave velocity of the seismic wave is larger than the overburden, which results in the positive intercept for the AVO reflection. The amplitude of reflected seismic waves always increase with increasing angle of incidence as more energy of the incident wave is reflected rather than transmitted at the interface between the reservoir and the overburden.

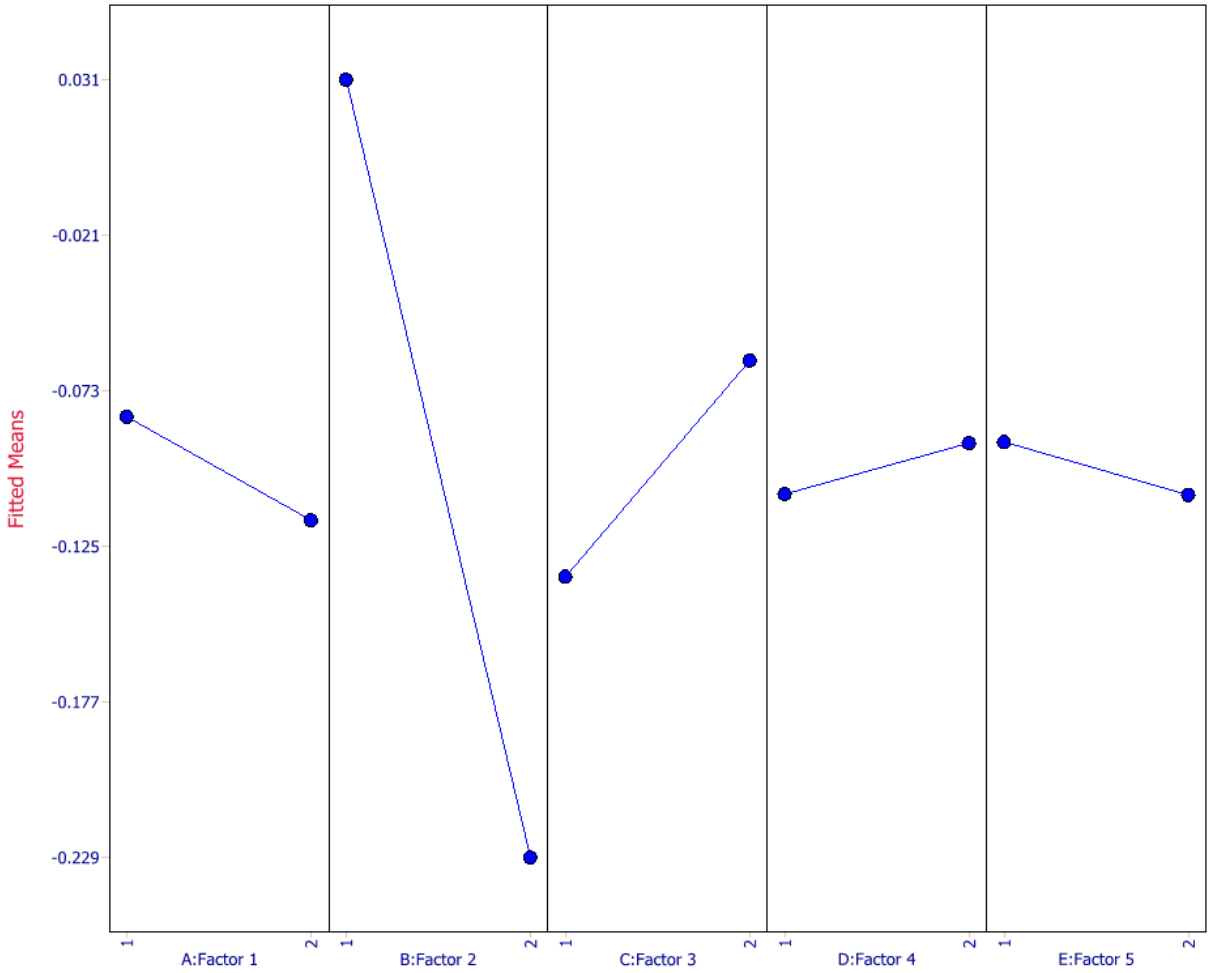


Figure 5.3: Term effect of temperature, porosity, pressure, brine saturation and oil API on the AVO intercept in the pre steam injection case.

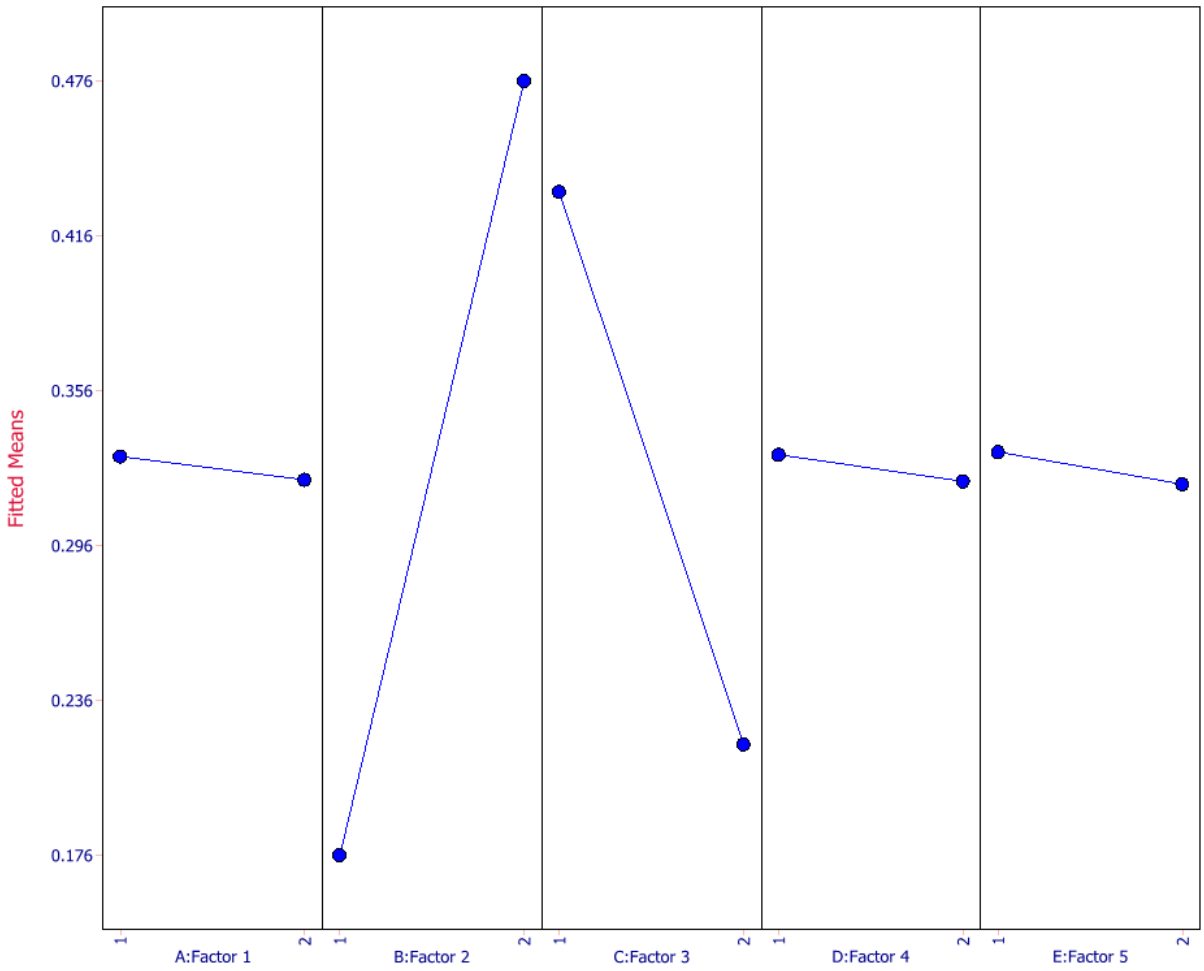


Figure 5.4: Term effect of temperature, porosity, pressure, brine saturation and oil API on the AVO gradient in the pre steam injection case.

Results obtained from the two-term effect plots shown in Figures 5.3 and 5.4 are combined and summarized in Figure 5.5. This plot shows how the intercept and gradient points move on the plot as we change the values of each parameter from low to high values, which are represented by blue and red, respectively. Points representing temperature, brine saturation and oil API are clustered in a small area of the forth quadrant of the plot, which indicates that both the AVO intercept and gradient are not as sensitive to these parameters. Temperature and pressure have opposite effects on the AVO intercept. This occurs because as temperature increases in the reservoir, the contrast in seismic wave velocity between the reservoir and the overburden increases and vice versa. On the other hand, as the effective pressure in the reservoir increases, or as the pore pressure decreases by injecting

less steam or increasing production, the contrast in seismic wave velocity between the reservoir and the overburden decreases and vice versa.

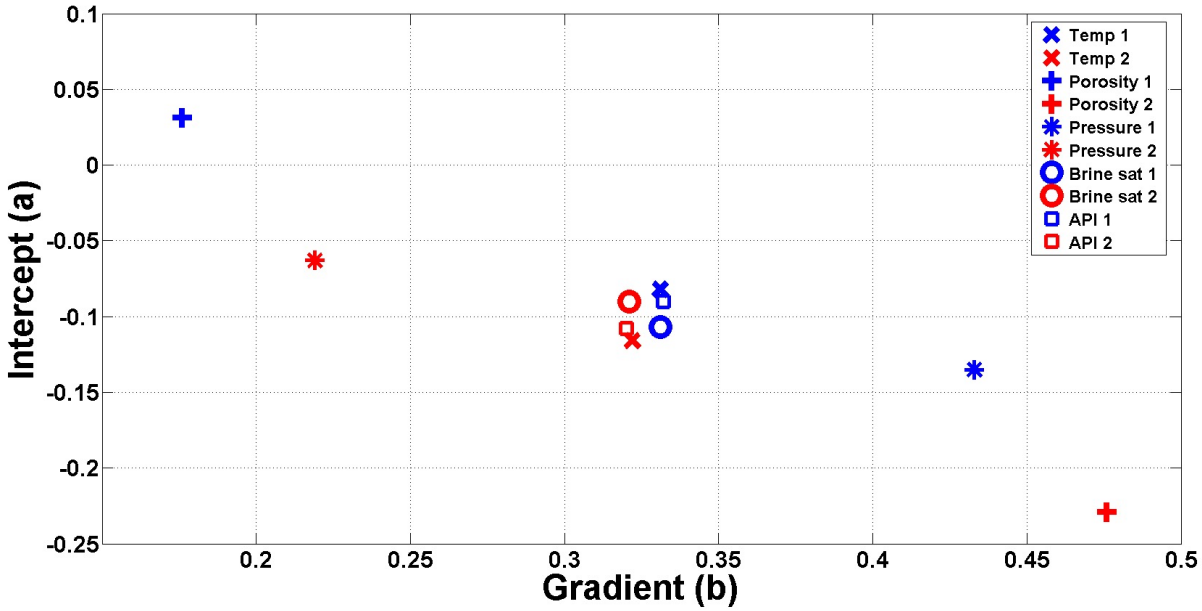


Figure 5.5: AVO intercept versus gradient for low and high values of temperature, porosity, effective pressure, brine saturation and oil API in the pre steam injection case.

The statistics of the multi variable linear regression along with the coefficients of the independent variables for the case of the intercept and gradient are shown in Table 5.3 and Table 5.4, respectively. The first part of the regression statistics table includes parameters that are indicative of the goodness of fit. They are indicative of how well the calculated linear regression equation fits the data. Multiple R is the correlation coefficient. It tells us how strong the linear relationship is. For example, a value of 1 means a perfect positive relationship and a value of zero means no relationship at all. R squared is the coefficient of determination. It tells us how many points fall on the regression line. For example, 90% means that 90% of the variation of y-values around the mean are explained by the x-values. In other words, 90% of the values fit the model. The adjusted R square adjusts for the number of terms in a model. This is used instead of R squared if there is more than one x variable, which is the case here. Standard error of the regression is an estimate of the standard

deviation of the error. This is not the same as the standard error in descriptive statistics. The standard error of the regression is the precision of the regression coefficient. If the coefficient is large compared to the standard error, then the coefficient is probably different from 0. The number of observations in the sample is listed at the end.

The second part of the regression statistics table gives very specific information about the components chosen to include in the data analysis. Coefficients give us the least squares estimates, which are basically the coefficients of the independent variables. Standard Error is the least squares estimate of the standard error.

Regression Statistics		
Multiple R	0.981960257	
R Square	0.964245947	
Adjusted R Square	0.957370167	
Standard Error	0.029182579	
Observations	32	
	Coefficients	*Standard Error*
Intercept	0.187692331	0.018774478
A (temp=0/75°C)	-0.000461167	0.000137568
B (porosity=15/38%)	-0.011305435	0.000448591
C (pressure=0.5/13MPa)	0.005785	0.000825408
D (brine sat=0/100%)	0.0001705	0.000103176
E API (8°-25°)	-0.001043382	0.000606918

Table 5.3: Regression statistics for the AVO intercept in the pre steam injection case.

Regression Statistics		
Multiple R	0.911221555	
R Square	0.830324722	
Adjusted R Square	0.79769486	
Standard Error	0.092329858	
Observations	32	
	Coefficients	*Standard Error*
Intercept	0.118183643	0.059399988
A (temp=0/75°C)	-0.000120417	0.000435247
B (porosity=15/38%)	0.013016033	0.001419284
C (pressure=0.5/13MPa)	-0.0170865	0.002611483
D (brine sat=0/100%)	-0.000102688	0.000326435
E API (8°-25°)	-0.000731985	0.001920208

Table 5.4: Regression statistics for the AVO gradient in the pre steam injection case.

The adjusted R square value show that 95.7% and 79.7% of the values fit the model for the AVO incident and gradient, respectively. The regression model does a good job fitting the values of the intercept but it is not as good in fitting the gradient. However, the models in both cases do not correctly predict the values of the intercept and gradient when different values of the independent variables were used. This is probably due to the fact that the dependent variable was calculated at only two end points of each independent variable, which does not capture the full complexity of the model. We conclude that it is best to do the full calculation of the intercept and gradient and not to rely on the least squares estimates.

5.3.1.2 Post steam injection

The AVO intercept and gradient of the Aki-Richards approximation were calculated using post injection conditions for both the top and bottom of the steam chamber. Results and ranges of each factor is summrized in Table 5.5.

Treatment name	Factors					Intercept		Gradient	
	A (temp=100 /300°C)	B (porosity= 15/38%)	C (effective pressure=0.5 /13MPa)	D (steam sat=0/100%)	E API (8°-25°)	Top of steam	Bottom of steam	Top of steam	Bottom of steam
1	-	-	-	-	-	-0.0352	0.0184	0.3474	-0.0562
a	+	-	-	-	-	-0.1455	0.0684	0.2512	0.0758
ab	+	+	-	-	-	-0.4726	0.0992	0.4693	0.1594
abc	+	+	+	-	-	-0.3467	0.0582	0.392	0.0785
abcd	+	+	+	+	-	-0.413	0.1258	0.4277	0.0786
abcde	+	+	+	+	+	-0.4424	0.1305	0.4171	0.0816
ac	+	-	+	-	-	0.0187	0.0148	-0.1166	0.0639
ad	+	-	-	+	-	-0.2171	0.145	0.2309	0.1971
ae	+	-	-	-	+	-0.1722	0.0511	0.2362	0.0564
abd	+	+	-	+	-	-0.6249	0.3216	0.4909	0.6309
abe	+	+	-	-	+	-0.5212	0.0926	0.4644	0.1478
acd	+	-	+	+	-	-0.0239	0.0583	-0.144	0.0854
ace	+	-	+	-	+	0.0101	0.0147	-0.1283	0.0604
ade	+	-	-	+	+	-0.2162	0.1041	0.2296	0.1157
b	-	+	-	-	-	-0.2957	0.0166	0.5218	0.0283
bc	-	+	+	-	-	-0.2278	0.0171	0.4473	0.0044
bcd	-	+	+	+	-	-0.4426	0.245	0.4152	0.3547
bce	-	+	+	-	+	-0.2517	0.0312	0.4344	0.0225
bcde	-	+	+	+	+	-0.4431	0.2372	0.417	0.3247
bd	-	+	-	+	-	-0.6245	0.1318	0.4847	0.3895
bde	-	+	-	+	+	-0.6251	0.1135	0.4885	0.3231
be	-	+	-	-	+	-0.3306	0.0444	0.512	0.0587
c	-	-	+	-	-	0.0726	-0.0249	-0.0242	0.0126
cd	-	-	+	+	-	-0.0338	0.0876	-0.1594	0.1328
cde	-	-	+	+	+	-0.0326	0.0848	-0.1574	0.1278
ce	-	-	+	-	+	0.0599	-0.0127	-0.033	0.0315
d	-	-	-	+	-	-0.2176	0.2139	0.2292	0.4055
de	-	-	-	+	+	-0.2175	0.207	0.2293	0.3781
e	-	-	-	-	+	-0.0581	0.0349	0.3225	-0.0221
acde	+	-	+	+	+	-0.0202	0.0451	-0.1389	0.0672
abde	+	+	-	+	+	-0.6239	0.2489	0.4863	0.3372
abce	+	+	+	-	+	-0.3718	0.058	0.3846	0.0759

Table 5.5: All combinations of five factors and the corresponding AVO intercept and gradient at the top and bottom of the steam chamber for the post steam injection case.

The upper limit of temperature has been changed from 75°C to 300°C to reflect reservoir conditions after steam injection has begun. Brine saturation was replaced by steam saturation assuming that the remainder of the pore space is equally filled with brine and oil.

For the post injection case, we start by considering the top of the steam front. Factors most influencial on the AVO intercept and gradient for the top of the steam front are shown using Pareto charts in Figures 5.6 and 5.7, respectively. The order of parameters from most to least influencial on the AVO intercept is porosity, effective pressure, steam saturation, then temperature. Gradient is most sensitive to porosity then effective pressure followed by a combination of both.

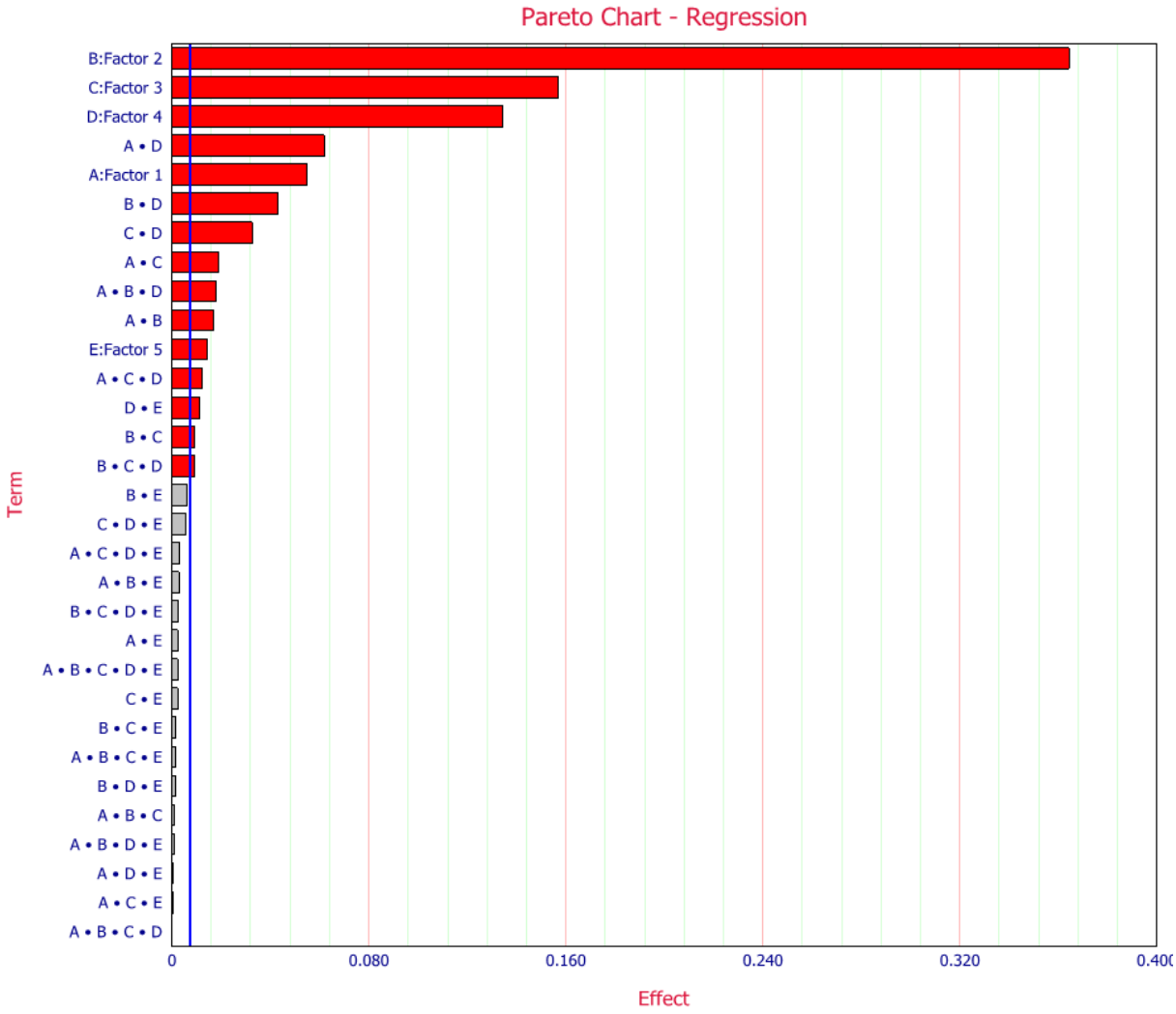


Figure 5.6: Top of steam chamber Pareto chart for AVO intercept.

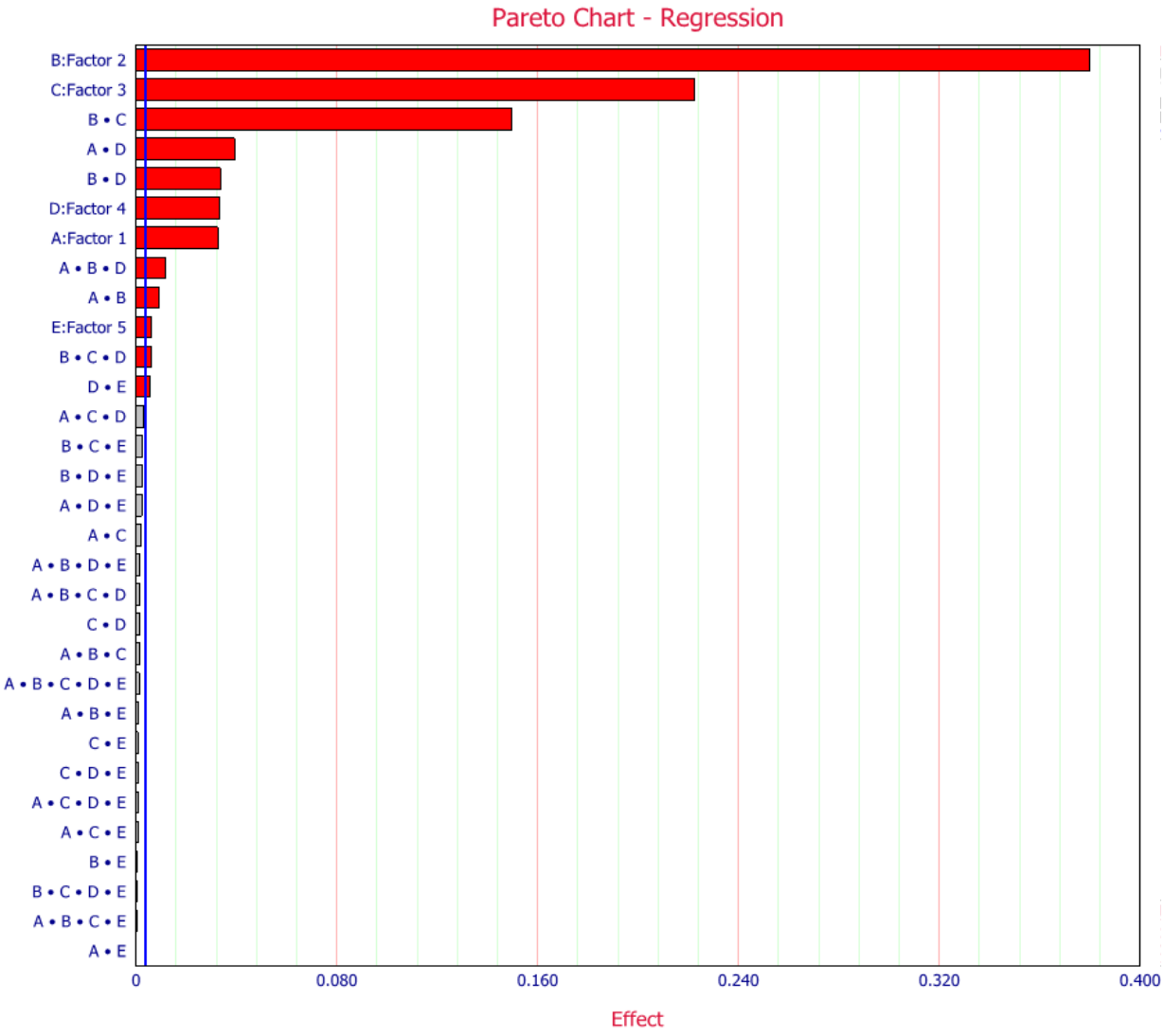


Figure 5.7: Top of steam chamber Pareto chart for AVO gradient.

The effects of temperature, porosity, pressure, brine saturation and oil API on the AVO intercept and gradient are shown in Figures 5.8 and 5.9, respectively. Temperature and oil API has the least effect on both the AVO intercept and gradient for the ranges specified in Table 5.5. Steam saturation has negligeble effect on the gradient as shown in Figure 5.9. Therefore, the AVO procedure used in determining the bottom of the steam chamber, which will be developed later in this chapter is not useful in detecting the top of the steam chamber because the gradient of the AVO in this case is not sensitive to changes in steam saturation.

The magnitude of the AVO intercept increases with increasing steam saturation because increasing steam saturation causes the contrast in P-wave velocities between the reservoir and the overburden to become larger. A decrease in the magnitude of the AVO intercept occurs when the effective pressure of the reservoir increases because the contrast in P-wave velocity between the reservoir and the overburden decreases. The amplitude of reflected seismic waves always increase with increasing angle of incidence as more energy of the incident wave is reflected rather than transmitted at the interface between the reservoir and the overburden.

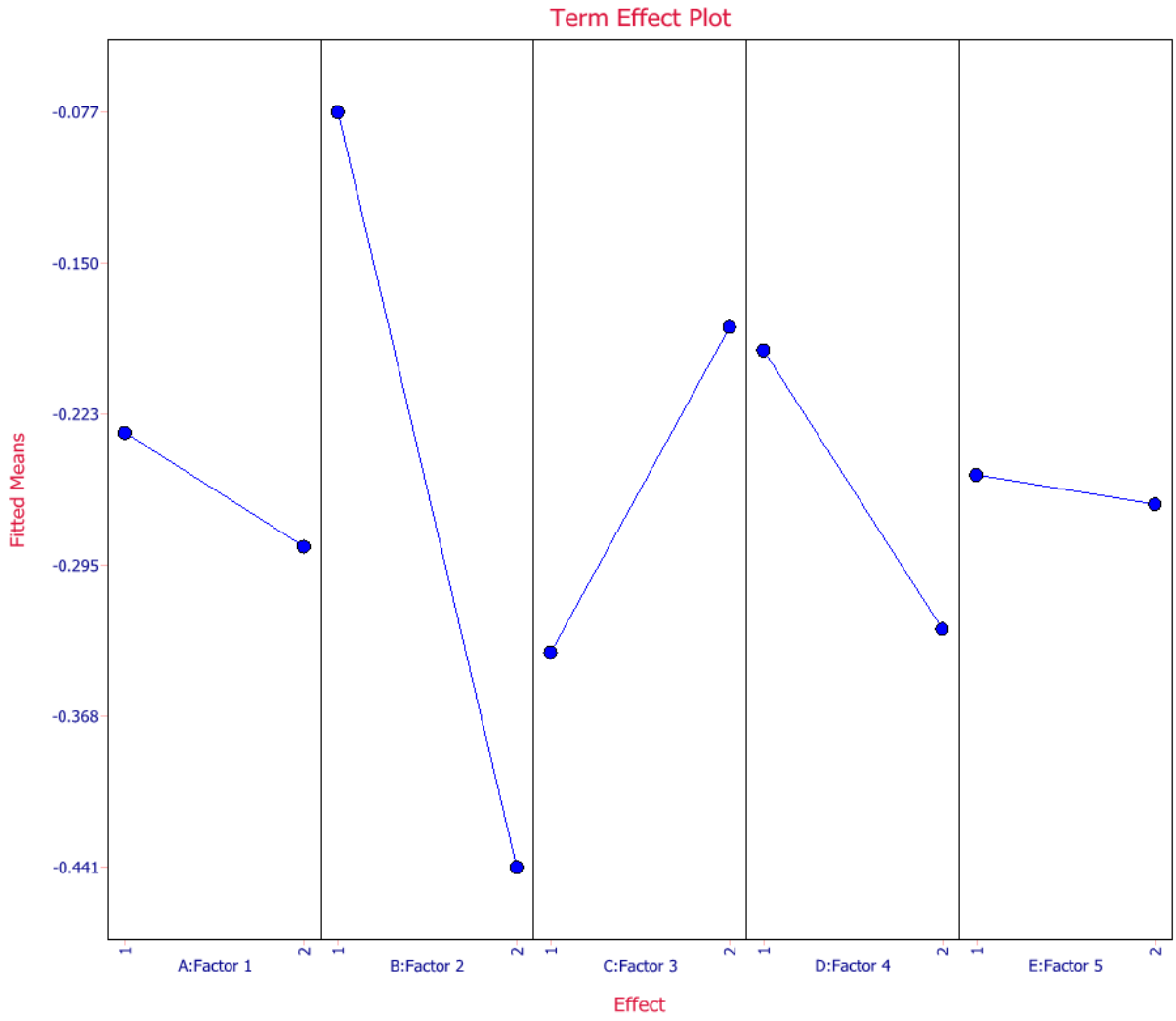


Figure 5.8: Term effect of temperature, porosity, pressure, brine saturation and oil API on the AVO intercept at the top of the steam chamber in the post steam injection case.

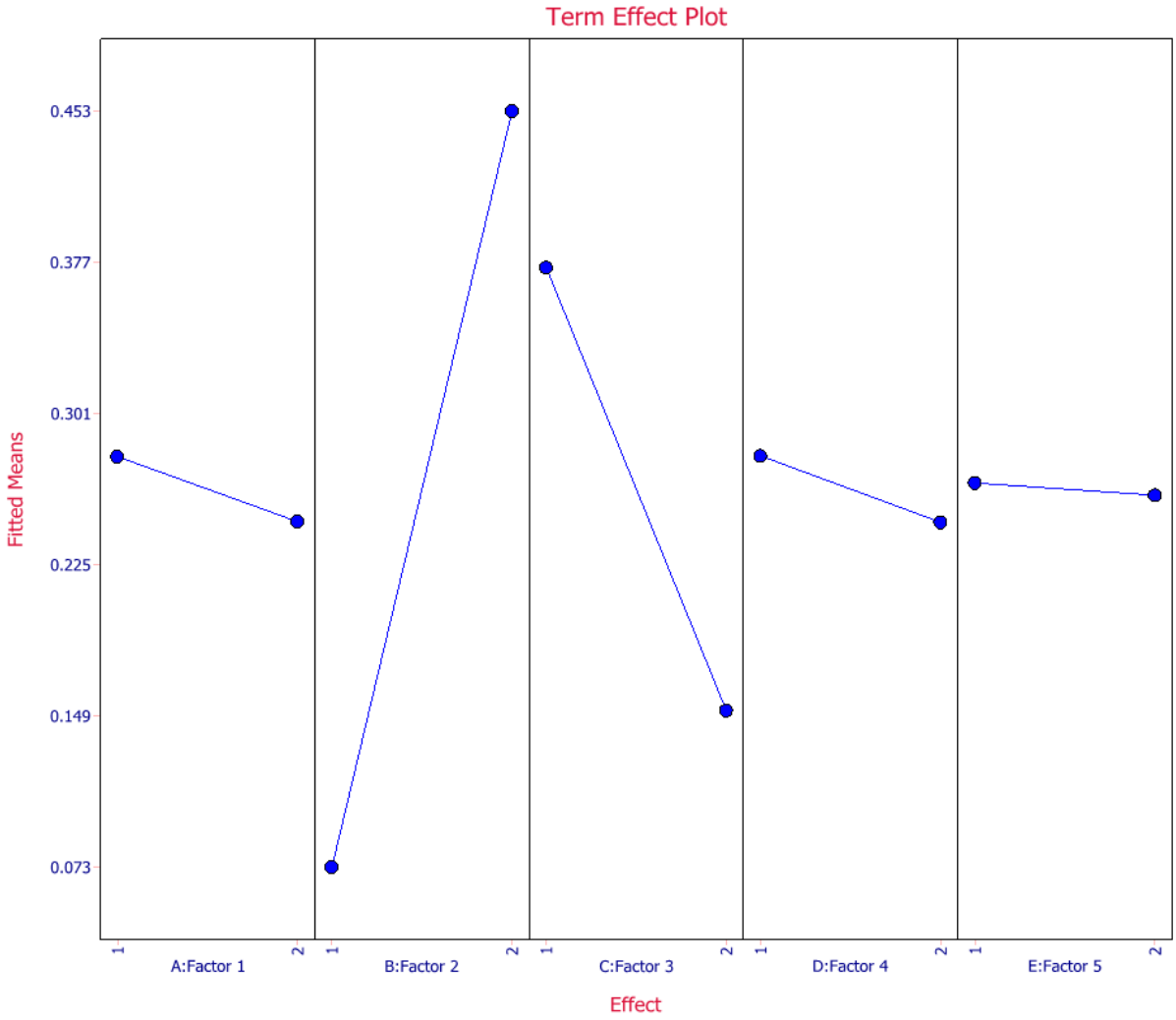


Figure 5.9: Term effect of temperature, porosity, pressure, brine saturation and oil API on the AVO gradient at the top of the steam chamber in the post steam injection case.

Amplitude versus offset results for the intercept versus gradient is shown in Figure 5.10. Results are similar to the pre injection case shown in Figure 5.5 with a few differences. There is no polarity shift in the intercept for the range of porosities considered in the post injection case. Temperature has a wider range causing a more spread out results for both intercept and gradient. AVO Intercepts tend to have a larger magnitude while AVO gradients tend to have a slightly smaller magnitude compared to the pre steam injection case.

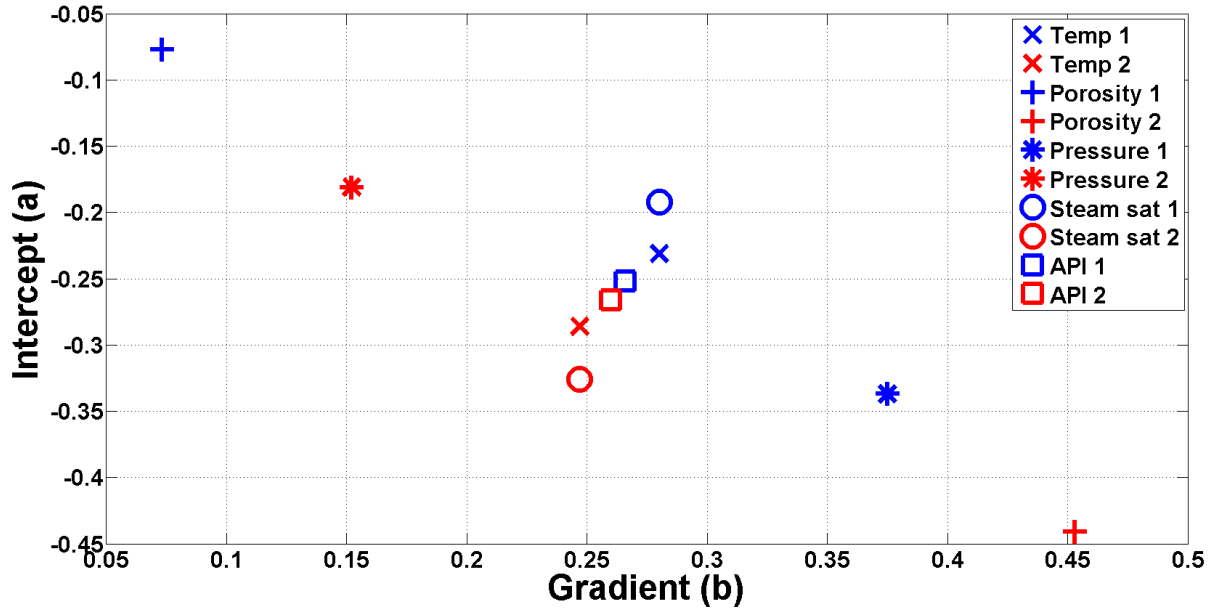


Figure 5.10: AVO intercept versus gradient for low and high values of temperature, porosity, effective pressure, brine saturation and oil API for the top of the steam chamber in the post steam injection case.

The statistics of the multi variable linear regression along with the coefficients of the independent variables for the case of the intercept and gradient at the top of the steam chamber are shown in Table 5.6 and Table 5.7, respectively. Details of what the different terms mean has been explained in section 5.3.1.1.

Regression Statistics		
Multiple R	0.977569364	
R Square	0.955641861	
Adjusted R Square	0.947111449	
Standard Error	0.050507472	
Observations	32	
	Coefficients	*Standard Error*
Intercept	0.212047579	0.035986114
A (temp=100/300°C)	-0.000274813	8.92854E-05
B (porosity=15/38%)	-0.015839674	0.000776395
C (effective pressure=0.5/13MPa)	0.012548	0.001428567
D (steam sat=0/100%)	-0.001344125	0.000178571
E API (8°-25°)	-0.000834559	0.001050417

Table 5.6: Regression statistics for the AVO intercept at the top of the steam chamber in the post steam injection case.

Regression Statistics		
Multiple R	0.94088063	
R Square	0.885256359	
Adjusted R Square	0.863190275	
Standard Error	0.088432295	
Observations	32	
	Coefficients	*Standard Error*
Intercept	0.001196483	0.063007205
A (temp=100/300°C)	-0.000163406	0.000156328
B (porosity=15/38%)	0.016518207	0.001359371
C (effective pressure=0.5/13MPa)	-0.0178035	0.002501243
D (steam sat=0/100%)	-0.000333938	0.000312655
E API (8°-25°)	-0.000364338	0.001839149

Table 5.7: Regression statistics for the AVO gradient at the top of the steam chamber in the post steam injection case.

The adjusted R square value show that 94.7% and 86.3% of the values fit the model for the AVO incident and gradient at the top of the steam chamber, respectively. The regression model does a good job fitting the values of both the intercept and the gradient. However, the models in both cases do not correctly predict the values of the intercept and gradient when different values of the independent variables were used. This is probably due to the fact that the dependent variable was calculated at only two end points of each independent variable, which does not capture the full complexity of the model. Therefore, it is best to do the full calculation for the intercept and gradient and not to rely on the least squares estimates.

We have looked at the boundary between the top of the steam chamber and the overburden. Next, we will study the behaviour of the AVO intercept and gradient at the boundary between the bottom of the steam chamber and the reservoir that it occupies. These values can be found in Table 5.5. We define the bottom of the

steam chamber as the last grid cell in the simulation with nonzero steam saturation. The grid cell beneath it always has a steam saturation value of zero. Factors most influential on the AVO intercept and gradient for the bottom of the steam chamber are shown using Pareto charts in Figures 5.11 and 5.12, respectively. Unlike the case at the top of the steam chamber, the order of parameters from most to least influential on the AVO intercept is steam saturation, porosity followed by effective pressure. In the case of the AVO gradient the order is steam saturation, effective pressure then porosity. Porosity is less effective than it was at the top of the steam chamber because we assume that the porosity is uniform across the reservoir, which was not the case when we considered the boundary between the top of the steam and the overburden. Temperature and oil API on their own have negligible effect on both the AVO intercept and gradient.

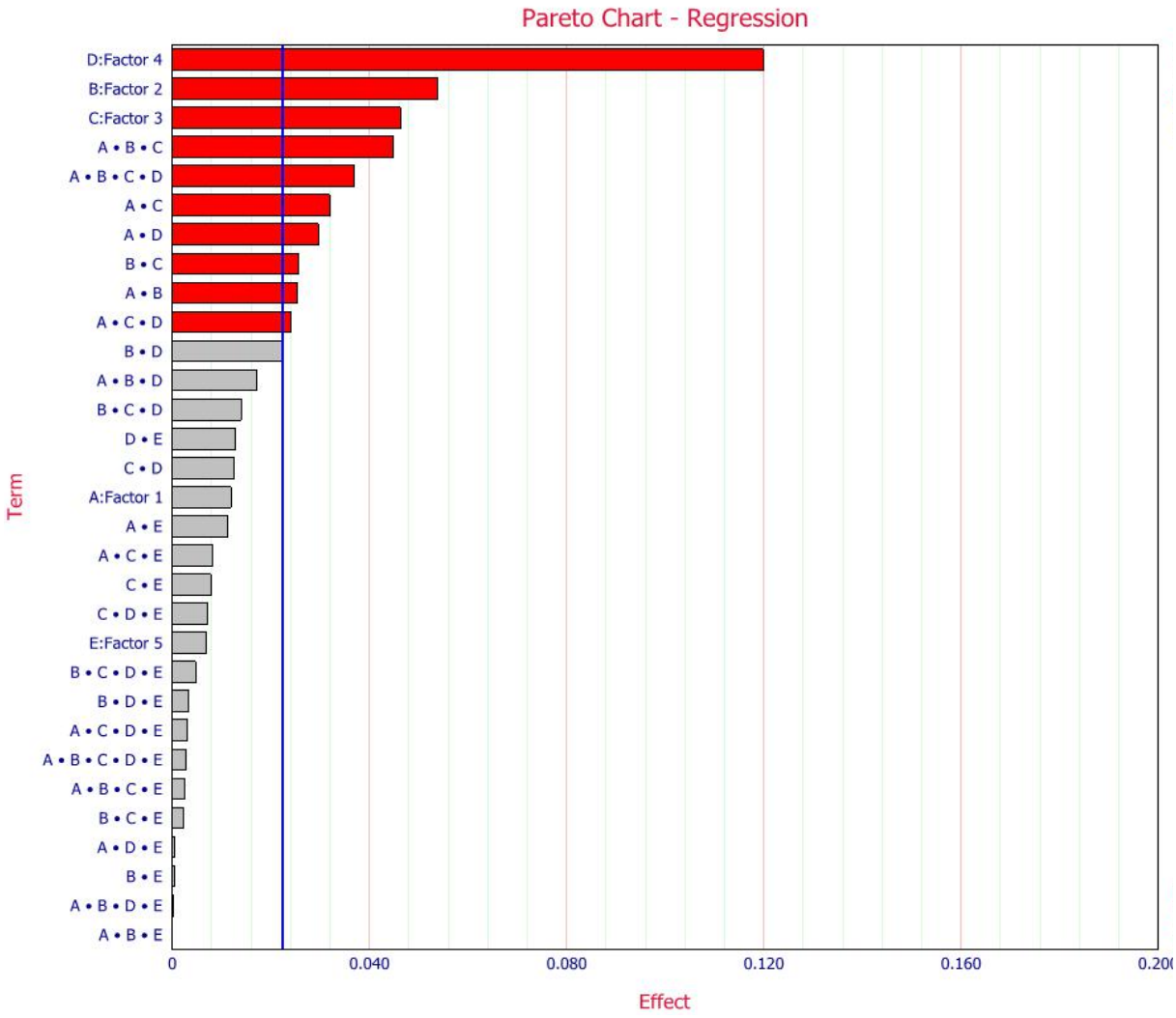


Figure 5.11: Bottom of steam chamber Pareto chart for AVO intercept.

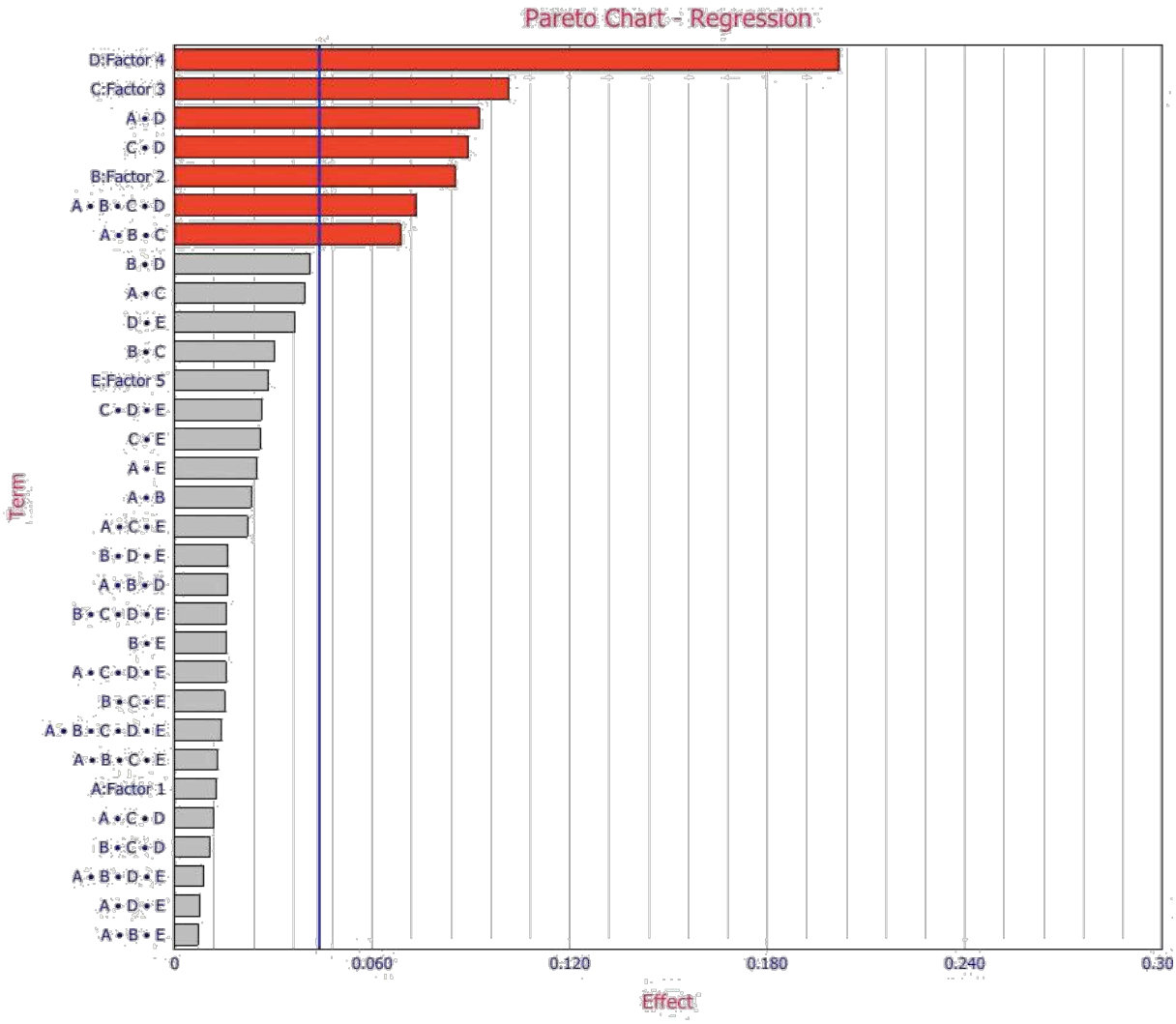


Figure 5.12: Bottom of steam chamber Pareto chart for AVO gradient.

The effects of temperature, porosity, effective pressure, brine saturation and oil API on the bottom of steam AVO intercept and gradient are shown in Figures 5.13 and 5.14, respectively. Higher steam saturations increase both the intercept and gradient significantly which can help to delineate the bottom part of the steam chamber. Larger values of porosity have to a lesser extent the same effect as the steam saturation. An increase in the effective pressure has the opposite effect as it decreases the contrast at the boundary between the bottom of the steam and the reservoir. Temperature increase slightly increases the intercept while slightly decreasing the gradient. Lighter oil in the pore space results in a slightly lower intercept and gradient.

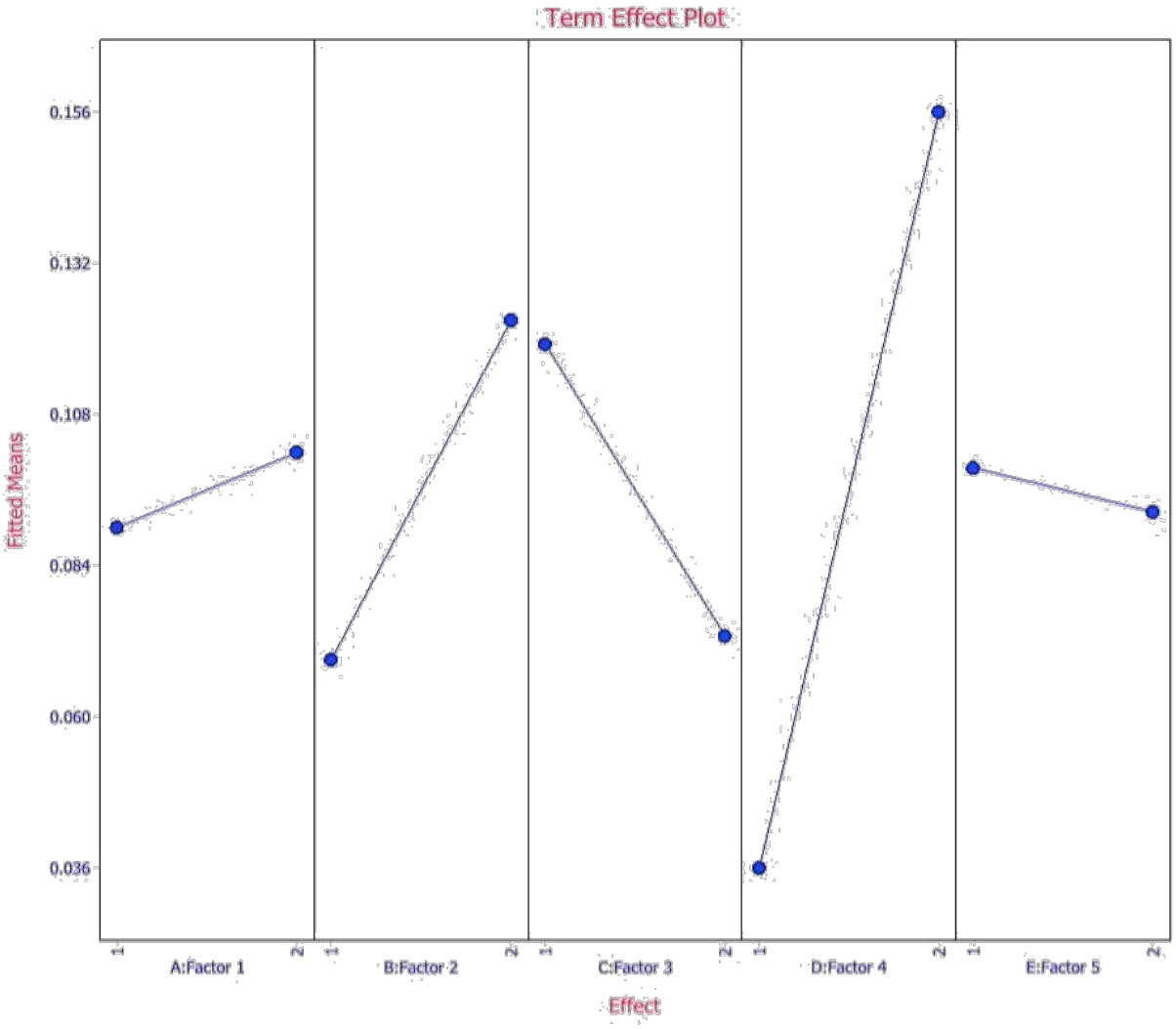


Figure 5.13: Term effect of temperature, porosity, pressure, brine saturation and oil API on the AVO intercept at the bottom of the steam chamber in the post steam injection case.

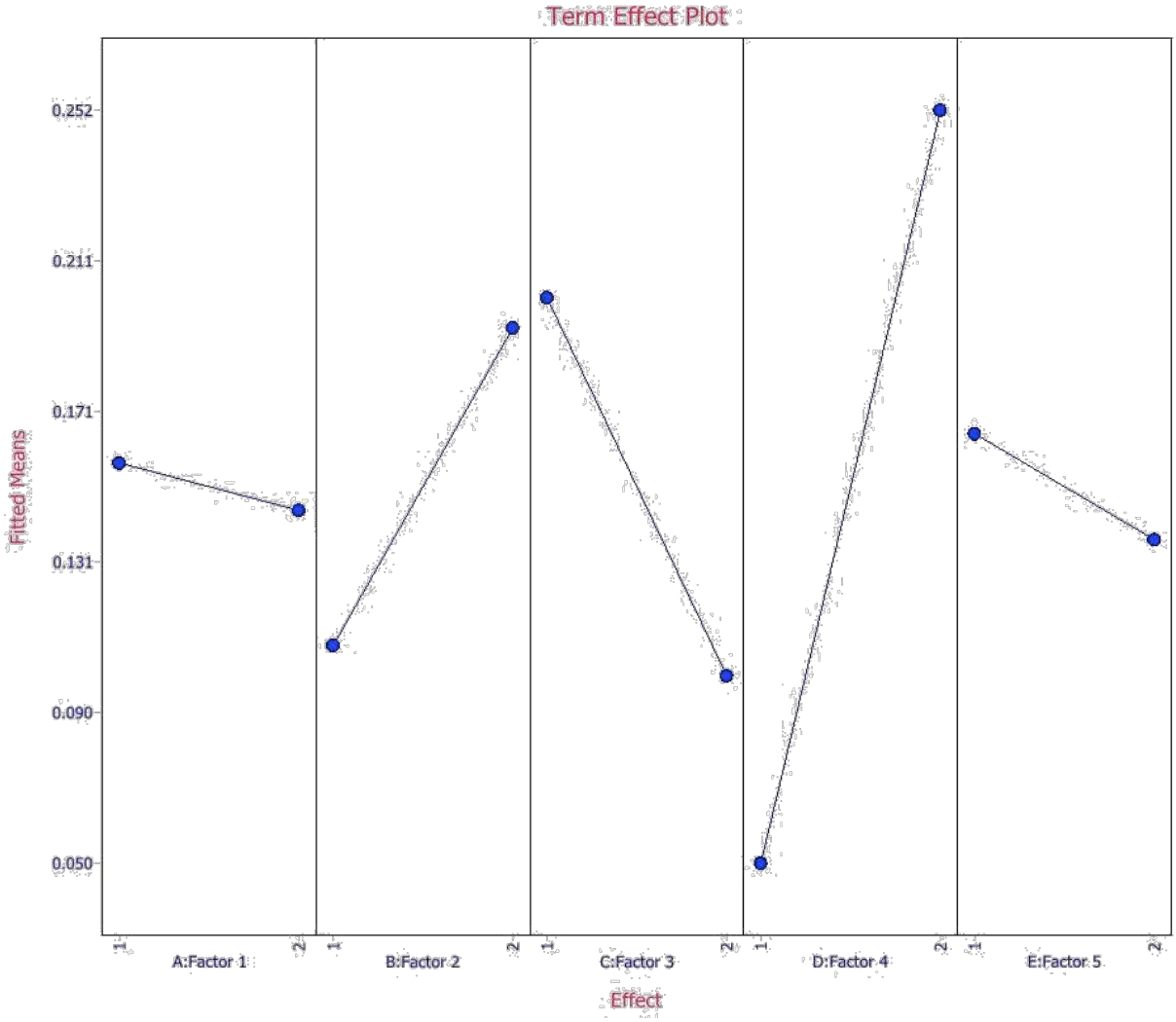


Figure 5.14: Term effect of temperature, porosity, pressure, brine saturation and oil API on the AVO gradient at the bottom of the steam chamber in the post steam injection case.

Amplitude versus offset results for the intercept versus gradient in the case of the bottom of the steam is shown in Figure 5.15. Results are different compared to the top of the steam chamber case. Most points on this plot are in the reverse order which is expected as we are moving from a steam saturated zone back to the reservoir with brine and oil occupying the pore space. Steam saturation has a larger effect on the intercept and gradient compared to porosity.

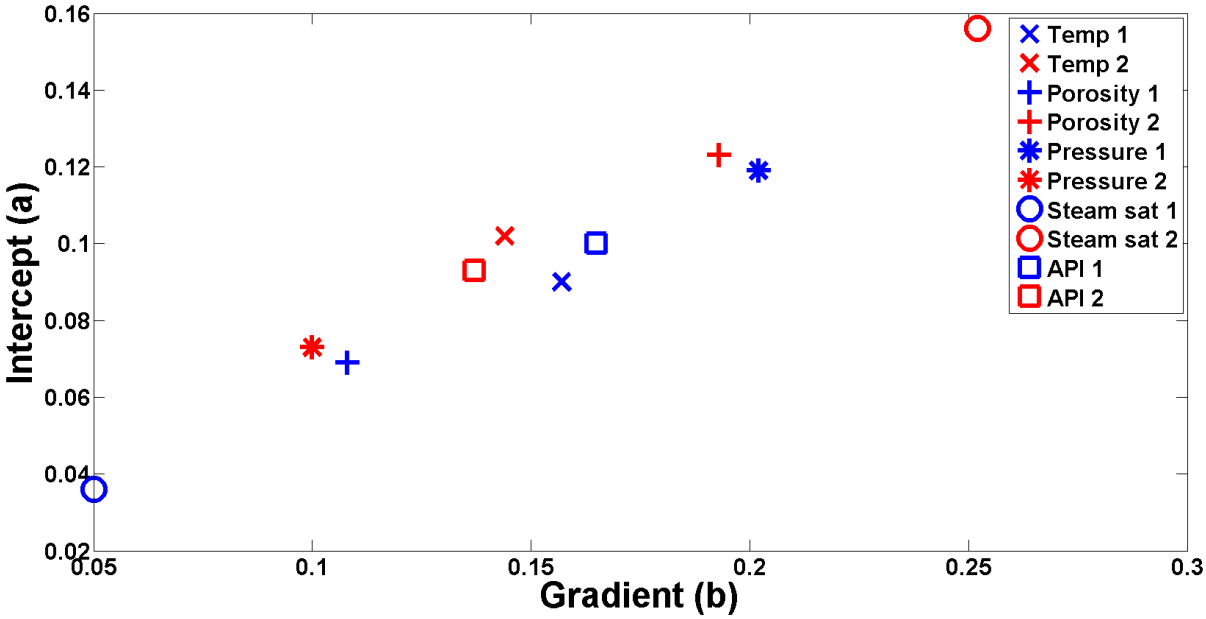


Figure 5.15: AVO intercept versus gradient for low and high values of temperature, porosity, effective pressure, brine saturation and oil API for the bottom of the steam chamber in the post steam injection case.

The statistics of the multi variable linear regression along with the coefficients of the independent variables for the case of the intercept and gradient at the bottom of the steam chamber are shown in Table 5.8 and Table 5.9, respectively. Details of what the different terms mean has been explained in section 5.3.1.1.

Regression Statistics		
Multiple R	0.830364969	
R Square	0.689505981	
Adjusted R Square	0.629795593	
Standard Error	0.052114614	
Observations	32	
	Coefficients	*Standard Error*
Intercept	-0.005777398	0.037131188
A (temp=100/300°C)	5.95313E-05	9.21265E-05
B (porosity=15/38%)	0.002339946	0.0008011
C (effective pressure=0.5/13MPa)	-0.0037035	0.001474024
D (steam sat=0/100%)	0.001198813	0.000184253
E API (8°-25°)	-0.000409926	0.001083841

Table 5.8: Regression statistics for the AVO intercept at the bottom of the steam chamber in the post steam injection case.

Regression Statistics		
Multiple R	0.782885077	
R Square	0.612909044	
Adjusted R Square	0.538468475	
Standard Error	0.107374416	
Observations	32	
	Coefficients	*Standard Error*
Intercept	0.046752154	0.076503294
A (temp=100/300°C)	-6.37813E-05	0.000189813
B (porosity=15/38%)	0.00370625	0.001650547
C (effective pressure=0.5/13MPa)	-0.0081135	0.003037007
D (steam sat=0/100%)	0.002020063	0.000379626
E API (8°-25°)	-0.001671691	0.002233093

Table 5.9: Regression statistics for the AVO gradient at the bottom of the steam chamber in the post steam injection case

The adjusted R square value show that 62.9% and 53.8% of the values fit the model for the AVO incident and gradient at the top of the steam chamber, respectively. The regression model does a poor job fitting the values of both the intercept and the gradient. In addition, the models in both cases do not correctly predict the values of the intercept and gradient when different values of the independent variables were used. This is probably due to the fact that the dependent variable was calculated at only two end points of each independent variable, which does not capture the full complexity of the model. Therefore, it is best to do the full calculation for the intercept and gradient and not to rely on the least squares estimates.

5.3.2 Using AVO to determine the thickness of steam chamber

We will analyse the intercept and gradient of the two-term Aki-Richards approximation of the AVO equation, which will lead us to a novel technique that helps

to delineate the steam chamber at and away from the steam injection well. In chapter 3, STARS was used for the reservoir simulation using a 2D grid comprised of 100×1×40 grid cells each measuring 5×10×2.5 ft where steam was injected on the left side while oil, brine and steam were produced from the right side of the grid. HampsonRussell software is used to calculate the intercept and gradient of the AVO approximation at every depth along the vertical cross section at a specific location in the model. The average P-wave velocity in the part of the reservoir with steam is about 2000 m/s, as will be shown in Figures 5.17, 5.20, 5.23, 5.30, 5.33, and 5.36. The frequencies of seismic waves used are 100 and 50 Hz, which results in wavelengths of 20m and 40m, respectively. Therefore, the tuning thickness of the seismic waves with dominant frequencies of 100 and 50 Hz is about $\lambda/4 = 20/4 = 5$m and $40/4 = 10$m, respectively. It is important to note that seismic waves with a dominant frequency of 100 Hz are very high for exploration seismology purposes yet we use it here only as a tool for comparison because it helps us to see the reservoir in higher resolution when the seismic waves with dominant frequency of 50 Hz is not enough to visually distinguish the bottom of the steam chamber. This will be helpful because at some instances we will not be able to recognize the bottom of the steam chamber visually using seismic waves with 50 Hz dominant frequency, yet our AVO procedure will enable use to pinpoint the approximate location of the bottom of the steam chamber. This is when we use seismic waves with 100 Hz dominant frequency to visually reconfirm that what our AVO procedure showed is indeed the bottom of the steam chamber.

This AVO procedure is applied to two different models for validation. The criteria for choosing which model to use to validate our AVO technique is that the steam tongue must vary in thickness from being larger to being smaller than the tuning thickness. The only two models from chapter 3 where this criterion is met is

the case where the horizontal permeability in both cases is 600mD while the vertical permeability is 60 mD in model A and 300 mD in model B with all other parameters set to the reference values listed in Table 3.5.

5.3.2.1 Validation using model A

Model A is taken from Chapter 3 and is namely the case where the horizontal permeability is 600 mD with all other parameters set to the reference value as per Table 3.5. The steam saturation after 10 years of steam flood corresponding to model A is shown in Figure 5.16.

We start by observing the steam thickness at location 1 in Figure 5.16, which corresponds to the vertical column at the 32nd grid cell of the cross-section in the x-axis. The thickness of the steam here is 50 ft and the last grid cell containing steam has a steam saturation of 36.01%. The corresponding elastic moduli showing the P- and S-wave velocities and densities are shown in Figure 5.17. These elastic moduli are used as input into HampsonRussell software, which calculates the intercept and gradient of the two-term Aki-Richards approximation of the AVO equation using seismic frequencies of 100 and 50 Hz as shown in Figures 5.18 and 5.19, respectively. The seismic trace produced by HampsonRussell software is basically the convolution of the reflection coefficient with the Ricker wavelet of the desired frequency. Ricker wavelet is used here because it is the standard wavelet used in exploration seismology (Gholamy & Kreinovich, 2014).

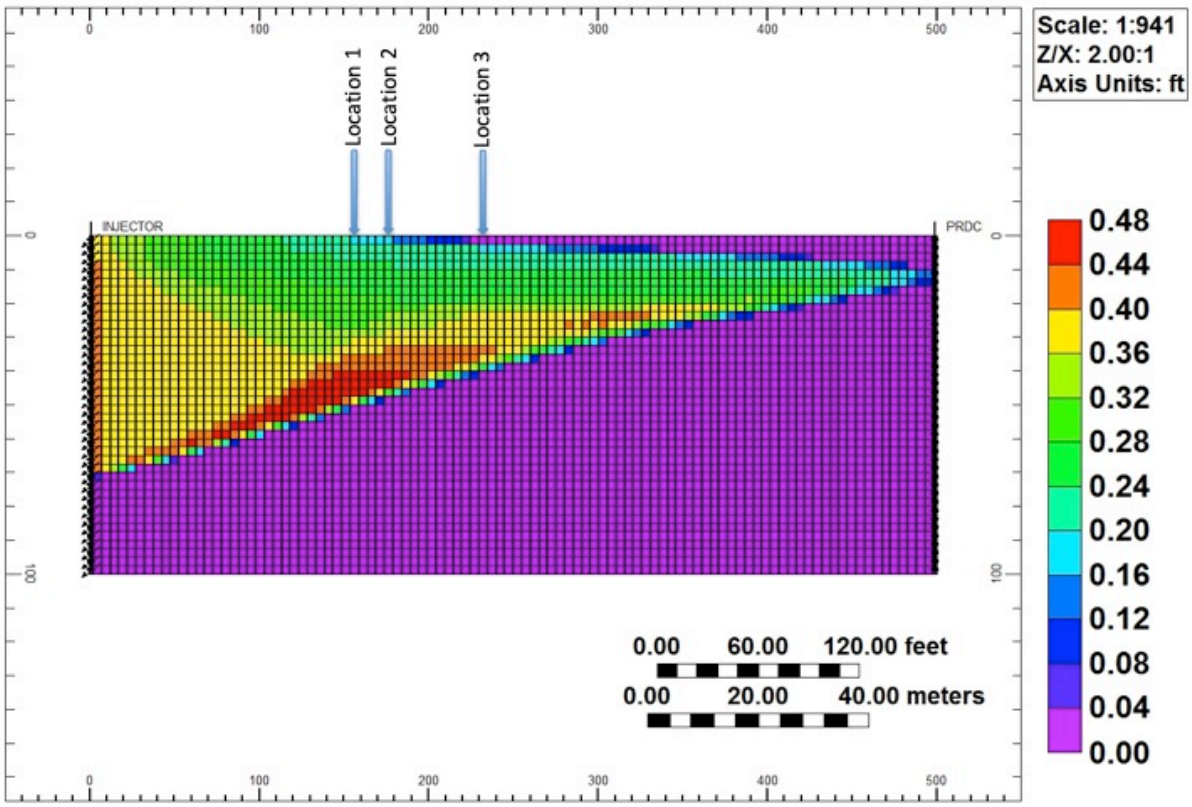


Figure 5.16: Model A: Cross-section showing steam saturation after 10 years of steam flood where the horizontal permeability is 600 mD while the other parameters are set to the reference value as per Table 3.5. Blue arrows mark the locations where steam thicknesses were studied. The injection well is to the left while the production well is to the right.

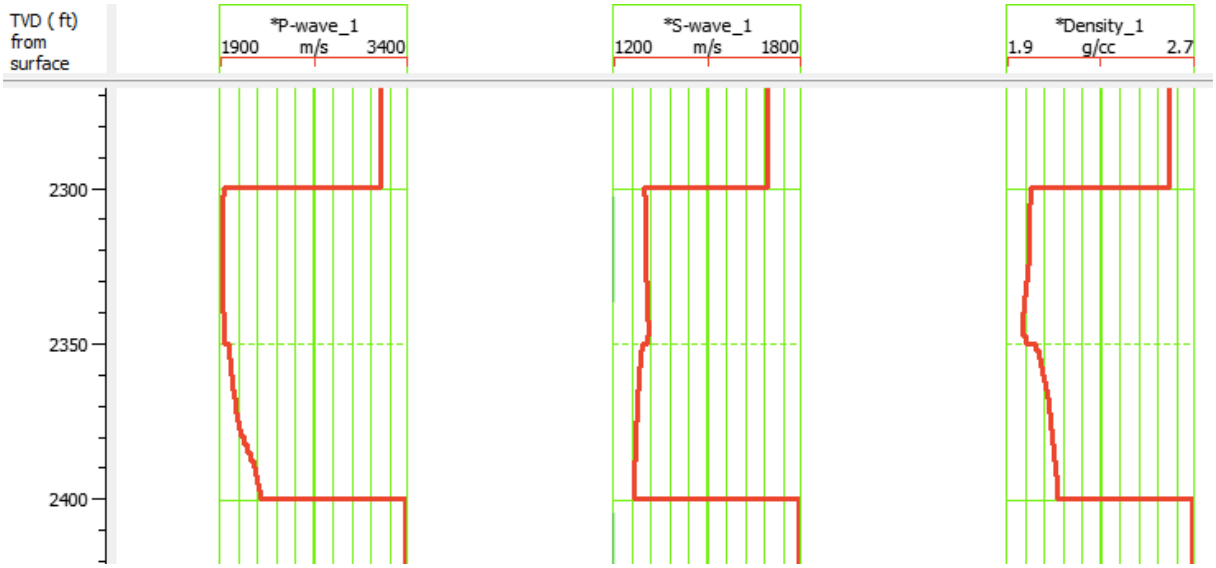


Figure 5.17: P- and S-wave velocities and densities at location 1 in model A calculated from the reservoir simulation results using the MATLAB rock physics code.

The boundary between the overlying formation and the top of the reservoir is represented by the first blue trough at the depth of 2300 ft as shown in Figure 5.18.

The side loop of this trough is the red peak just below, which we picked using the red event 1. The criterion for picking peaks in this AVO analysis study is to pick them at a depth where the amplitude of the AVO intercept is the greatest. The bottom of the steam is picked using the green event 2 at a depth of 2350 ft. The amplitude of the intercept is much smaller for the case of the bottom of the steam compared to the side loop of the top of the reservoir because the contrast in seismic impedance is much smaller in the case of the bottom of the steam. The AVO gradient is positive in the case of the bottom of the steam while it is negative for the side loop of the trough representing the top of the reservoir.

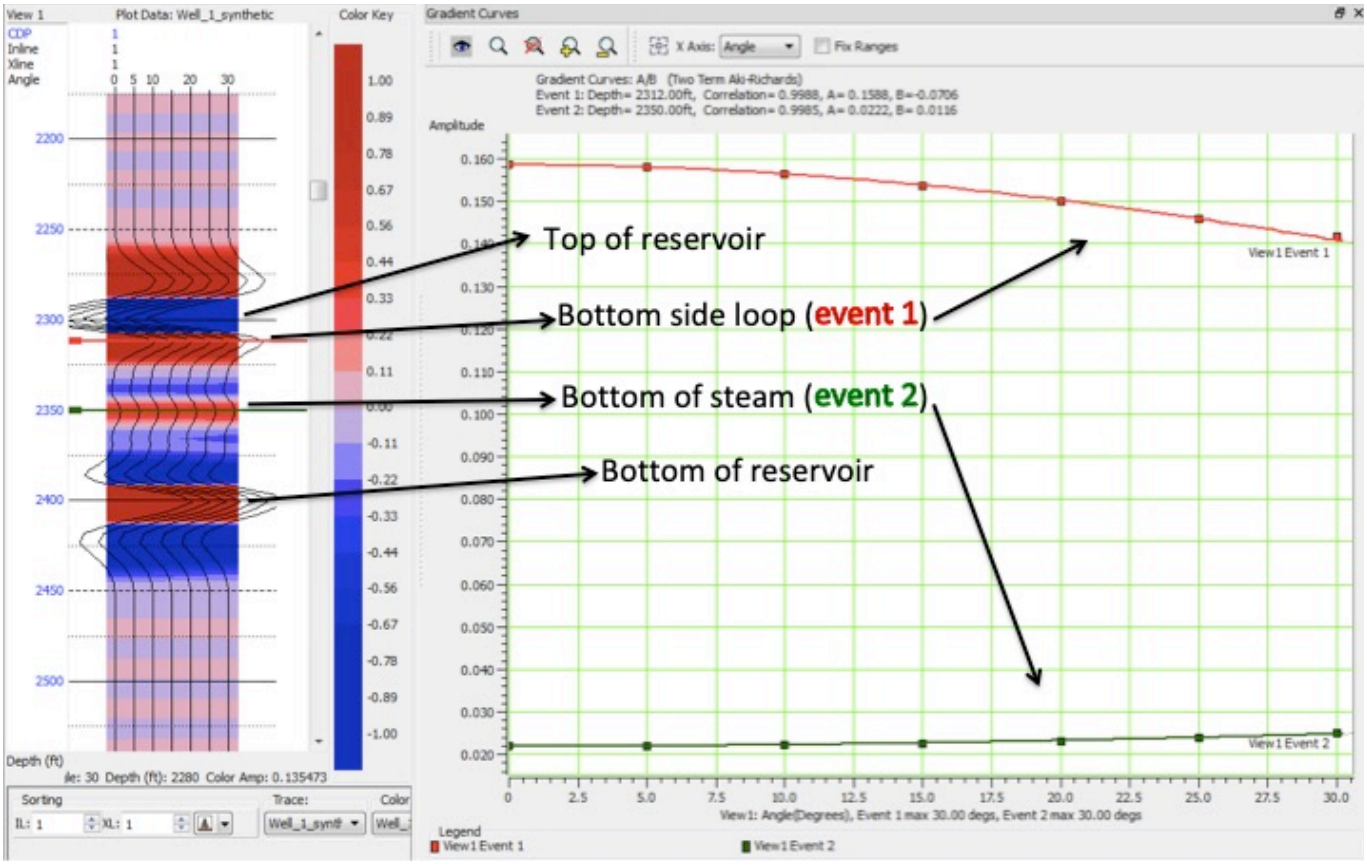


Figure 5.18: The intercept and gradient of the two-term Aki-Richards approximation of the AVO equation at location 1 in model A using a 100 Hz Ricker wavelet.

The peak representing the bottom of the steam tongue is still evident when using the 50Hz wavelet and it is picked using the green event 2 as shown in Figure

5.19. The reason the peak is harder to see is due to the fact that it starts to overlap with the side loops below and above it. However, we can still distinguish that it is the bottom of the steam because of its positive gradient and intercept. We will study the gradient of the AVO at other locations along the steam tongue to see if this behaviour is consistent.

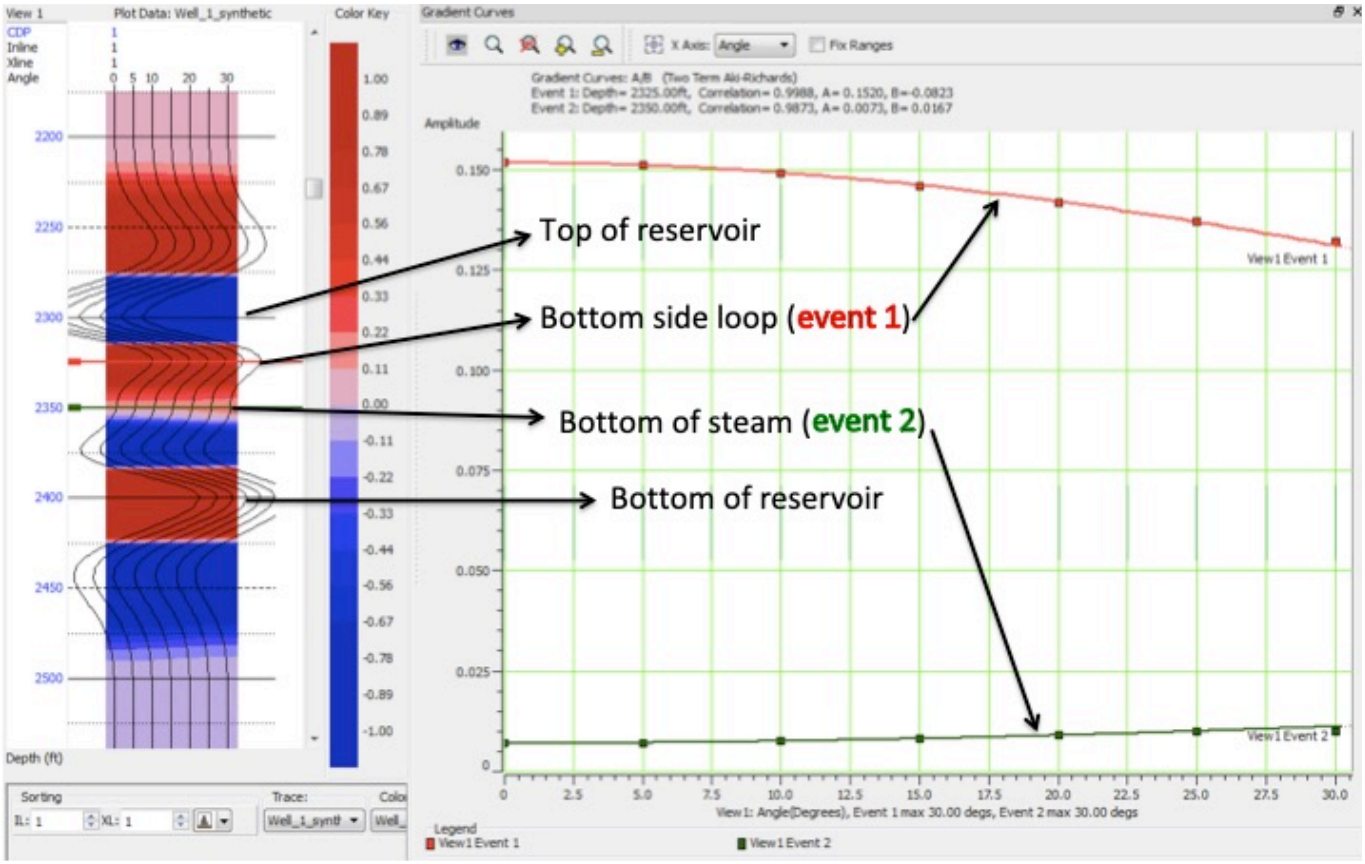


Figure 5.19: The intercept and gradient of the two-term Aki-Richards approximation of the AVO equation at location 1 in model A using a 50 Hz Ricker wavelet.

The second location in Figure 5.16 corresponds to the vertical column at the 36th grid cell of the cross-section in the x-axis. The thickness of the steam here is 47.5 ft and the last grid cell containing steam has a steam saturation of 30.6%. The corresponding elastic moduli showing the P- and S-wave velocities and densities are shown in Figure 5.20. The intercept and gradient of the two-term Aki-Richards approximation of the AVO equation are shown in Figure 5.21 and Figure 5.22 using seismic frequencies of 100 Hz and 50 Hz, respectively.

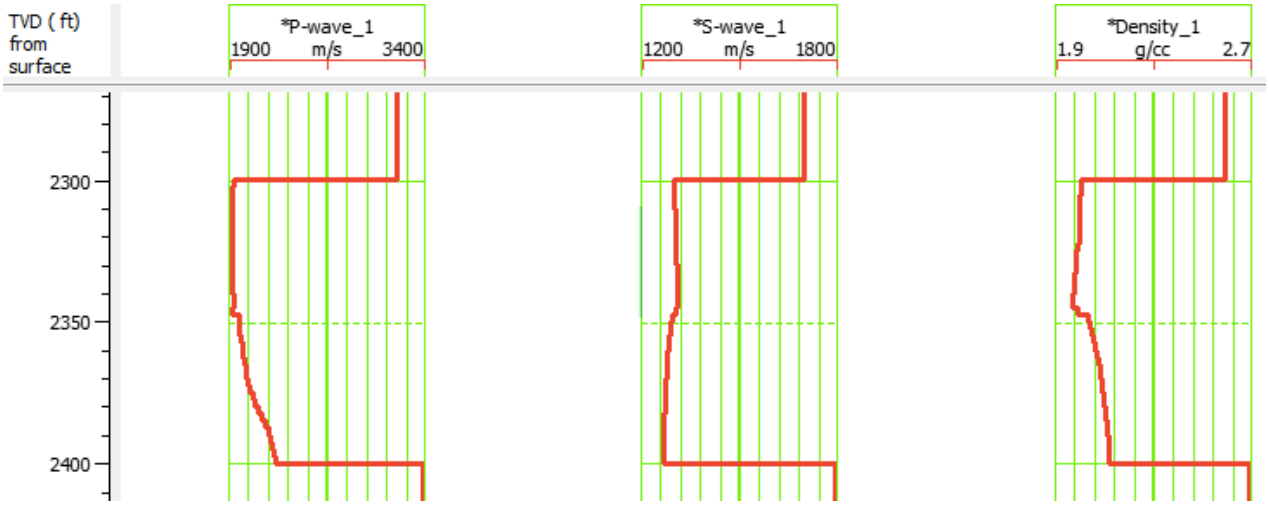


Figure 5.20: P- and S-wave velocities and densities at location 2 in model A calculated from the reservoir simulation results using the MATLAB rock physics code.

The side loop is picked using the red event 1 while the bottom of the steam is picked using the green event 2 as shown in Figure 5.21 while using a seismic frequency of 100 Hz. The same criterion as before is used in picking the two peaks. Once again, the bottom of the steam has a positive gradient compared to the side loop of the top of the reservoir, which has a negative gradient. Looking at Figure 5.22, it becomes difficult to visually distinguish the peak corresponding to the bottom of the steam when using a Ricker wavelet with a dominant frequency of 50 Hz. However, the positive gradient and intercept, which we associate with the bottom of the steam, can still be observed. This enables us to pick the bottom of the steam even when we are unable to visually distinguish the bottom of the steam.

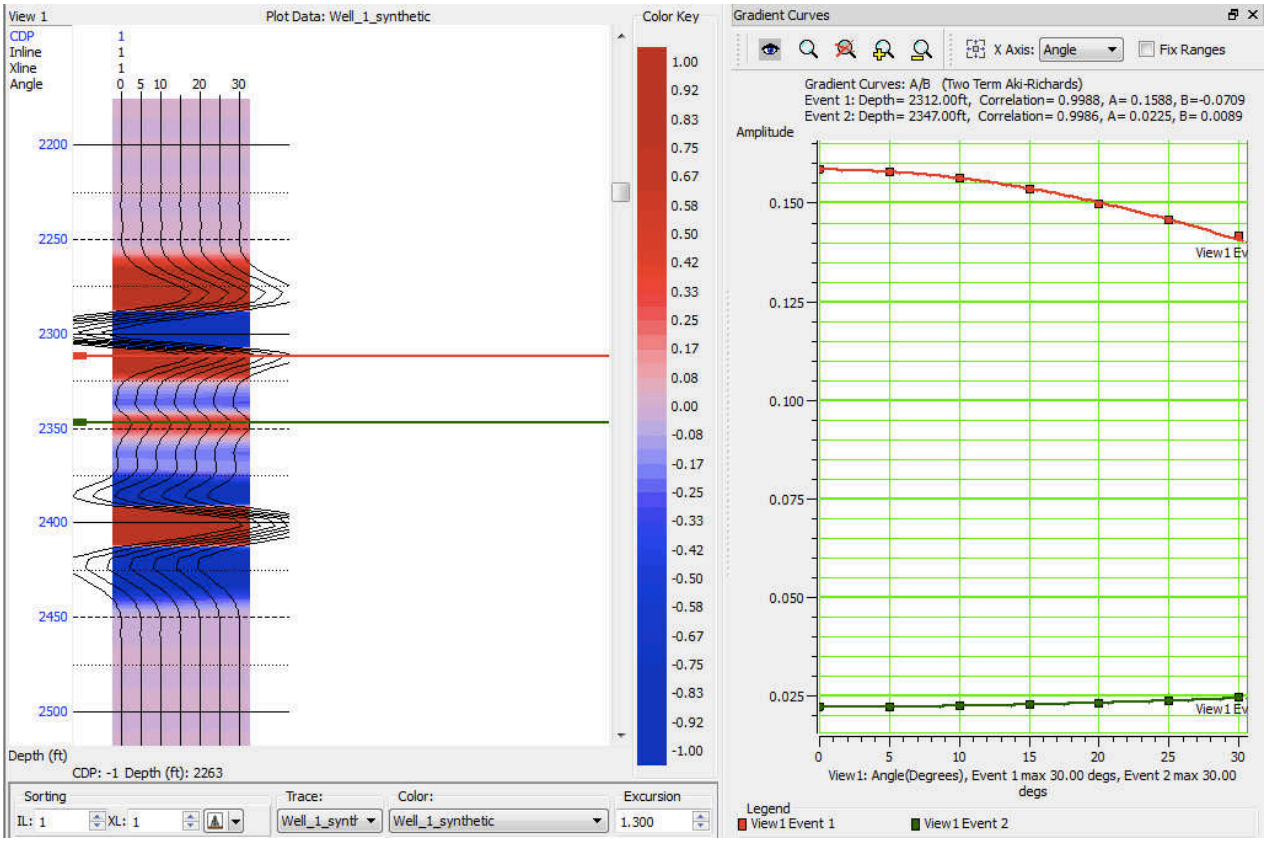


Figure 5.21: The intercept and gradient of the two-term Aki-Richards approximation of the AVO equation at location 2 in model A using a 100 Hz Ricker wavelet.

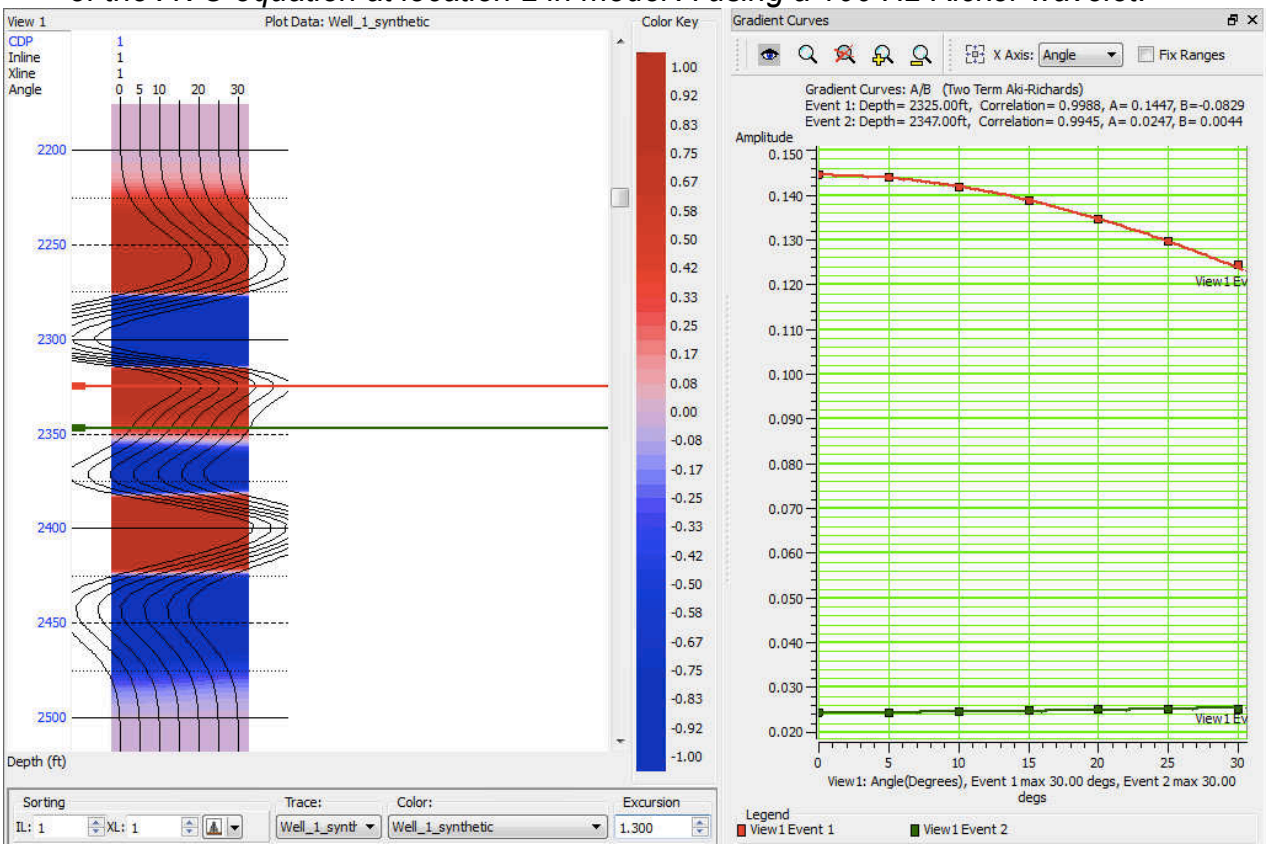


Figure 5.22: The intercept and gradient of the two-term Aki-Richards approximation of the AVO equation at location 2 in model A using a 50 Hz Ricker wavelet.

The steam at location 3 in Figure 5.17 corresponds to the vertical column at the 47th grid cell of the cross-section in the x-axis. The thickness of the steam in this case is 40ft and the last grid cell containing steam has a steam saturation of 26%. The corresponding elastic moduli showing the P- and S-wave velocities and densities are shown in Figure 5.23.

It is important to note that we assume that the top of the reservoir is also the top of the steam. This is because it is the case in most of the reservoir simulations. In this case, the simulation shows that there is a 2.5 ft gap between the top of the reservoir and the top of the steam. The P wave velocity drops by about 30% going from the overlying formation to the top of the reservoir, and then it drops again by another 10% going from the reservoir that does not contain steam to the top of the steam within the same reservoir. In both cases, this is marked by a trough in the seismic response. However, these two troughs will overlap and appear as one trough due to the fact that they are too close to each other for the seismic waves that we use, which has a dominant frequency of 50 Hz, to resolve them. We would need a seismic frequency of more than 600 Hz to be able to resolve the difference, if any, between the top of the steam and the top of the reservoir in this case. For the above reasons and for this case in particular, it is reasonable to assume that the top of the reservoir is also the top of the steam. It is also worth mentioning that as we move away from the injection well, the thickness of the steam tongue usually becomes too thin to be resolved using reflection exploration seismology. The intercept and gradient of the two-term Aki-Richards approximation of the AVO equation are shown in Figure 5.24 and Figure 5.25 using seismic frequencies of 100 Hz and 50 Hz, respectively.

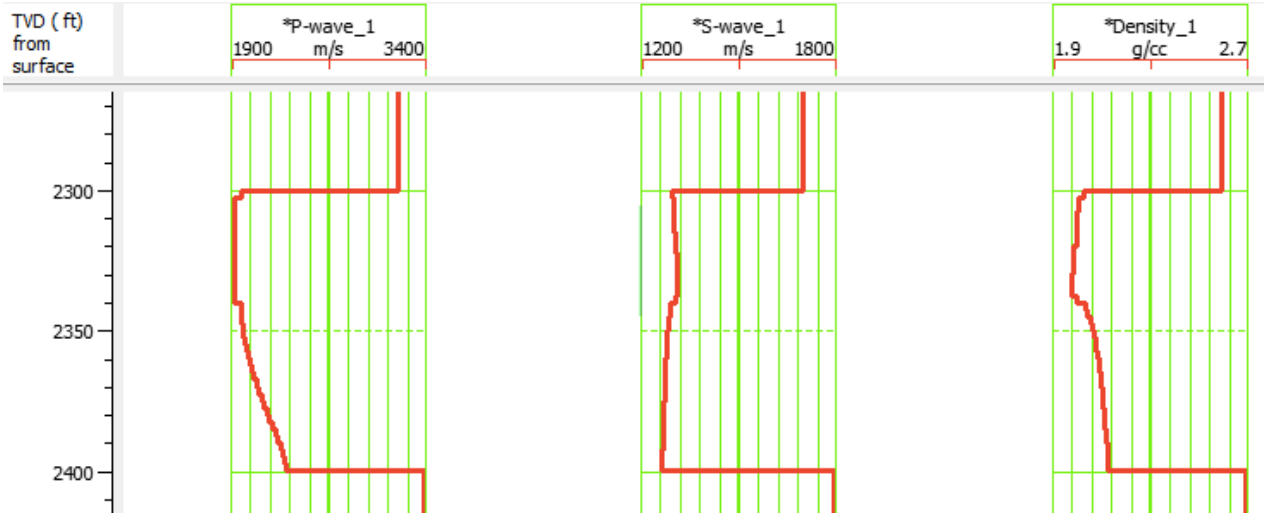


Figure 5.23: P- and S-wave velocities and densities at location 3 in model A calculated from the reservoir simulation results using the MATLAB rock physics code.

It was possible to visually distinguish between the bottom of the steam and the overlying peak representing the side loop at location 1 even when using a 50 Hz wavelet. However, as the steam tongue becomes thinner the two peaks slowly start to overlap. At the early stages of this overlapping, it might be difficult to visually distinguish between the two peaks as shown in Figure 5.22. However, by calculating the gradient of the two term Aki-Richards approximation to the AVO equation, we can identify the lower peak as being the bottom of the steam because of its positive AVO gradient and intercept. This can enable us to delineate the vertical extent of the steam tongue when it is difficult or impossible to do so visually.

As the steam tongue becomes even thinner and approaches the resolution of the seismic waves, we reach the limit of this technique as we lose the ability to distinguish the bottom of the steam both visually and by calculating the gradient of the AVO as shown in Figure 5.25 for the case of seismic waves with dominant frequency of 50 Hz. The steam thickness in this case is known and the peak in the seismic trace corresponding to it should appear at the depth of 2340 ft as can be seen in Figure 5.24 when using a 100 Hz wavelet. However, in Figure 5.25 we are

unable to identify the bottom of the steam at the depth of 2340 ft visually or by the positive AVO gradient and intercept when using seismic waves with dominant frequency of 50 Hz. The side loop of the strong reflection from the top of the reservoir overwhelms or masks the relatively weak reflection representing the bottom of the steam chamber. In Figure 5.25, the depth at which the bottom of the steam is supposed to be was picked using the green line for event 2, which shows a positive intercept but negative gradient, thus we are unable to detect the bottom of the steam using our AVO procedure in this case.

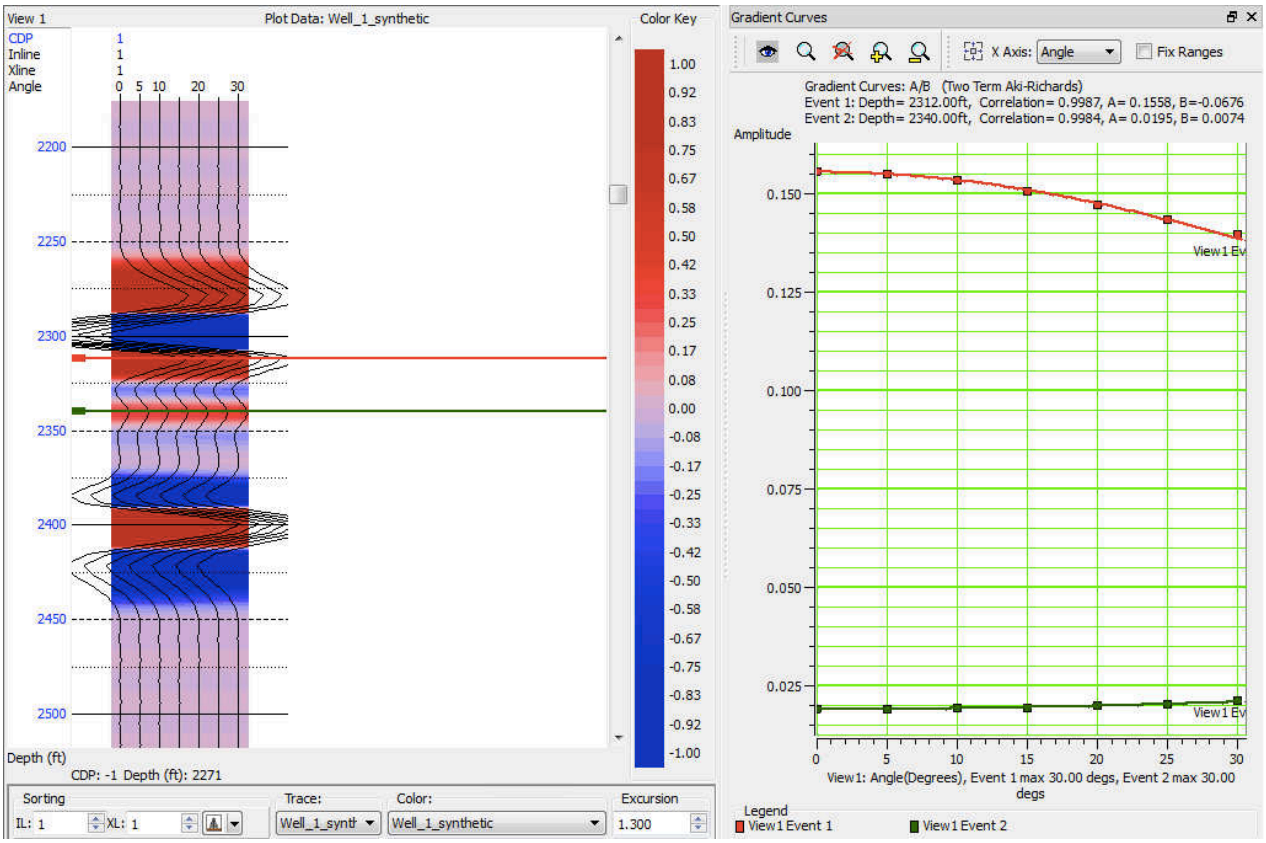


Figure 5.24: The intercept and gradient of the two-term Aki-Richards approximation of the AVO equation at location 3 in model A using a 100 Hz Ricker wavelet.

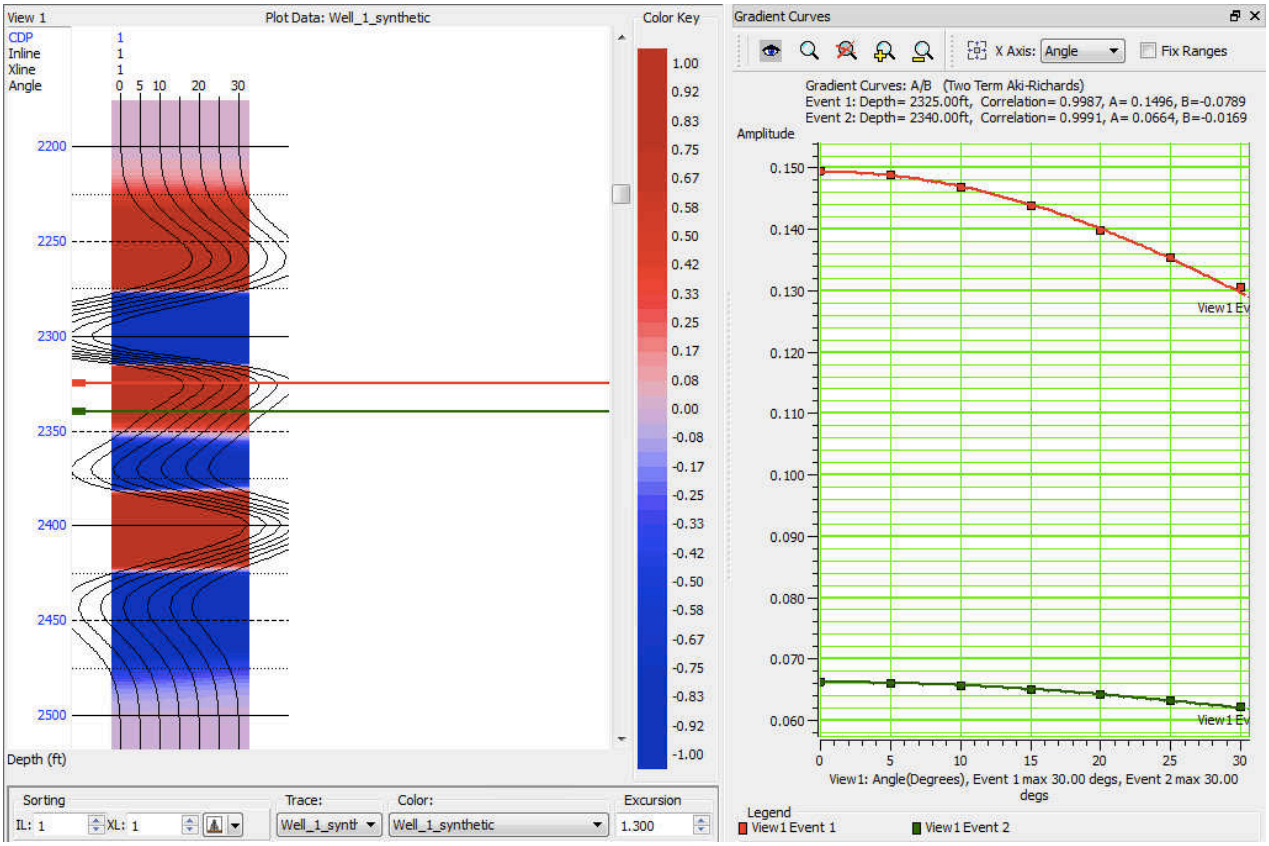


Figure 5.25: The intercept and gradient of the two-term Aki-Richards approximation of the AVO equation at location 3 in model A using a 50 Hz Ricker wavelet.

5.3.2.1 Validation using model B

The second model we will use to test our hypothesis on is model B. The steam saturation after 10 years of steam flood corresponding to model B is shown in Figure 5.26. In model B, the horizontal and vertical permeabilities are 600 mD and 300 mD, respectively, while all other parameters are set to the reference values as per Table 3.5. Three locations with different steam thicknesses are chosen along model B to study the AVO behaviour.

The steam at location 1 in model B in Figure 5.26 corresponds to the vertical column at the 2nd grid cell of the cross-section in the x-axis. The thickness of the steam at location 1 in model B is 52.5 ft and the last grid cell containing steam has a steam saturation of 27.3%. The corresponding elastic moduli showing the P- and S-wave velocities and densities are shown in Figure 5.27. The P-wave velocity

increases at a depth of 2352.5 ft, which corresponds to the bottom of the steam. However, an unexpected drop in the P-wave velocity occurs at a depth of about 2375 ft. The cross section showing the steam saturation in Figure 5.26 does not explain this behaviour of the P-wave velocity. To understand the cause of this behaviour, we must look at the cross section showing the ternary saturation in Figure 5.28. The reservoir simulation results show that as we move vertically from top to bottom, we go from a mostly steam, to mostly brine, then to mostly oil saturated reservoir. The steam-brine contact causes the P-wave velocity to increase while the brine-oil contact causes the P-wave velocity to decrease.

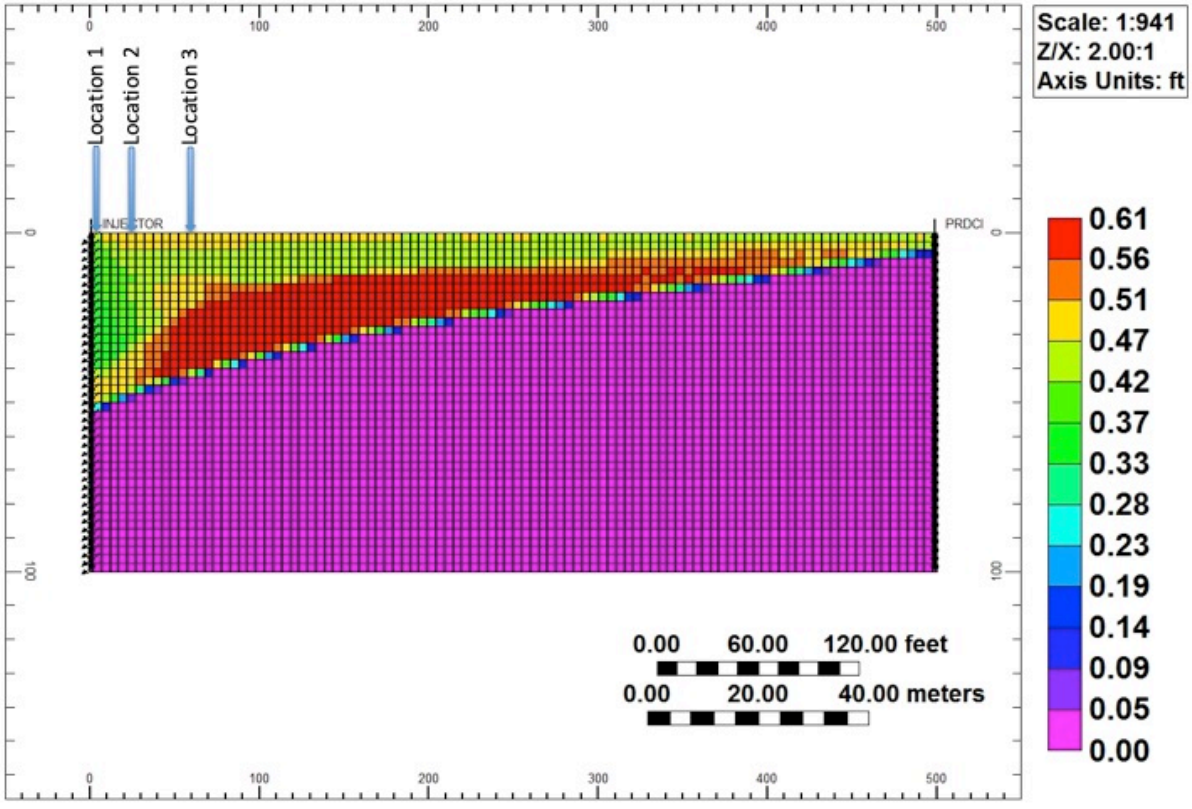


Figure 5.26: Model B: Cross-section showing steam saturation after 10 years of steam flood where the horizontal and vertical permeabilities are 600 mD and 300 mD, respectively. Other parameters are set to the reference value as per Table 3.5. Blue arrows mark the locations where steam thicknesses were studied. The injection well is to the left while the production well is to the right.

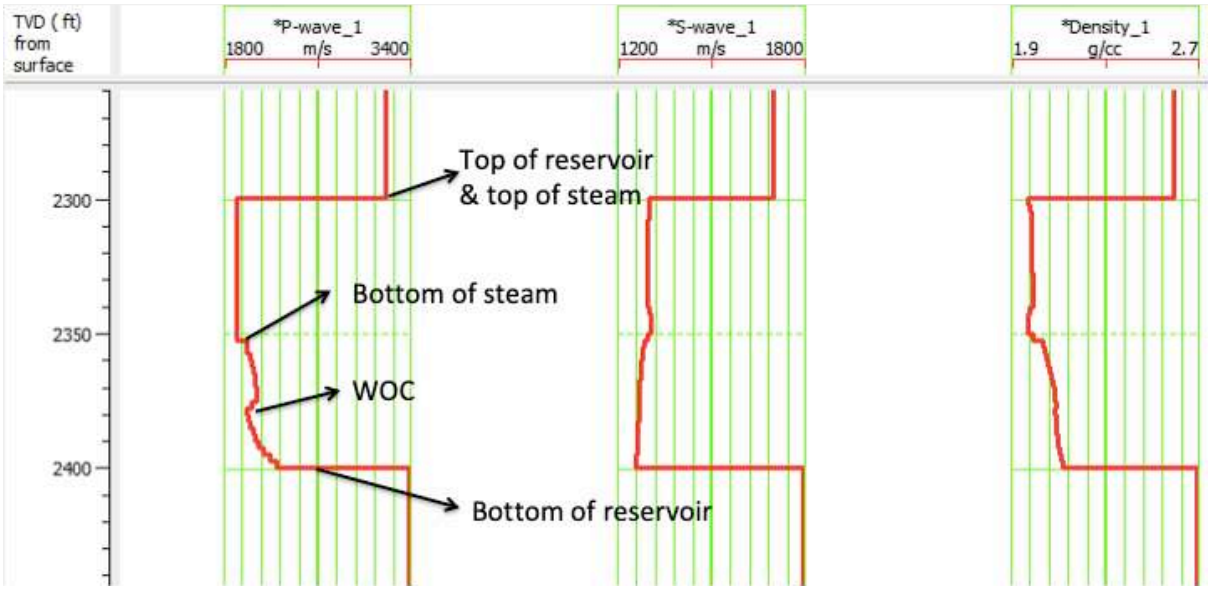


Figure 5.27: P- and S-wave velocities and densities at location 1 in model B calculated from the reservoir simulation results using the MATLAB rock physics code.

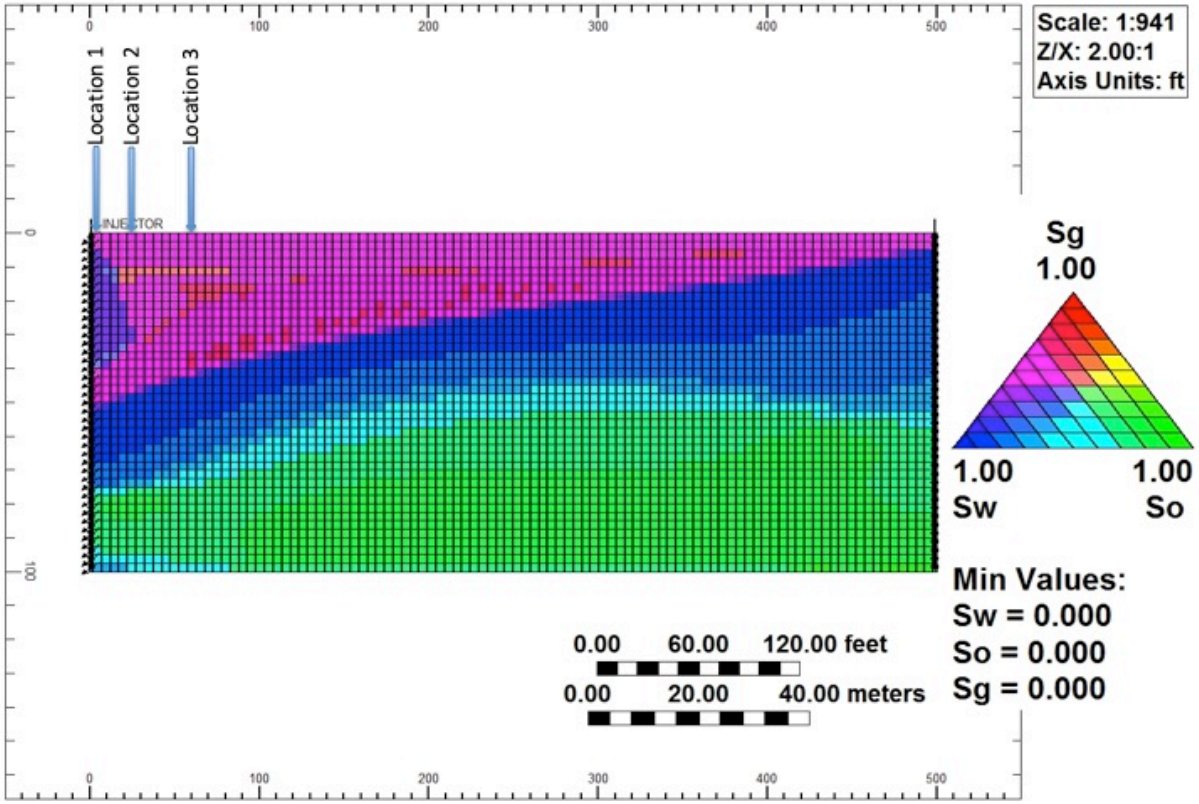


Figure 5.28: Model B: Cross-section showing ternary saturation after 10 years of steam flood where the horizontal and vertical permeabilities are 600 mD and 300 mD, respectively. Other parameters are set to the reference value as per Table 3.5. Blue arrows mark the locations where steam thicknesses were studied. The injection well is to the left while the production well is to the right.

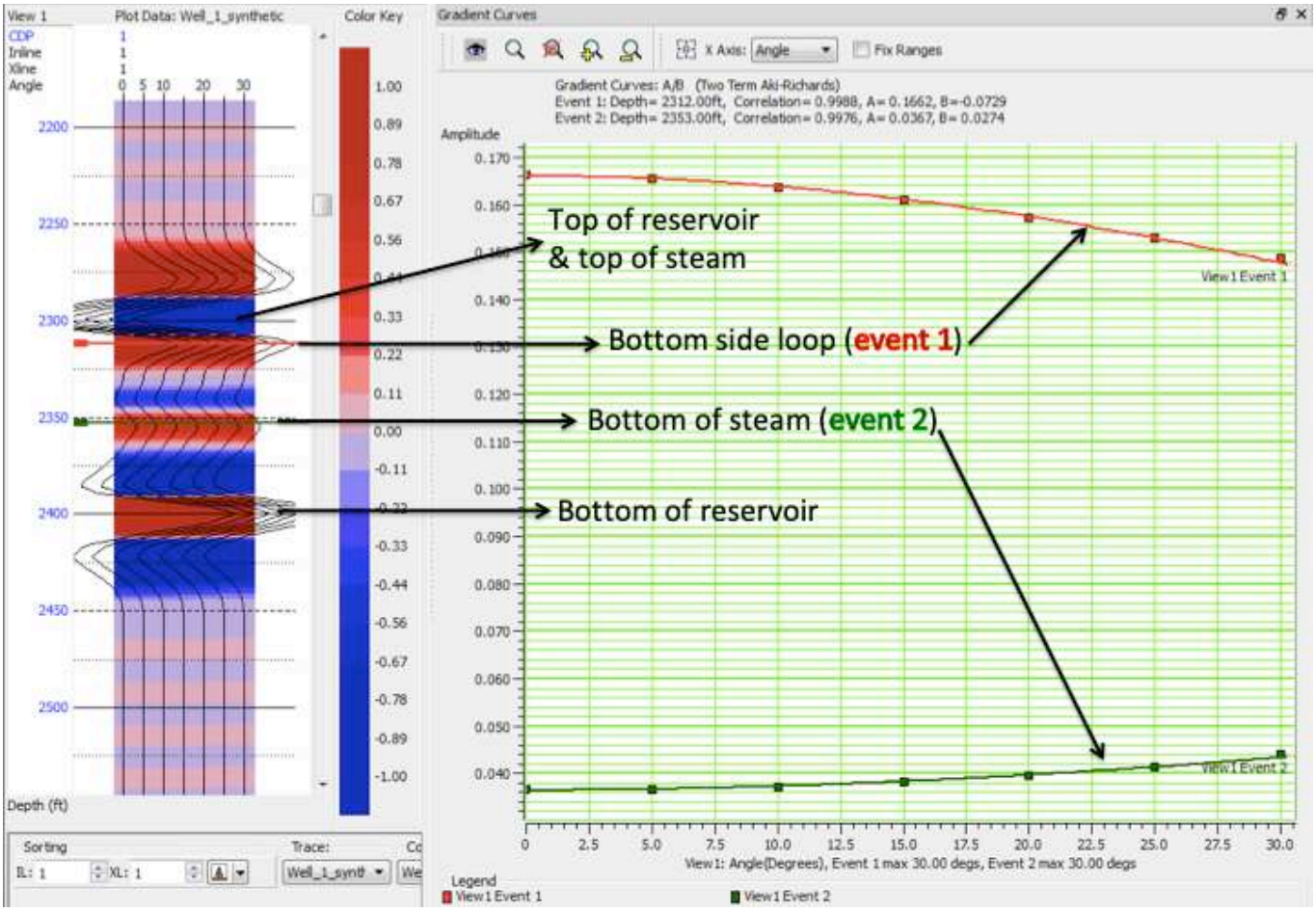


Figure 5.29: The intercept and gradient of the two-term Aki-Richards approximation of the AVO equation at location 1 in model B using a 100 Hz Ricker wavelet.

The intercept and gradient of the two-term Aki-Richards approximation of the AVO equation using frequencies of 100 Hz and 50 Hz are shown in Figure 5.29 and Figure 5.30, respectively. The side loop, which is picked using the red line for event 1, has a negative gradient while the bottom of the steam is picked using the green line for event 2 and has a positive AVO gradient and intercept. In this case, the peak corresponding to the bottom of the steam was identifiable both visually and by our AVO procedure. The water-oil contact seen at a depth of around 2375 ft in Figure 5.27 is unidentifiable in Figure 5.29 and Figure 5.30 because it is too close to the strong reflection from the bottom of the reservoir and would require higher frequencies to be able to distinguish it from the bottom of the reservoir.

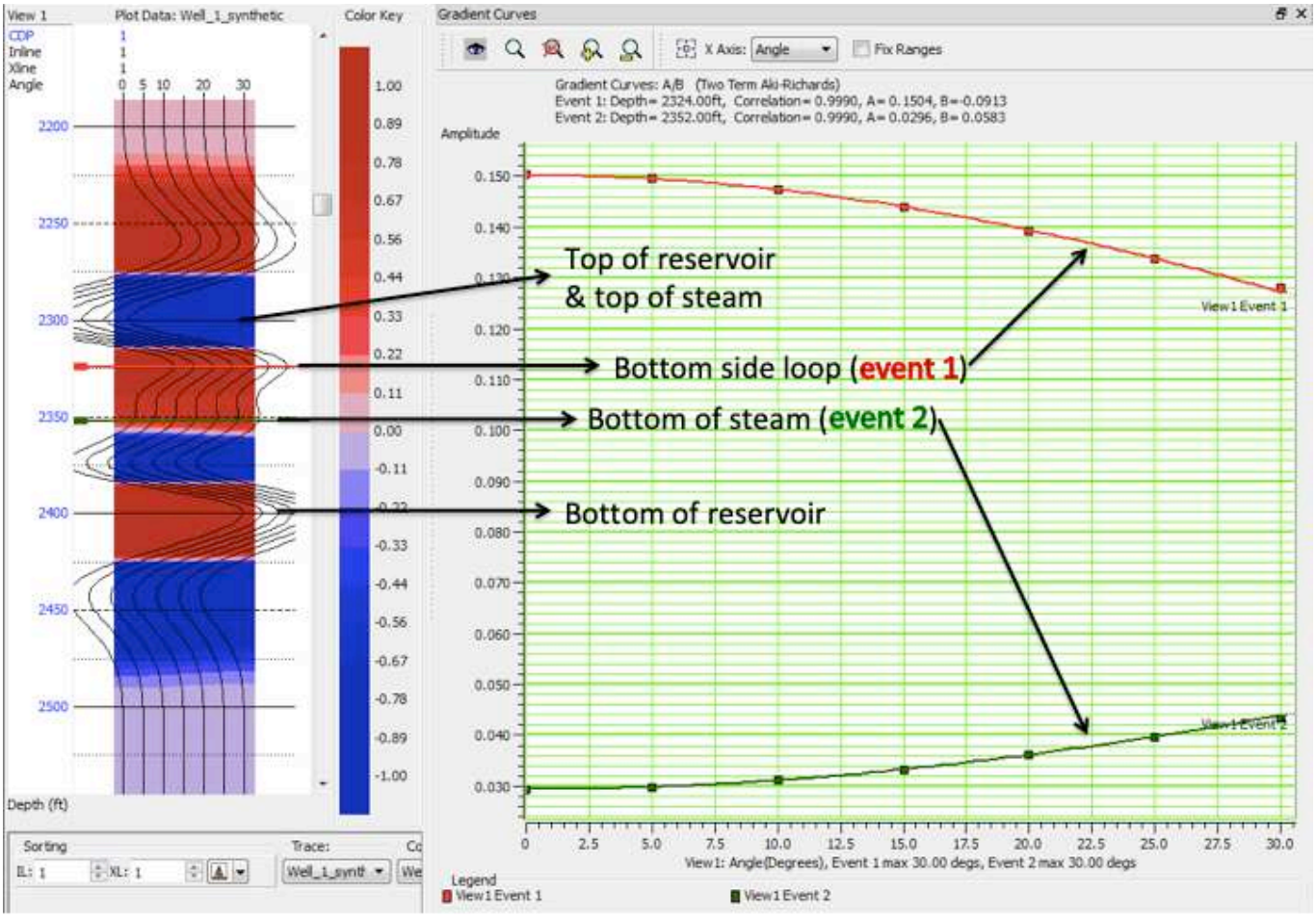


Figure 5.30: The intercept and gradient of the two-term Aki-Richards approximation of the AVO equation at location 1 in model B using a 50 Hz Ricker wavelet.

The steam at location 2 in Figure 5.28 corresponds to the vertical column at the 6th grid cell of the cross-section in the x-axis. The thickness of the steam at location 2 in model B is 50 ft and the last grid cell containing steam has a steam saturation of 9.1%, which is significantly less than all other cases in this study. This is a good thing as it shows that our AVO procedure is valid even when the steam saturation towards the bottom of the steam is low. The corresponding elastic moduli showing the P- and S-wave velocities and densities are shown in Figure 5.31. The water-oil contact is apparent at a depth of 2375 ft. The intercept and gradient of the two-term Aki-Richards approximation of the AVO equation using 100 and 50 Hz Ricker wavelet are shown in Figure 5.32 and Figure 5.33, respectively.

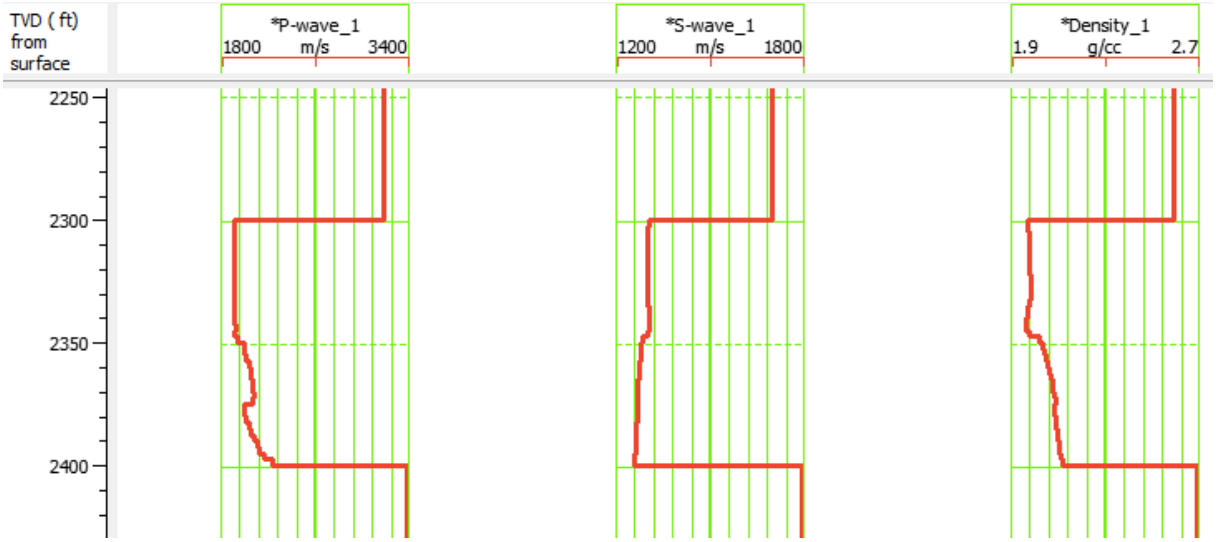


Figure 5.31: P- and S-wave velocities and densities at location 2 in model B calculated from the reservoir simulation results using the MATLAB rock physics code.

The behaviour of the AVO gradient is similar to the previous cases. The side loop picked using the red line for event 1 has a negative AVO gradient in both the 100 Hz and 50 Hz case. The bottom of the steam was picked using the green line for event 2 and can still be seen as a slight peak at a depth of 2350 ft using a 50 Hz wavelet. The AVO gradient and intercept at the bottom of the steam is positive as expected.

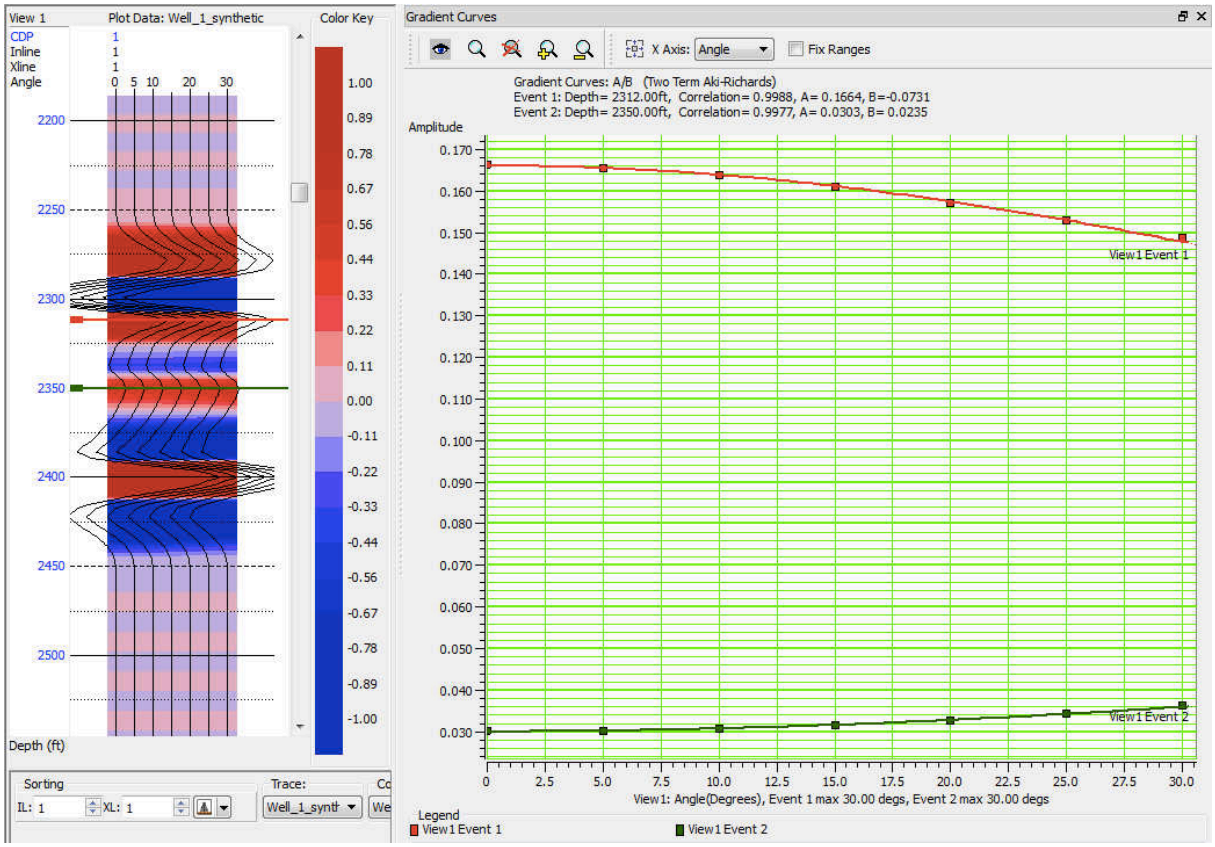


Figure 5.32: The intercept and gradient of the two-term Aki-Richards approximation of the AVO equation at location 2 in model B using a 100 Hz Ricker wavelet.

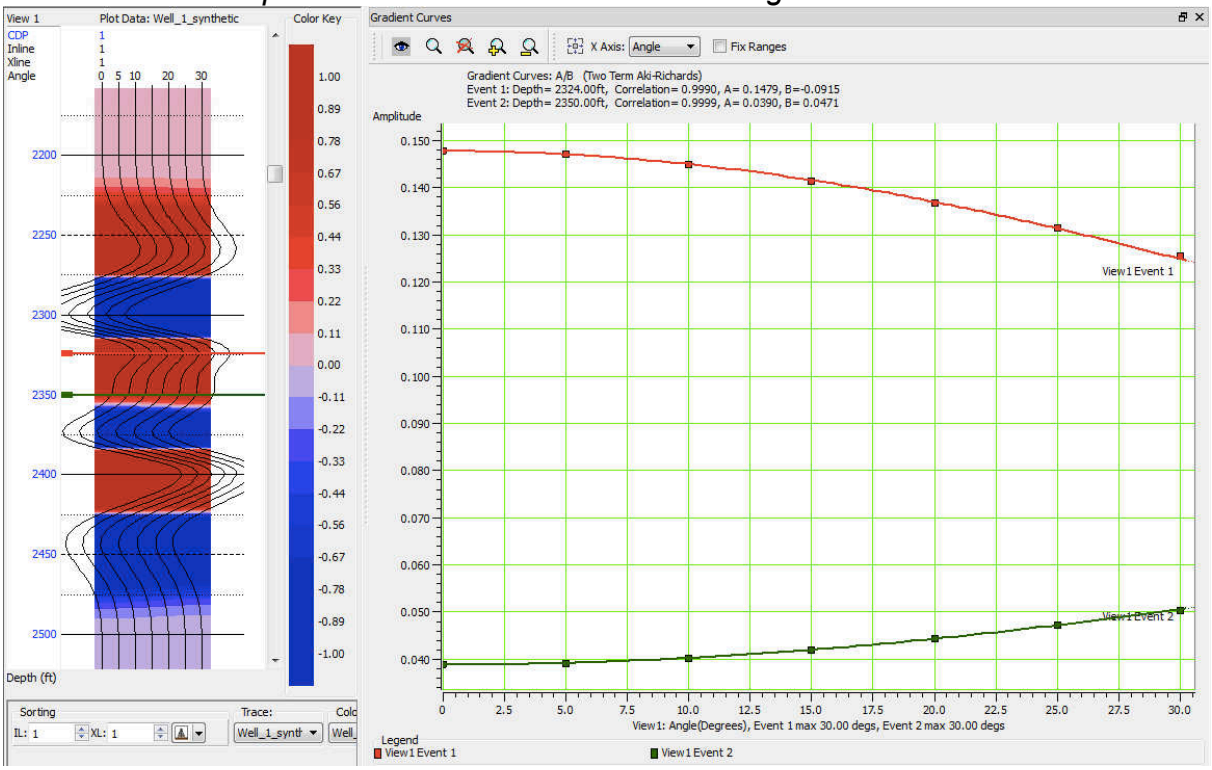


Figure 5.33: The intercept and gradient of the two-term Aki-Richards approximation of the AVO equation at location 2 in model B using a 50 Hz Ricker wavelet.

The steam at location 3 in Figure 5.28 corresponds to the vertical column at the 13th grid cell of the cross-section in the x-axis. The thickness of the steam at location 3 in model B is 42.5 ft and the last grid cell containing steam has a steam saturation of 42.7%. The corresponding elastic moduli showing the P- and S-wave velocities and densities are shown in Figure 5.34. The intercept and gradient of the two-term Aki-Richards approximation of the AVO equation using 100 and 50 Hz Ricker wavelet are shown in Figure 5.35 and Figure 5.36, respectively.

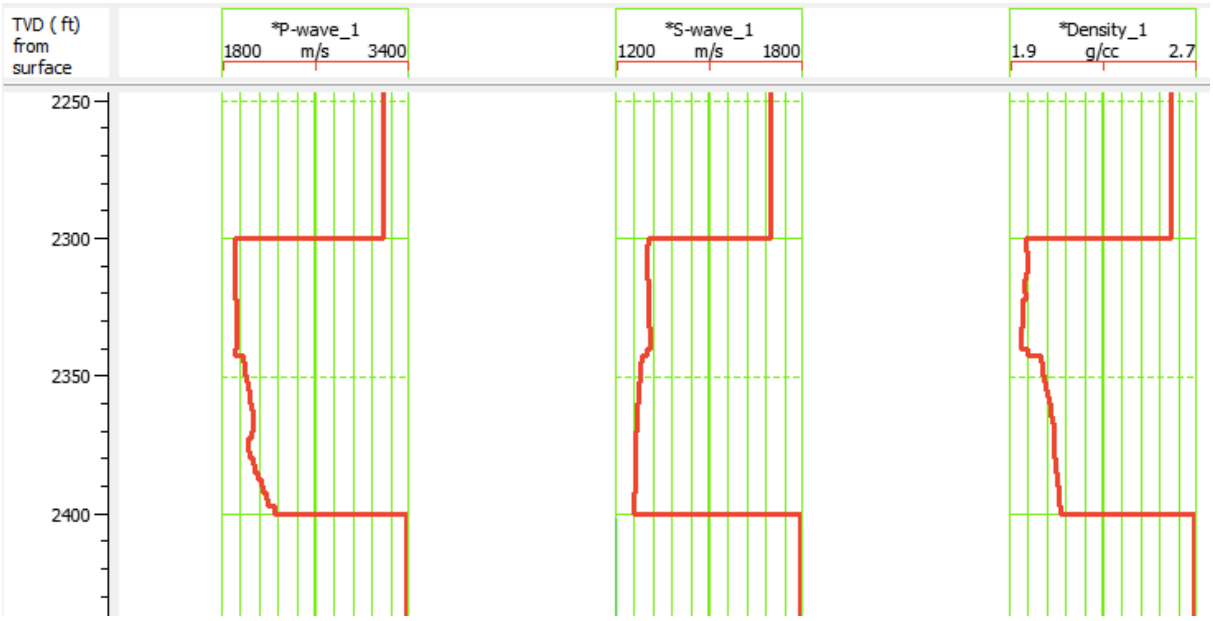


Figure 5.34: P- and S-wave velocities and densities at location 3 in model B calculated from the reservoir simulation results using the MATLAB rock physics code.

The bottom of steam is identifiable using the 100 Hz wavelet and is picked using the green line for event 2 as shown in Figure 5.35. The gradient and intercept are both positive as expected when using a wavelet with a dominant frequency of 100 Hz. However, when using the more realistic 50 Hz wavelet, shown in Figure 5.36, we notice that the bottom of the steam is visually unidentifiable yet the AVO gradient and intercept are both positive which is indicative of the bottom of the steam. This demonstrates how our AVO procedure can identify the bottom of the steam when it is not possible to do so using 4D seismic data.

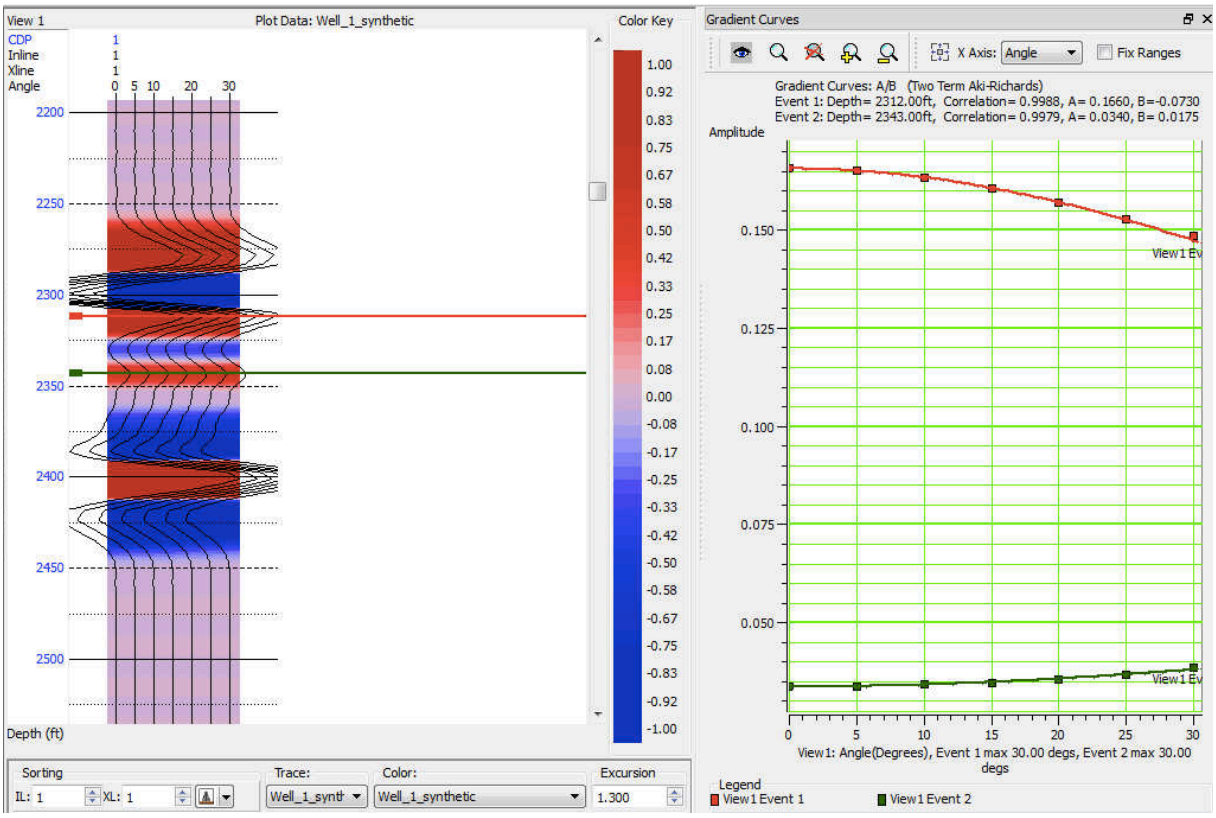


Figure 5.35: The intercept and gradient of the two-term Aki-Richards approximation of the AVO equation at location 3 in model B using a 100 Hz Ricker wavelet.

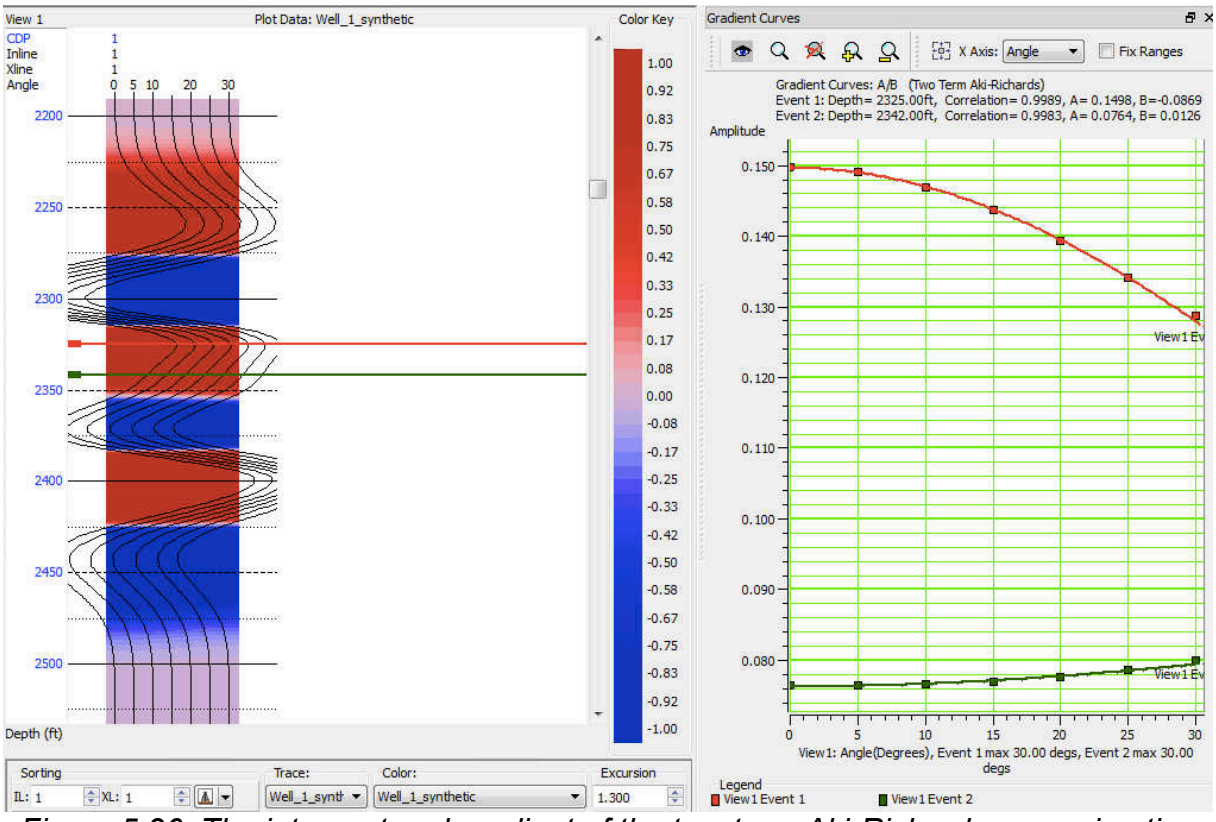


Figure 5.36: The intercept and gradient of the two-term Aki-Richards approximation of the AVO equation at location 3 in model B using a 50 Hz Ricker wavelet.

5.4 Summary

In the first part of chapter 5, we performed a sensitivity analysis to identify the factors that most influence the intercept and gradient of the AVO at the top and bottom of the steam chamber. Pre steam injection, the AVO intercept and gradient at the top of the steam chamber is most sensitive to porosity and effective pressure. Post steam injection, the AVO intercept and gradient at the top of the steam chamber is most sensitive to porosity and effective pressure, while at the bottom of the steam chamber they are most sensitive to steam saturation, effective pressure and porosity. The oil API effect on the intercept and gradient of the AVO was insignificant in all cases. The fact that both the intercept and gradient of the AVO are most sensitive to the steam saturation at the bottom of the reservoir will be taken advantage off when developing the AVO procedure to detect the bottom of the steam chamber.

A multi variable linear regression is performed in an effort to predict the values of the AVO intercept and gradient by knowing the values of porosity, effective pressure, steam saturation, temperature and oil API. The regression was successful in fitting the available data at the top of the reservoir pre and post steam injection. However, the regression did not do a good job fitting the available data for the case of the bottom of the steam chamber. In all cases, the regression was unable to accurately predict the AVO intercept and gradient values which is attributed to the fact that the dependent variables were calculated at the end points of each of the independent variables which does not capture the complexity of the model.

In the second part of chapter 5, we tested our AVO analysis procedure at 3 different locations in two different models. A clear peak represents the bottom of the steam when a seismic wave with a dominant frequency of 100 Hz is used. However, that is not always the case when using the more realistic 50 Hz seismic waves. In the

case of location 1 in model A, where the steam thickness is 50ft, the bottom of the steam chamber was identifiable both visually and by the AVO procedure. In the case of location 2 in model A, where the steam thickness is 47.5 ft, it was difficult to identify the bottom of the steam visually. This is where our AVO procedure is important and useful as it enables us to identify the bottom of the steam with confidence at a depth where both the intercept and gradient of the AVO are positive. In the case of location 3 in model A, where the steam thickness is 40ft, we were unable to identify the bottom of the steam chamber visually nor with the AVO analysis procedure. In model B, we were able to identify the bottom of the steam chamber at locations 1 and 2, where the steam thickness is 52.5 ft and 50 ft, respectively, both visually and by using the AVO procedure. However, it was harder to identify the bottom of the steam visually in the case of location 2 in model B using a seismic wave with dominant frequency of 50 Hz. In the case of location 3 in model B, where the steam thickness is 42.5ft, we were unable to identify the bottom of the steam chamber visually nor with the AVO analysis procedure.

The locations at which the steam chambers were studied ranged from being close to the injection well to midway between the injection and production wells. The criteria for choosing these locations were based on the thickness of the steam chamber being close to 50 ft. This is because the thickness of the reservoir is only 100 ft, which is relatively thin for the use of seismic waves with dominant frequency of 50 Hz. In other words, the bottom of the steam has to be at or close to the middle of the reservoir, namely at a depth of 2350 ft. As the steam chamber gets thicker, closer to the injection well, or thinner, closer to the production well, the seismic reflection representing the bottom of the steam is masked by the strong reflection from the top or bottom of the reservoir.

The AVO procedure developed in this thesis can be applied at any location so long as the steam thickness is within the range that is resolvable by the seismic waves that are used. This includes using the AVO procedure to delineate the steam chamber pro and post steam breakthrough. So far, we tested our AVO procedure with no noise added. In reality, all real data include noise. The next step is to test the limits of our AVO procedure with varying levels of noise, which is what will be done in chapter 6.

6. Sensitivity of the AVO analysis to noise

Noise is one of the main problems in near-surface reflection seismology (Robertsson et al., 1996). In seismic data acquisition, noise can be divided into two categories; noise caused by external sources, such as wind or moving objects, and noise resulting from the seismic source. External noise can be removed using different processing techniques, such as muting and filtering. Seismic waves from the seismic source causes reflections and refractions from near-surface heterogeneities, which interferes with the original signal due to its proximity from the seismic source and receiver (Butler, 2005). Besides noise coming from perturbations to the observed signal, noise can also come from uncertainties in the data or rock physics model.

In this chapter we test the robustness of the AVO procedure in identifying the bottom of the steam chamber by adding uniformly distributed random noise to the P-wave and S-wave velocities and densities because it is the most general type of random noise which represent any of the sources of noise mentioned above or a combination of them. The bottom of the steam chamber is identified by analyzing the intercept and gradient of the two-term Aki-Richards approximation of the AVO equation. The bottom of the steam chamber is determined to be where both the intercept and gradient of the AVO are positive within the reservoir. The intercept must be positive at the bottom of the steam chamber because the seismic waves are travelling from a slow medium, which is the reservoir rock containing steam, to a faster medium, which is the reservoir rock containing oil and brine without any steam. The gradient of the AVO must be positive because that was identified to be the signature of the bottom of the steam chamber as discussed in chapter 5.

If the intercept and gradient are both positive over a range of depths, then we determine that the criteria for choosing the bottom of the steam chamber is for it to be at a depth corresponding to the middle of that range. This is because we could not find any pattern in the intercept or gradient behaviour in that range which might be a better indication for the actual depth of the bottom of the steam chamber. Nevertheless, we will see that this assumption results in a fairly accurate prediction for the depth of the bottom of the steam chamber, hence the thickness of the steam chamber. This will be tested at a different location in models A and B as seen in chapter 5.

6.1 Testing AVO procedure robustness using model A

The AVO analysis was applied to three different locations in model A as shown in chapter 5 in Figure 5.16 without any noise added. In this section, we will test the robustness of the AVO procedure by adding uniformly distributed random noise to the seismic velocities and densities at location 1 in model A. The resulting P-wave and S-wave velocities and densities after adding the uniformly distributed random noise are shown in Figure 6.1. The reason we choose location 1 of model A to test the robustness of our AVO procedure is because the thickness of the steam chamber there is 50 ft which puts the bottom of the steam chamber exactly at the middle of the 100 ft reservoir, hence as far as possible from the strong reflections from above, which represents the top of the reservoir, and below, which represents the bottom of the reservoir. This is important because we use seismic waves with dominant frequency of 50 Hz, which results in a tuning thickness of only about 10m. This would not be enough to differentiate between the strong reflection from the top and bottom of the reservoir from one side and the relatively weaker reflection representing the bottom of the steam chamber from the other side if the bottom of the

steam chamber were further away from being at the middle of the reservoir. In other words, we want to test the robustness of our AVO procedure without adding the complication of seismic resolution issues caused by conducting the robustness tests at locations where the bottom of the steam chamber is shallower or deeper within the reservoir.

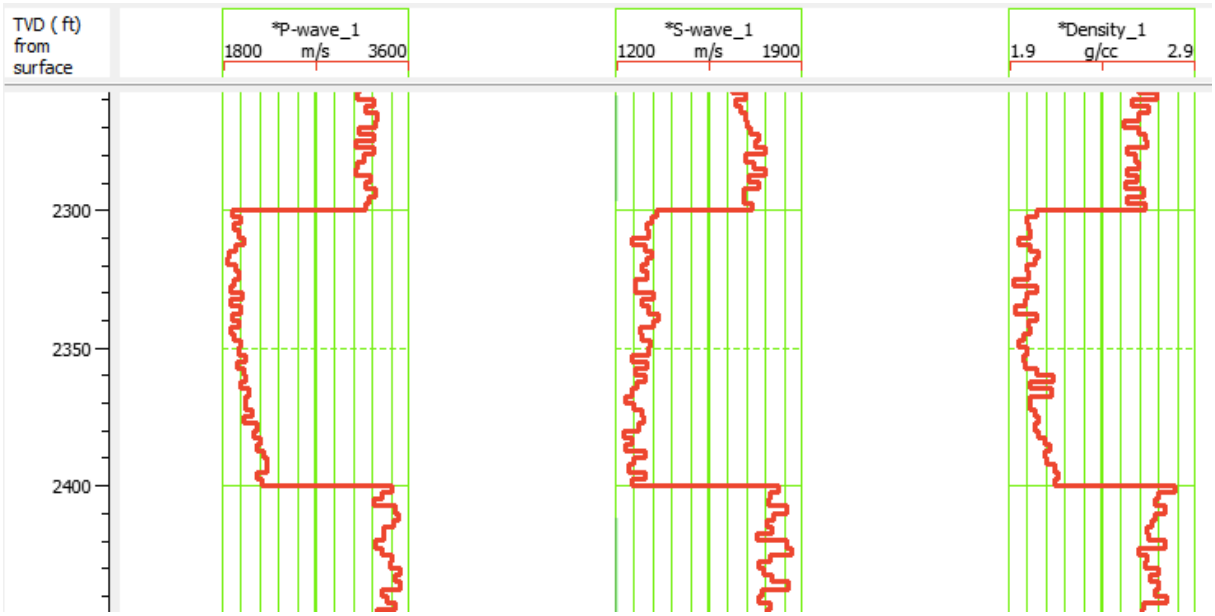


Figure 6.1: P-wave and S-wave velocities and densities at location 1 in model A after adding 4% uniformly distributed random noise.

The velocities and densities shown in Figure 6.1 are used as input into HampsonRussell software, which calculated the intercept and gradient of the two-term Aki-Richards approximation of the AVO. Figure 6.2 shows the intercept and gradient of the AVO for the case of 4% added noise. The red line in all of the AVO figures are picked where the intercept of the side loop of the trough caused by the reflection at the top of the reservoir is greatest. It is used as a reference point to show that the gradient of the AVO is always negative at the peak corresponding to the side loop of the trough above it, which as mentioned before corresponds to the top of the reservoir. The bottom of the steam chamber is always picked using the green line. The intercept and gradient of the AVO are both positive in the depth range 2345 ft to

2350 ft, which results in a steam chamber thickness range of 45 to 50 ft. We pick the bottom of the steam chamber at the midpoint depth of 2347.5 ft. However, since depth in our HampsonRussell software model is in increments of 1 ft, we round it to the next integer and estimate that the bottom of the steam chamber is at the depth of 2348 ft making our estimate of the steam chamber thickness to be 48 ft.

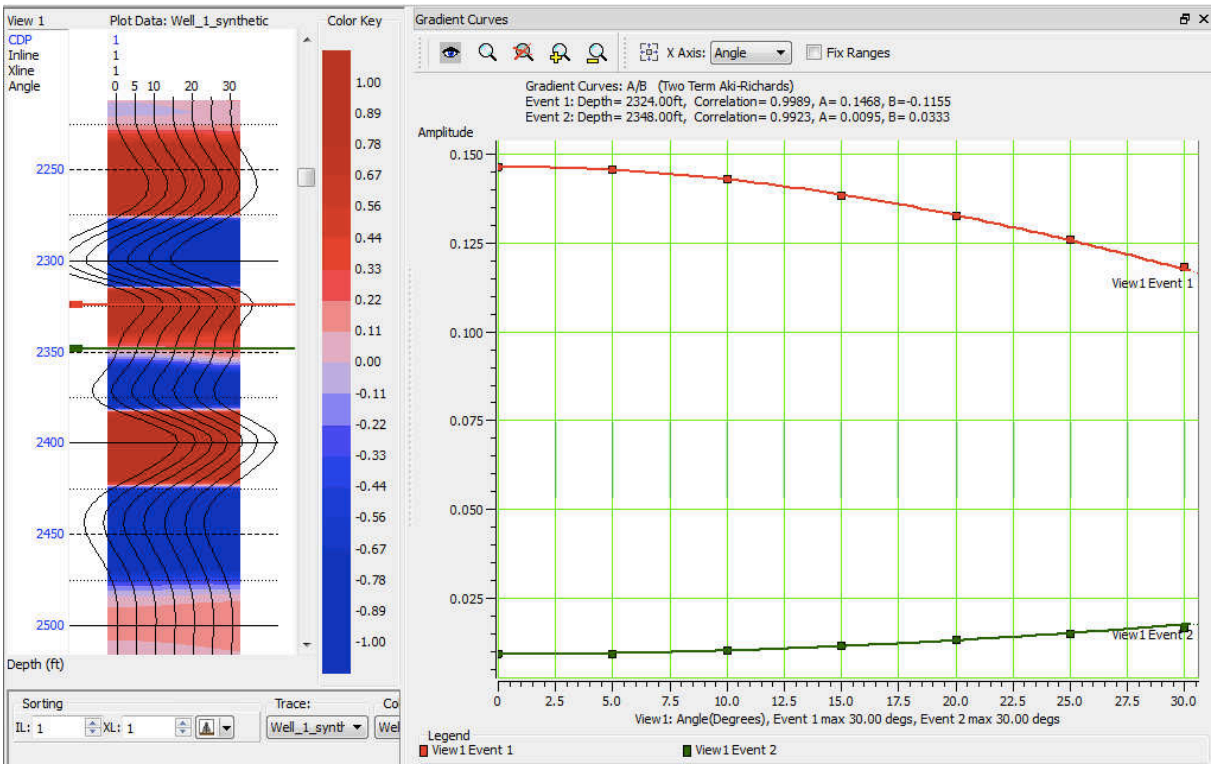


Figure 6.2: Intercept and gradient of the AVO at location 1 in model A for the case of 4% uniformly distributed added noise.

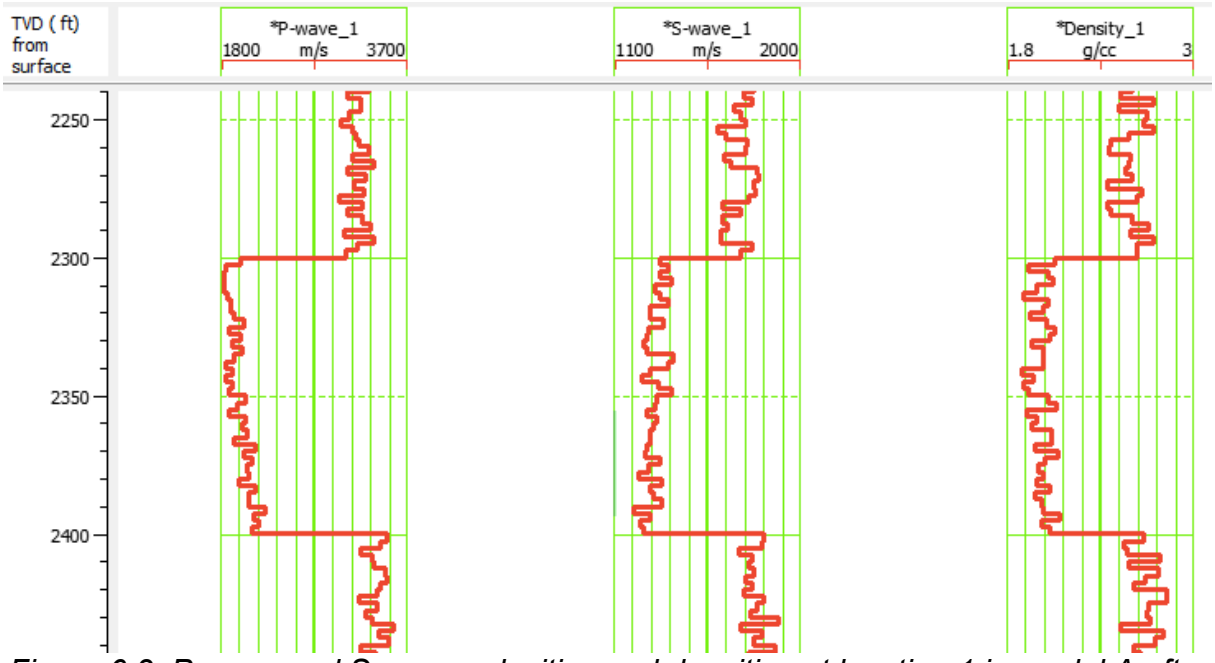


Figure 6.3: P-wave and S-wave velocities and densities at location 1 in model A after adding 6% uniformly distributed random noise.

The noise is increased to 6% and the resulting V_p, V_s and density are shown in Figure 6.3. The resulting intercept and gradient of the AVO for this case are shown in Figure 6.4. The intercept and gradient of the AVO are both positive in the depth range 2352 to 2356ft resulting in a steam chamber thickness range of 52 to 56 ft. We pick the bottom of the steam chamber at the midpoint depth of 2354 ft making our estimate of the steam chamber thickness to be 54 ft.

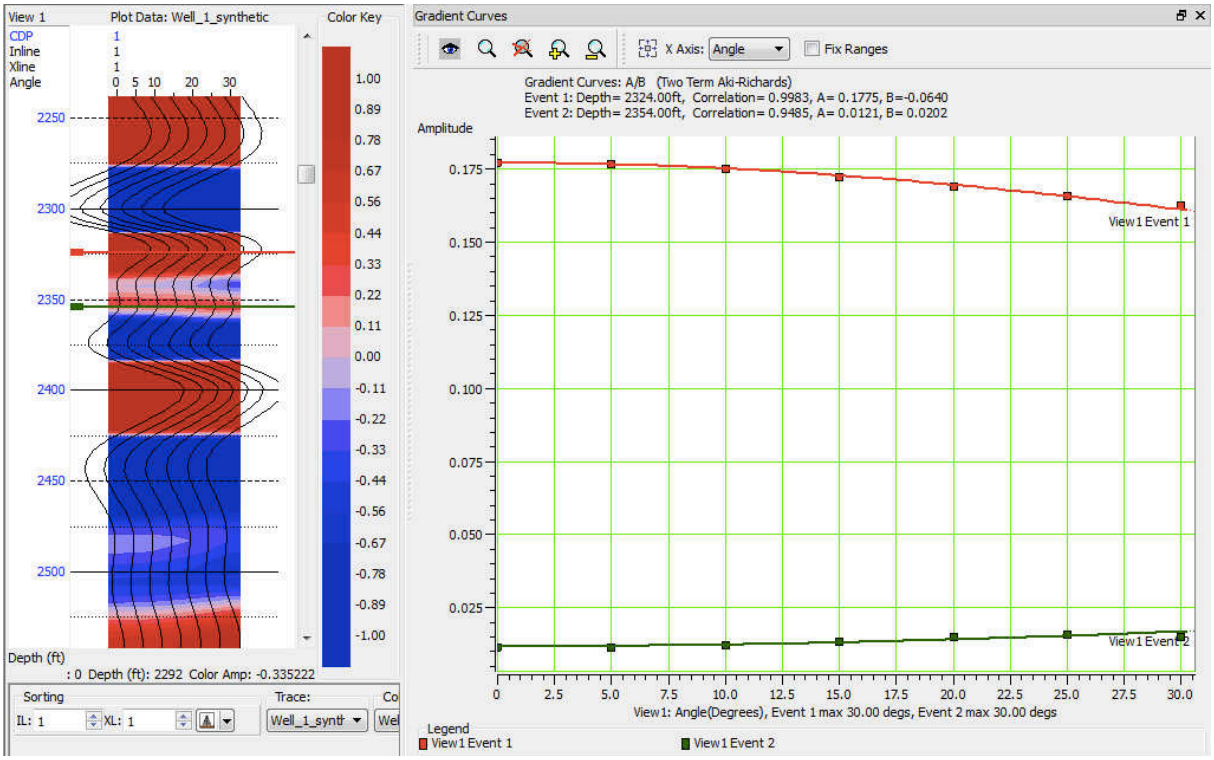


Figure 6.4: Intercept and gradient of the AVO at location 1 in model A for the case of 6% uniformly distributed added noise.

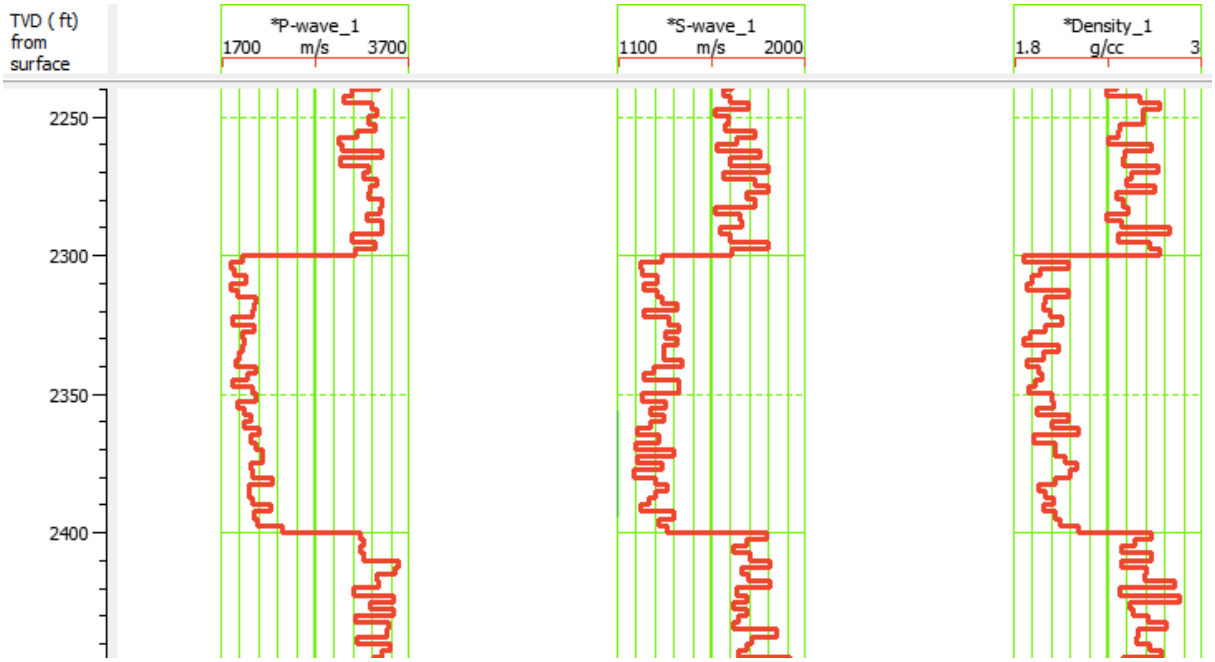


Figure 6.5: P-wave and S-wave velocities and densities at location 1 in model A after adding 8% uniformly distributed random noise.

The noise is increased to 6% and the resulting V_p, V_s and density are shown in Figure 6.5. The resulting intercept and gradient of the AVO for this case are shown in Figure 6.6. The intercept and gradient of the AVO are both positive in the depth

range 2332 to 2359ft resulting in a steam chamber thickness range of 32 to 59 ft. Therefore, the bottom of the steam chamber is picked at the midpoint of that range which is 2346ft making our estimate of the steam chamber thickness to be 46 ft.

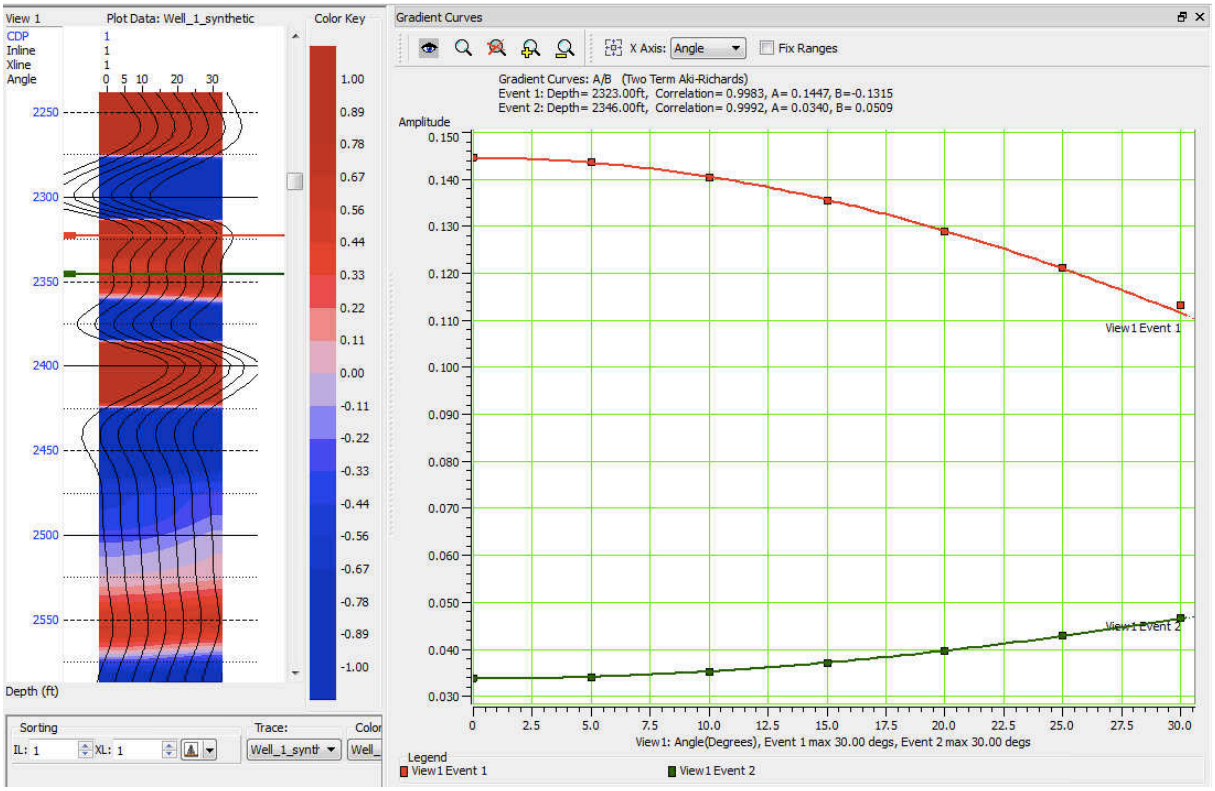


Figure 6.6: Intercept and gradient of the AVO at location 1 in model A for the case of 8% uniformly distributed added noise.

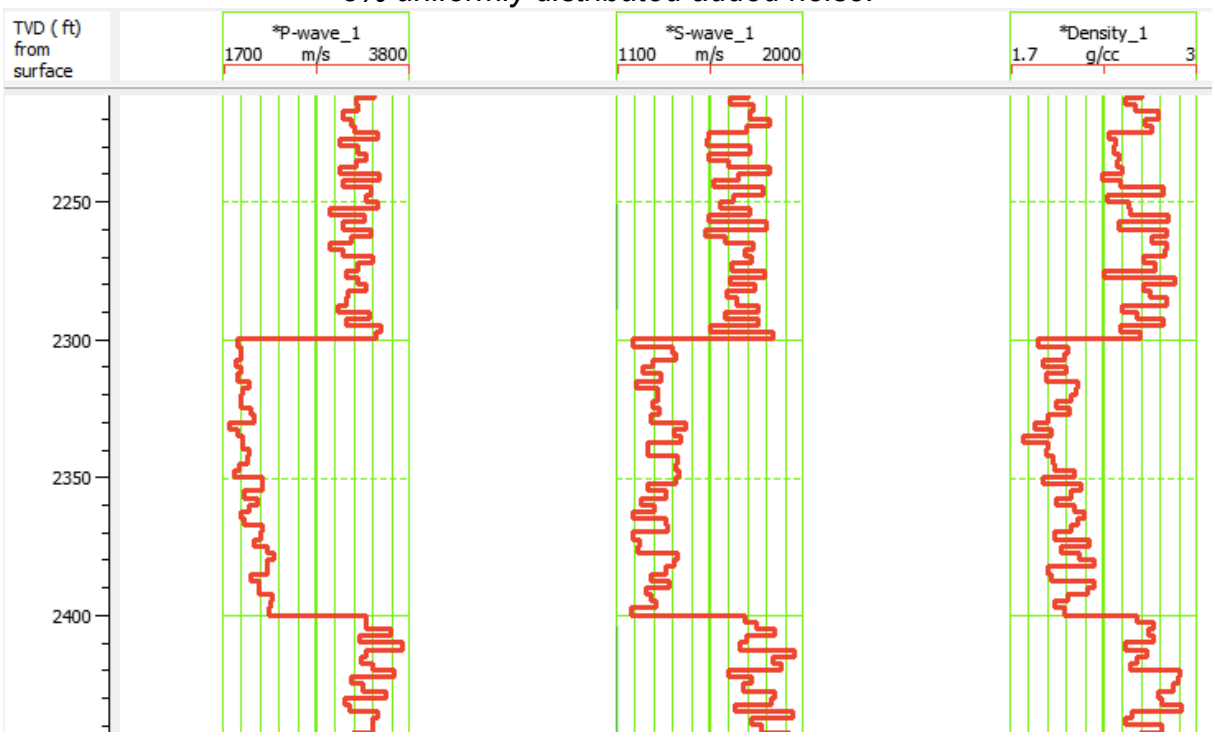


Figure 6.7: P-wave and S-wave velocities and densities at location 1 in model A after adding 10% uniformly distributed random noise.

The noise is increased to 10% and the resulting V_p, V_s and density are shown in Figure 6.7. The resulting intercept and gradient of the AVO for this case are shown in Figure 6.8. The intercept and gradient of the AVO are both positive in the depth range 2348 to 2357ft resulting in a steam chamber thickness range of 48 to 57 ft. Therefore, the bottom of the steam chamber is picked at the midpoint of that range which is 2353ft making our estimate of the steam chamber thickness to be 53 ft.

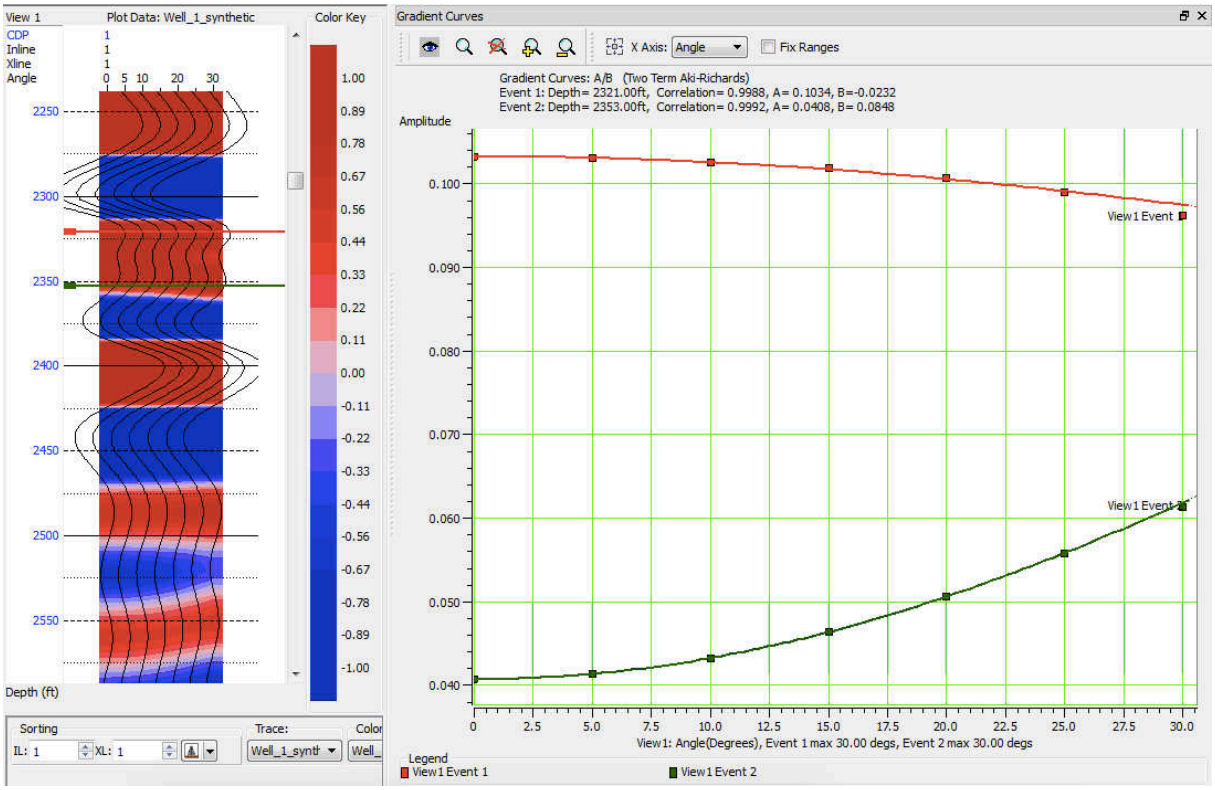


Figure 6.8: Intercept and gradient of the AVO at location 1 in model A for the case of 10% uniformly distributed added noise.

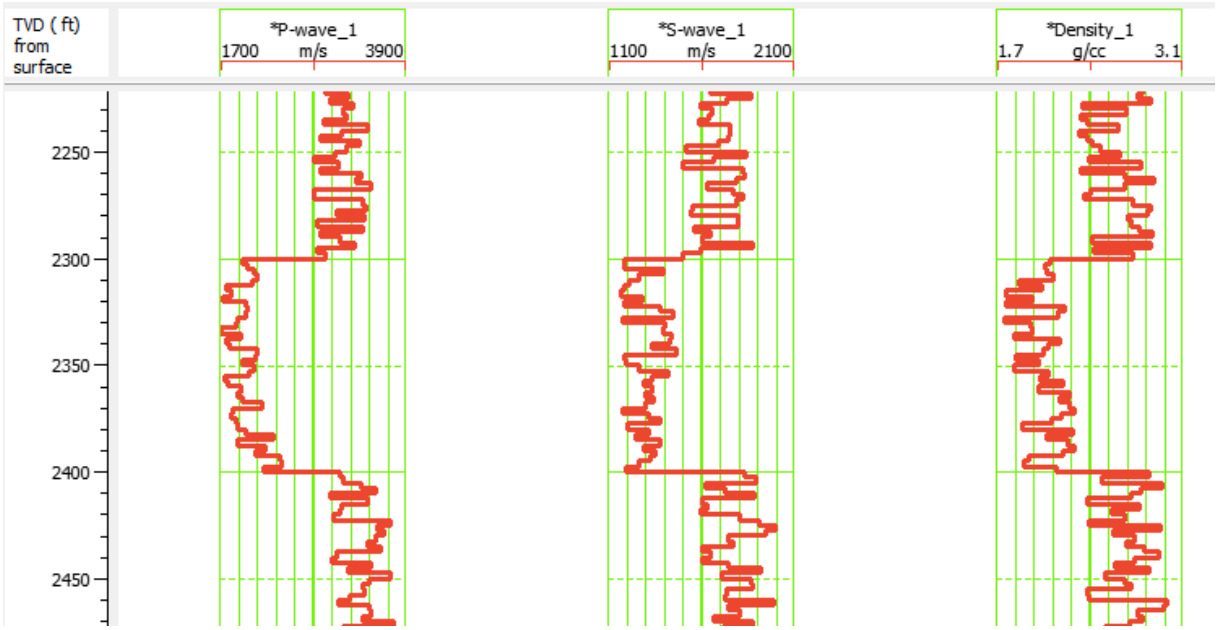


Figure 6.9 P-wave and S-wave velocities and densities at location 1 in model A after adding 12% uniformly distributed random noise.

The noise is increased to 12% and the resulting V_p, V_s and density are shown in Figure 6.9. The resulting intercept and gradient of the AVO for this case are shown in Figure 6.10. The intercept and gradient of the AVO are never both positive within the reservoir depth range of 2300 to 2400 ft. We use the green line in Figure 6.10 to show that the gradient is negative at the depth of 2350ft, which is where the bottom of the steam chamber is supposed to be. In this case, the AVO procedure breaks down and we are unable to pick the bottom of the steam chamber.

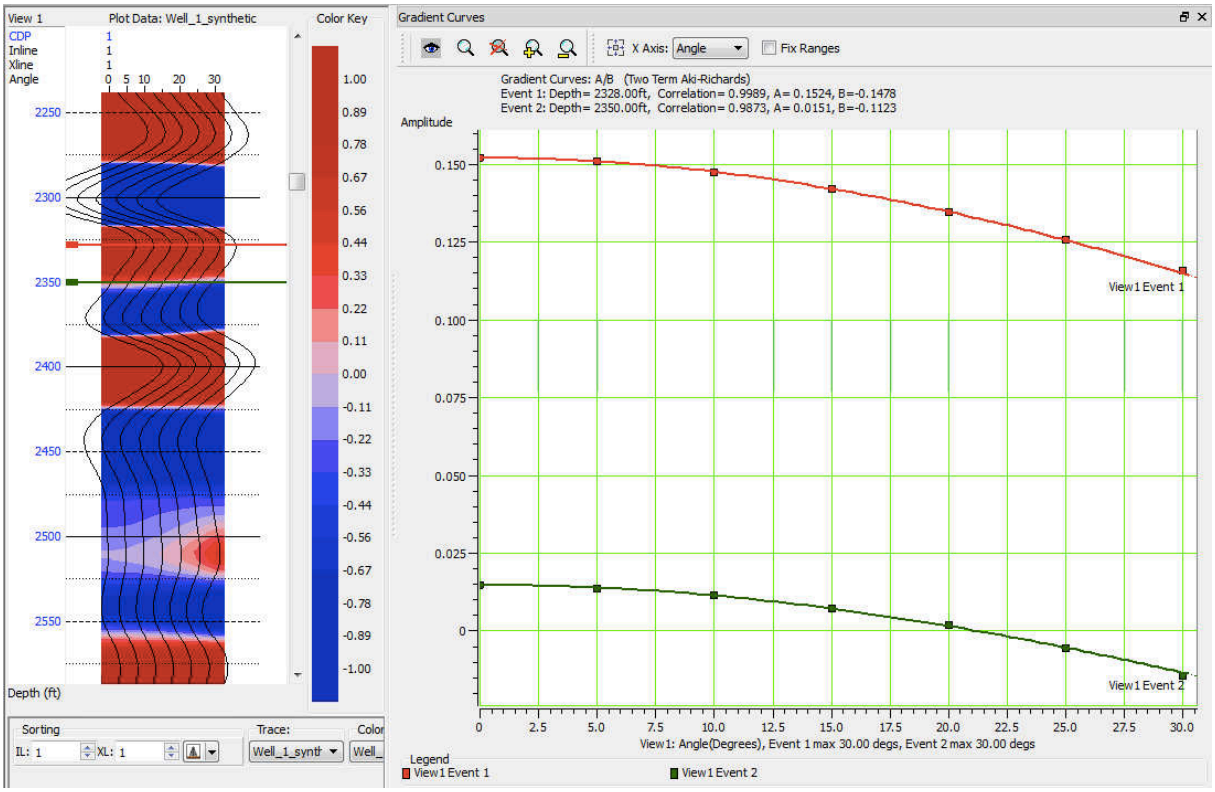


Figure 6.10: Intercept and gradient of the AVO at location 1 in model A for the case of 12% uniformly distributed added noise.

6.2 Testing AVO procedure robustness using model B

The AVO analysis was applied to three different locations in model B as shown in chapter 5 in Figure 5.26 without any noise added. In this section, we will test the robustness of the AVO procedure by adding uniformly distributed random noise to the seismic velocities and densities at location 2 in model B. The reason we choose location 2 of model B to test the robustness of our AVO procedure is the same reason we choose location 1 in model A, namely, because the thickness of the steam chamber there is 50 ft which puts the bottom of the steam chamber exactly at the middle of the 100 ft reservoir, hence as far as possible from the strong reflections from above, which represents the top of the reservoir, and below, which represents the bottom of the reservoir. This is important because we use seismic waves with a dominant frequency of 50 Hz, which results in a tuning thickness of only about 10m. This would not be enough to differentiate between the strong reflection from the top

and bottom of the reservoir from one side and the relatively weaker reflection representing the bottom of the steam chamber from the other side if the bottom of the steam chamber were further away from being at the middle of the reservoir. In other words, we want to test the robustness of our AVO procedure without adding the complication of seismic resolution issues caused by conducting the robustness tests at locations where the bottom of the steam chamber is shallower or deeper within the reservoir.

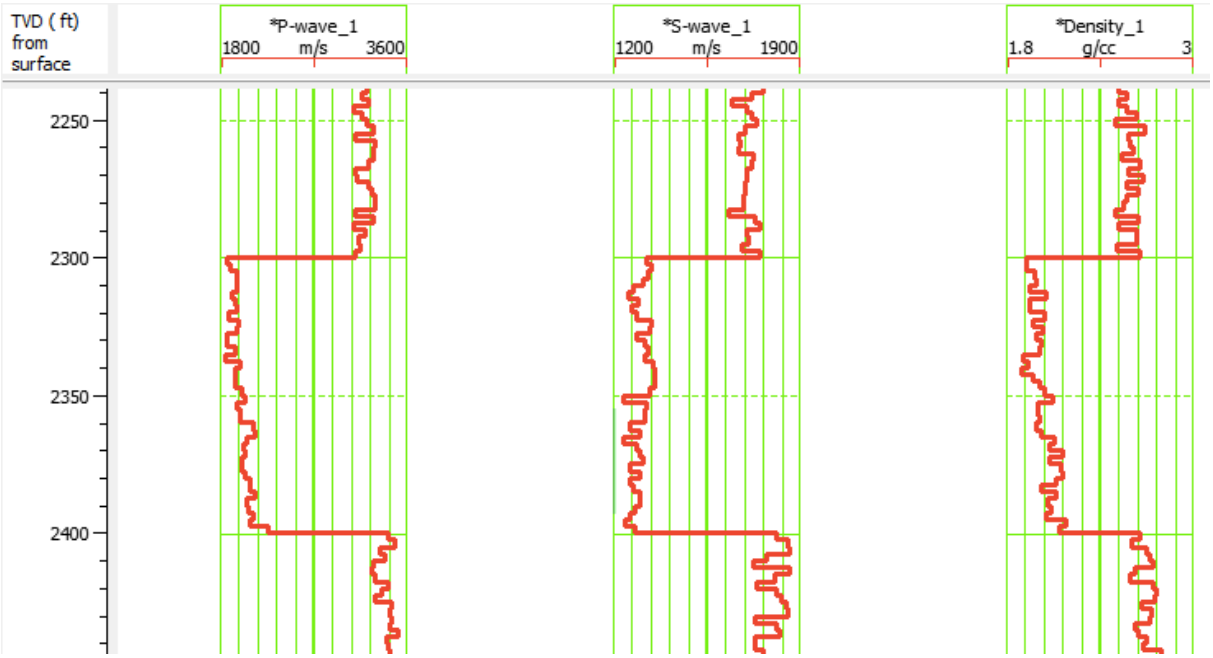


Figure 6.11: P-wave and S-wave velocities and densities at location 2 in model B after adding 4% uniformly distributed random noise.

We start by adding 4% uniformly distributed noise to the seismic velocities and densities. The resulting V_p, V_s and density are shown in Figure 6.11. The resulting intercept and gradient of the AVO for this case are shown in Figure 6.12. The intercept and gradient of the AVO are both positive in the depth range 2342 to 2355ft resulting in a steam chamber thickness range of 42 to 55 ft. Therefore, the bottom of the steam chamber is picked at the midpoint of that range which is 2349ft making our estimate of the steam chamber thickness to be 49 ft.

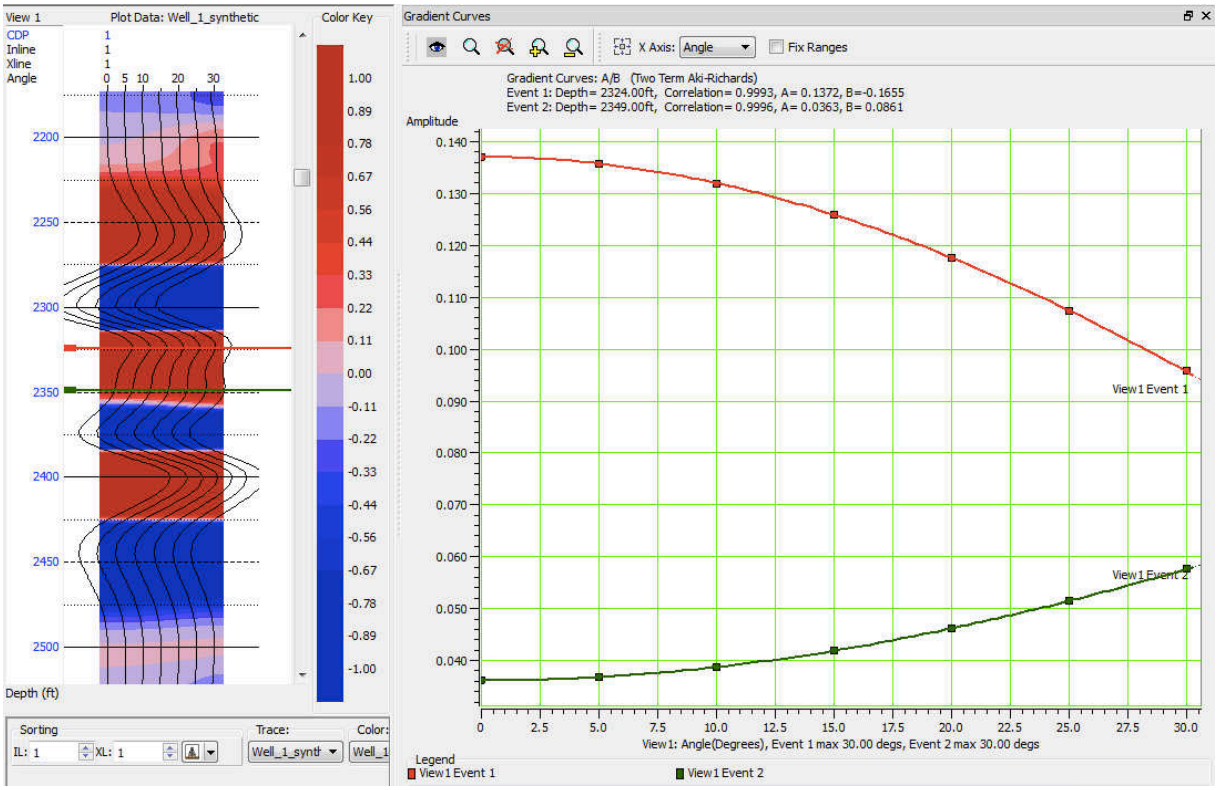


Figure 6.12: Intercept and gradient of the AVO at location 2 in model B for the case of 4% uniformly distributed added noise.

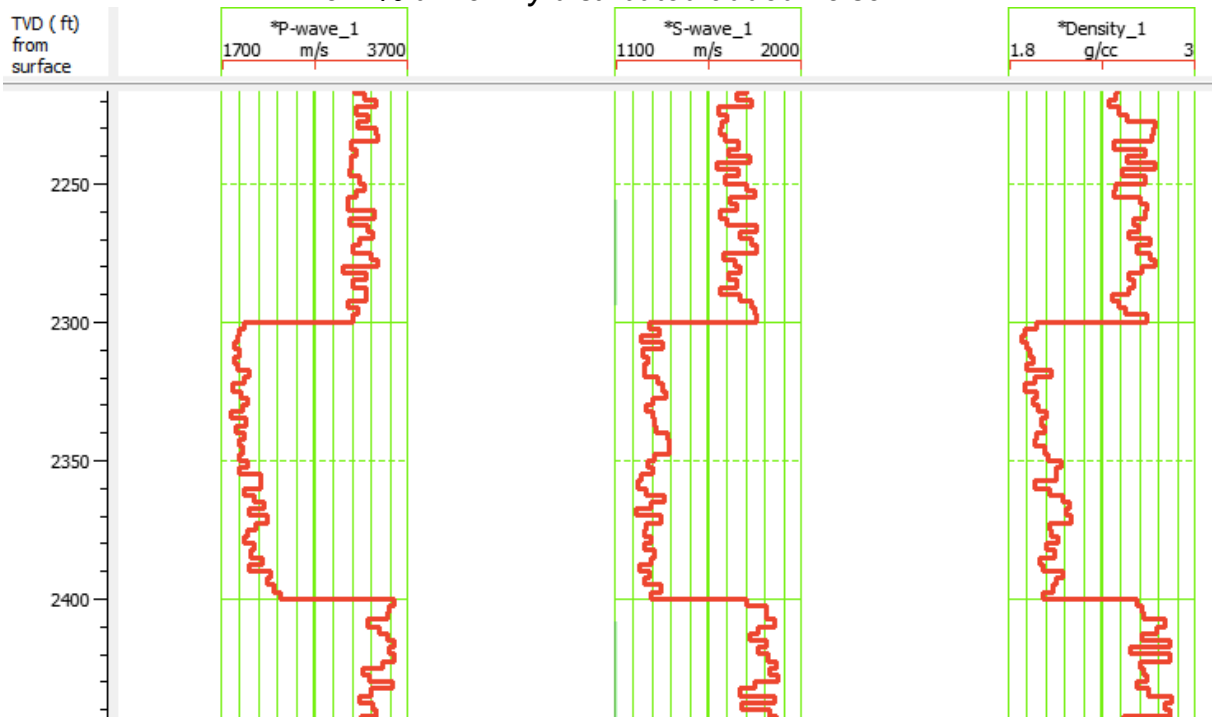


Figure 6.13: P-wave and S-wave velocities and densities at location 2 in model B after adding 6% uniformly distributed random noise.

The noise is increased to 6% and the resulting V_p, V_s and density are shown in Figure 6.13. The resulting intercept and gradient of the AVO for this case are shown in Figure 6.14. The intercept and gradient of the AVO are both positive in the depth

range 2342 to 2356ft resulting in a steam chamber thickness range of 42 to 56 ft. Therefore, the bottom of the steam chamber is picked at the midpoint of that range which is 2349ft making our estimate of the steam chamber thickness to be 49 ft.

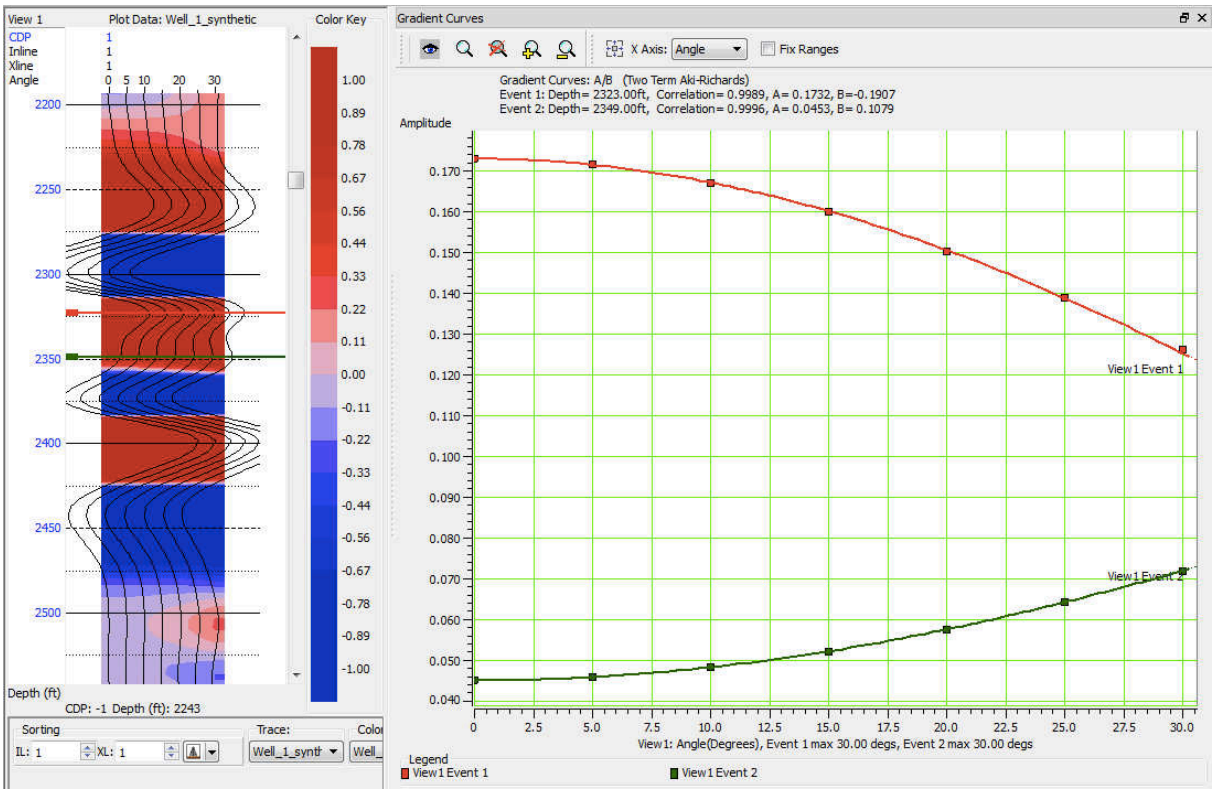


Figure 6.14: Intercept and gradient of the AVO at location 2 in model B for the case of 6% uniformly distributed added noise.

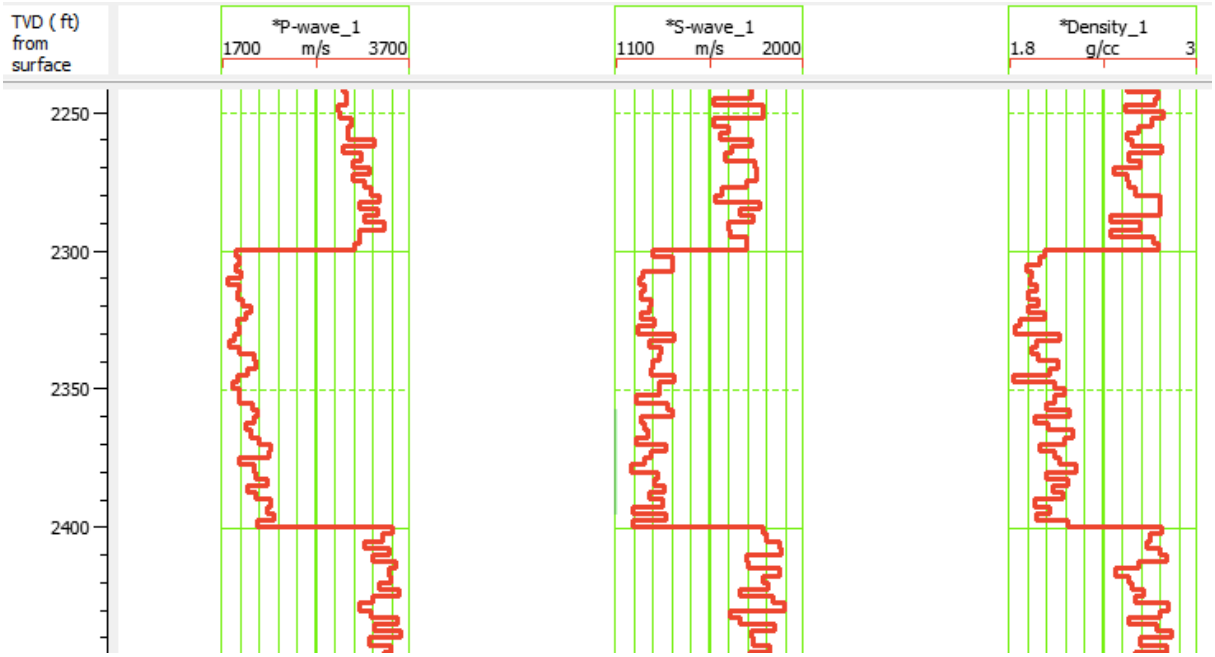


Figure 6.15: P-wave and S-wave velocities and densities at location 2 in model B after adding 8% uniformly distributed random noise.

The noise is increased to 8% and the resulting V_p, V_s and density are shown in Figure 6.15. The resulting intercept and gradient of the AVO for this case are shown in Figure 6.16. The intercept and gradient of the AVO are both positive in the depth range 2351 to 2355ft resulting in a steam chamber thickness range of 51 to 55 ft. Therefore, the bottom of the steam chamber is picked at the midpoint of that range which is 2353ft making our estimate of the steam chamber thickness to be 53 ft.

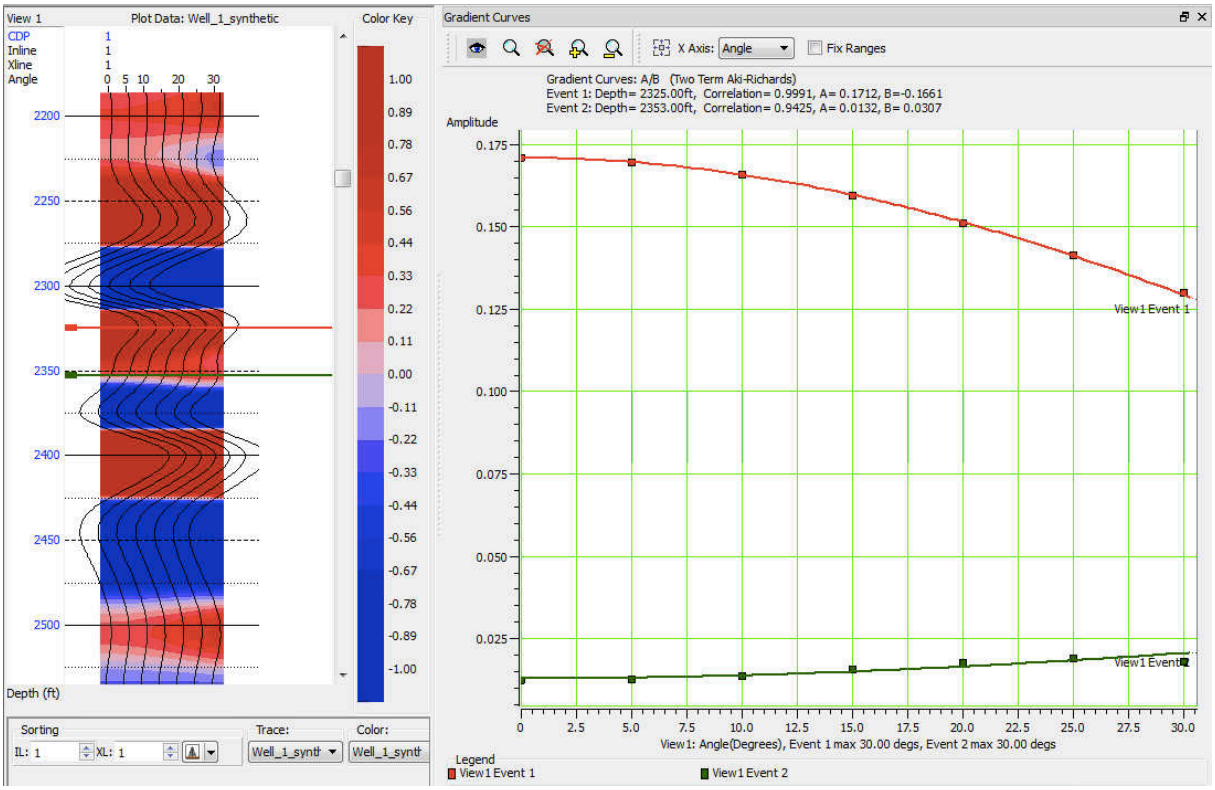


Figure 6.16: Intercept and gradient of the AVO at location 2 in model B for the case of 8% uniformly distributed added noise.

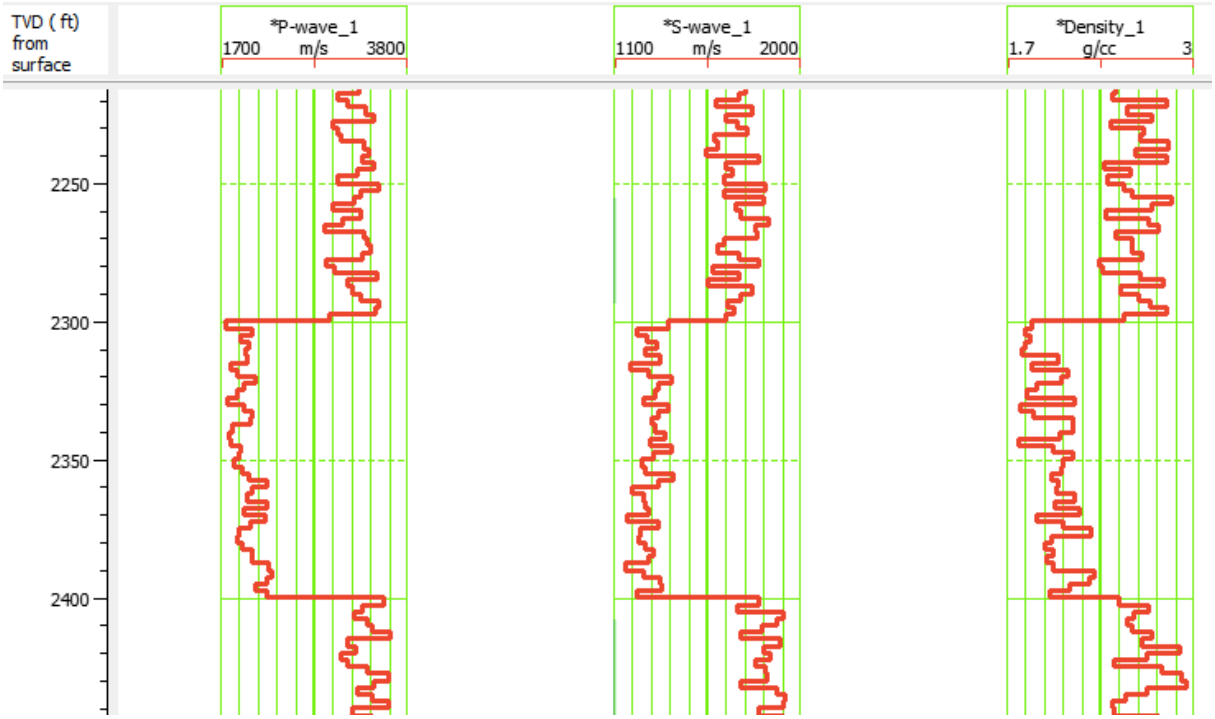


Figure 6.17: P-wave and S-wave velocities and densities at location 2 in model B after adding 10% uniformly distributed random noise.

The noise is increased to 10% and the resulting V_p, V_s and density are shown in Figure 6.17. The resulting intercept and gradient of the AVO for this case are shown in Figure 6.18. The intercept and gradient of the AVO are both positive in the depth range 2347 to 2356ft resulting in a steam chamber thickness range of 47 to 56 ft. Therefore, the bottom of the steam chamber is picked at the midpoint of that range which is 2352ft making our estimate of the steam chamber thickness to be 52 ft.

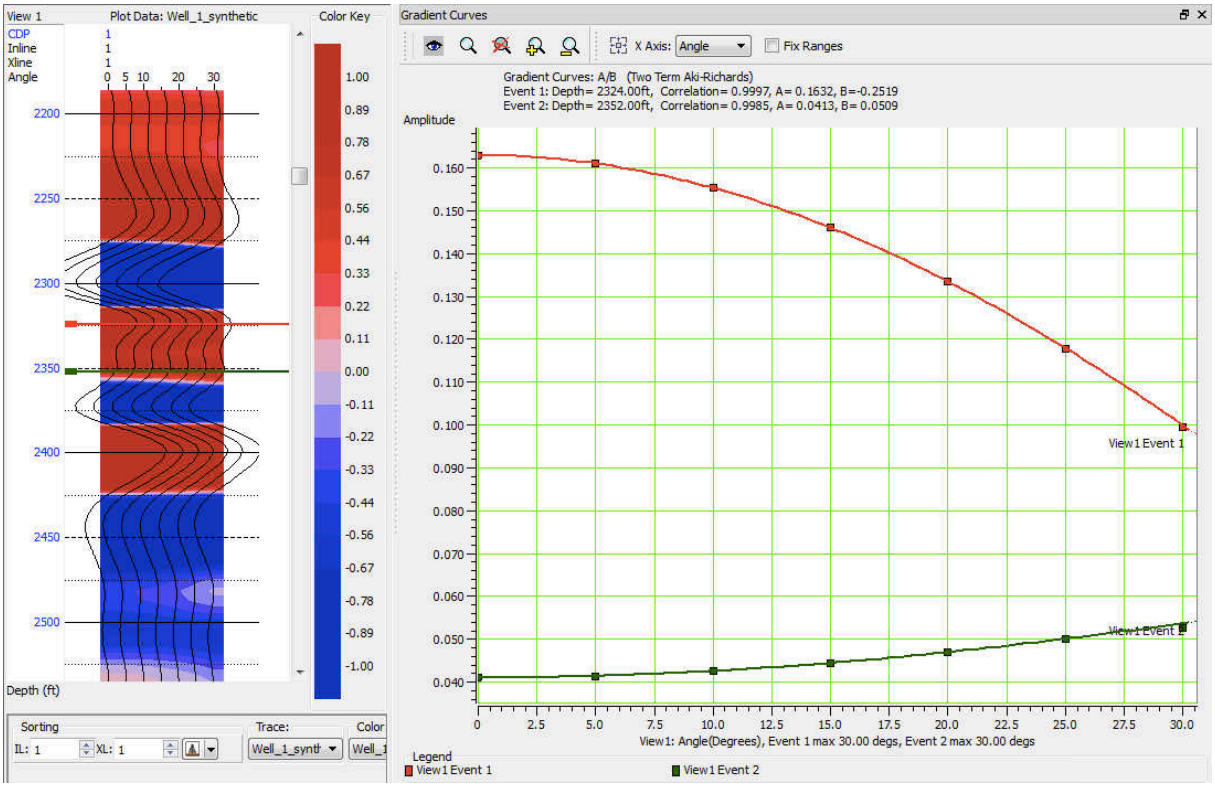


Figure 6.18: Intercept and gradient of the AVO at location 2 in model B for the case of 10% uniformly distributed added noise.

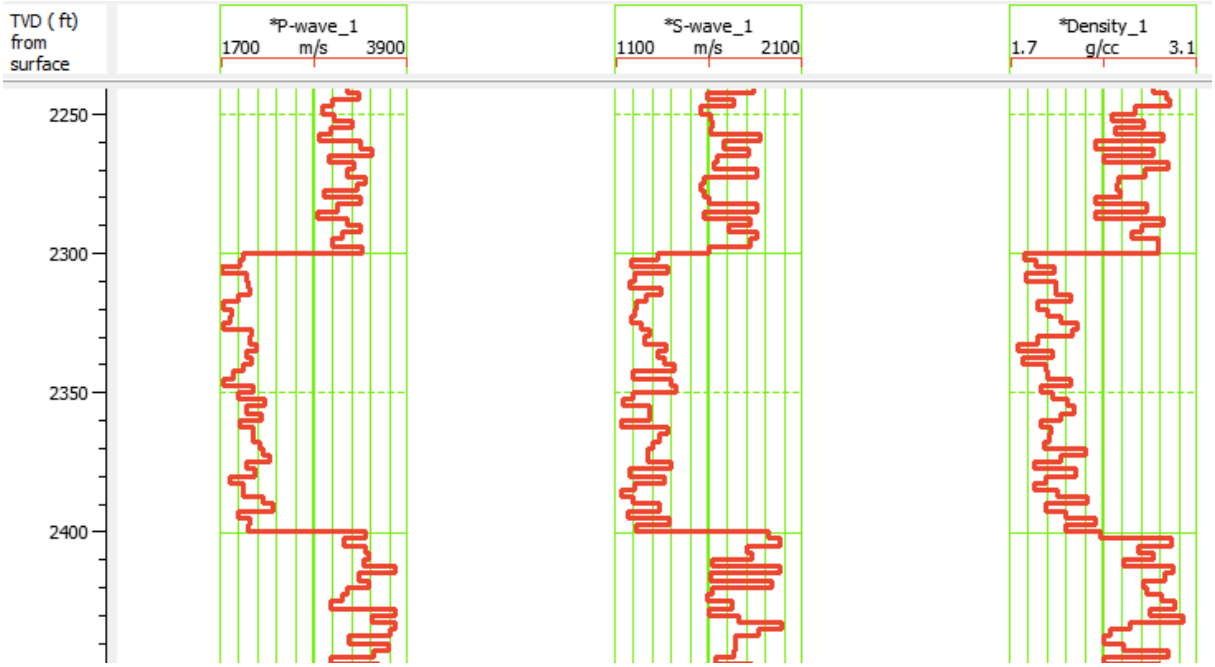


Figure 6.19: P-wave and S-wave velocities and densities at location 2 in model B after adding 12% uniformly distributed random noise.

The noise is increased to 12% and the resulting V_p, V_s and density are shown in Figure 6.19. The resulting intercept and gradient of the AVO for this case are shown in Figure 6.20. The intercept and gradient of the AVO are both positive in the

depth range 2343 to 2356 ft resulting in a steam chamber thickness range of 43 to 56 ft. Therefore, the bottom of the steam chamber is picked at the midpoint of that range which is 2350 ft making our estimate of the steam chamber thickness to be 50 ft.

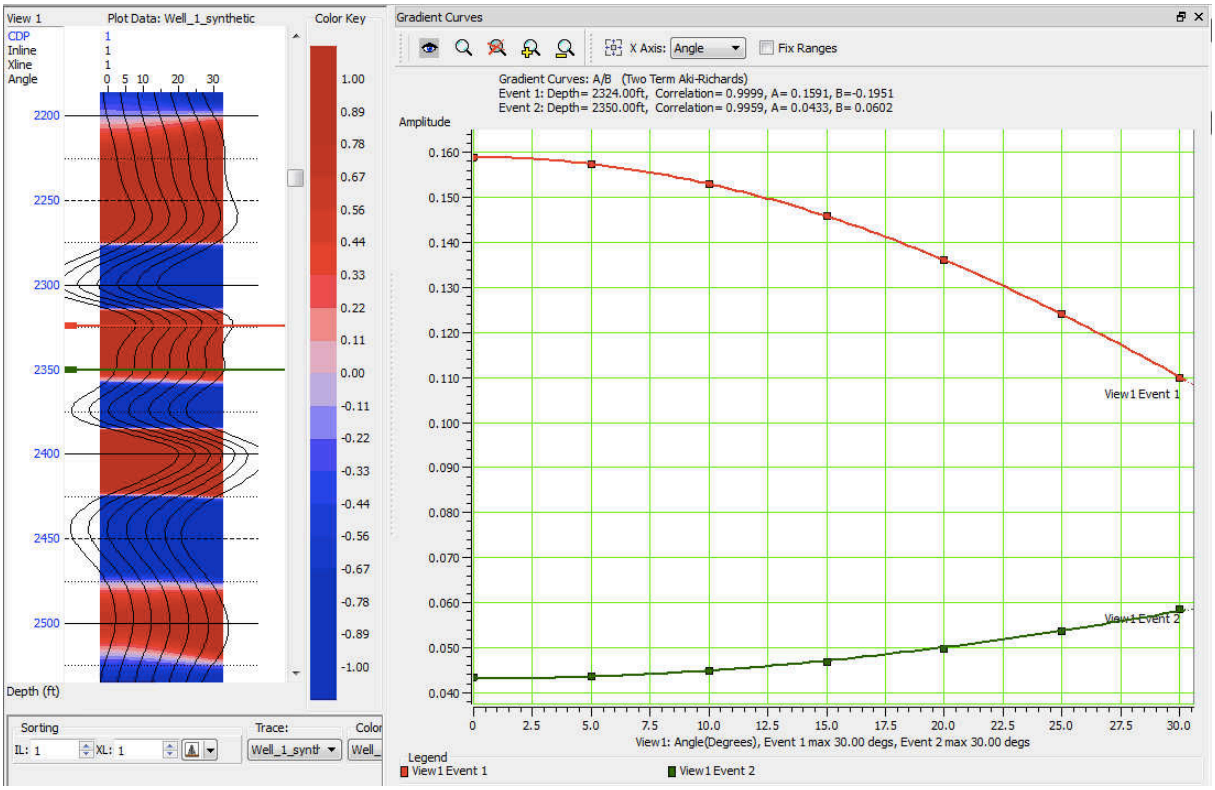


Figure 6.20: Intercept and gradient of the AVO at location 2 in model B for the case of 12% uniformly distributed added noise.

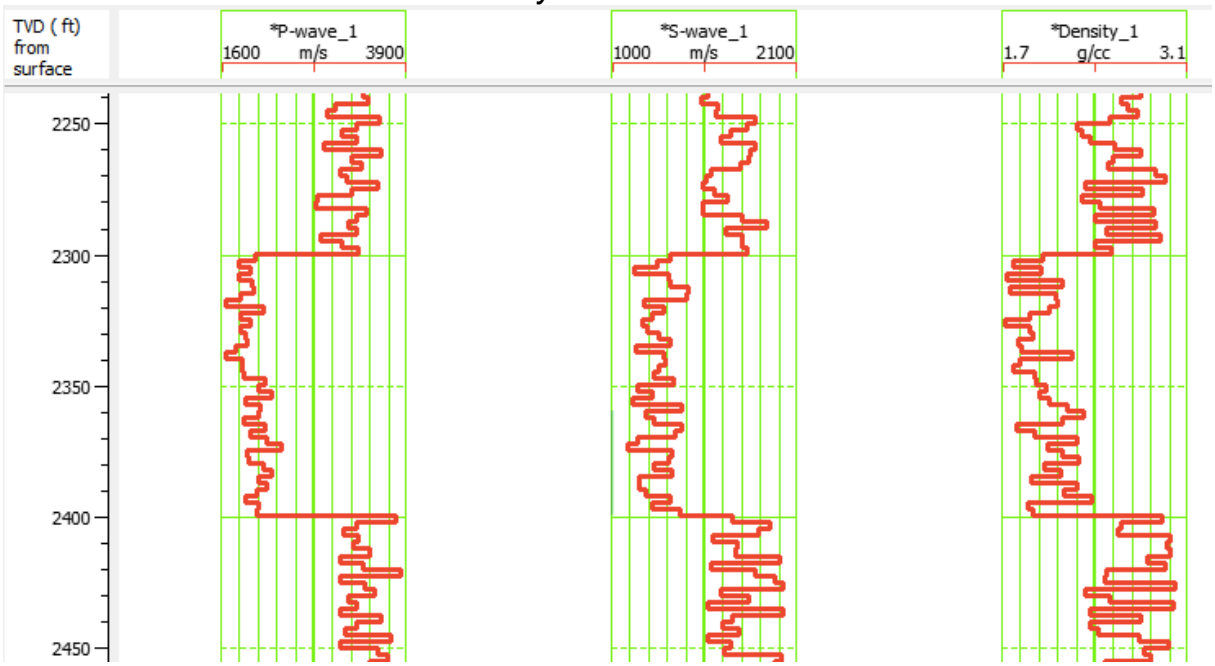


Figure 6.21: P-wave and S-wave velocities and densities at location 2 in model B after adding 14% uniformly distributed random noise.

The noise is increased to 14% and the resulting V_p, V_s and density are shown in Figure 6.21. The resulting intercept and gradient of the AVO for this case are shown in Figure 6.22. The intercept and gradient of the AVO are never both positive within the reservoir depth range of 2300 to 2400 ft. We use the green line in Figure 6.22 to show that the gradient is negative at the depth of 2350ft, which is where the bottom of the steam chamber is supposed to be. In this case, the AVO procedure breaks down and we are unable to pick the bottom of the steam chamber.

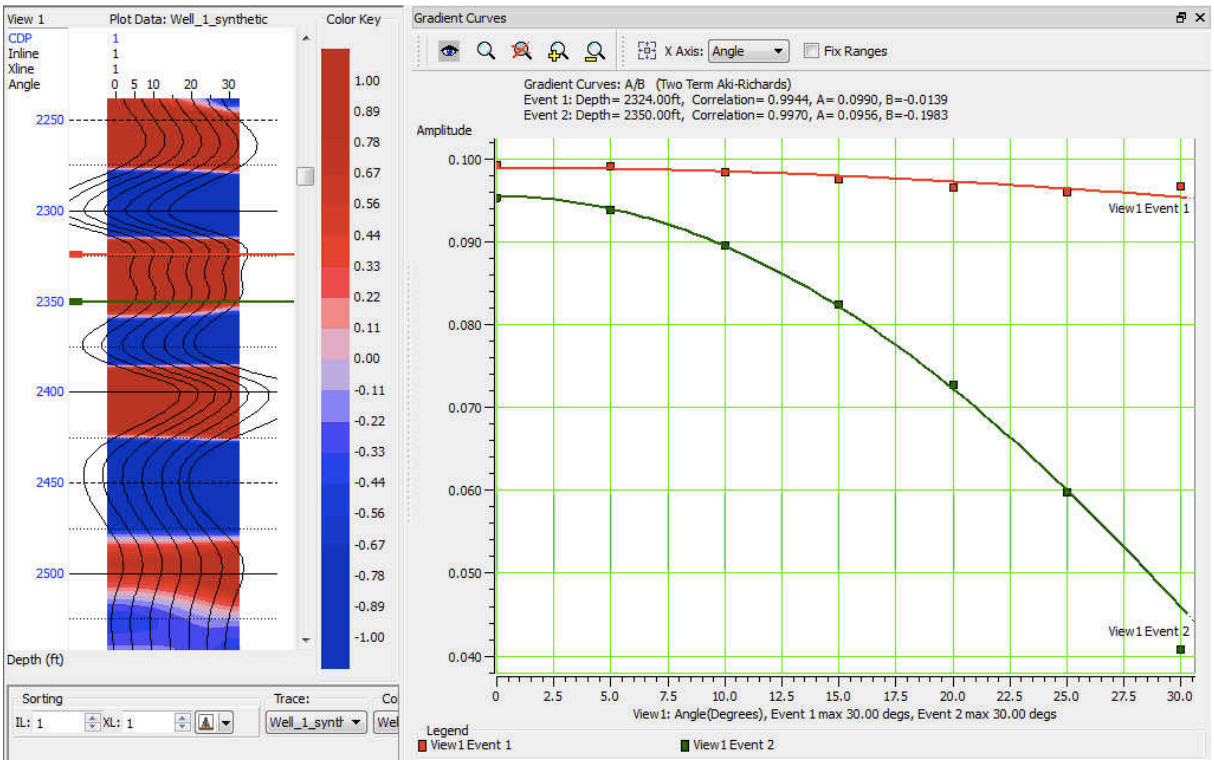


Figure 6.22: Intercept and gradient of the AVO at location 2 in model B for the case of 14% uniformly distributed added noise.

6.3 Summary

The AVO procedure was tested using two different models A and B as seen in Figures 5.16 and 5.26, respectively. Uniformly distributed noise was added to the V_p, V_s and density in increments of 2 starting from 4%. The bottom of the steam chamber was picked at the midpoint of the depth range at which both the AVO intercept and gradient were positive within the reservoir. The AVO procedure breaks down when the AVO intercept and gradient are both not positive anywhere within the reservoir. In

this case, we determine that we have reached the limit of our AVO procedure. The results after adding uniformly distributed noise to locations 1 in model A and location 2 in model B are summarized in Tables 6.1 and 6.2, respectively.

Added uniformly distributed noise (%)	Range of possible depths at which steam chamber bottom occurs (ft)	Depth at which bottom of steam chamber is picked (ft)	Deviation from actual depth of bottom of steam chamber (ft)
0	2350	2350	0
4	2345 to 2350	2348	-2
6	2352 to 2356	2354	+4
8	2332 to 2359	2346	-4
10	2348 to 2357	2353	+3
12	None	NA	NA

Table 6.1: Summary of results after adding uniformly distributed noise to location 1 in model A.

Added uniformly distributed noise (%)	Range of possible depths at which steam chamber bottom occurs (ft)	Depth at which bottom of steam chamber is picked (ft)	Deviation from actual depth of bottom of steam chamber (ft)
0	2350	2350	0
4	2342 to 2355	2349	-1
6	2342 to 2356	2349	-1
8	2351 to 2355	2353	+3
10	2347 to 2356	2352	+2
12	2343 to 2356	2350	0
14	None	NA	NA

Table 6.2: Summary of results after adding uniformly distributed noise to location 2 in model B.

Noise can come from perturbations to the observed signal. This includes noise caused by external sources during seismic data acquisition such as wind or moving objects, or noise caused by reflections and refractions from near-surface heterogeneities. Noise can also come from uncertainties in the data or rock physics model. For example, the reservoir can have a different relative permeability curve; a different vertical to horizontal permeability ratio, or the reservoir can be heterogeneous. We chose to add a uniformly distributed random noise to the P-wave and S-wave velocities and densities because it is a general representation of the sources of noise mentioned above or a combination of them. The results in Tables 6.1 and 6.2 show that our AVO procedure is robust and applicable to real data with as much as about 12% noise and possibly even a little more.

Lateral heterogeneity can affect the AVO results. Unfortunately, the noise added in this chapter does not account for this because HampsonRussell software assumes uniform layers and does not accept lateral variations in the elastic moduli and densities. However, this issue can be resolved by conducting the AVO procedure over a narrower range of angles, e.g. zero to 20°. The intercept in this case would not change, but the gradient value would change without changing polarity. This would not affect our AVO procedure because it predicts where the bottom of the steam chamber is based on the intercept and gradient both being positive without regard to the actual value of the gradient of the AVO.

7. Conclusions and Future Work

7.1 Conclusions

This thesis investigates the feasibility for using AVO to better monitor steam injection in heavy oil reservoirs. A sensitivity study was conducted using reservoir simulation to study the sensitivity of production behaviour and steam chamber growth to different ranges of oil API, horizontal permeability, temperature of injected steam, initial reservoir pressure and porosity. The production behaviour and thickness of the steam chamber is most sensitive to variations in horizontal permeability for the range of parameters used in this study. Over the whole period of the simulation, which was 10 years, smaller horizontal permeabilities resulted in more recovered oil, lower steam to oil ratio, lower water cut at production well and thicker steam tongue.

In reality all reservoirs are heterogeneous which results in a more complicated production behaviour and steam chamber growth. For example, permeability heterogeneity could result in the development of multiple steam tongues at different locations within the reservoir. The simulations in this thesis represent a more idealized case, as we are interested in a well-developed steam tongue that varies in thickness from larger to smaller than the seismic resolution of about 35 ft. The AVO analysis is applied on the steam tongue to better identify the bottom of the steam, thus improve the delineation of the steam chamber and increase the sweep efficiency and ultimately the recovery factor of oil.

The rock physics code predicts the percentage change in V_p and V_s due to predefined changes in different reservoir parameters. A sensitivity study was conducted to investigate what V_p and V_s are most sensitive to. Any change smaller

than 5% is considered undetectable. Changes in temperature, porosity and brine saturation are detectable using V_p. On the other hand only porosity and pressure changes are detectable using V_s. Changes in brine salinity is undetectable in either case which is why it is not included in the AVO analysis.

Pre steam injection, the AVO intercept and gradient at the top of the reservoir is most sensitive to porosity and effective pressure. Post steam injection, the AVO intercept and gradient at the top of the steam chamber is most sensitive to porosity and effective pressure, while at the bottom of the steam chamber they are most sensitive to steam saturation, effective pressure and porosity. This suggests that steam saturation, effective pressure and porosity could be used to detect the bottom of the steam chamber. The oil API effect on the intercept and gradient of the AVO was insignificant in all cases.

A multi variable linear regression is performed to predict the AVO intercept and gradient by knowing the values of porosity, effective pressure, steam saturation, temperature and oil API. The regression was successful in fitting the available data at the top of the reservoir pre and post steam injection. However, the regression did not do a good job fitting the available data for the case of the bottom of the steam chamber. In all cases, the regression was unable to accurately predict the AVO intercept and gradient at points other than were the independent variables were originally tested, which is attributed to the fact that the dependent variables were calculated at the end points of each of the independent variables which does not capture the full complexity of the model.

The intercept and gradient of the two-term Aki-Richards approximation of the amplitude versus offset (AVO) equation was observed to be positive at the bottom of the steam chamber. This led to the development of the hypothesis that it is possible

to identify the bottom of the steam chamber using this and thus estimating the thickness of the steam chamber.

The AVO analysis procedure developed in this thesis was tested at 3 different locations in two different model reservoirs undergoing steam injection. A clear peak represents the bottom of the steam when a seismic wave with a dominant frequency of 100 Hz is used. However, that is not always the case when using the more realistic 50 Hz seismic waves. When the steam thickness is 50ft, the bottom of the steam chamber was identifiable both visually using the seismic trace and by the AVO procedure. However, when the steam thickness is 47.5 ft, it was difficult to identify the bottom of the steam visually using the seismic trace. This is where our AVO procedure is important and useful as it enables us to identify the bottom of the steam with confidence at a depth where both the intercept and gradient of the AVO are positive. In the case where the steam thickness is 40ft, we were unable to identify the bottom of the steam chamber visually using the seismic trace nor with the AVO analysis procedure. In model B, we were able to identify the bottom of the steam chamber at locations 1 and 2, where the steam thickness is 52.5 ft and 50 ft, respectively, both visually using the seismic trace and by using the AVO procedure. However, it was harder to identify the bottom of the steam visually using the seismic trace in the case of location 2 in model B, where the steam chamber is 50ft thick, using a seismic wave with the more realistic dominant frequency of 50 Hz. In the case of location 3 in model B, where the steam thickness is 42.5ft, we were unable to identify the bottom of the steam chamber visually using the seismic trace nor with the AVO analysis procedure.

In reality, data obtained from the field is always noisy. Noise can come from perturbations to the observed signal. This includes noise caused by external sources during seismic data acquisition such as wind or moving objects, or noise caused by

reflections and refractions from near-surface heterogeneities. We chose to add a uniformly distributed random noise to the P-wave and S-wave velocities and densities because it is a general representation of the sources of noise mentioned above or a combination of them.

To test the robustness and limitation of the AVO procedure, uniformly distributed noise was gradually added starting from 4% and in increment of 2% to the seismic velocities and densities at two locations. The AVO intercept and gradient were both positive at a range of depth. No pattern in the intercept or gradient of the AVO was observed that is indicative of the exact location of the bottom of the steam chamber within this depth range. Therefore, we specified the range of thickness of the steam chamber as an uncertainty, which is due to the presence of noise. We also propose a criteria to pick the bottom of the steam chamber when this uncertainty exists. The suggested criteria involve picking the bottom of the steam chamber at the midpoint of the range where the AVO intercept and gradient are both positive. Nevertheless, this assumption results in a fairly accurate prediction for the depth of the bottom of the steam chamber, hence the thickness of the steam chamber.

The AVO procedure developed in this thesis presents a novel way to determine the thickness of the steam chamber that complements current available methods involving using reflection seismology. As shown in this thesis, in some cases the AVO procedure was vital in determining the thickness of the steam chamber because it was not possible to pick the bottom of the steam visually using reflection seismology.

Lateral heterogeneity can affect the AVO results. Unfortunately, the noise added in this chapter does not account for this because HampsonRussell software assumes uniform layers and does not accept lateral variations in the elastic moduli

and densities. However, the effect of lateral heterogeneity can be mitigated by conducting the AVO procedure over a narrower range of angles, e.g. zero to 20°. The intercept in this case would not change, but the gradient value would change without changing polarity. This would not affect our AVO procedure because it predicts where the bottom of the steam chamber is based on the intercept and gradient both being positive without regard to the actual value of the gradient of the AVO. This hypothesis needs to be investigated in future work.

The AVO procedure developed in this thesis can be applied at any location and time to delineate the vertical extent of a steam chamber in a steam flood operation so long as the steam thickness is within the range that is resolvable by the seismic waves that are used. Initially, reservoir simulation results can help estimate the thickness of the steam chamber, thus helping in deciding where to apply the AVO analysis. This includes using the AVO procedure to delineate the steam chamber pro and post steam breakthrough. This helps to delineate the steam front, which can be used for history matching to improve the reservoir simulation results. This enables reservoir managers to make informed decisions that would increase the sweep efficiency and ultimately increase the oil recovery factor.

The AVO procedure developed in this thesis is intended for relatively shallow reservoirs with medium to heavy oil, which is the case for most oil reservoirs undergoing steam flooding. The AVO procedure was robust up to a noise level of about 12% assuming no lateral heterogeneity. It breaks down when the AVO intercept and gradient are both not positive anywhere within the reservoir. In this case, we determine that we have reached the limit of our AVO procedure.

7.2 Future Work

This study involved integrating 3 different disciplines from reservoir simulation to rock physics to exploration seismology. In each part, many parameters interact in a complex manner to generate the data needed to input into the next stage. It would be interesting to quantify different sources of noise and study the effect of that on the elastic moduli and densities and ultimately the AVO procedure developed in this thesis. It would also be useful to study the effect of lateral heterogeneity on the flow pattern and seismic signal and ultimately the robustness of the AVO procedure. Finally it would be useful to improve the least square regression by calculating the intercept and gradient of the AVO at more evenly spaced interval for the regression to capture the complexity of the actual AVO model and result in an improved multi variable linear regression model which can more accurately predict the dependent variables and save the full calculation process.

Appendix

Appendix A: Reservoir Simulation (STARS input file)

```
** OVERVIEW
** ========
** This is based on the STARS data set sttst07 for Problem 2A in "Fourth SPE
** Comparative Solution Project - A Comparison of Steam Injection
** Simulators", paper SPE 13510, presented at the eighth SPE symposium
** on reservoir simulation at Dallas, Texas, Feb 10-13, 1985.
** The original problem was oil displacment by steam in an inverted nine-spot
** pattern.  The oil consists of a single 14 deg API pseudo-component.
** Steam breakthrough times are sensitive to grid orientation effects.
** This problem has the same oil and reservoir properties as problem 1a.
** Only the grid and well data are different.
** This has been modified to be a simple vertical cross-section

** ==============  INPUT/OUTPUT CONTROL  ======================


** 2014-10-16, 16:27:37, hb1612
** 2014-10-16, 18:26:29, hb1612
** 2014-10-16, 19:20:21, hb1612
** 2014-10-16, 19:24:14, hb1612
** 2019-02-11, 12:50:22 PM, hb1612
** 2019-02-11, 12:51:03 PM, hb1612
** 2019-02-11, 01:29:30 PM, hb1612
** 2019-02-11, 01:38:48 PM, hb1612
** 2019-02-11, 02:36:11 PM, hb1612
** 2019-02-13, 01:22:14 PM, hb1612
** 2019-02-13, 02:24:22 PM, hb1612
** 2019-02-13, 02:32:41 PM, hb1612
** 2019-02-13, 02:49:05 PM, hb1612
** 2019-02-13, 03:55:29 PM, hb1612
** 2019-02-18, 11:43:51 AM, hb1612
RESULTS SIMULATOR STARS 201110
```

```
INTERRUPT STOP
TITLE1 'Steam flood'


*inunit *field   ** output same as input
OUTPRN GRID KRG KRO KRW MASDENG MASDENO MASDENW OBHLOSS PRES SG
SO SOLCONC
          SW TEMP VISO W X Y
OUTPRN WELL ALL
WRST 300
WPRN GRID 300
WPRN ITER 300
OUTSRF WELL LAYER ALL
OUTSRF GRID ALL
OUTSRF SPECIAL MATBAL  WELL 'OIL'
             SOR  'INJECTOR' 'PRDCR' CUM
             OBHLOSS
OUTSRF GRID ALL
OUTSRF GRID ALL
PARTCLSIZE 3.53147e-016

**  ==============  GRID AND RESERVOIR DEFINITION  =================


*grid *cart 100 1 40
*kdir *down

*DI *IVAR 1*2 98*5.06122 1*2
*dj *con 10
*dk *con 2.5
**$ Property: NULL Blocks  Max: 1  Min: 1
**$  0 = null block, 1 = active block
NULL CON           1

*por *con 0.3
*permi kvar
 10000 9751 9502 9253 9005 8756 8507 8258 8010 7761 7512 7264 7015 6766 6517 6269
6020 5771 5523 5274 5025 4776 4528 4279 4030 3782 3533 3284 3035 2787 2538 2289
```

```
2041 1792 1543 1294 1046 797 548 300
*permj *equalsi
*permk *equalsi  / 10
**$ Property: Pinchout Array  Max: 1  Min: 1
**$  0 = pinched block, 1 = active block
PINCHOUTARRAY CON           1

*end-grid
ROCKTYPE 1

*cpor 5e-4
*prpor 75
*rockcp 35
*thconr 24
THCONW 8.5
THCONO 4
THCONG 0.27
*hlossprop  overbur 35 24  underbur 35 24
**  ==============  FLUID DEFINITIONS  ======================
**$ Model and number of components
**$ Model and number of components
MODEL 2 2 2 1
** properties are defaulted (=0).  Dead oil K values
** are zero, and no gas properties are needed.
COMPNAME 'WATER' 'OIL'
**              -----    -------
CMM
18.02 600
** These four properties
PCRIT
3206.2 0
** are for the gas phase.
TCRIT
705.4 0
PRSR 1250
TEMR 99
PSURF 1250
```

```
TSURF 99
CPL1
0 300
MASSDEN
0 60.678
CP
0 5.e-6
CT1
0 3.8e-4
** The dead oil component does
AVG
1.13e-5 0
** not appear in the gas phase.
BVG
1.075 0
VISCTABLE
**$      temp
          99         0       175
         150         0        50
         200         0        22
         250         0        12
         300         0         7
         350         0         5
         400         0       3.5
         450         0       2.5
         500         0       1.8
         550         0       1.3
         600         0       1.0
         650         0       0.8
         700         0       0.7

**  ==============  ROCK-FLUID PROPERTIES  ======================

*rockfluid
RPT 1 WATWET

*swt   **  Water-oil relative permeabilities
```

```
**   Sw        Krw        Krow
** ----     --------    -------
   0.08     0.0         0.4
   0.1185   0.000056    0.361
   0.17625  0.000552    0.30625
   0.2725   0.00312     0.225
   0.36875  0.00861     0.15625
   0.465    0.01768     0.1
   0.56125  0.03088     0.05625
   0.6575   0.04871     0.025
   0.696    0.05724     0.016
   0.75375  0.07162     0.00625
   0.79225  0.08229     0.00225
   0.85     0.1         0.0

*slt   **  Liquid-gas relative permeabilities

**   Sl        Krg         Krog
** ----     -------     -------
   0.08     0.2         0.0
   0.55     0.14202     0.0
   0.57     0.13123     0.00079
   0.60     0.11560     0.00494
   0.62     0.10555     0.00968
   0.65     0.09106     0.01975
   0.67     0.08181     0.02844
   0.70     0.06856     0.04444
   0.72     0.06017     0.05709
   0.75     0.04829     0.07901
   0.77     0.04087     0.09560
   0.80     0.03054     0.12346
   0.83     0.02127     0.15486
   0.85     0.01574     0.17778
   0.87     0.01080     0.20227
   0.90     0.00467     0.24198
   0.92     0.00165     0.27042
```

```
   0.94     0.0         0.30044
   1.       0.0         0.4

**  ==============  INITIAL CONDITIONS  ======================

*initial

** Automatic static vertical equilibrium
*vertical *depth_ave

REFPRES 1200

REFBLOCK 1 1 1

*temp *con 99

**  ==============  NUMERICAL CONTROL  ======================

*numerical   ** All these can be defaulted.  The definitions
** here match the previous data.
NORM PRESS 200 SATUR 0.2 TEMP 50

*run

**  ==============  RECURRENT DATA  ======================
** Project starts on Jan 1, 2014
date 2014 1 1

  dtwell 1
**
**                                      **
**    well 1 'INJECTOR'    vert 1 1  frac .125    **
**$
**$
**$
**$
WELL  'INJECTOR'  VERT  1  1  FRAC  0.125
```

```
                                ** 1 o o o o o o o 2
INJECTOR MOBWEIGHT EXPLICIT 'INJECTOR'

INCOMP  WATER  1.  0.

TINJW  600.

QUAL  0.8

OPERATE  MAX  BHP  3000.  CONT REPEAT

OPERATE  MAX  STW  100.  CONT REPEAT

        **  k  wi       ** Inject only in the bottom layer

                    ** .007082*k*h / ln(cc*sqrt((dx**2+dy**2)/pi)/rw)

**$ UBA    wi       Status  Connection

**$ UBA    ff  Status  Connection

**$         rad  geofac  wfrac  skin

GEOMETRY  K  1.  0.249  1.  0.

PERF  GEO  'INJECTOR'

**$ UBA     ff  Status  Connection

   1 1 1   1.  OPEN    FLOW-FROM  'SURFACE'  REFLAYER
   1 1 2   1.  OPEN    FLOW-FROM  1
   1 1 3   1.  OPEN    FLOW-FROM  2
   1 1 4   1.  OPEN    FLOW-FROM  3
   1 1 5   1.  OPEN    FLOW-FROM  4
   1 1 6   1.  OPEN    FLOW-FROM  5
   1 1 7   1.  OPEN    FLOW-FROM  6
   1 1 8   1.  OPEN    FLOW-FROM  7
   1 1 9   1.  OPEN    FLOW-FROM  8
   1 1 10  1.  OPEN    FLOW-FROM  9
   1 1 11  1.  OPEN    FLOW-FROM  10
   1 1 12  1.  OPEN    FLOW-FROM  11
   1 1 13  1.  OPEN    FLOW-FROM  12
   1 1 14  1.  OPEN    FLOW-FROM  13
   1 1 15  1.  OPEN    FLOW-FROM  14
   1 1 16  1.  OPEN    FLOW-FROM  15
   1 1 17  1.  OPEN    FLOW-FROM  16
   1 1 18  1.  OPEN    FLOW-FROM  17
```

```
   1 1 19  1.  OPEN    FLOW-FROM  18
   1 1 20  1.  OPEN    FLOW-FROM  19
   1 1 21  1.  OPEN    FLOW-FROM  20
   1 1 22  1.  OPEN    FLOW-FROM  21
   1 1 23  1.  OPEN    FLOW-FROM  22
   1 1 24  1.  OPEN    FLOW-FROM  23
   1 1 25  1.  OPEN    FLOW-FROM  24
   1 1 26  1.  OPEN    FLOW-FROM  25
   1 1 27  1.  OPEN    FLOW-FROM  26
   1 1 28  1.  OPEN    FLOW-FROM  27
   1 1 29  1.  OPEN    FLOW-FROM  28
   1 1 30  1.  OPEN    FLOW-FROM  29
   1 1 31  1.  OPEN    FLOW-FROM  30
   1 1 32  1.  OPEN    FLOW-FROM  31
   1 1 33  1.  OPEN    FLOW-FROM  32
   1 1 34  1.  OPEN    FLOW-FROM  33
   1 1 35  1.  OPEN    FLOW-FROM  34
   1 1 36  1.  OPEN    FLOW-FROM  35
   1 1 37  1.  OPEN    FLOW-FROM  36
   1 1 38  1.  OPEN    FLOW-FROM  37
   1 1 39  1.  OPEN    FLOW-FROM  38
   1 1 40  1.  OPEN    FLOW-FROM  39
**    well 2 'PRDCR'  vert 30 1  frac .125    **
**$
**$
**$
**$
WELL  'PRDCR'  VERT  30  1  FRAC  0.125
                     ** k = 2000 md, h = 25 ft, dx = dy = 29.17 ft,
                     ** cc = 0.249, rw = 0.3 ft
                    ** Steam CWE in bbl/day
PRODUCER 'PRDCR'
OPERATE  MIN  BHP  15.  CONT REPEAT
OPERATE  MAX  STL  100.  CONT REPEAT
          ** k   wi
```

```
**$ UBA    wi      Status  Connection
**$ UBA    ff  Status  Connection
**$ UBA      ff  Status  Connection
**$          rad  geofac  wfrac  skin
GEOMETRY  K  1.  0.249  1.  0.
PERF  GEO  'PRDCR'
**$ UBA      ff  Status  Connection
   100 1 1   1.  OPEN    FLOW-TO  'SURFACE'  REFLAYER
   100 1 2   1.  OPEN    FLOW-TO  1
   100 1 3   1.  OPEN    FLOW-TO  2
   100 1 4   1.  OPEN    FLOW-TO  3
   100 1 5   1.  OPEN    FLOW-TO  4
   100 1 6   1.  OPEN    FLOW-TO  5
   100 1 7   1.  OPEN    FLOW-TO  6
   100 1 8   1.  OPEN    FLOW-TO  7
   100 1 9   1.  OPEN    FLOW-TO  8
   100 1 10  1.  OPEN    FLOW-TO  9
   100 1 11  1.  OPEN    FLOW-TO  10
   100 1 12  1.  OPEN    FLOW-TO  11
   100 1 13  1.  OPEN    FLOW-TO  12
   100 1 14  1.  OPEN    FLOW-TO  13
   100 1 15  1.  OPEN    FLOW-TO  14
   100 1 16  1.  OPEN    FLOW-TO  15
   100 1 17  1.  OPEN    FLOW-TO  16
   100 1 18  1.  OPEN    FLOW-TO  17
   100 1 19  1.  OPEN    FLOW-TO  18
   100 1 20  1.  OPEN    FLOW-TO  19
   100 1 21  1.  OPEN    FLOW-TO  20
```

100 1 22 1. OPEN FLOW-TO 21

100 1 23 1. OPEN FLOW-TO 22

100 1 24 1. OPEN FLOW-TO 23

100 1 25 1. OPEN FLOW-TO 24

100 1 26 1. OPEN FLOW-TO 25

100 1 27 1. OPEN FLOW-TO 26

100 1 28 1. OPEN FLOW-TO 27

100 1 29 1. OPEN FLOW-TO 28

100 1 30 1. OPEN FLOW-TO 29

100 1 31 1. OPEN FLOW-TO 30

100 1 32 1. OPEN FLOW-TO 31

100 1 33 1. OPEN FLOW-TO 32

100 1 34 1. OPEN FLOW-TO 33

100 1 35 1. OPEN FLOW-TO 34

100 1 36 1. OPEN FLOW-TO 35

100 1 37 1. OPEN FLOW-TO 36

100 1 38 1. OPEN FLOW-TO 37

100 1 39 1. OPEN FLOW-TO 38

100 1 40 1. OPEN FLOW-TO 39

time 90

time 180

time 270

time 360

time 450

time 540

time 630

time 720

time 810

time 900

time 990

time 1080

time 1260

time 1440

time 1800

time 2160

time 2520

time 2880

time 3240

time 3600

stop

RESULTS SPEC 'Permeability J'

RESULTS SPEC SPECNOTCALCVAL -99999

RESULTS SPEC REGION 'All Layers (Whole Grid)'

RESULTS SPEC REGIONTYPE 'REGION_WHOLEGRID'

RESULTS SPEC LAYERNUMB 0

RESULTS SPEC PORTYPE 1

RESULTS SPEC EQUALSI 0 1

RESULTS SPEC SPECKEEPMOD 'YES'

RESULTS SPEC STOP

RESULTS SPEC 'Permeability K'

RESULTS SPEC SPECNOTCALCVAL -99999

RESULTS SPEC REGION 'All Layers (Whole Grid)'

RESULTS SPEC REGIONTYPE 'REGION_WHOLEGRID'

RESULTS SPEC LAYERNUMB 0

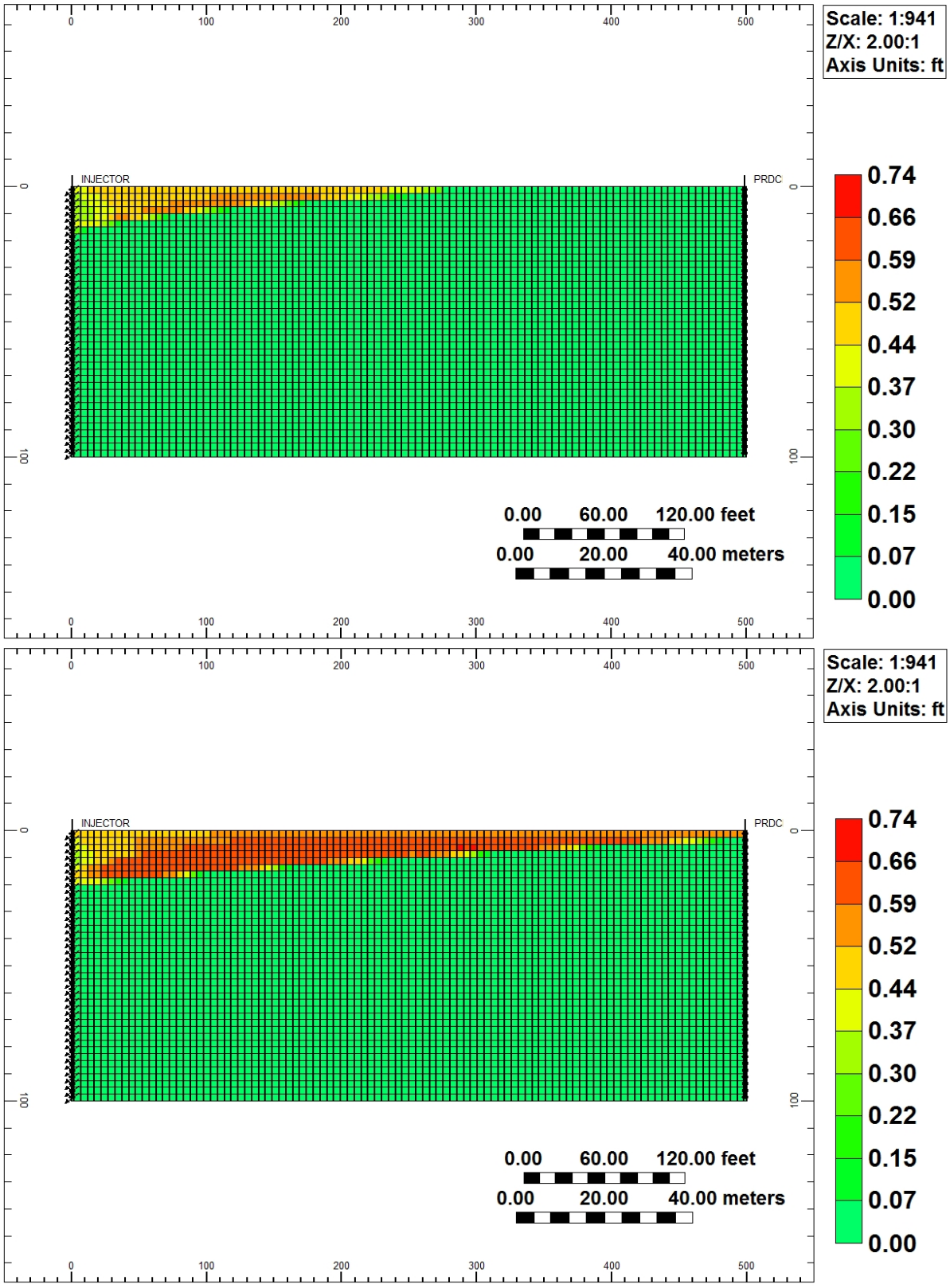
RESULTS SPEC PORTYPE 1

RESULTS SPEC EQUALSI 2 2

RESULTS SPEC SPECKEEPMOD 'YES'

RESULTS SPEC STOP

Appendix B: Steam saturations for the 7 other models in the sensitivity study



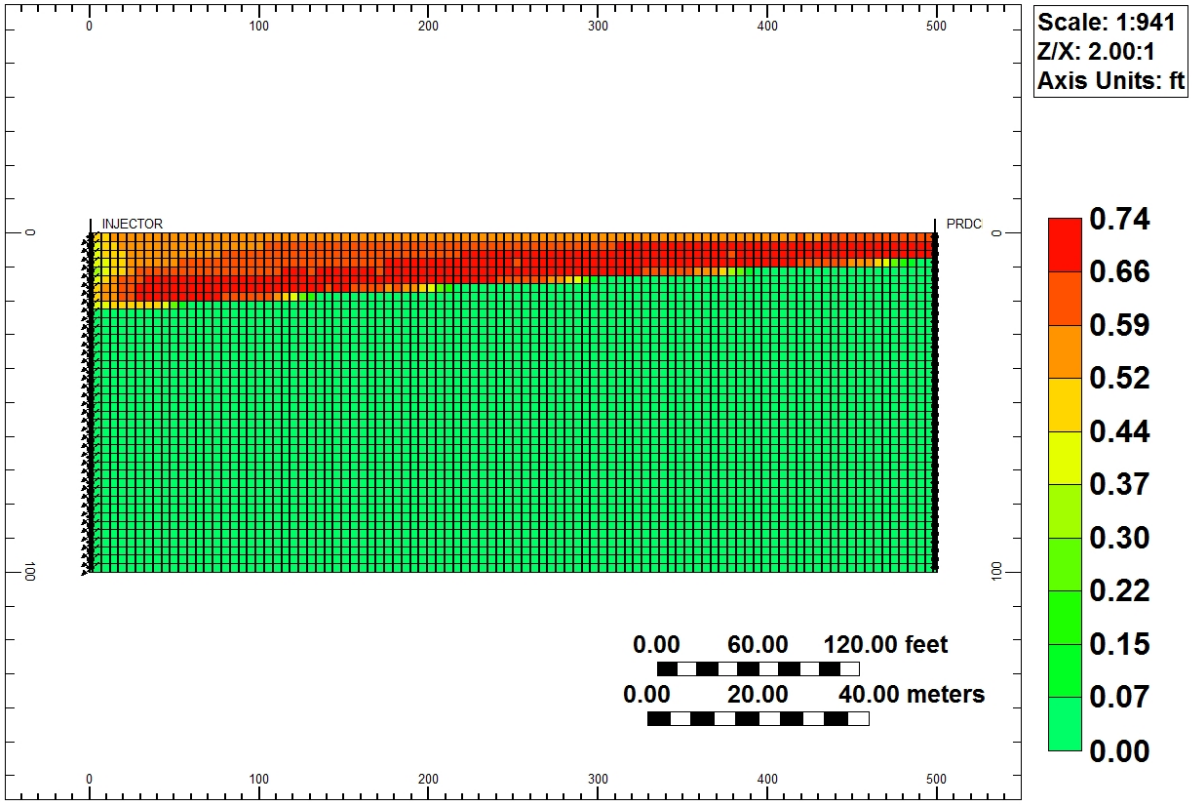
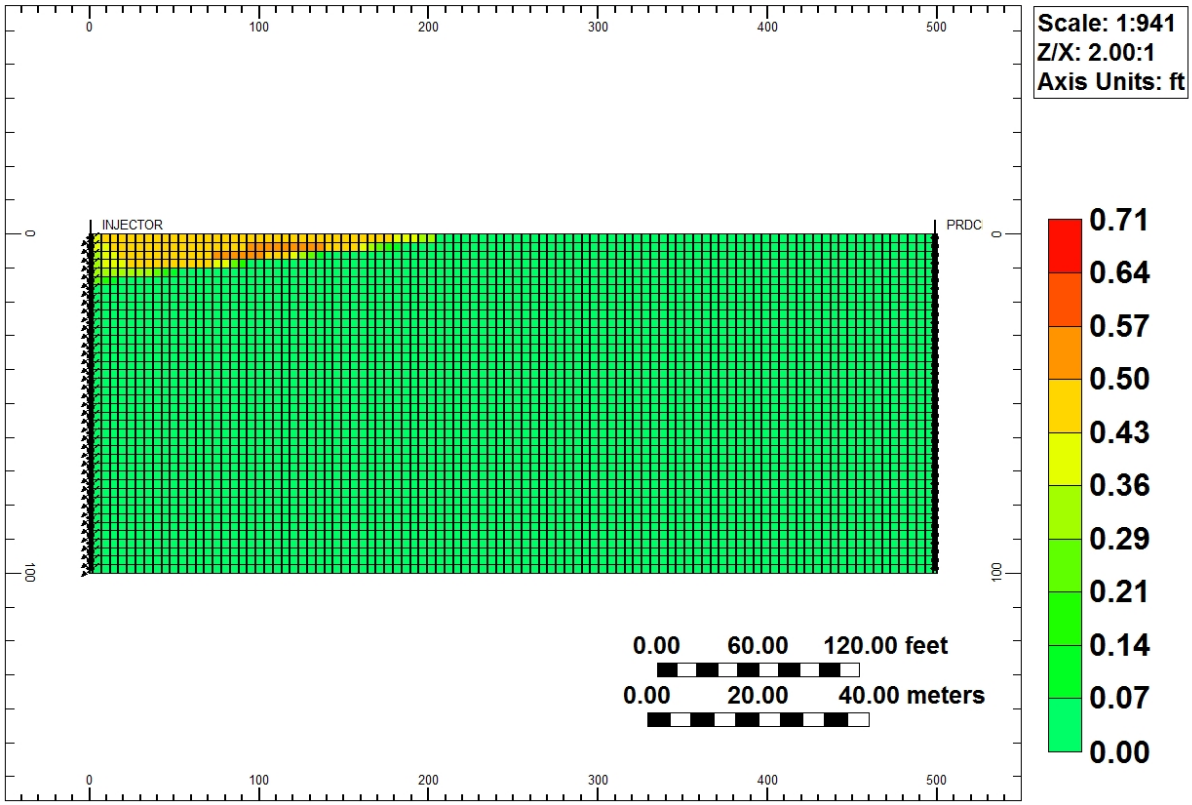


Figure B-1: Cross-section showing steam saturation for the case where the initial reservoir pressure is 4 MPa after 1, 4 and 10 years of steam injection with all other parameters set to the reference values listed in Table 3.5. The injection well is on the left while production well is on the right.



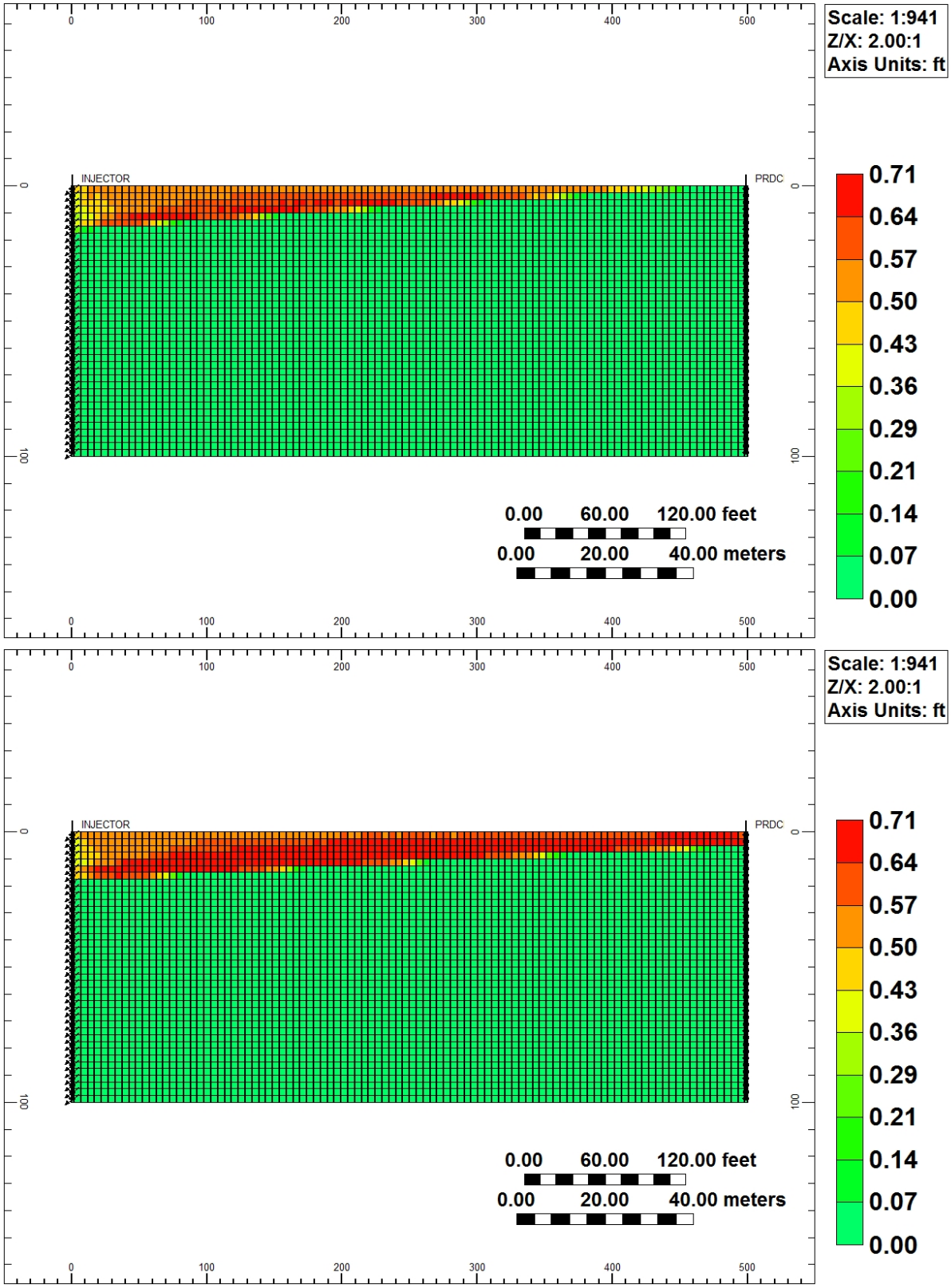
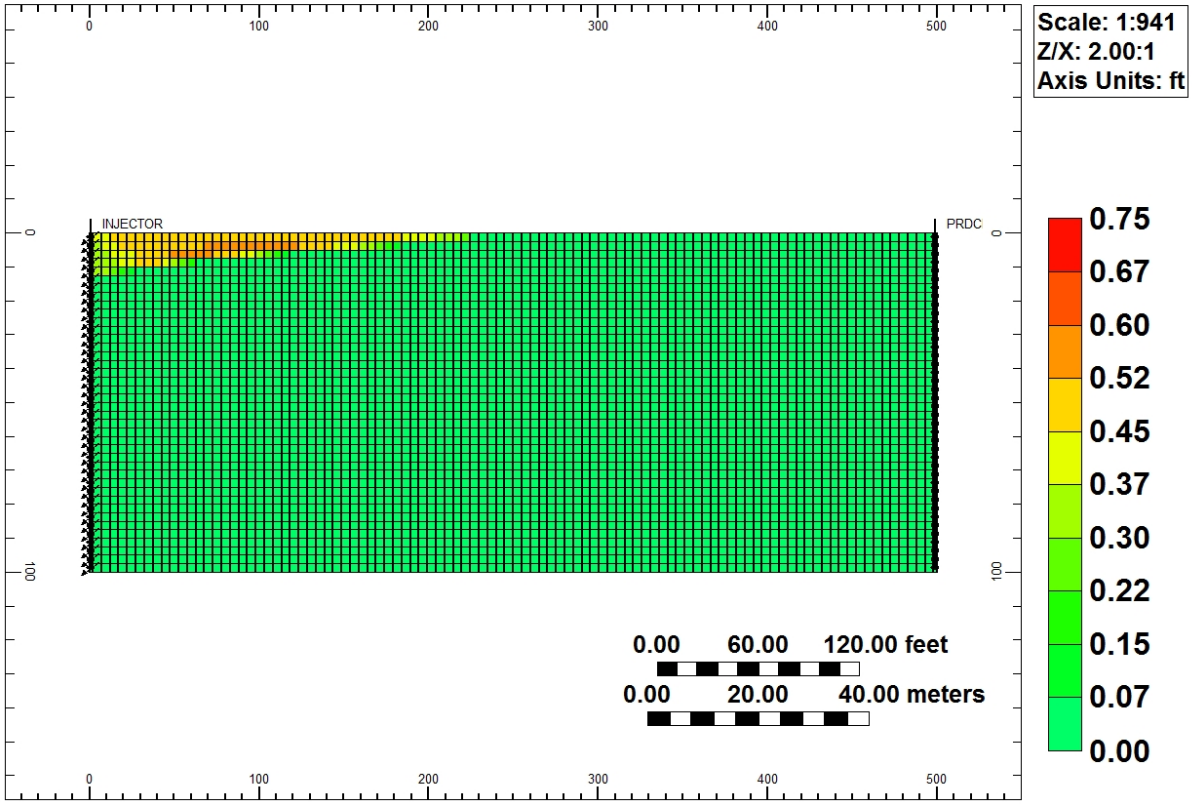
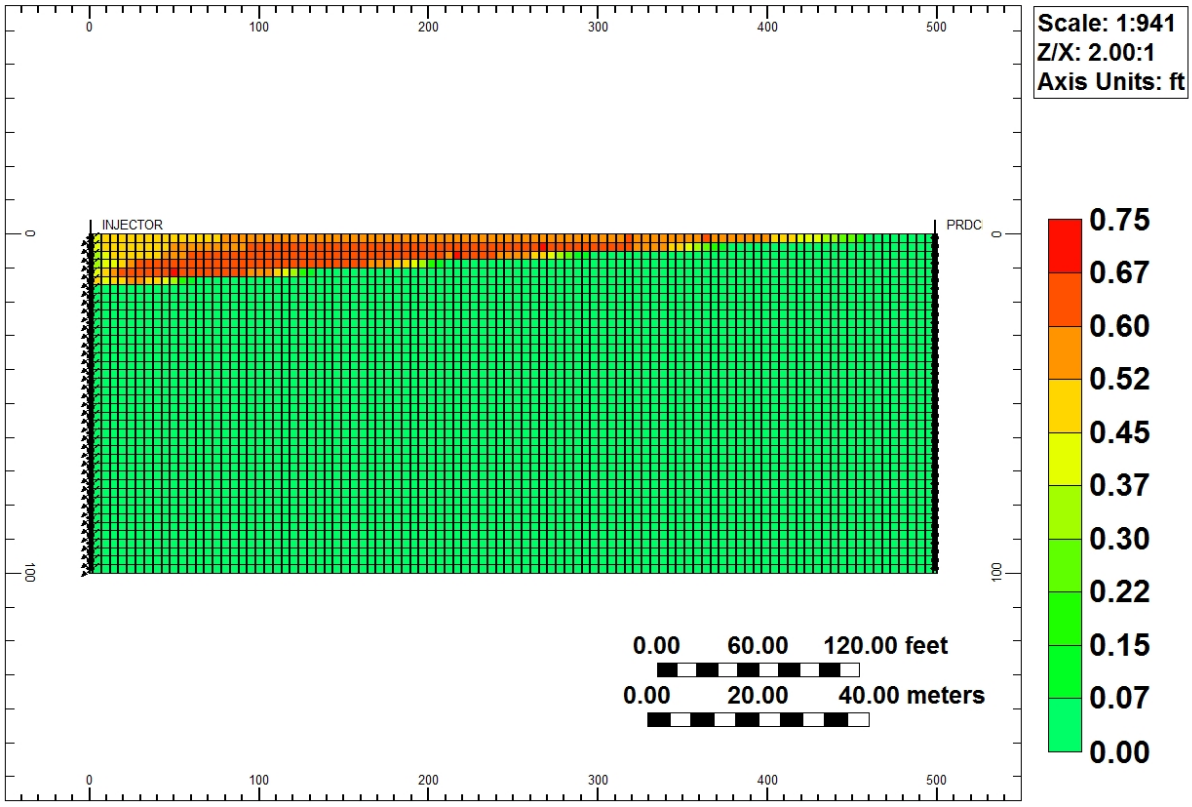


Figure B-2: Cross-section showing steam saturation for the case where the horizontal permeability is 10 Darcy after 1, 4 and 10 years of steam injection with all other parameters set to the reference values listed in Table 3.5. The injection well is on the left while production well is on the right.


Scale: 1:941
Z/X: 2.00:1
Axis Units: ft
INJECTOR
PRDC
0.00 60.00 120.00 feet
0.00 20.00 40.00 meters
0.75
0.67
0.60
0.52
0.45
0.37
0.30
0.22
0.15
0.07
0.00


Scale: 1:941
Z/X: 2.00:1
Axis Units: ft
INJECTOR
PRDC
0.00 60.00 120.00 feet
0.00 20.00 40.00 meters
0.75
0.67
0.60
0.52
0.45
0.37
0.30
0.22
0.15
0.07
0.00

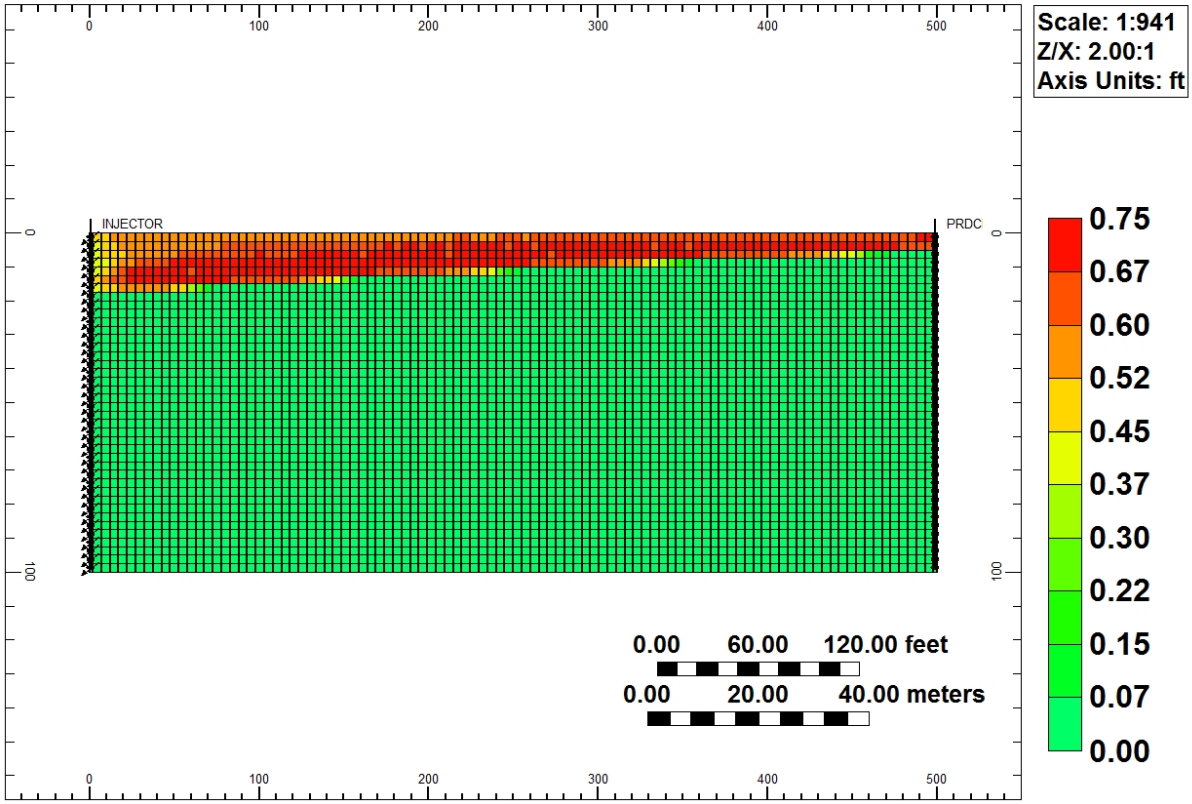
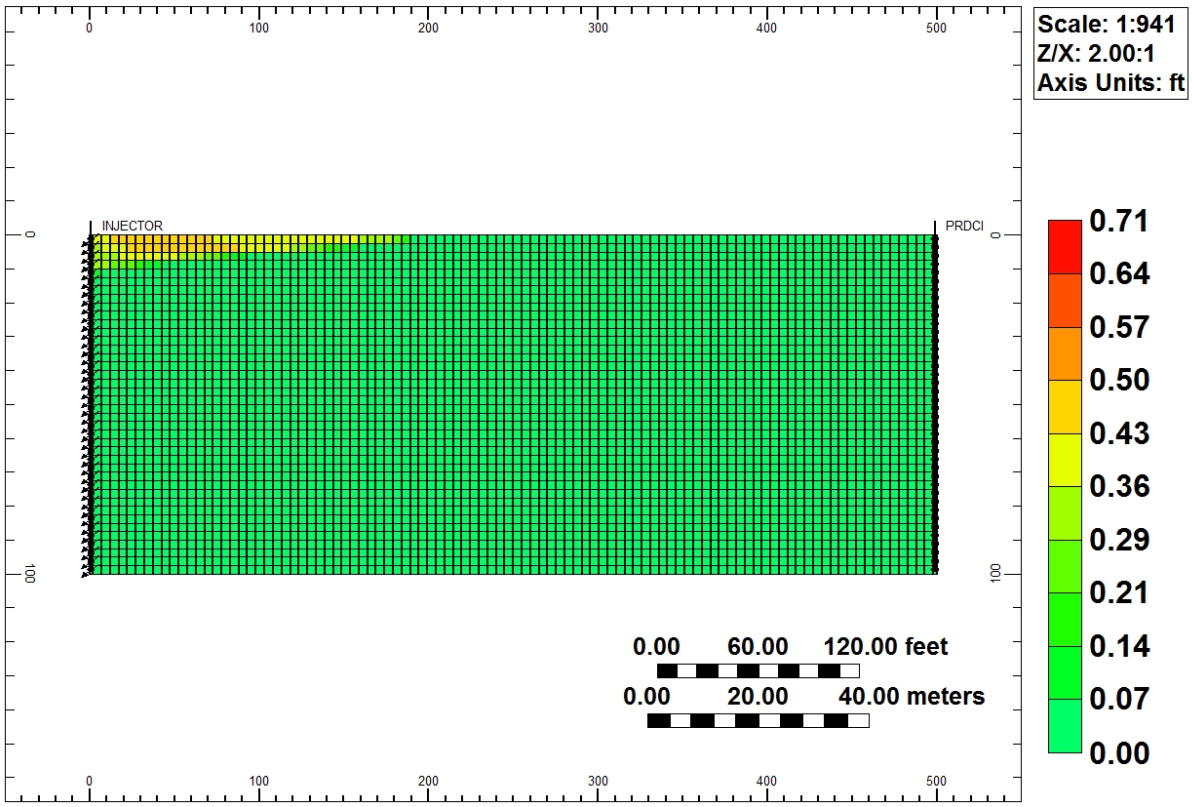


Figure B-3: Cross-section showing steam saturation for the case where the steam injection temperature is 270 °C after 1, 4 and 10 years of steam injection with all other parameters set to the reference values listed in Table 3.5. The injection well is on the left while production well is on the right.



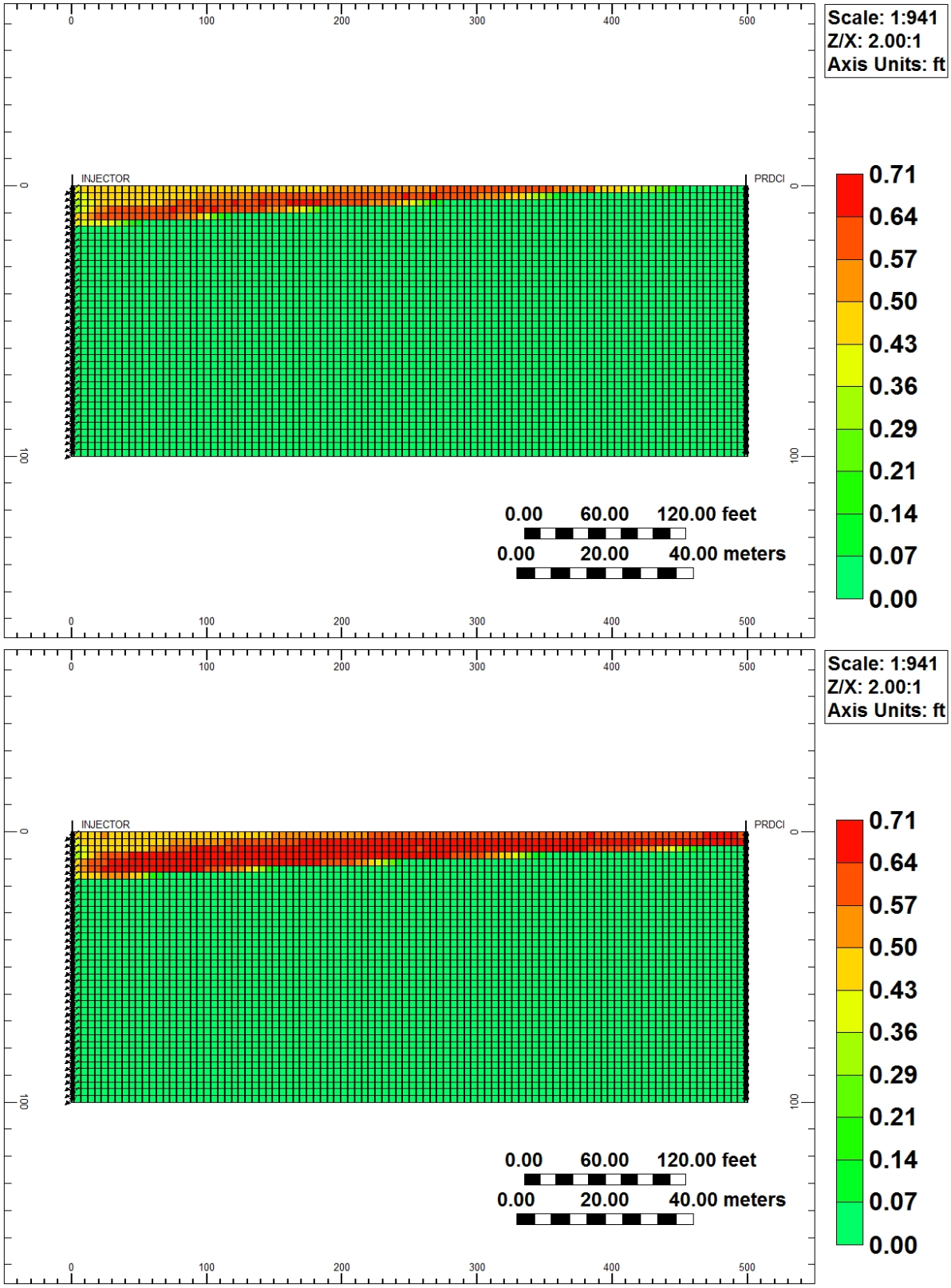
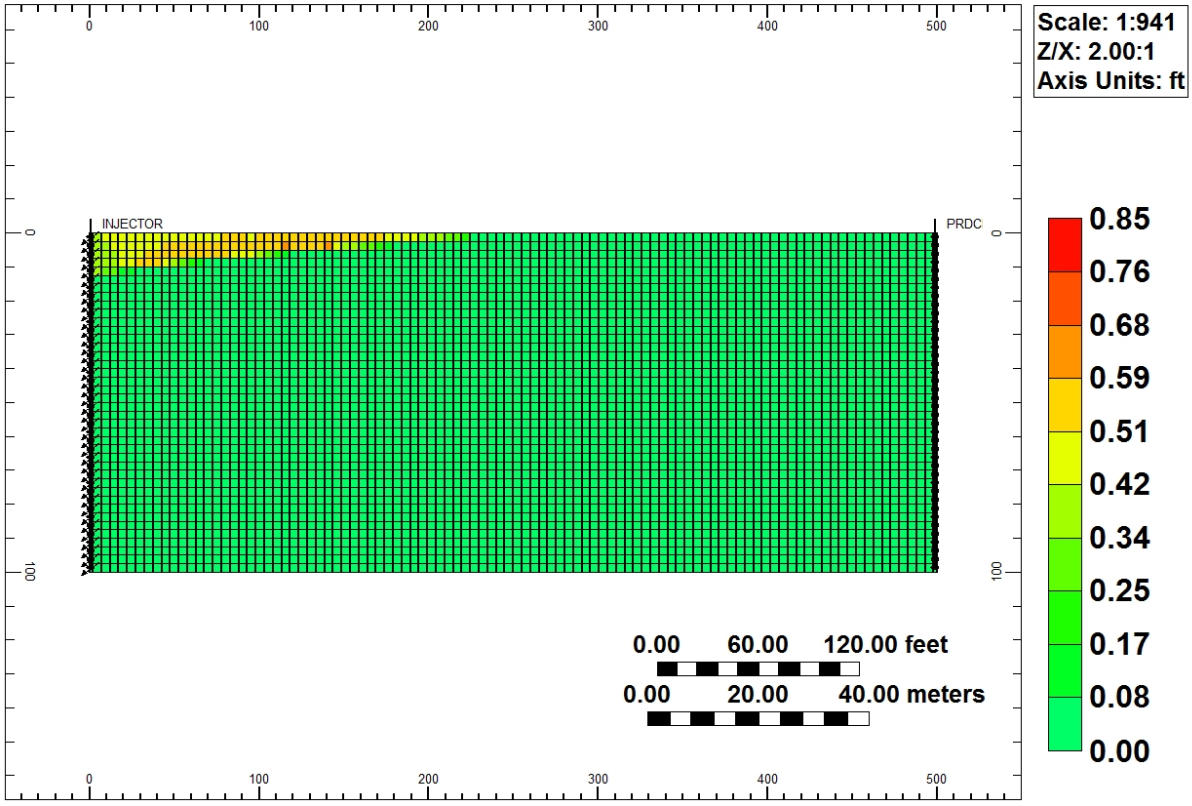
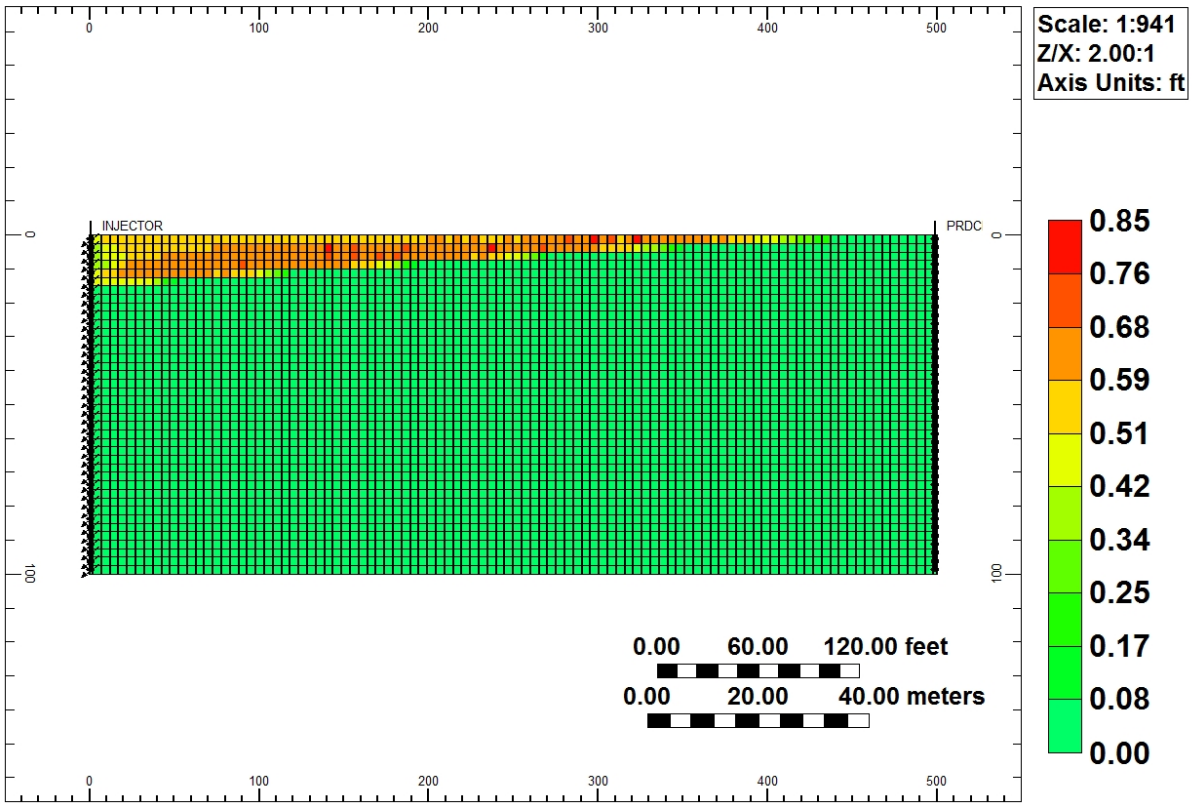


Figure B-4: Cross-section showing steam saturation for the case where the oil API is 14° after 1, 4 and 10 years of steam injection with all other parameters set to the reference values listed in Table 3.5. The injection well is on the left while production well is on the right.


Scale: 1:941
Z/X: 2.00:1
Axis Units: ft
INJECTOR
PRDC
0.00 60.00 120.00 feet
0.00 20.00 40.00 meters
0.85
0.76
0.68
0.59
0.51
0.42
0.34
0.25
0.17
0.08
0.00


Scale: 1:941
Z/X: 2.00:1
Axis Units: ft
INJECTOR
PRDC
0.00 60.00 120.00 feet
0.00 20.00 40.00 meters
0.85
0.76
0.68
0.59
0.51
0.42
0.34
0.25
0.17
0.08
0.00

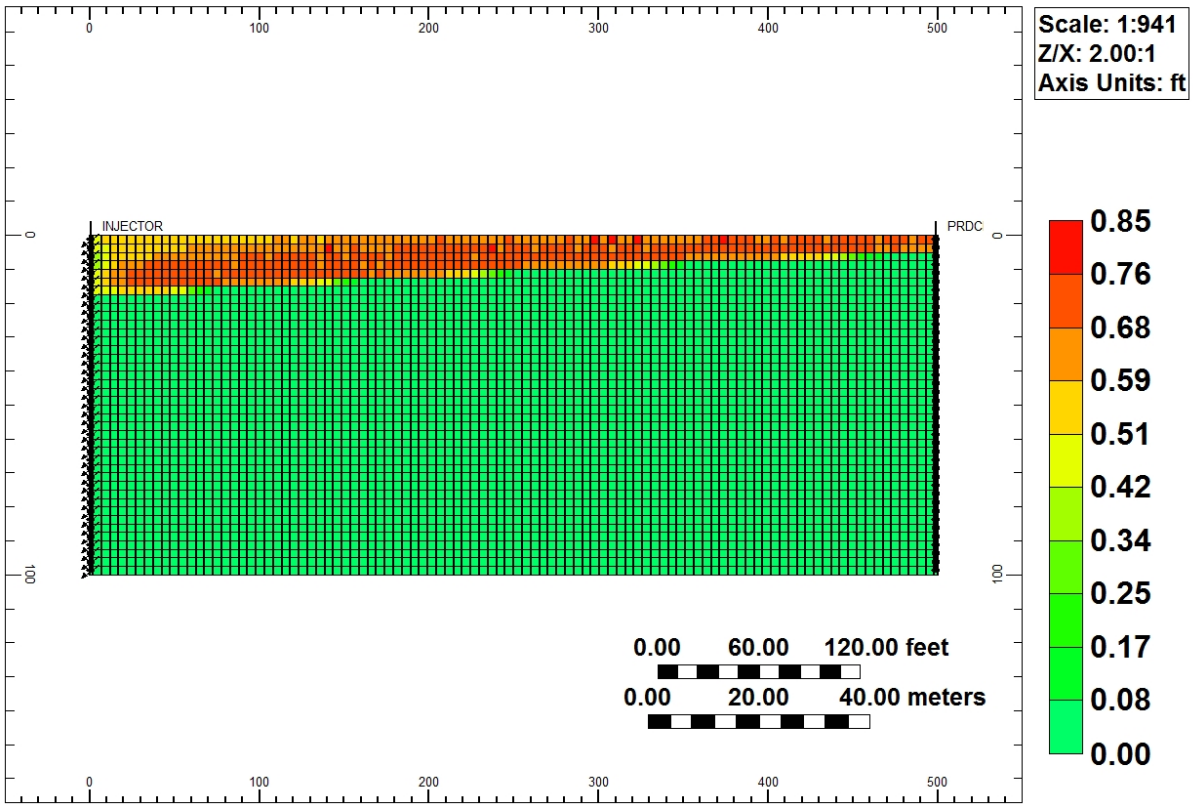
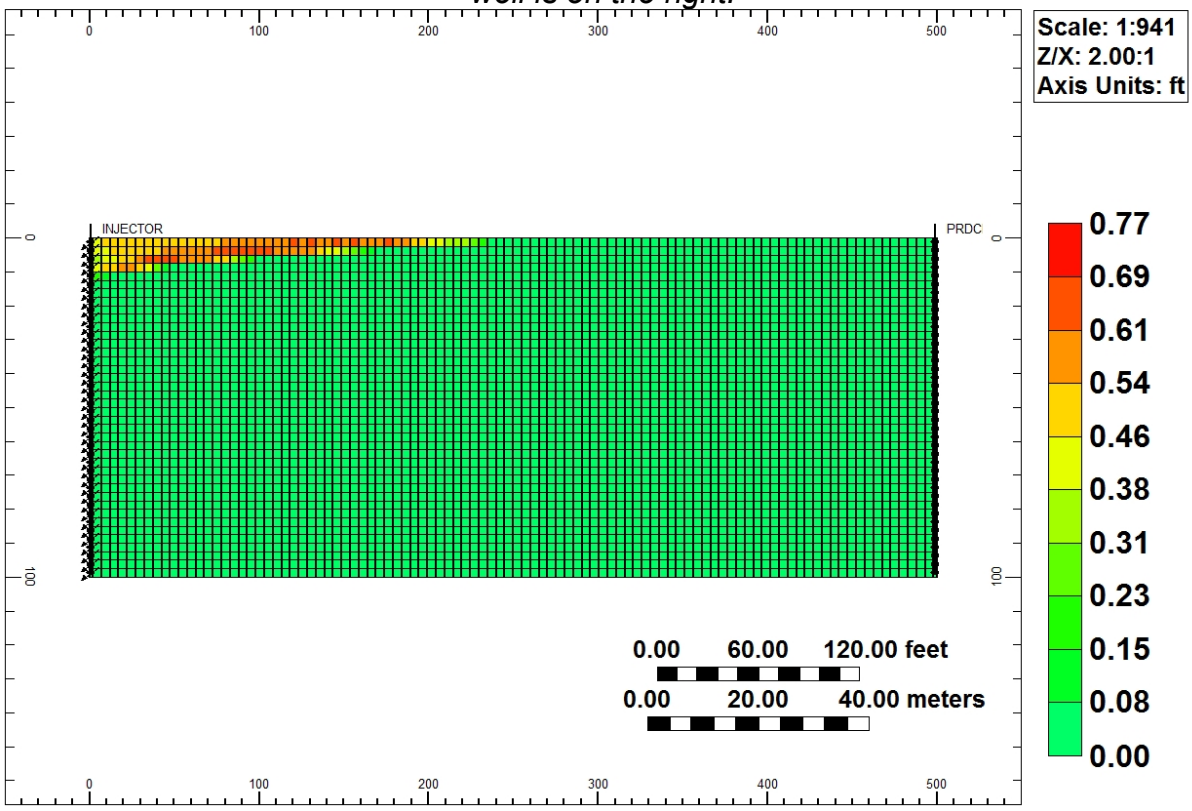


Figure B-5: Cross-section showing steam saturation for the case where porosity is 20% after 1, 4 and 10 years of steam injection with all other parameters set to the reference values listed in Table 3.5. The injection well is on the left while production well is on the right.



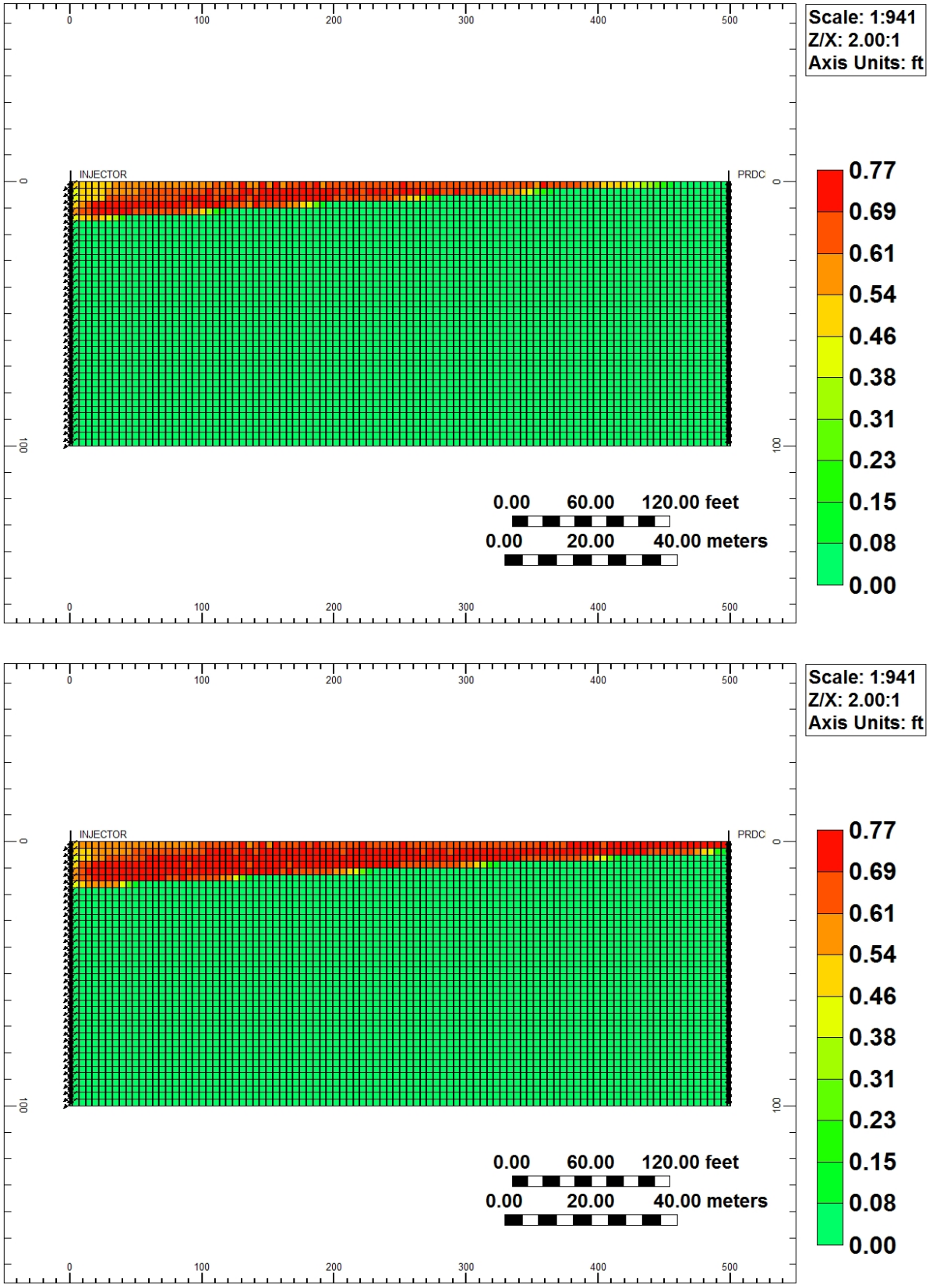
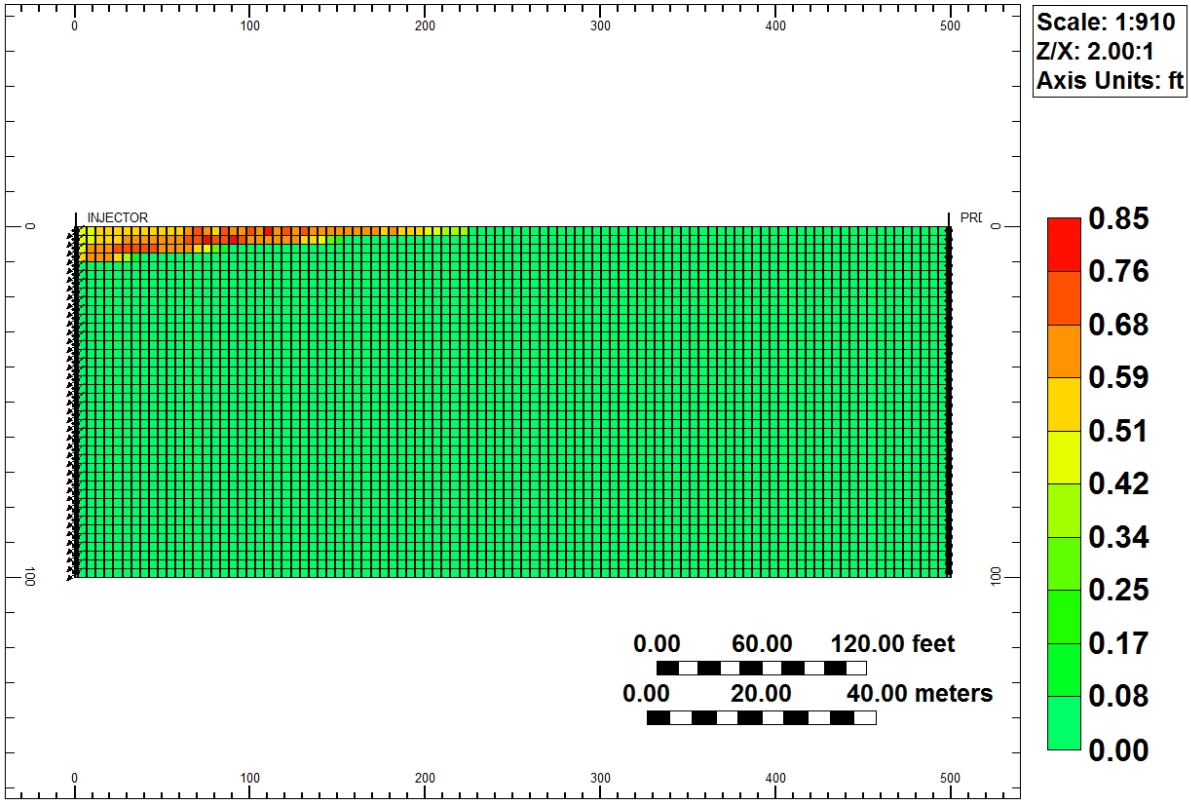
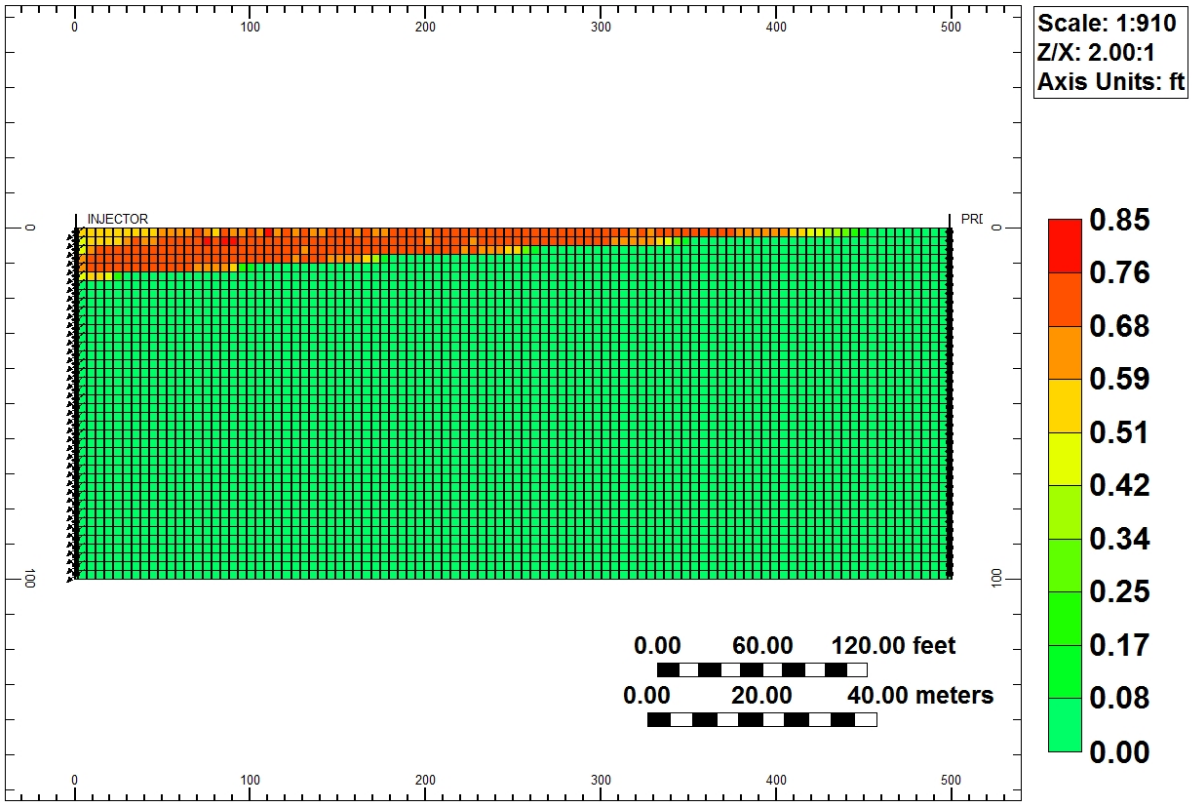


Figure B-6: Cross-section showing steam saturation for the case where the vertical permeability is 0.2 of the horizontal permeability after 1, 4 and 10 years of steam injection with all other parameters set to the reference values listed in Table 3.5. The injection well is on the left while production well is on the right.


Scale: 1:910
Z/X: 2.00:1
Axis Units: ft
INJECTOR
0.85
0.76
0.68
0.59
0.51
0.42
0.34
0.25
0.17
0.08
0.00
0.00 60.00 120.00 feet
0.00 20.00 40.00 meters


Scale: 1:910
Z/X: 2.00:1
Axis Units: ft
INJECTOR
0.85
0.76
0.68
0.59
0.51
0.42
0.34
0.25
0.17
0.08
0.00
0.00 60.00 120.00 feet
0.00 20.00 40.00 meters

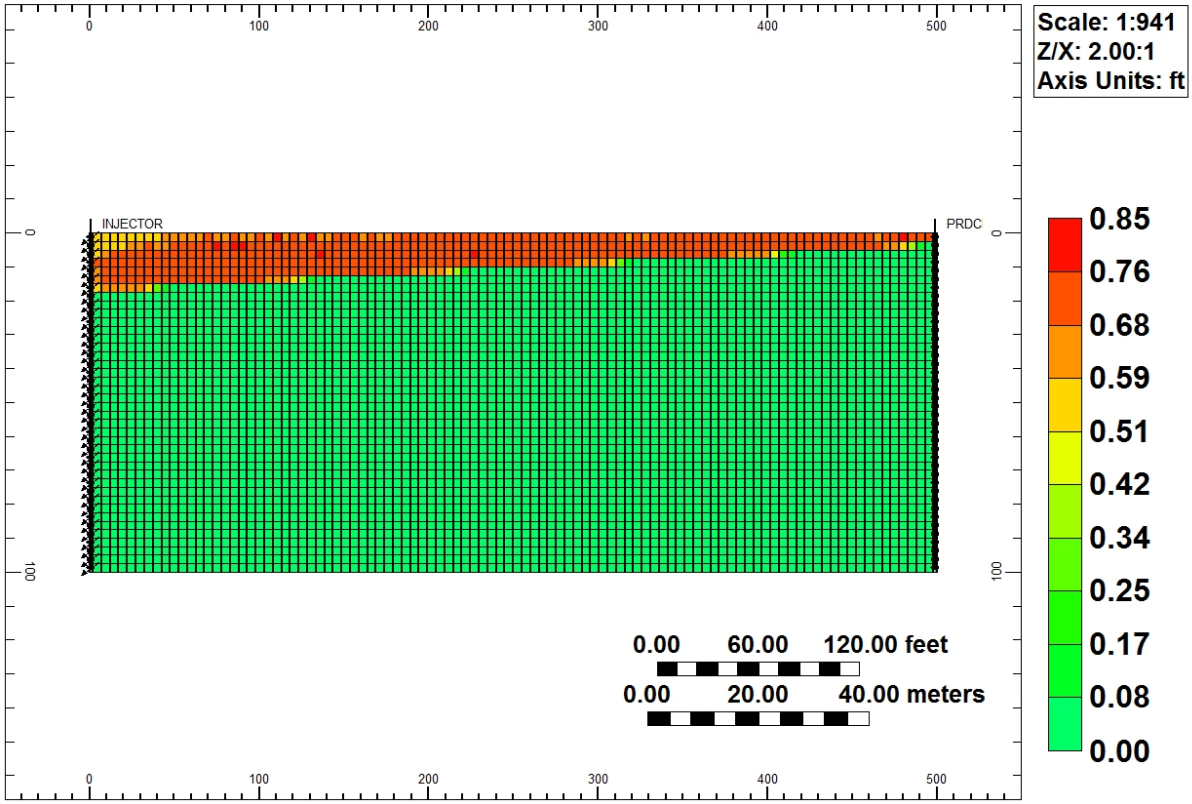


Figure B-7: Cross-section showing steam saturation for the case where the vertical permeability is 0.5 of the horizontal permeability after 1, 4 and 10 years of steam injection with all other parameters set to the reference values listed in Table 3.5. The injection well is on the left while production well is on the right.

Appendix C: MATLAB Rock Physics Code

```
clear all
clc
o=0.30; %porosity
oc=0.36; %critical porosity (o<=oc)
p=0.02; %litho pressure(in GPa)
kg=37; %(in GPa) grain bulk modulus
mg=44; %(in GPa) grain shear modulus
dr=2.65; % density of quartz rock in gm/cm3
T=(0:1:300)'; %Temperature range in Celcius
TT=repmat(T,[1 size(T,1)]);
pp=(0:0.1:30);% pore pressure range in MPa
pppp=repmat(pp,[size(pp,2) 1]);
bs=0.2; % brine salinity in fraction of 1
bsat=0.4; %brine saturation
osat=1-bsat;
api=24;
%%% The grain modulus is calculated from the mineral composition of the
%%%%% rock which is assumed to be known here).
%%% calculating the dry bulk modulus
vg=(3*kg-2*mg)/(6*kg+2*mg);
n=9;%number of grain contacts
kHM=((n^2)*((1-oc)^2)*(mg^2)*p/(18*(pi^2)*((1-vg)^2)))^(1/3);
mHM=((5-4*vg)/(10-5*vg))*(((3*(n^2))*(((1-oc)^2))*(mg^2)*p/(2*(pi^2)*((1-vg)^2)))^(1/3));
z=(mHM/6)*((9*kHM+8*mHM)/(kHM+2*mHM));
a=(o/oc)/(kHM+((4/3)*mHM));
b=(1-(o/oc))/(kg+((4/3)*mHM));
c=(o/oc)/(mHM+z);
d=(1-(o/oc))/(mg+z);
kd=((a+b)^(-1))-((4/3)*mHM); %dry bulk modulus
md=((d+c)^(-1))-z;%dry shear modulus
%%% fluid (brine and oil) bulk modulus calculations
% Brine bulk modulus
dw=1+1e-6.*(-80.*TT-3.3.*TT.^2+0.00175.*TT.^3+489.*pppp-2.*TT.*pppp+0.016.*TT.^2.*pppp-
1.3e-5.*TT.^3.*pppp-0.333.*pppp.^2-0.002.*TT.*pppp.^2);
db=dw+bs.*(0.668+0.44*bs+1e-6.*((300*pppp)-2400.*pppp*bs+TT.*(80+3.*TT-3300*bs-
13.*pppp+47.*pppp*bs)));
w=[ 1402.85 1.524 3.437e-3 -1.197e-5;
```

```
4.871 -0.0111 1.739e-4 -1.628e-6;
-0.04783 2.747e-4 -2.135e-6 1.237e-8;
1.487e-4 -6.503e-7 -1.455e-8 1.327e-10;
-2.197e-7 7.987e-10 5.23e-11 -4.614e-13];
vw=zeros(size(T,1),size(pp,2));
for I=1:size(T,1) % temperature loop
for J=1:size(pp,2) %pressure loop
for i=1:5 %temps coef
for j=1:4 %pressures coef
vw(I,J)=vw(I,J)+w(i,j).*(T(I).^(i-1)).*(pp(J).^(j-1));
end
end
end
end
vb=vw+bs*(1170-9.6*TT+0.055*(TT.^2)-(TT.^3)*8.5e-5+2.6*pppp-0.0029.*TT.*pppp-
0.0476.*(pppp.^2))+(bs^(3/2))*(780-10.*pppp+0.16*(pppp.^2))-1820*(bs^2);
kb=db.*1e3.*(vb.^2);
kw=dw.*1e3.*(vw.^2);
% Dead oil bulk modulus
d0=((api+131.5)/141.5)^-1; %in g/cm^3
dp=d0+(0.00277*pppp-(1.71e-7*(pppp.^3)))*((d0-1.15).^2)+((3.49e-4)*pppp); %pressure
dependance of oil's density
do=dp./(0.972+3.81e-4*((TT+17.78).^1.175)); %in g/cm^3
vo=2096*sqrt(d0./(2.6-d0))-3.7*TT+4.64*pppp+(0.0115.*TT.*pppp.*(4.12*((1.08*(d0^-1)-1)^1.2)-
1)); % in m/s
ko=do.*1e3.*(vo.^2);
%total fluid bulk modulus (oil + brine)
kf=((bsat./kb)+(osat./ko)).^-1; % Reuss fluid average in Pa
%kf2=bsat*kb+osat*ko % Voigt fluid average
a1=1/kg;
a2=1e9./kf;
a3=1/kd;
ksat=kd+(((1-(kd/kg))^2)./((o./(1e-9*kf))+((1-o)*a1)-(kd*(a1^2)))); % in GPa
msat=md; % in GPa
df=1e3*((db.*bsat)+(osat.*do)); %in kg/m^3
vf=sqrt(kf./df);
dsat=o.*df+(1e3*(1-o)*dr); %in kg/m^3
vpsat=sqrt(((1e9*ksat)+((4/3)*1e9*msat))./dsat); % in m/s
vssat=sqrt(1e9*msat./dsat);
```

```
pp=(0:0.25:25);% pore pressure range in MPa
pppp=repmat(pp,[size(pp,2) 1]);
subplot(3,3,1),imagesc(kf');set(gca,'YTickLabel',5:5:30);xlabel('Temperature
(∞C)','FontWeight','bold','FontSize',16);ylabel('Pressure
(MPa)','FontWeight','bold','FontSize',16);title('Pore fluid (oil +
brine)','FontWeight','bold','FontSize',18);
subplot(3,3,4),imagesc(df');set(gca,'YTickLabel',5:5:30);xlabel('Temperature
(∞C)','FontWeight','bold','FontSize',16);ylabel('Pressure (MPa)','FontWeight','bold','FontSize',16)
subplot(3,3,7),imagesc(vf');set(gca,'YTickLabel',5:5:30);xlabel('Temperature
(∞C)','FontWeight','bold','FontSize',16);ylabel('Pressure (MPa)','FontWeight','bold','FontSize',16)
%subplot(4,3,10),imagesc(vssat');set(gca,'YTickLabel',10:10:30);xlabel('Temperature
(∞C)','FontWeight','bold','FontSize',16);ylabel('Pressure (MPa)','FontWeight','bold','FontSize',16)
```

References

Abdel-Halim, T., & Subramanian, M. (2002). U.S. Patent No. 6,357,526. Washington, DC: U.S. Patent and Trademark Office.

Abdalla, A. (1976, January). Practical Application Of Steam Flood Model To The Design Of Emlechheim Steam Injection Project. In Annual Technical Meeting. Petroleum Society of Canada.

Abubakar, S. (2016). Upscaling for thermal recovery.

Aleklett, K., Höök, M., Jakobsson, K., Lardelli, M., Snowden, S., & Söderbergh, B. (2010). The Peak of the Oil Age-Analyzing the world oil production Reference Scenario in World Energy Outlook 2008. Energy Policy, 38(3), 1398-1414. doi: 10.1016/j.enpol.2009.11.021

Altunina, L. K., & Kuvshinov, V. A. (2008). Improved oil recovery of high-viscosity oil pools with physicochemical methods and thermal-steam treatments. Oil & Gas Science and Technology-Revue de l'IFP, 63(1), 37-48.

Alusta G, Mackay E, Fennema J, Armih K, Collins I. (2012). EOR vs. infill well drilling: sensitivity to operational and economic parameters. In Proc. North Africa Technical Conf. and Exhibition, Cairo, Egypt, 20-22 February 2012. Tusla, OK: Society of Petroleum Engineers. SPE-150454 MS

Alvarado, V., & Manrique, E. (2010). Enhanced Oil Recovery: An Update Review. Energies, 10, 1529-1575. doi: 10.3390/en3091529

Alvarado, V., & Manrique, E. (2010). Enhanced oil recovery: Field planning and development strategies. Gulf Professional Publishing.

Alvarez, J., & Han, S. (2013). Current overview of cyclic steam injection process. Journal of Petroleum Science Research.

Ambastha, A. (2008). Heavy-oil Recovery. Society of Petroleum Engineers.

Avseth, P., Mukerji, T. & Mavko, G. (2005) Quantitative Seismic Interpretation, Cambridge University Press.

Bao, Y., Wang, J., & Gates, I. D. (2016). On the physics of cyclic steam stimulation. Energy, 115, 969 985. doi:10.1016/j.energy.2016.09.031

Batzle, M. and Wang, Z. (1992). Seismic properties of pore fluids. Geophysics, 57, 1396-1408.

Batzle, M., Hofmann, R., Han, D. (2006). Heavy oils-Seismic properties; The Leading Edge, 25, 750-756.

Bauer, A., Korndorffer, F. and van der Linden, A. (2011, June). Thermal rock physics of heavy- oil saturated sands. 45 th US rock mechanics/ geomechanics symposium, San Francisco, U.S.A.

Bell, F., Cripps, J., & Culshaw, M. (1986). A review of the engineering behaviour of soils and rocks with respect to groundwater. Geological Society, London, Engineering Geology Special Publications, 3(1), 1-23. doi:10.1144/gsl.eng.1986.003.01.01

Berron, C., Michou, L., Cacqueray, B. D., Duret, F., Cotton, J., & Forgues, E. (2015). Permanent, continuous & unmanned 4D seismic monitoring: Peace River case study. In SEG Technical Program Expanded Abstracts 2015 (pp. 5419-5423). Society of Exploration Geophysicists. doi: 10.1190/segam2015-5813292.1

Berryman, J.G. (1995). Mixture theories for rock properties. In Rock Physics and Phase Relations: a Handbook of Physical Constants, ed. T.J. Ahrens. Washington, DC: American Geophysical Union, pp. 205-228.

Bjorkum, P. A., & Nadeau, P. H. (1998). Temperature controlled porosity/permeability reduction, fluid migration, and petroleum exploration in sedimentary basins. The APPEA Journal, 38(1), 453-465.

Brandt, A. R., & Unnasch, S. (2010). Energy Intensity and Greenhouse Gas Emissions from Thermal Enhanced Oil Recovery. Energy Fuels, 24, 4581-4589.

doi: 10.1021/ef100410f

Busfar, H., & Toksöz, M. N. (2013). Determining the focal mechanisms and depths of relatively small earthquakes using a few stations by full waveform modelling. Geophysical Prospecting,1-13. doi:10.1111/1365-2478.12018

Butler, D. K. (2005). Near-surface geophysics. Society of Exploration Geophysicists.

Butler, R. M. (1994). Steam-assisted gravity drainage: concept, development, performance and future. Journal of Canadian Petroleum Technology, 33(02), 44-50. doi: 10.2118/94-02-05

Cairns, G. (2012). Time-lapse seismic monitoring of CO_2 storage in saline aquifers: a model-based sensitivity study. (Unpublished doctoral dissertation).

Cengel, Yunus A., & Boles, Michael A. (2002). Thermodynamics: an engineering approach. Boston, Massachusetts*:* McGraw-Hill*. p. 79.* ISBN 0-07-121688-X*.*

Chen, M. A. P., Riedel, M., & Dosso, S. E. (2010). Seismic AVO for gas-hydrate-related reflections. In Geophysical Characterization of Gas Hydrates (pp. 73-93). Society of Exploration Geophysicists.

Chopra, S., Lines L., Schmitt D. & Batzle M. (2010). Heavy oil Reservoirs: Their Characterization and Production. Heavy Oils 1-69

Chuhan, F. A., Kjeldstad, A., Bjørlykke, K., and Høeg, K. (2003). Experimental compression of loose sands: relevance to porosity reduction during burial in sedimentary basins. Canadian Geotechnical Journal, 40, 995-1011. doi: 10.1139/ T03-050

Cooper, M. (2010). Methods and applications in reservoir geophysics. (1 ed., Vol. 15, p. 114). Society of Exploration Geophysicists.

Cotton, J., Forgues, E., & Hornman, J. C. (2012). Land seismic reservoir monitoring: Where is the steam going? In SEG Technical Program Expanded Abstracts 2012 (pp. 1-5). Society of Exploration Geophysicists.

Curtis, C., Kopper, R., Decoster, E., Guzmán-Garcia, A., Huggins, C., Knauer, L., Minner, M., Kupsch, N., Linares, L., Rough, H., Waite, M. (2002). Heavy-oil reservoirs. Oilfield Review, 14(3), 30-51.

Dadashpour, M., Echeverria-Ciaurri D., Kleppe J. & Landro M. (2009). Porosity and permeability estimation by integration of production and time-lapse near and far offset seismic data. Journal of Geophysics and Engineering 6(4): 325-244

Dale, S., & Fattouh, B. (2018). Peak oil demand and long-run oil prices. Energy Insight, 25.

Dandekar, A. Y. (2013). Petroleum reservoir rock and fluid properties. CRC press.

Davis, T. L., Bibolova, A., O'Brien, S., Klepacki, D., & Robinson, H. (2013). Prediction of residual oil saturation and cap-rock integrity from time-lapse, multicomponent seismic data, Delhi Field, Louisiana. The Leading Edge, 32(1), 26-31.

Dreier, M. (2009, April). The Emlichheim Oilfield-45 Years of EOR and No End. In IOR 2009-15th European Symposium on Improved Oil Recovery.

Dusseault M.B. (1980) Sample disturbance in Athabasca oil sand, Journal of Canadian Petroleum Technology. 19 (4), 85-92. doi: 10.2118/80-02-06

Eastwood, J. (1993). Temperature-dependent propagation of p- and s-waves in cold lake oil sands: Comparison of theory and experiment. Geophysics, 58(6), 863-872.

Fanchi, John R. (2001). Time-lapse seismic monitoring in reservoir management. The Leading Edge, 20(10), 1140-1147. doi:10.1190/1.1487246

Fawad, M., Mondol, N. H., Jahren, J., & Bjørlykke, K. (2011). Mechanical compaction and ultrasonic velocity of sands with different texture and mineralogical composition. Geophysical Prospecting, 59(4), 697-720. doi:10.1111/j.1365-2478.2011.00951.x

Ferguson, M. A., Mamora, D. D., & Goite, J. G. (2001, January). Steam-propane

injection for production enhancement of heavy Morichal oil. In SPE International Thermal Operations and Heavy Oil Symposium. Society of Petroleum Engineers. doi:10.2118/69689-MS

Forgues, E., Meunier, J, Grésillon, FX, Hubans, C. & Druesne, D. (2006, October). Continuous High-resolution monitoring of SAGD. SEG Technical Program Expanded Abstracts 2006: pp.3165-3169. New Orleans, Louisiana, U.S.A. doi: 10.1190/1.2370186

Forgues, E., Schisselé, E., & Cotton, J. (2011). Simultaneous active and passive seismic monitoring of steam-assisted heavy oil production. The Leading Edge, 30(11), 1288 1294.

Fossen, H. (2016). *Structural geology*. Cambridge: Cambridge University Press.

Fourie, C., & van Dam, C. (2008, Nov/Dec). Planning for Shallow high-resolution seismic surveys. PositionIT, 22-25.

Francese, R., Hajnal, Z., & Prugger, A. (2002). High-resolution images of shallow aquifers - A challenge in near-surface seismology. Geophysics, 67(1), 177-187. doi: 10.1190/1.1451490

García, X. and Medina, E. (2006). Hysteresis effects studied by numerical simulations: Cyclic loading-unloading of a realistic sand model. GEOPHYSICS, 71(2), F13– F20.doi:10.1190/1.2181309

Gassmann, F. (1951). Über die Elastizität poroser Medien. Veirteljahrss-chrift der Naturforschenden Gesellschaft in Zürich, 96, 1-23

Geo ExPro (2006). Time to redevelop an abandoned European oilfield? URL: https://assets.geoexpro.com/legacy-files/articles/Time%20to%20Redevelop%20an%20Abandoned%20European%20Oilfield.pdf [30 January 2019]

Gholamy, A., & Kreinovich, V. (2014, December). Why Ricker wavelets are successful in processing seismic data: Towards a theoretical explanation. In 2014 IEEE Symposium on Computational Intelligence for Engineering Solutions (CIES)(pp. 11-16). IEEE.

Gray, N. D., Sherry, A., Hubert, C., Dolfing, J., & Head, I. M. (2010). Methanogenic degradation of petroleum hydrocarbons in subsurface environments: remediation, heavy oil formation, and energy recovery. Advances in applied microbiology, 72, 137-161.

Gu, F., Chan, M., Fryk, R. (2011). Geomechanical-Data Acquisition, Monitoring, and Applications in SAGD. Journal of Canadian Petroleum Technology, 50(6), 9-21. doi:10.2118/145402-PA

Han, D. H., & Batzle, M. (2002). Fizz water and low gas-saturated reservoirs. *The Leading Edge*, *21*(4), 395-398.

Han, D., Liu, J., & Baztle, M. (2008). Seismic properties of heavy oils-measured data. The Leading Edge, 27(9), 1108-1115. doi: 10.1190/1.2978972

Han, D., Zhao, H., Yao, Q., Batzle, M. (2007) Velocity of heavy oil sand. SEG Technical Program Expanded Abstracts: pp. 1619-1623.

Hanor, J. S. (1994). Origin of saline fluids in sedimentary basins. Geological Society, London, Special Publications, 78(1), 151-174.

Hashin, Z. and Shtrikman, S. (1963). A variational approach to the theory of elastic behaviour of multiphase materials. Journal of the Mechanics and Physics of Solids, 11, 127-140.

Hoversten, G. M., Milligan, P., Byun, J., Washbourne, J., Knauer, L. C., & Harness, P. (2004). Crosswell electromagnetic and seismic imaging: An examination of coincident surveys at a steam flood project. Geophysics, 69(2), 406-414.

Iglauer, S., Wu, Y., Shuler, P., Tang, Y., & Goddard, W. A. (2010). New surfactant

classes for enhanced oil recovery and their tertiary oil recovery potential. Journal of Petroleum Science and Engineering, 71(1), 23-29.

Issa, M., & Fleming, J. (2011, December). Heavy oil production with steam injection using ESPs. Society of Petroleum Engineers, Kuwait City, Kuwait. doi: 10.2118/150646-MS

Istchenko, C. M., & Gates, I. D. (2013). Well/Wormhole Model of Cold Heavy-Oil Production with Sand. Society of Petroleum Engineers. Annual Conference & Exhibition held on 2nd October 2013 in New Orleans, Louisiana, USA SPE-150633-PA

Jenkins, S. D., Waite, M. W., & Bee, M. F. (1997). Time-lapse monitoring of the Duri steamflood: A pilot and case study. The Leading Edge, 16(9), 1267-1274.

Kato, A., Onozuka, S., Nakayama, T. (2008). Elastic property changes in a bitumen reservoir during steam injection . The Leading Edge, 27(9), 1124-1131. doi: 10.1190/1.2978974

Kockel, F., Wehner, H., & Gerling, P. (1994). Petroleum Systems of the Lower Saxony Basin, Germany: Chapter 34: Part VI. Case studies—Eastern Hemisphere.

Laine, E. F. (1987). Remote monitoring of the steam-flood enhanced oil recovery process. Geophysics, 52(11), 1457-1465.

Larter, S., Adams, J., Gates, I. D., Bennett, B., & Huang, H. (2008, January 1). The Origin, Prediction and Impact of Oil Viscosity Heterogeneity on the Production Characteristics of Tar Sand and Heavy Oil Reservoirs. Petroleum Society of Canada. doi:10.2118/08-01-52

Leonhardt, B. (2001). Enhanced steamflood effectiveness by horizontal producers. In Proc. SPE International Thermal Operations and Heavy Oil Symposium held on 12-14 March 2001 in Porlamar, Margarita Island, Venezuela. SPE-69707

Lerat, O., Adjemian, F., Baroni, A., Etienne, G., Renard, G., Bathellier, E., Forgues,

E., Aubin, F. (2010). Modelling of 4D Seismic Data for the Monitoring of Steam Chamber Growth During the SAGD Process. Journal of Canadian Petroleum Technology, 49(6), 21-29. doi: 10.2118/138401-PA

Li, G., Purdue, G., Weber, S., & Couzens, R. (2001). Effective processing of nonrepeatable 4-D seismic data to monitor heavy oil SAGD steam flood at East Senlac, Saskatchewan, Canada. The Leading Edge, 20(1), 54-62.

Liu, W. Z. (1987). Pilot steam soak operations in deep wells in China. Journal of petroleum technology, 39(11), 1-441.

Lopez, J.L., Wills, P.B., La Follett, J.R., Barker, T.B., Xue, Y., Przybysz-Jarnut, J.K., Potters, J.H.H.M., van Lokven, M., Brouwer, D.R. and Berron, C. (2015, June). Real-time seismic surveillance of thermal EOR at Peace River. In SPE Canada Heavy Oil Technical Conference. Society of Petroleum Engineers.

Lumley, D. E. (1995). 4-D seismic monitoring of an active steamflood. In SEG Technical Program Expanded Abstracts 1995 (pp. 203-206). Society of Exploration Geophysicists.

Lumley DE. (2001). Time-Lapse seismic reservoir monitoring. Geophysics 66, 50-53.

Lumley, D. E., Bee, M., Jenkins, S., & Wang, Z. (1995). 4-D seismic monitoring of an active steamflood. 65th Ann. Internat. Mtg: Soc. of Expl. Geophys, 203-206.

Magoon, L. B. (1988). The petroleum system—a classification scheme for research, exploration, and resource assessment. Petroleum systems of the United States: US Geological Survey Bulletin, 1870, 2-15.

Mavko, G., Mukerji, T. and Dvorkin, J. (2009) The Rock Physics Handbook. Tools for Seismic Analysis of Porous Media. (2nd ed.). New York, NY: Cambridge University Press.

Meents, W. F., Friedman, I., & Shimp, N. F. (1966). The origin of saline formation waters, III: Calcium chloride waters. State of Illinois, Department of Registration and Education, Illinois State Geological Survey.

Mindlin, R. D. (1949) Compliance of elastic bodies in contact. Journal of Applied Mechanics, 16, 259-1360.

Mochinaga, H., Onozuka, S., Kono, F., Ogawa, T., Takahashi, A., Torigo, T. (2006) Properties of oil sands and bitumen in Athabasca. Canadian Society of Exploration Geophysics Annual convention. Expanded Abstracts: pp. 39-44.

Moulds, T.P., Trussell P, Haseldonckx SA, Carruthers RA. (2005). Magnus field: reservoir management in a mature field combining waterflood, EOR and new area developments. In Proc. SPE Offshore Europe Conference held on 6-9 September 2005 at Aberdeen, UK. SPE-96292-MS

Muggeridge, A., Cockin, A., Webb, K., Frampton, H., Collins, I., Moulds, T., & Salino, P. (2014). Recovery rates, enhanced oil recovery and technological limits. Philosophical Transactions of the Royal Society A: Mathematical, Physical and Engineering Sciences, 372(2006), 20120320. doi:10.1098/rsta.2012.0320

Nalonnil, A., Marion, B. (2012). High-resolution reservoir monitoring using crosswell seismic. Society of Petroleum Engineers. 15(1), 25-30. doi:10.2118/132491-PA

Nauroy, J., Doan, D., Guy, N., Baroni, A., Delage, P. and Mainguy, M. (2012). Evolution of seismic velocities in heavy oil sand reservoirs during thermal recovery process. Oil and Gas Science and Technology , 67(6), 1029-1039. doi: 10.2516/ ogst/2012027

Oil Market Report. International Energy Agency, 13 Mar 2013. Web. 5 Apr 2013.

Owen, N.A., Inderwildi, O.R. and King, D.A. (2010). The status of conventional world oil reserves - Hype or cause for concern?. Energy Policy, 38(8), 4743-4749. doi: 10.1190/1.1567211

Passalacqua, H., & Strack, K. (2016). Integrated Geophysical Reservoir Monitoring for Heavy Oil. SPE Heavy Oil Conference and Exhibition, 6-8 December, Kuwait City, Kuwait. SPE-184089-MS.

Paydayesh, M., Murineddu, A., Mukherjee, A., & Koeninger, C. (2018, November). Quantitative Interpretation of a time-lapse seismic for steam injection monitoring in a heavy oil reservoir. In EAGE Workshop on 4D Seismic and Reservoir Monitoring: Bridge from Known to Unknown.

Reuss, A., 1929. Berechnung der Fließgrenze von Mischkristallen auf Grund der Plastizitätsbedingung für Einkristalle. Z. Ang. Math. Mech., 9, 49-58.

Rivero, J. A., & Mamora, D. D. (2005). Production acceleration and injectivity enhancement using steam-propane injection for Hamaca extra-heavy oil. Journal of Canadian Petroleum Technology, 44(02).

Robertson, J. O., Chilingar, G. V., Khilyuk, L. F., & Endres, B. (2012). The environmental aspects of oil and gas production subsidence. Energy

Robertsson, J., Holliger, K., Green, A., Pugin, A., & De Iaco, R. (1996). Effects of near-surface waveguides on shallow high-resolution seismic refraction and reflection data. Geophysical Research Letters, 23(5), 495-498.

Ross, Christopher P., & Altan, M. Suat (1997). Time lapse seismic monitoring: Some shortcomings in nonuniform processing. The Leading Edge, 16(6), 931-937. doi:10.1190/1.1437701

Sarma, P., Fowler, G., Henning, M., Kyriacou, S., Thakur, G., Sloss, D., & Shipley, W. (2017, April). Cyclic Steam Injection Modeling and Optimization for Candidate Selection, Steam Volume Optimization, and SOR Minimization, Powered by Unique, Fast, Modeling and Data Assimilation Algorithms. In SPE Western Regional Meeting. Society of Petroleum Engineers. doi: 10.2118/185747-MS

Schlumberger (2017). Tertiary recovery. Retrieved September 15, 2017, from

http://www.glossary.oilfield.slb.com/Terms/t/tertiary_recovery.aspx

Sengupta, M., Mavko, G. (2003). Impact of flow-simulation parameters on saturation scales and seismic velocity. Geophysics,68(4), 1267-1280. doi: 10.1190/1.1598119

Setiawan, A., Suekane, T., Deguchi, Y., & Kusano, K. (2014). Pore-scale investigation of the effect of connate water on water flooding behavior. Journal of Fluid Science and Technology, 9(2), JFST0012-JFST0012.

Shabelansky, A. H., Malcolm, A. and Fehler, M. (2015), Monitoring viscosity changes from time lapse seismic attenuation: case study from a heavy oil reservoir. Geophysical Prospecting, 63: 1070-1085. doi:10.1111/1365-2478.12229

Shah, A., Fishwick, R., Wood, J., Leeke, G., Rigby, S., & Greaves, M. (2010). A review of novel techniques for heavy oil and bitumen extraction and upgrading. Energy & Environmental Science, 3, 700-714. doi: 10.1039/b918960b

Sheng, J. J. (2013). Cyclic steam stimulation. In Enhanced Oil Recovery Field Case Studies (pp. 389-412). doi: 10.1016/B978-0-12-386545-8.00016-6

Smith, T., Sondergeld, C. and Rai, C. (2003). Gassmann fluid substitutions: A tutorial. Geophysics, 68(2), 430-440. doi: 10.1190/1.1567211

Solaimany-Nazar, A. R., & Zonnouri, A. (2011). Modeling of asphaltene deposition in oil reservoirs during primary oil recovery. Journal of Petroleum Science and Engineering, 75(3), 251-259.doi: 10.1016/j.petrol.2010.11.017

Sorrell, S., Miller, R., Bentley, R., & Speirs, J. (2010). Oil futures: A comparison of global supply forecasts. Energy Policy, 38, 4990-5003. doi: 10.1016/j.enpol.2010.04.020

Spetzler, J. (2006, October). Time-lapse seismic crosswell monitoring of steam injection in tar sand. SEG annual meeting, New Orleans, Louisiana Tanaka, M.,

Endo, K., Onozuka, S. (2010). Estimation of Steam Chamber Extent Using 4D Seismic. Journal of Canadian Petroleum Technology 49(5), 50-55.

Sydansk RD, Seright RS. (2007). When and where relative permeability modification water-shut-off treatments can be successfully applied. SPE/DOE Symposium on Improved Oil Recovery, 22-26 April, Tulsa, Oklahoma, USA. SPE-99371-MS

Thomas, S. (2008). Enhanced oil recovery-an overview. Oil & Gas Science and Technology-IFP Review, 63(1), 9-19. doi:10.2516/ogst:2007060

Trigos, E. M., Avila, R. D., Lozano, M. E., Jimenez, A. M., & Osorio, C. A. (2016, October). Strategies to Increase Production in a Colombian Heavy Oil Field with Cyclic Steam Stimulation. In SPE Latin America and Caribbean Heavy and Extra Heavy Oil Conference. Society of Petroleum Engineers. doi:10.2118/181198-MS

Upadhyay, S. K. (2004). Seismic reflection processing: with special reference to anisotropy. Berlin: Springer. doi:10.1007/978-3-662-09843-1

Walpole, L. J. (1966). On bounds for the overall elastic moduli of inhomogeneous systems- Journal of the Mechanics and Physics of Solids, 14, 151-162. doi: 10.1016/0022-5096(66)90035-4

Wang, J., Dong, M., & Asghari, K. (2006). Effect of Oil Viscosity on Heavy Oil-Water Relative Permeability Curves. SPE/DOE Symposium on Improved Oil Recovery, 22-26 April, Tulsa, Oklahoma, USA. doi:10.2118/99763-MS

Wang, Z. (2001). Fundamentals of seismic rock physics. Geophysics, 66(2), 398-412. doi:10.1190/1.1444931

Wang, Z., & Nur, A. (1986). Effect of temperature on wave velocities in sands and sandstones with heavy hydrocarbons. In SEG Technical Program Expanded Abstracts 1986 (pp. 3-5). Society of Exploration Geophysicists. doi:10.1190/1.1893070

Wang, Z., Nur, A. (1990). Wave velocities in hydrocarbon-saturated rocks: Experimental results. Geophysics, 55(6), 723-733. doi:10.1190/1.1442884

Waxman, M. H., & Smits, L. J. M. (1968). Electrical conductivities in oil-bearing shaly sands. Society of Petroleum Engineers Journal, 8(02), 107-122. doi:10.2118/1863-A

Wilson, A. (2014). Continuous Seismic Reservoir Monitoring of Thermal Enhanced Oil Recovery. Journal of Petroleum Technology, 66(06), 119-121.

Wintershall (2012) 10 million tons of crude oil from Emlichheim. URL: http://www.reading.ac.uk/library/finding-info/guides/lib-citing-web.aspx [26 April 2013]

Yitang, Z., Xiuluan, L., & Xia, Z. (2008). Four fundamental principles for design and follow-up of steam flooding in heavy oil reservoirs. Petroleum Exploration and Development, 35(6), 715-719.

Yuan, H. and Han, D. (2013) Pressure and temperature effect on heavy-oil sand properties. SEG Technical Program Expanded Abstracts: pp. 2984-2988. doi: 10.1190/segam2013-1196.1

Zhang, W., Youn, S., & Doan, Q. T. (2007). Understanding reservoir architectures and steam-chamber growth at Christina Lake, Alberta, by using 4D seismic and crosswell seismic imaging. SPE Reservoir Evaluation & Engineering, 10(05), 446-452. doi: 10.2118/97808-PA

Zoeppritz, K. (1919) Erdbebenwellen VIIIB, On the reflection and propagation of seismic waves. Gottinger Nachr, I, 66-84.